Distinct Element Modelling of Jointed Rock Masses: Algorithms and Their Verification

by

Chia Weng Boon

A thesis submitted for the degree of
Doctor of Philosophy
at the University of Oxford

St Cross College
Trinity Term 2013

ABSTRACT

DISTINCT ELEMENT MODELLING OF JOINTED ROCK MASSES: ALGORITHMS AND THEIR VERIFICATION

A thesis submitted for the degree of Doctor of Philosophy

Chia Weng Boon
St Cross College, Oxford
Trinity Term, 2013

The distinct element method (DEM) is a useful tool in rock engineering to model jointed rock masses. To simulate a jointed rock mass realistically, the main challenge is to be able to capture its complex geometry which consists of blocks with various shapes and sizes, and to model the interactions between these blocks.

The main contribution of this thesis is the development of novel algorithms in the DEM to model jointed rock masses, namely rock slicing procedures for block generation, and algorithms for contact detection between polygonal blocks in 2-D or polyhedral blocks in 3-D. These algorithms make use of convex optimisation techniques, for which there exist efficient solution procedures. They do not rely on conventional vertex-edge-face hierarchical data structures and tedious housekeeping algorithms. The algorithms have been verified against analytical and numerical solutions, as well as validated against experimental results published in the literature. Among those, the results of DEM simulations were compared against the experimental model tests and numerical simulations of jointed beams carried out by Talesnick et al. (2007) and Tsesarsky & Talesnick (2007) respectively. Emphasis was placed on modelling the stiffness of the block interfaces accurately, and this was accomplished by reinterpreting the laboratory data published by the investigators.

The capabilities of the numerical tools are also examined and demonstrated in areas for which the DEM has found practical application. A substantial fraction of this thesis is devoted to illustrating how these tools can assist the engineer in designing support systems; for example, designing the length and spacing of rock bolts and the lining thickness for a tunnel. Algorithms to model rock bolt and lining support were implemented for this purpose. Interesting comparisons with elastic solutions for supported openings were obtained. Further, it is shown that the relative benefit of introducing more rock bolts or thicker lining can be evaluated using the numerical tools with the aid of an interaction diagram. In the final part of this thesis, the case history of the 1963 Vaiont rock slide in Italy is studied. The 2-D analyses led to useful insights concerning the influence of the reservoir water level, the rock mass strength and deformability, and the slide surface shear stiffness. 3-D analyses were undertaken to investigate the influence of the eastern boundary of the slope, and interesting insights were obtained concerning the slope kinematics. Overall, the case study shows that the tools are capable of modelling problems with specific physical and geometrical detail in both 2-D and 3-D.

ACKNOWLEDGEMENTS

My heartfelt appreciation to my supervisors, to whom this thesis is dedicated: Professor Guy Houlsby and Dr. Stefano Utili. I owe a particular debt of gratitude to Guy for inspiring me to carry out a dissertation on a subject of my interest. Guy had been generous with his time and guidance, despite having to contend with the numerous administrative duties required of the Head of Department. Guy's suggestions with regard to mathematics, classic elastic solutions and addressing numerical artifacts, and advice on managing the overall progress of the project, are particularly appreciated. They had been invaluable in overcoming the obstacles and difficulties that I had encountered throughout this dissertation. I am indebted to Stefano for his encouragement and enthusiasm, which helped me persevere with the numerous numerical iterations. Stefano's advice on the expression of ideas, and persistent questions concerning the technical content of my work throughout this dissertation taught me to be meticulous, and ensured that I had given the best of my ability, and more. Stefano had continued to follow the progress of my dissertation closely at Oxford, even after he had taken up the appointment at Warwick University as an associate professor since the third year of this dissertation. Guy and Stefano had also advised and made constructive comments on the draft of this thesis, for which I am extremely grateful.

I am indebted to the DEM research group at Oxford University: Chiara Modenese, Kovthaman Murugaratnam, Tao Zhao and Giulia Macaro, all of whom I have had rewarding discussions concerning the distinct element method. I am grateful to Dr. Erling Andersen who suggested the use of slack variables for "potential particles" referred to in Appendix A, and to Giacomo Perantoni for the discussions concerning rotation matrices. I am grateful also to Dr. Danial Robinson who allowed me to attend his lectures and classes on numerical optimisation at the Mathematical Institute, and for answering my questions whilst I was learning the subject during my first year. My sincere gratitude to Dr. Esteban Ferrer, Dr. Hiu Fai Law, Giacomo Perantoni, Dr. Geoffe Wilde and Dr. Chris Martin for sharing their knowledge on numerical algorithms and software. I am also indebted to the members of YADE community, in particular Dr. Vaclav Šmilauer and Dr. Bruno Chareyre, who generously guided and answered all my questions while learning to use the DEM software, YADE. My thanks to my fellow colleagues in Room 11 and 12 who had been inspirational, and to my friends here in Oxford who had been supportive. My sincere appreciation to Andres Biehl, Ahmad Helmi Azhar, Andrew Chan, Ghows Azzam, Ridza Haniffah and Syarif Yahya for their continuing support at Oxford since my first year, and to Laith Tapper, Yuepeng Dong and Yang Li who had kept me motivated whilst I was writing this thesis.

I am particularly grateful to the Public Service Department of Malaysia for the King's (Yang di-Pertuan Agong) Scholarship which covers my tuition fees and living allowance. I am also grateful to the Department of Engineering Science and St Cross College for supporting me to present my research at conferences and symposiums. Finally, I wish to thank my parents, my brother, and friends back home for their support.

Contents

NOTATION

Geometrical variables

A, a	normal vector of a block face
a, b, c	coefficients defining a plane normal vector
D	numerical scaling matrix
d	distance of a plane from particle centre
f	mathematical function defining a particle
i	the i^{th} plane defining a particle
k	fraction of spherical term for a potential particle
$\mathbf{N}_{plane}$	normal vector of a rock joint
n	contact normal
p	point in global coordinates
$\mathbf{p}_c$	contact point
q	unit quaternion
Q	rotation matrix
r	distance by which a plane is expanded for a potential partcle
R	radius of a sphere
u	numerical scaling vector
v	vector in global coordinates
$\mathbf{x}_0$	joint centre or block centroid
x	vector notation for global coordinates
x, y, z	global coordinates of rock blocks
α	vector notation for local coordinates
α, β, γ	local coordinates of rock joints or rock blocks
ε	numerical tolerance representing zero
θ	angle of rotation
θ_{dip}	dip angle
θ_{dir}	dip direction
θ_{strike}	strike angle
s, v, w,p	auxiliary variables

Physical variables

a	radius of a circular tunnel
A_b	cross sectional area of a bolt
A_c	contact area
c	cohesion
D	diameter of tunnel
E	Young's modulus of rock mass
E_b	Young's modulus of rock bolt
E_L	Young's modulus of lining
F	bolt axial force (per unit metre along the tunnel axis)
F^n	normal force
F^s	shear force
$\mathbf{F}^s$	shear force vector
$\Delta\mathbf{F}^s$	increment of shear force vector
F^s_{max}	maximum shear force
$F^{tensile}_{max}$	maximum tensile force
F^u	upthrust due to buoyancy
G	shear modulus of rock mass
g	gravity
I	second moment of area
k_L	lining interface stiffness (GPa/m)
k_n	normal stiffness (GPa/m)
k_s	shear stiffness (GPa/m)
$k_{s\_initial}$	initial shear stiffness (GPa/m)
K_0	in-situ stress ratio (horizontal to vertical) for the special 2-D case with the major and minor principal stresses being horizontal and vertical
K_a	axial stiffness of rock bolt (N/m)
K_n	normal stiffness (N/m)
K_s	shear stiffness (N/m)
M	bending moment in lining (per unit metre along the tunnel axis)
L_b	characteristic distance between reinforced rock joints
l	length
m	weighted average of mass between two bodies
N	hoop force in lining (per unit metre along the tunnel axis)
n_b	number of bolts
p_0	ground pressure at the tunnel centre

Δp	pressure at the tunnel lining
Δr	radial convergence
s_θ	tangential spacing between rock bolts (unit: m)
s_l	longitudinal spacing between rock bolts
s_{mean}	mean spacing
t	lining thickness
u_n	normal displacement
u_{peak}	peak shear displacement
u_s	shear displacement
Δu_{ground}	convergence of rock mass
Δu_{lining}	convergence of lining
Δu_{node}	penetration of lining nodes into rock blocks
v	Poisson's ratio
V_n	relative normal velocity between two bodies
$V_{submerged}$	submerged volume
δ_0	initial overlap distance for which the normal force is nil
θ_s	spacing between bolts in angles (°)
ξ	viscous damping coefficient
λ	Lame's constant
μ_0	initial friction coefficient
μ	friction coefficient
ρ_w	density of water
σ_n	normal stress
σ_t	tensile strength
τ_s	shear stress
φ	friction angle between rock joints
φ_L	friction angle of rock-lining interface

CHAPTER 1 INTRODUCTION

1.1 BACKGROUND

Most rocks encountered in civil engineering projects contain discontinuities, such as rock joints and faults. The properties of these discontinuities, such as their roughness and orientations, dominate the strength and deformability of the rock mass, because they act as planes of weakness along which deformations can occur more readily. It is therefore desirable for the engineer to consider in his design calculations the influence of these discontinuities. Intersections between rock joints and the exposed surface of an excavation could lead to the formation of polyhedral blocks which are prone to sliding, falling or toppling from the surrounding rock mass, making continuum models inappropriate for design purposes. Several numerical methods for discontinuum analysis have been developed to model explicitly the geometrical fabric of the rock mass and the interactions between polyhedral rock bodies; for instance, the distinct element method (DEM) (Cundall, 1971), the discontinuous deformation analysis (DDA) (Shi & Goodman, 1985; Shi, 1988) and the combined finite-discrete element method (Munjiza et al., 1995; Pine et al., 2006).

This thesis is about the numerical modelling of jointed rock masses using the DEM, in which the particles (or blocks) are considered to be rigid and the contacts between them are compliant. The DEM was developed approximately 40 years ago, and the key original papers of the DEM can be found in Cundall (1971) and Cundall & Strack (1979). It has been used in various engineering applications; for instance, the modelling of quasi-static laboratory load tests, high-speed granular flow in manufacturing processes and large-scale geotechnical boundary value problems such as rock slopes and underground openings (Barton et al., 1994; Bhasin et al., 1996; Thornton, 2000; Kulatilake et al., 2001; Cleary & Sawley, 2002; Stead et al, 2006; Wu & Cocks, 2006; Jing & Stephansson, 2007; Vardakos et al., 2007; Cleary 2010; O'Sullivan, 2011; Bym et al., 2013).

The DEM has been used mainly in two ways to model jointed rock masses. The first of the two is to use spherical particles based on the bonded particle (or clustering) method (Potyondy & Cundall, 2004; Ivars et al., 2011), while the second is to model the rock blocks as polygons or polyhedra (Cundall, 1988). This thesis is concerned with the latter. In some commercial codes (Itasca, 2004; Itasca, 2007), the DEM is coupled with other numerical methods, such as the finite difference method to model the deformation of intact rock material and the boundary element method to model far field stresses. The combined finite-discrete element method, which is capable of modelling fracture propagation, is also being used increasingly through the commercial code ELFEN (Rockfield, 2003). In this thesis, the original DEM based on rigid particles is used. For practical engineering design purposes, it is reasonable to assume that the rock blocks are rigid and that the rock joints are compliant, unless the in-situ stresses are high and the rock mass is sparsely jointed (with low joint network connectivity).

Because the DEM is a particle based method, the jointed rock mass has to be represented in a DEM model as an assembly of polygons or polyhedra. Since the rock mass is dissected by discontinuities whose spatial distribution and orientations are rarely regular, the rock blocks are of different sizes and shapes, and they cannot be generated using the same block shape like a stencil. The engineer therefore needs to invest significant effort in pre-processing the field data into a format suitable for DEM calculation, i.e. identifying the polyhedral blocks from the discontinuities in the field. The implementation of a block identification computer code typically requires very careful bookkeeping procedures to maintain and update the data structures which are used to define the polyhedron, e.g. vertices, edges and faces.

In addition to block generation, the success of a DEM calculation depends on the correct modelling of the interactions between the polyhedral blocks, i.e. detecting contacts and applying contact forces based on their overlap distances. The task of contact detection is

well-known to consume a large fraction of computational effort in a DEM calculation. Tedious housekeeping algorithms are normally necessary to account for the different contact scenarios between polyhedral blocks, i.e. vertex-vertex, vertex-edge, vertex-face, edge-edge, edge-face and face-face. Because contacts between blocks could involve sharp corners and parallel faces, the calculation of the contact point, i.e. the point at which contact forces are applied, could be ambiguous. The calculation of the contact normal at sharp corners and edges is also non-trivial.

1.2 PURPOSE

The purpose of this thesis is to propose efficient algorithms for block generation and contact detection between polygonal (2-D) or polyhedral (3-D) blocks for the DEM. They are simpler and more well-defined than existing algorithms which use a multi-level data structure to define a polyhedron (vertices, edges and faces). The proposed block generation algorithm requires information only on the faces that define the polyhedron. Likewise, the proposed contact detection algorithm between polyhedral blocks requires information only on the block faces, i.e. adopting the same data structure that is used by the proposed block generation algorithm. These algorithms are developed from a well-defined mathematical framework, and the main calculations are solved using well-established convex optimisation procedures which are known to be robust and efficient.

Whilst the main aim of the thesis is to propose efficient and robust numerical tools by which the geotechnical engineer can use to model jointed rock masses, another aim is to demonstrate that these tools are also robust for modelling rock engineering problems through verification against analytical solutions, numerical simulations and experimental model tests published in the literature. The final objective is to illustrate that the models are capable of solving practical geotechnical engineering problems.

1.3 OUTLINE OF THE THESIS

The literature is reviewed in Chapter 2, before detailing in Chapter 3 the proposed algorithms for rock slicing and contact detection between 2-D polygonal or 3-D polyhedral blocks. In Chapter 4, the algorithms are verified against several benchmark tests, comprising of analytical solutions, numerical simulations and physical model tests published in the literature. The computational efficiencies of the algorithms are also examined.

The modelling of underground openings is discussed in Chapter 5. Algorithms to model lining and rock bolt support were implemented and coupled with the rock slicing and contact detection algorithms proposed in Chapter 3. The results are compared with elastic solutions for a supported circular opening to examine the robustness of the algorithms. A series of simulations were carried out for a hypothetical case to show how the engineer can use these numerical tools for support design, i.e. choosing the rock bolt spacing and lining thickness.

A case history is studied in Chapter 6 to verify the capabilities of these numerical tools to model specific geological detail and to give important insights from sensitivity analyses. The 1963 Vaiont rock slide was chosen as the case history. The chapter also presents the results of 3-D simulations to investigate the influence of the eastern boundary of the rock slope.

Chapter 7 presents the overall conclusions of the thesis, which relate mainly to the algorithms proposed in Chapter 3 and their capabilities demonstrated in Chapter 4, 5 and 6. Some of the algorithm implementations undertaken in this dissertation are presented in the appendices at the end of the thesis to maintain the coherence of the text. The development of contact detection algorithm for polyhedral particles was first explored in this dissertation by modelling very angular non-spherical convex “potential particles” (Houlsby, 2009) using more robust optimisation techniques (Boon et al., 2011; Boon et al., 2013). The mathematics of this work is presented in Appendix A.

CHAPTER 2
LITERATURE REVIEW

This chapter presents a literature survey of the relevant work concerning block generation algorithms and contact detection algorithms between polygonal/polyhedral particles. The block generation algorithms in the literature are reviewed first, and the research gaps are summarised (Section 2.1.3). This is followed by a review on contact detection algorithms, and, likewise, the research gaps are summarised (Section 2.2.3).

2.1 BLOCK GENERATION ALGORITHMS

Before reviewing the algorithms proposed for block generation, i.e. identifying polyhedral blocks from discontinuities, it is helpful to introduce briefly the geometrical characteristics of discontinuities. The geometrical descriptors, which are used commonly in practice and given as input to block generation algorithms, are highlighted.

2.1.1 Geometry of discontinuities

For most engineering applications, fractures or discontinuities are assumed to be planar. The roughness and waviness of the discontinuities are attributed to the physical shear strength of the discontinuities. Folded and undulating discontinuities require a separate mathematical treatment. The orientation of a discontinuity is normally defined using two angles, i.e. the dip and dip-direction (see Fig. 2.1). And by assuming that the discontinuities are persistent, i.e. infinite in extent, they can be spatially characterised by their spacing.

It is now known, however, that rock joints are non-persistent, i.e. finite in extent. To

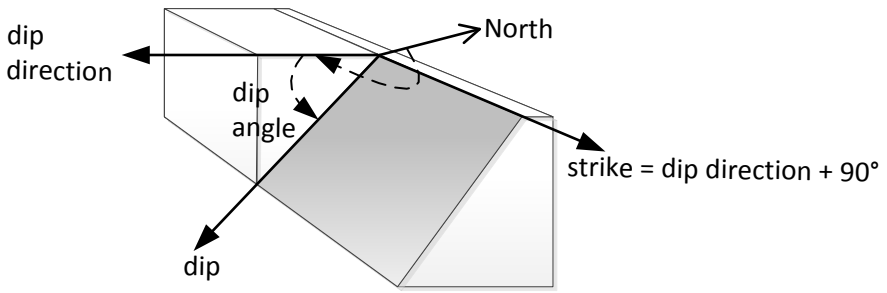

Fig. 2.1. Orientation of a planar discontinuity in 3-D (redrawn after Hoek et al., 1995)

characterise the degree of jointing, Einstein et al. (1983) proposed the concept of "persistence", which is defined as the ratio of the actual patchwork of joints to the total extent of a "slice" in a domain (see Fig. 2.2). Using this concept, a non-persistent joint set can be characterised using its spacing and persistence.

More recent studies have placed emphasis on the three-dimensional nature of discontinuities, the probabilistic nature of joint extents, and the probabilistic spatial distribution of joints. Various fracture system models have been proposed to replicate the rock joints in the field (Dershowitz & Einstein, 1988; Odling, 1992; Ivanova, 1995; Zhang et al., 2002). In most models, a non-persistent joint is associated with a two-dimensional shape; for instance, a circle, a polygon, or an ellipse (see Fig. 2.3). The spatial distribution of a joint set associated with a 2-D shape is better characterised using its intensity, which is defined as the number of joints per unit volume, or alternatively as the total joint area per unit volume. In fact, intensity can also be defined as the joint trace length per unit area (2-D) or the number of joints per unit length of scan line (1-D). A review of the different measures of intensity can be found in Dershowitz & Herda (1992). In short, a non-persistent joint set could be characterised using its joint shape (e.g. circle, ellipse or polygon), joint extent (e.g.

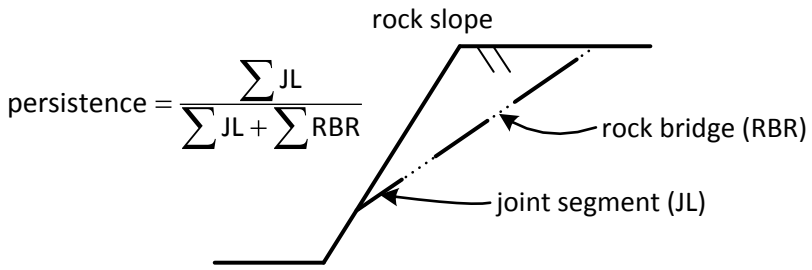

Fig. 2.2. Joint persistence in 2-D (redrawn after Einstein et al., 1983)

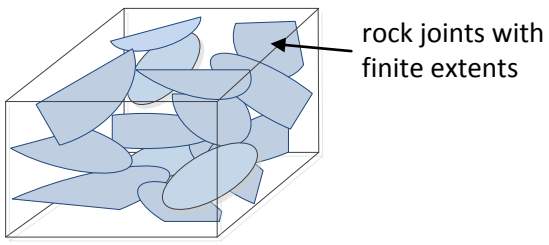

Fig. 2.3. Rock joints in 3-D with finite extents (elliptical) (cf. Dershowitz & Einstein, 1988)

diameter along the major and minor axis for an ellipse) and joint intensity (e.g. number of joint centres per unit volume), all of which could be defined using statistical distributions. The parameters defining these geometrical characteristics can be derived from field investigations, i.e. 2-D trace data found on rock exposures, such as outcrops or excavation surfaces (Warburton, 1980; Kulatilake et al., 1993; Zhang & Einstein, 2000; Zhang et al., 2002; Einstein & Locsin, 2012). Note that none of the models for rock joints are universal because there is a vast range of joint patterns, which are related to the rock type and weathering history (cf. Ivanova, 1995). For example, the discontinuities in a columnar jointed basalt or evenly bedded sandstone are more or less evenly spaced, whilst the discontinuities in a homogeneous igneous rock could be considered as being generated following a Poisson's process. Alternating layers of rock type may contain discontinuities which manifest in clusters. In geologically more complex cases, a combination of these may occur (cf. Priest & Hudson, 1976; Pollard & Aydin, 1988).

In general, the main input for a block generation computer code, which is reviewed later in Section 2.1.2, comprises of the positions and orientations of the rock joints. And depending on the capabilities of the block generation algorithm, the shapes and extents of non-persistent rock joints could also be considered. This information can be obtained either from deterministic or statistical models. The rock joints generated from the latter is known commonly as a discrete fracture network (DFN) in the literature.

2.1.2 Literature survey of block generation algorithms

A discrete fracture network provides information only with regard to the positions, orientations and extents of rock joints. The number of blocks as well as the size and shape of each block are still unknown. To carry out more useful mechanical analyses based on the given rock joint information, it is necessary to identify the rock blocks making up the rock mass (see Fig. 2.4). The reconstruction of the blocky rock mass structure is known as block generation or identification in the literature, and the subject has been concerned mainly with algorithms as regards computer implementation. Several block generation algorithms have been proposed in the past so that the stability of polyhedral blocks could be analysed using calculation methods such as vector analysis (Warburton, 1981), key block analysis

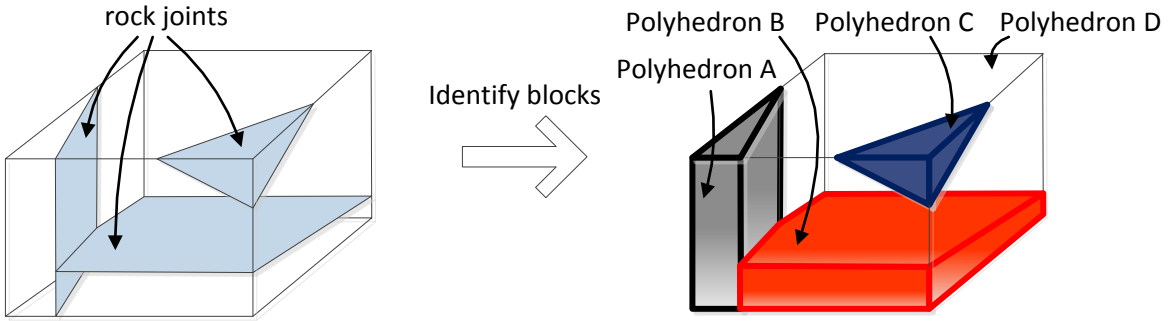

Fig. 2.4. Illustration of a simple set of rock joints, resulting in polyhedral rock blocks

(Goodman & Shi, 1985), discontinuous deformation analysis (DDA) (Shi & Goodman, 1985) and the DEM (Cundall, 1988).

Broadly, there exist two approaches in block generation algorithms. The first is based on subdivision (rock-slicing), in which discontinuities are introduced sequentially (Warburton, 1985; Heliot, 1988; Yu et al. 2009; Fu et al., 2010; Zhang et al., 2012; Zhang & Lei, 2013) (see Fig. 2.5). Each discontinuity is introduced one-at-a-time. If the discontinuity intersects a block, the parent block is subdivided into a pair of so-called child blocks. This process is repeated until all the discontinuities are introduced. The number of blocks increases as more "slices" are introduced, and a data structure for every block is maintained throughout the slicing process. On the other hand, in the second approach (face-tracing), the discontinuities are introduced all-at-once. From the vertices and edges which

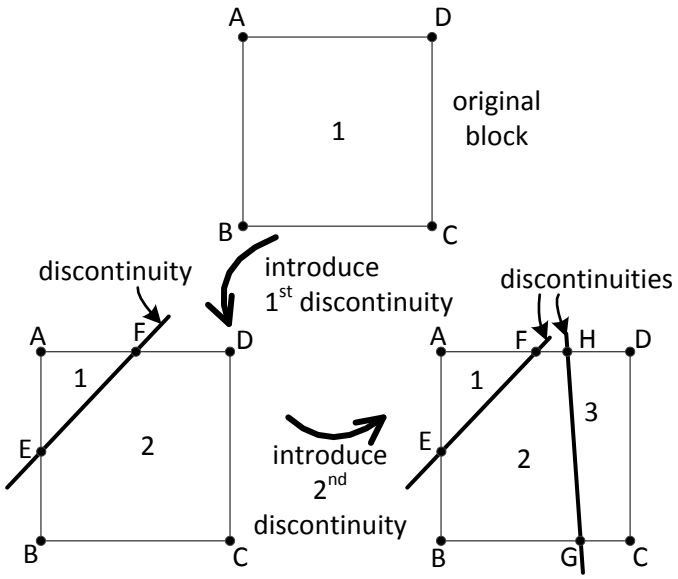

Fig. 2.5. Block generation algorithm based on sequential subdivision (slicing)

can be calculated from the intersections, there are ways by which the faces and polyhedra in the rock mass can be identified (Lin et al., 1987; Ikegawa & Hudson, 1992; Jing, 2000; Lu, 2002; Elmouttie et al., 2010; Xu et al. 2011) (see Fig. 2.6). The necessary algorithms are, however, rather complex. Unlike rock slicing algorithms, face-tracing algorithms are able to identify concave blocks and "dangling joints", i.e. non-persistent joints which terminate inside intact rock (see Fig. 2.7). Dangling joints are important in engineering problems involving fluid flow or fracture propagation, and they can be modelled more appropriately using other numerical methods such as the finite-discrete element method (Pine et al., 2006). However, since they do not contribute to the formation of polygons or polyhedra, these dangling joints are normally removed prior to a DEM analysis. Note that there is another approach of generating polyhedral blocks based on inferring 2-D trace maps found on rock exposures (Dershowitz & Carvalho, 1996; Li et al., 2012). This approach, however, is mainly used for key block analysis, and is less suitable for DEM modelling because only the blocks near the excavation surfaces could be generated.

The block generation algorithm proposed in this thesis is based on the first approach, i.e. rock slicing (sequential subdivision). The key aspects of a rock slicing algorithm are the

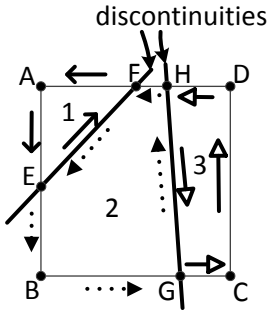

Fig. 2.6. Block generation algorithm based on face-tracing (all-at once)

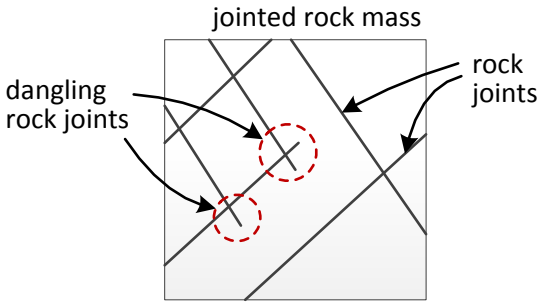

Fig. 2.7. Illustration of dangling joints in 2-D, terminating inside intact rock

choice of the data structures (used to represent the polyhedron) and the corresponding algorithm that is used to managing and updating the data structures. These details are important for the purpose of implementation in computer code.

An algorithm using a three-level hierarchical data structure consisting of faces, edges and vertices was originally proposed by Warburton (1985), after which an algorithm with a two-level data structure was proposed by Heliot (1988). In Warburton (1985), it is necessary to identify the faces and edges, which are intersected by the joint plane. New vertices and edges are created for the faces which are subdivided. The lists of faces, edges and vertices are then rebuilt for each child block. In the algorithm proposed by Heliot (1988), it is not necessary to calculate and store the edges. Each vertex consists of three indices, each of which is identified with one of the planes forming the vertex. An intersection check with the joint plane is performed for every pair of vertices which has two indices in common (e.g. between vertex-146 and vertex-346). New vertices are created from the intersections, and their indices are identified. Old vertices are allocated to the new child blocks depending on whether they are on the positive or negative halfspace of the joint plane. The lists of faces and vertices are then rebuilt for each child block. The details of their algorithms are summarised in Fig. 2.8 (a) and (b) respectively. It is obvious that the algorithm becomes simpler and less error-prone during the development stage when the management of the data structures is less involved (compare between Fig. 2.8 (a) and (b)). Moreover, algorithms using complex data structures may require special implementation in code to guard against robustness issues arising from rounding errors (cf. Warburton, 1985; Elmouttie et al., 2010). Most of the rock slicing algorithms proposed to-date (Yu et al., 2009; Fu et al., 2010; Zhang et al. 2012; Zhang & Lei, 2013) employ the algorithms proposed by Warburton (1985) and Heliot (1988) for updating the data structures. Ülker & Turanboy (2009) proposed a linked-list and tree-structure programming approach for the three-level data structure proposed by

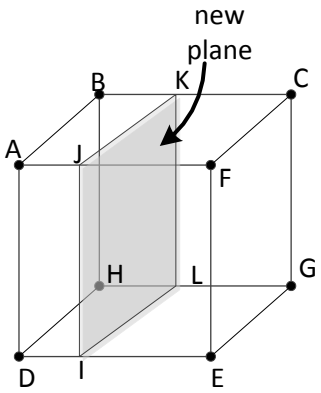

Triple-level data structure under the polyhedron (face-edge-vertex)
Subdivision algorithm is based on the classification of existing data structures:
Possible outcomes for a vertex:
- lies on the positive halfspace of the plane
- lies on the negative halfspace of the plane
- just touches the plane

Possible outcomes for an edge (line in 2-D):
- both ends lie entirely on the positive halfspace of the plane
- both ends lie entirely on the negative halfspace of the plane
- crosses the plane (one end is on the positive halfspace and the other on the negative halfspace)
- one end just touches the plane and the other is on the positive halfspace
- one end just touches the plane and the other is on the negative halfspace
- both ends touch the plane (the edge is fully contained in the plane)

Possible outcomes for a face:
- crosses the plane
- just touches the plane on an edge
- just touches the plane on a vertex

General flow of algorithm:
- Identify intersections and update old edges (e.g. BC subdivided into BK and KC)
- Introduce new edges (e.g. JK but not JL) by identifying (i) old faces which crosses the plane and (ii) their edges which crosses the plane
- Identify faces of child blocks through the above classifications

(a)

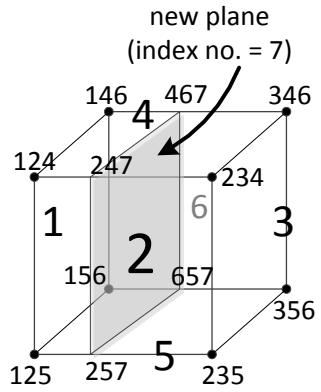

Double-level data structure under the polyhedron (vertex-face)
Every face of a polyhedron is indexed. A vertex is formed by intersections of three planes and consists of three indices. If a pair of vertices has two indices in common, they belong to an edge of the polyhedron.
Gist of algorithm:
- Allocate vertices to the positive or negative halfspaces of the new plane
- Calculate intersections between vertices of different half spaces. An intersection is calculated between a pair of vertices if they have two indices in common; e.g. an intersection is calculated between 146 and 346 but not between 146 and 234.
- Allocate old vertices to the child blocks based on which halfspace of the new plane they occupy. The new vertices are duplicated and allocated to each child block.

(b)

Fig. 2.8. Rock slicing algorithms derived from (a) three-level (Warburton, 1985) and (b) two-level (Heliot, 1988) data structures

Warburton (1985). Shi (2006) recently presented his work on 3-D block generation, but the mathematics is not given; only the features and capabilities of the tool were illustrated.

Because a block is either subdivided or not subdivided in a rock slicing algorithm, the generated blocks are convex. Concave blocks can, nonetheless, be generated through clustering two or more convex blocks by imposing a kinematic constraint which prevents any relative movement between the two sides of the joints (Warburton, 1985). Warburton

(1985) proposed the use of fictitious construction joints, so that blocks subdivided by a construction joint are automatically clustered together (see Fig. 2.9). This method can be applied to model excavation boundaries, where concave blocks are likely to exist. As some blocks belonging to a cluster are removed (excavated), the remaining blocks belonging to the cluster may form a concave-shaped block.

The sequential subdivision approach was developed originally to handle persistent joints, i.e. joints with infinite extents (Warburton, 1985). To handle non-persistent joints, i.e. joints with finite extents, Heliot (1988) proposed to pre-define several slicing sub-domains so that a joint can be instructed to slice through only certain sub-domains (see Fig. 2.10). This method is used, for instance, by the commercial DEM code, 3DEC (Itasca, 2007), which allows the users to hide certain sub-domains from being sliced. Using this software, Wang (1992), based on the preliminary work of Kulatilake et al. (1992) in 2-D, proposed to account for non-persistent joints in 3-D by introducing fictitious joints so that they would

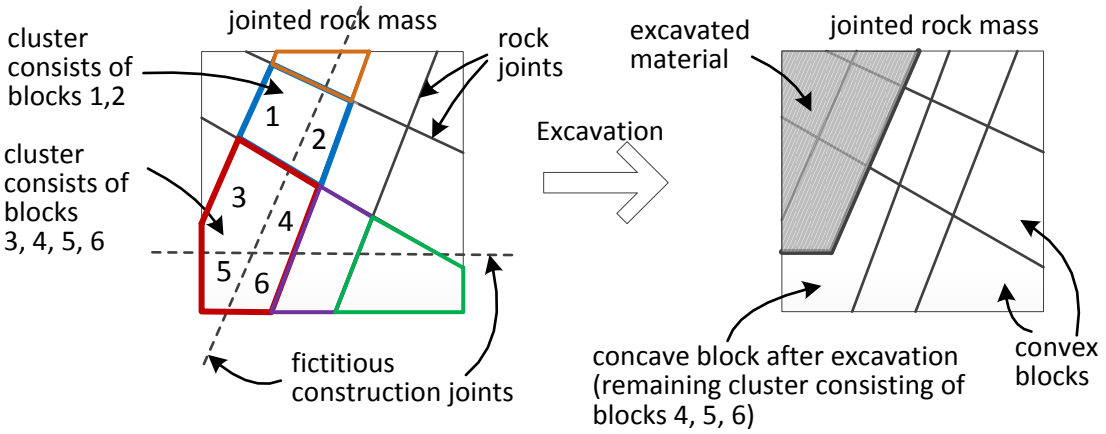

Fig. 2.9. Illustration of fictitious construction joints to create concave blocks near excavations

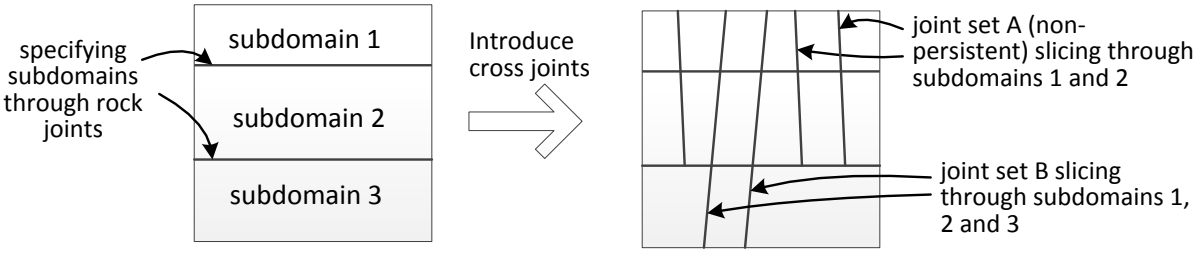

Fig. 2.10. Use of subdomains to create non-persistent joints

intersect the non-persistent joints at the locations where they terminate. The fictitious joints could then be used to demarcate the boundaries of the non-persistent joints. The fictitious joints are assigned with mechanical properties to mimic intact rock (see Fig. 2.11). These approaches of handling non-persistent joints, however, are very prescriptive, and can be an impractical undertaking for large numbers of rock joints.

Several automated methods for handling non-persistent joints have been proposed in the literature, and they are reviewed here (Yu et al., 2009; Fu et al., 2010; Zhang et al., 2010; Zhang et al., 2012; Zhang & Lei, 2013). Note that it is not trivial to establish intersection between a three-dimensional rock block and a rock joint with a two dimensional shape; the calculation of the actual intersections has been avoided by most rock slicing algorithms. Take for instance the commercial code 3DEC version 4.1 (Itasca, 2007) which permits the user to specify the persistence of a joint set. The algorithm assumes that the joints are infinite to establish intersection, and persistence is treated as the probability that a block is 'sliced'. It can, therefore, be inferred that at least one joint set should be persistent (cf. Kim et al., 2007). This way of handling non-persistent joints for the purpose of generating polyhedral blocks for DEM calculations indirectly imposes restrictions on the types of fractures (rock joints) which could be used to generate the blocks (Section 2.1.1). The algorithms proposed by Yu et al. (2009) and Fu et al. (2010) assume that a rock joint is associated with a finite two-dimensional shape (disc in Yu et al. (2009) and polygon in Fu et al. (2010)). But the rock joints are assumed to be infinite during the subdivision procedure, and only the block edges are checked for intersections with the joint plane. At the end of

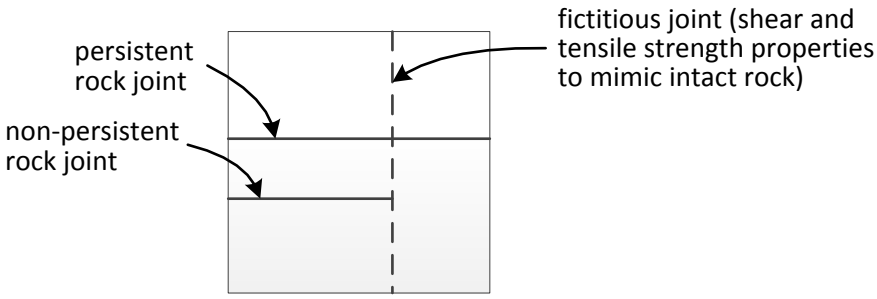

Fig. 2.11. Illustration of fictitious joints in 2-D so that non-persistent joints can terminate against it

block generation (after all the rock joints are introduced), the subdivided blocks are checked against the actual extents of the joints. If a pair of blocks on opposite sides of a joint is touching and not sliced completely, they are clustered together. This approach is analogous to removing dangling joints. To distinguish between blocks which are sliced completely and partially, Yu et al. (2009) proposed to check whether the vertices created by the joint plane all fall within the joint area (Fig. 2.12 (a)). Note that the algorithm proposed by Yu et al. (2009) has been developed into an object-oriented computer program by Zhang & Lei (2013). In another algorithm (Zhang et al., 2012), the finite extents of the rock joints are considered from the beginning of the slicing algorithm, and only blocks which touch the non-persistent joints are subdivided. During the slicing calculation between a rock joint and a rock block, intersections with the block edges are calculated. If one or more of the intersections fall inside the actual joint area, the block is subdivided. Note that this calculation procedure does not consider the special case in which the polyhedron edges are not intersected (Fig. 2.12 (b)). As with Zhang et al. (2012), the very recent algorithm proposed by Itasca (2013) for the new release of the commercial DEM code, 3DEC, subdivides only blocks which touch the actual extents of the rock joints. But the mathematics that is used to establish intersection between a non-persistent rock joint and a rock block is not given.

Some block generation algorithms were developed specifically to generate polyhedral blocks for finite element analyses (Zhang et al., 2010; Zhang et al., 2012). Their slicing algorithms begin with a gridded mesh, and the subdivided mesh elements are

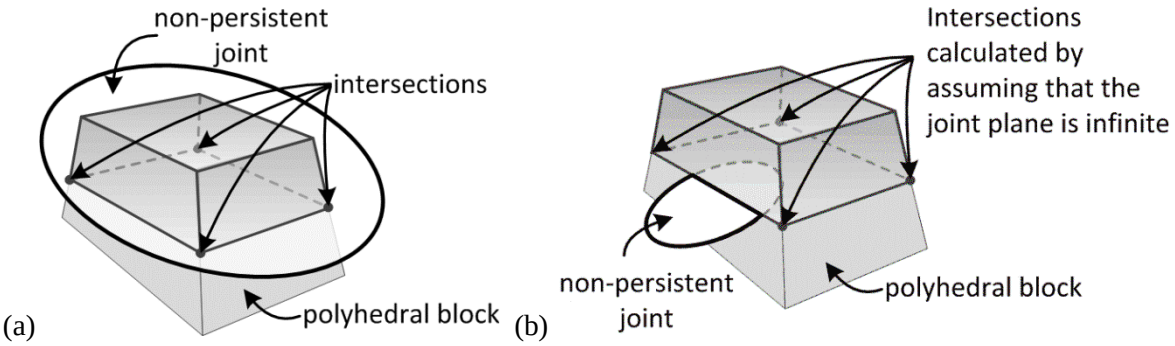

Fig. 2.12. Illustration of a non-persistent rock joint intersecting a polyhedral block (a) completely sliced (b) partially sliced without intersecting the polyhedron edges

clustered together to form polyhedral blocks at the end of the rock slicing algorithm. During clustering, dangling joints are removed. Analogous to using element meshes is to introduce a systematic distribution of fictitious joints before introducing the actual joints, so that the actual joints could terminate against the fictitious joints. In this way, the extents of the actual joints could be modelled more accurately during slicing; this was recommended by Itasca (2013) in the new release of the commercial DEM code, 3DEC. Note, however, that using too many fictitious joints can be computationally inefficient from a DEM standpoint because it increases the number of blocks for which contacts have to be checked.

Ways to increase the efficiency of the rock slicing algorithms proposed for non-persistent rock joints were also proposed, so that the unnecessary subdivision of blocks is avoided. Yu et al. (2009) proposed the use of bounding boxes enclosing the rock blocks and rock joints. If the bounding boxes do not overlap, it is not necessary to check for intersections with the joint plane.

2.1.3 Gaps in the literature and further discussion on block generation algorithms

It has been shown in the literature survey that the level of housekeeping (or bookkeeping) algorithms, which is required in a block generation computer code, depends on the choice of data structures. Heliot (1988) has, for instance, made bookkeeping more manageable by reducing the original three-level data structure (Warburton, 1985) to a two-level data structure consisting of only vertices and faces, without edges. The subdivision operations used in recent rock slicing algorithms (Yu et al., 2009; Fu et al., 2010; Zhang & Lei, 2013) employ the data structures and bookkeeping algorithms proposed by Warburton (1985) and Heliot (1988). A rock slicing algorithm which uses a single-level data structure, consisting of block faces only, has not been developed to-date. By reducing the level of data structure to one-level only, the need to update and maintain the hierarchical relationships between multiple levels of data structures will be obviated.

Recent algorithms in the literature have placed emphasis on handling non-persistent joints in an automated and efficient manner (Yu et al., 2009; Fu et al., 2010; Zhang et al., 2010; Zhang et al., 2011; Itasca, 2013). These features should therefore be considered in the development of the new algorithm to generate polyhedral blocks. For an algorithm which

uses a more compact data structure consisting of block faces only, it is unlikely that calculation techniques proposed previously in the literature are directly portable; take for instance, when establishing intersection between a non-persistent joint and a polyhedron.

In most rock slicing algorithms, blocks which are not completely sliced by a non-persistent rock joint are clustered together at the end of the entire slicing calculation; this is analogous to the erasing of dangling joints. The reduction of fracture intensity is likened to increasing the rock mass strength, and could lead to unsafe support predictions for excavation designs. Depending on the excavation dimensions relative to the joint spacing and extents, a small difference in the joint positions could affect the kinematic removability of a block near an excavation (compare between Fig. 2.13 (a) and (b)). Other investigators have also recognised the need for a less optimistic algorithm with regard to treating dangling joints (Itasca, 2013). The algorithm proposed in Chapter 3 contains comparable features to the latest release of the commercial DEM code, 3DEC (Itasca, 2013). The implementation details are, however, not in the public domain, and there are strong reasons to believe that the algorithms have been developed based on conventional data structures.

2.2 CONTACT DETECTION ALGORITHMS

There are several methods by which a 2-D polygon or 3-D polyhedron can be represented in a DEM model. The methods that have been proposed in the literature to create a polygonal or polyhedral particle are first reviewed, before discussing their corresponding algorithms for contact detection.

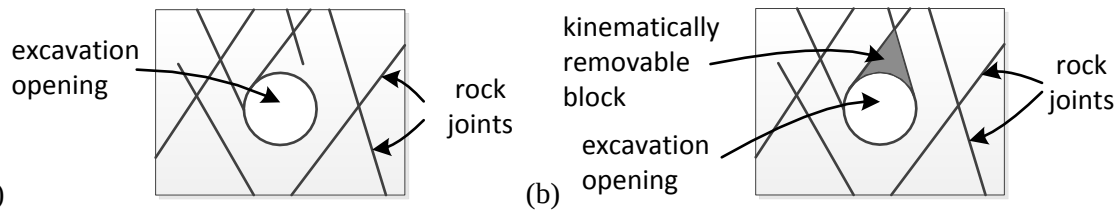

Fig. 2.13. Illustration of the sensitivity of block removability to minor perturbations in joint patterns (a) no falling wedge (b) existence of a roof wedge. Both cases are probable in a statistical sense

2.2.1 Creating polyhedral particles in the DEM

Prior to a DEM calculation, data containing information about the particle shape has to be first defined and stored. The size of the data set depends on the level of information that is required in the DEM calculation, particularly when establishing contacts between particles. In common discourse, 2-D polygons and 3-D polyhedra are defined in terms of the edge-vertex and face-edge-vertex hierarchical data structures respectively, i.e. edges by pairs of vertices, faces by bounding edges, polyhedra by bounding faces (Ghaboussi & Barbosa, 1990; Liu & Lemos, 2001).

There are, however, other ways of creating polyhedral particles in a DEM code. A simple way to approximately create a polyhedral particle is to aggregate spherical particles into clusters (see Fig. 2.14) (Favier et al., 1999; Jensen et al., 1999). Each cluster consists of spherical particles that are bound rigidly together, between which contacts (or overlaps) are ignored. Contacts between spheres of distinct clusters are calculated in the usual way. The forces on an entire cluster are aggregated, and the motion of the whole cluster is calculated as if it were a single rigid body. The advantage is that this method simply involves housekeeping procedures in attributing constituent spheres to clusters, without the need of introducing major algorithms. Moreover, unlike other methods for contact detection, this method is suitable for modelling concave particles. Rather than binding atoms rigidly, it is possible to include a non-rigid bond between the atoms, for which there is a criterion for breakage. The main disadvantage of this method is that very large numbers of constituent spherical particles are required to make up a realistically-shaped polyhedral particle (Lu & McDowell, 2007). The resulting cluster is likely to contain "grooves" on its surface and can be too knobbly. The "smooth joint method" has been proposed by Ivars et al. (2008) to

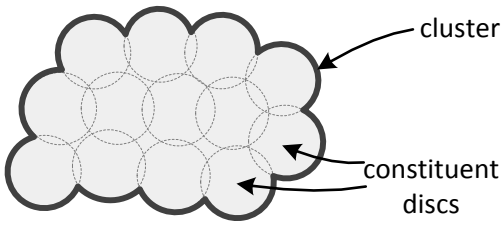

Fig. 2.14. Illustration of a 2-D cluster consisting of an aggregate of discs glued together

discard the effects of "grooves" when calculating the overlap, chiefly by identifying the mating particles at the beginning of the DEM simulation; they are therefore spatially restricted.

To model polygonal particles in 2-D, Crammond (2007) and Fraige et al. (2008) proposed the method of "racetrack particles". This method is also discussed in Houlsby (2009). In 2-D, circular particles are used to represent the vertices of the polygon, and the gap between the circular particles are bridged by straight segments (see Fig. 2.15 (a)). In 3-D, spheres are used to represent the vertices, whereas cylinders are used to represent the edges (Wang et al., 2011). Another method which is very similar to racetrack particles is the method of spheropolygons. A spheropolygon is defined as a Minskowski sum of a base polygon which represents the general shape and a circular disc which represents the roundness at the corners (cf. Alonso-Marroquín, 2008); it is like sweeping a disc around a "backbone polygon" (see Fig. 2.15 (b)). This method has also been developed to 3-D (Pournin & Liebling, 2005; Galindo-Torres, 2010; Dobrohotoff et al., 2012).

Superquadrics or superellipsoids (Williams & Pentland, 1992; Cleary et al., 1997; Wellman et al., 2008) could be used to model roughly angular particles but they are restricted in shape due to the way they are mathematically defined. Houlsby (2009) recently proposed the concept of potential particles which can model any convex particle shape (see Fig. 2.16). A potential particle in 3-D can be defined as a polynomial function which is constructed from an assembly of planes (each of which is enclosed in a ramp function and squared); the degree of angularity is governed by a constant representing the fraction of

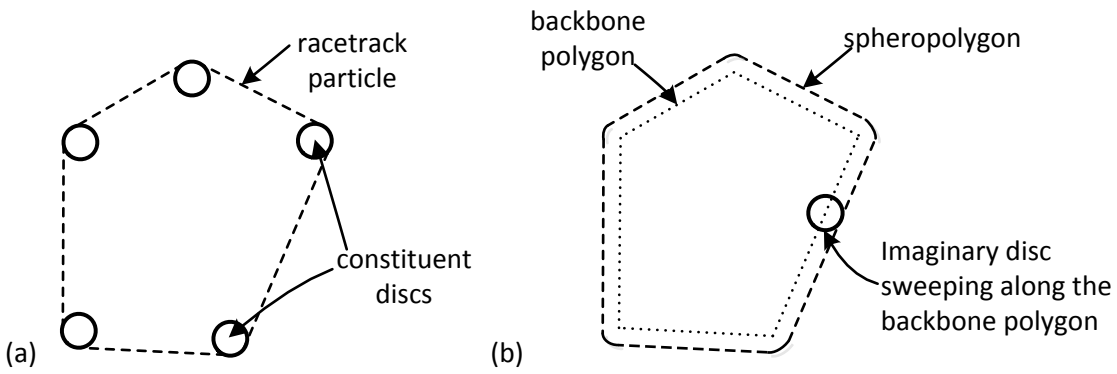

Fig. 2.15. Spherogpolygon (2-D) based on (a) positioning discs at sharp corners (b) sweeping a disc around a backbone polygon

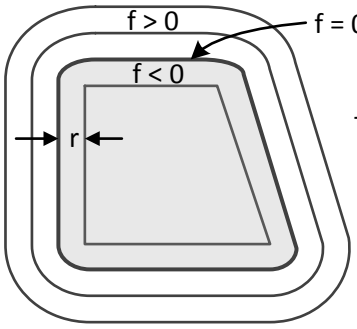

$$f = \sum_{i=1}^{N} \left\langle a_i x + b_i y - d_i \right\rangle^2 - r^2$$

Fig. 2.16. Construction of a potential particle (2-D) as an assembly of lines, before a circular term ($x^2 + y^2 - R^2$) is added to make it strictly convex (cf. Houlsby (2009)). The symbol $\langle\ \rangle$ is for Macaulay brackets (ramp function), i.e. if $x > 0, \langle x \rangle = x$; otherwise, $x = 0$.

sphericity and another constant which represents the radius of curvature at the corners. This method is therefore more suitable to model a polyhedron whose shape could be defined by an arbitrary set of planes. Note that the concept of potential particles can also be used to model rounded bodies with patches of flat areas (Harkness, 2010); Harkness et al. (2010) demonstrated that a flat area could be defined as the base of a cone.

Instead of using a continuous function to model the particle surface, several researchers have proposed to model the particle surface using patchworks of simpler objects. The concept of discrete function representation has been proposed by Williams & O'Conner (1995) and Williams & O'Connor (1999). According to this concept, a 2-D superquadric can be modelled as an assembly of points (Williams & O'Conner, 1995; Han et al., 2006). 3-D superquadrics, on the other hand, can be modelled by covering the particles with triangulated facets (Williams & O'Connor, 1999) or with points (Hogue, 1998). A recent comparison conducted by Lu et al. (2012) between the method of continuous function representation (Cleary et al., 1997) and discrete function representation (Hogue, 1998) showed that they are roughly of the same efficiency; in their comparison, they ensured that the accuracy of the discrete function representation was close to the continuous function representation by using a sufficiently large number of points. Apart from using points or triangulated facets, another method of creating a roughly polyhedral particle is to model the particle surface as a patchwork of ellipsoids (Peters et al., 2009). It is necessary, however, to perform an additional check, when performing contact detection, to determine which of these

ellipsoids are potentially in the contact zone. Several other methods have been proposed to capture in higher resolution the irregular surfaces of the particles using techniques such as spherical harmonics (Garboczi & Bullard, 2013; Mollon & Zhao, 2013), non-uniform rational basis-splines (Andrade et al., 2012) and through coordinate mapping (Johnson & Williams, 2009). But the application of these high-resolution methods is still restricted to either shape characterisation or very simple simulations. In contrast to these methods, Jin et al. (2011) proposed a probabilistic based contact detection algorithm for polyhedral particles; spheres are still used for overlap calculation, but the existence of contact forces are treated in a probabilistic manner. This method is not suitable to model small number of particles.

2.2.2 Literature survey of algorithms for contact detection

The different ways of creating polygons and polyhedra have been reviewed in Section 2.2.1. The corresponding contact detection algorithms are reviewed here. It would be helpful, however, to introduce the important terminologies and concepts using spherical particles. Between a pair of spherical particles, the overlap distance is the difference between the sum of the two radii and the two particle centres (see Fig. 2.17). The contact point, i.e. the point at which contact forces are applied, is the point at the particle boundary, minus half the overlap distance. The contact normal, i.e. the direction of the normal contact force, is directed along the line joining the two particle centres.

The contact detection algorithms for polygonal and polyhedral particles are more complex than spherical particles. Note also that the contact detection algorithms developed for 3-D polyhedra are significantly more complex than those developed for 2-D polygons.

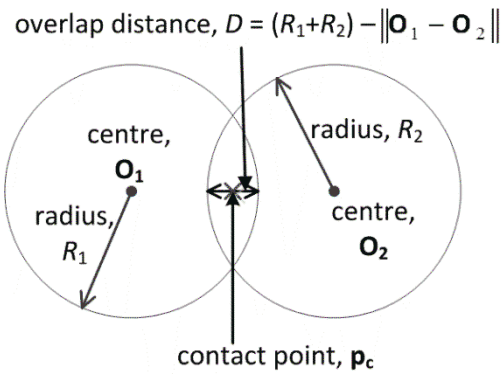

Fig. 2.17. Contact detection between a pair of circular particles

In 2-D, the contact types (or scenarios) are either vertex-vertex, vertex-edge or edge-edge. In 3-D, more contact types could take place, such as vertex-vertex, vertex-edge, vertex-face, edge-edge, edge-face and face-face. The majority of algorithms developed for 2-D polygons are not directly portable to 3-D, and would require non-trivial extensions (Hogue & Newland, 1994; Tillemans & Herrmann, 1995; Mirghasemi et al., 1997; Feng & Owen, 2004; Wu & Cocks, 2006; Han et al., 2006; Fraige et al., 2008; Alonso-Marroquín, 2008; Fu et al., 2012). Therefore, it is reasonable to be satisfied with reviewing mainly the algorithms which have been shown to be applicable in 3-D.

It is well-known that a pair of polyhedra is in contact if there are one or more intersections between their geometrical features, i.e. vertices, edges, faces or other primitive components (e.g. triangles). The most primitive way to establish intersection is to check exhaustively for every possible intersection scenario. This is known to be inefficient, and methods to avoid checking similar outcomes have been proposed; for example, the algorithm proposed by Ghaboussi & Barbosa (1990) considers face-face contacts as a combination of vertex-face and edge-edge contacts. Because some contact types are more 'versatile', some publications attempt to only address the calculation of specific contact types, such as vertex-face (Wu et al., 2005) and edge-edge (Yeung et al., 2007; Wu, 2008). There are other ways of reducing the number of intersection checks; for instance, faces whose normal vectors are pointing toward each other are prioritised for checking (Ghaboussi & Barbosa, 1990; Liu & Lemos, 2001; Keneti et al., 2008). The separating axis method (Eberly, 2001), also known as the "shadow overlap method" in Saussine et al. (2006), was proposed so that overlap between particles could be ruled out quickly (cf. Dubois, 2011). Another way to improve efficiency is to create useful information which could be stored from the beginning of a simulation; for instance, Williams & O'Connor (1999) proposed to enclose every facet defining the non-spherical body with a bounding box so that the neighbouring facets potentially in contact can be identified efficiently.

The aforementioned algorithms, however, rely heavily on housekeeping procedures (i) to identify the faces or triangles of each particle which are most likely in contact, and (ii) to calculate the intersections between them, e.g. vertex-face or edge-edge (O'Rourke, 1998).

Because of the possibility of multiple contact scenarios and the existence of sharp corners, the calculation procedures for the overlap distance and the contact normal are sketchy. The consequence is that, in some codes, a combination of algorithms is used. Take for instance the DEM code LMGC90 developed based on the non-smooth contact dynamics method (Dubois et al., 2011). Its contact detection algorithm principally uses the procedure in Saussine (2004) but the common-plane method proposed by Cundall (1988) (discussed in the next paragraph) is used for special cases involving vertex-vertex or vertex-edge interactions to calculate the contact normal.

Cundall (1988) realised that the calculation of contact normal between a pair of polyhedra should be addressed adequately because an important concern in rock engineering is to study the stability of wedges along discontinuities with 3-D orientations. Cundall (1988) proposed that the vertices of a pair of polyhedra could be tested against a "common-plane" to establish intersection (see Fig. 2.18 (a)). This is the most widely used algorithm in the DEM modelling of rock engineering problems because it has been implemented into the commercial DEM code, 3DEC (Itasca, 2007). The orientation of the common-plane is determined by iteratively rotating the common plane about its reference point to minimise the overlap between the common-plane and the vertex with the greatest overlap (see Fig. 2.18 (b)). The normal of the common-plane defines the direction of the contact normal and the reference point defines the contact point. Other algorithms based on the common-plane concept have been proposed, most of which address only the calculation of contact normals

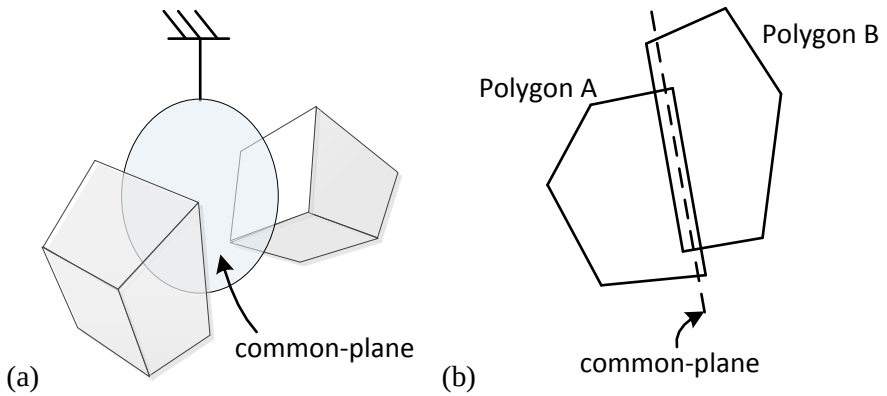

Fig. 2.18. Visualisation of common-plane concept (a)in 3-D and (b) overlapping particles in 2-D (redrawn after Cundall (1988))

(Nezami et al., 2004; Nezami et al., 2006; Chang & Chen, 2008; Beyabanaki, 2008). Note that in some of these algorithms, saddle points (Cundall, 1988) or special cases involving infinite loops (Nezami et al., 2006) may be encountered. For example, in the shortest-link method proposed by Nezami et al. (2006), the shortest-link between a pair of blocks is well-defined when the closest features of the polyhedra involve vertices (see Fig. 2.19), but is not well-defined when the closest geometrical features involve parallel faces. The original algorithm proposed by Cundall (1988) only attempts to produce a good-enough contact point quickly (also known as a *heuristic* in computer science terminology). The calculated contact point is not unique and may require correction procedures if it falls outside the overlap region. This calculation procedure (Cundall, 1988) is ambiguous for certain interactions such as edge-edge contacts (see Fig. 2.20), in which the calculation of intersections is normally required (cf. Zhao et al., 2006; Lawrence, 2009; Höhner et al., 2012).

Contact detection algorithms between polyhedra developed for computer graphics are mainly concerned with establishing intersections quickly (e.g. Lin & Canny, 1991; Mirtich, 1998; Gilbert et al., 1988), and are not directly portable for DEM calculations which also require information on the overlap distance and contact normal. The Gilbert-Johnson-Keerthi (GJK) algorithm (Gilbert et al., 1988) has been adopted for discontinuum modelling

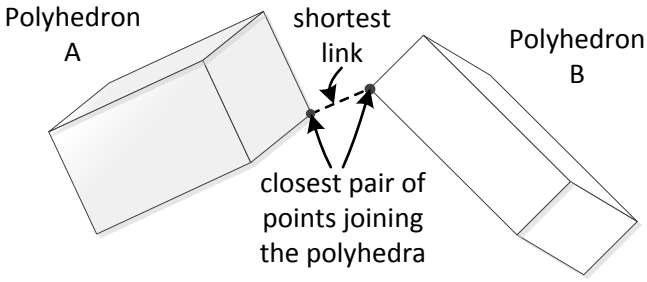

Fig. 2.19. Illustration of the closest pair of points (or shortest link) joining the polyhedra

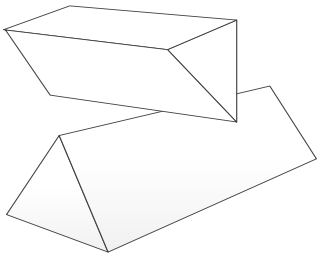

Fig. 2.20. Illustration of an edge-edge contact between a pair of polyhedra in 3-D

(Koziara, 2008; Petit et al.; 2001; Wachs et al., 2012). The GJK algorithm calculates the distance between the closest pair of points between two polyhedra (see Fig. 2.19, p. 23), and the two points meet each other when there is overlap. This information is not useful enough for DEM calculations because there is no information concerning the contact normal and overlap distance. A similar problem is also present in the shortest-link method proposed by Nezami et al. (2006) (an extension of the common-plane method mentioned in the previous paragraph). In the shortest-link method, particles have to be separated artificially if they are overlapping initially, so that the contact normal could be calculated from the vector joining the closest pair of points. Care has to be taken when separating the particles because the way by which they are separated could affect the solution. Wachs et al. (2012), based on the preliminary work of Petit et al. (2001), proposed to run the GJK algorithm on the 'shrinked' homothetic transformations of particles, so that the contact normal, contact point and overlap distance could be calculated for a pair of overlapping particles (see Fig. 2.21). The GJK algorithm inherently involves numerical convergence issues (cf. Bergen, 1999). Wachs et al. (2012) maintained, however, that this problem was not encountered in their paper because particles of similar sizes were modelled. Another shortcoming of this method is that the contact point is not unique for parallel faces in contact, because the solution of the GJK algorithm relies on a heuristic approach and depends on the starting point of the algorithm. This choice is reasonable for high-speed flow problems involving large number of particles, where the exact contact details are less crucial. For problems in which the deformation of contacts are important, an algorithm which gives a unique solution is more desirable than an algorithm which considers many solutions as legitimate; an algorithm which is inconsistent in its outcome can obscure the interpretation of results.

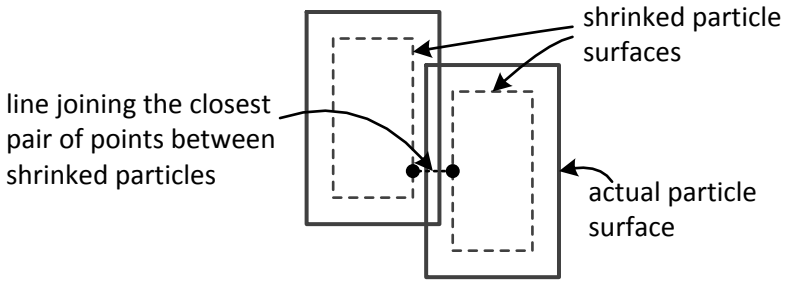

Fig. 2.21. Illustration of the shrinked particle approach proposed by Wachs et al. (2012) to adopt the GJK algorithm used in computer graphics for DEM calculations

It has been shown at the beginning of this subsection that contact detection between spherical particles can be calculated efficiently. Therefore, the contact detection between clusters of spherical particles is obvious. On the other hand, the contact detection algorithms with regard to racetrack particles (Wang et al., 2011) or spheropolyhedron (Pournin & Liebling, 2005; Galindo-Torres et al., 2009), in which the sharp vertices are replaced with spheres, and edges with cylinders, are less straightforward (see Fig. 2.15, p. 18, for 2-D illustration). Pournin (2005) proposed that all the interactions between 3-D spheropolyhedra can be calculated as edge-edge by ensuring that the size of the 'sphere' is large enough. Pournin (2005) proposed that the closest pair of (imaginary) spheres between a pair of spheropolyhedra (with each sphere lying on a different particle) can be calculated by finding the closest pair of points between the edges which define the 'backbone polyhedron'. For the special case when the particle faces are parallel, the closest pair of points is obtained as the geometrical centres of the faces. Recently, an algorithm for modelling spheropolyhedra without imposing a restriction on the sphere size was developed by Galindo-Torres et al. (2009) and Galindo-Torres (2010) based on the previous two-dimensional algorithm proposed by Alonso-Marroquín (2008). In this algorithm, contact points are assigned at all vertex-face and edge-edge contacts. A similar algorithm was proposed by Wang et al. (2011), but the particle faces are triangulated (see also Mack et al. (2011)). It is noteworthy that the radius of the sphere is related to the stiffness of the particle; a smaller radius requires a smaller DEM timestep (Wang et al., 2011; Dobrohotoff et al., 2012). Recently, Höhner et al. (2013) made a comparison between the algorithm proposed by Wang et al. (2011) and the "fast common-plane method" proposed by Nezami et al. (2004) (but combined with their own implementation to calculate the contact points). They found that the hopper discharge rates obtained using these two algorithms in their DEM calculations were comparable.

As mentioned previously in Section 2.2.1, polyhedral particles which are slightly rounded can be created using polynomial functions. Equations can be formulated so that the problem of contact detection, i.e. the calculation of contact point, contact normal and overlap distance, is mathematically well-defined. The system of equations, however, needs to be solved using iterative numerical techniques, concerning which convergence issues have been

reported. In particular, Cleary et al (1997) reported convergence problems with the Newton-Raphson method, while Wellmann et al. (2008) reported similar problems with the Levenberg-Marquardt method. Non-convergence was addressed by taking new starting points (Wellmann et al., 2008). Peters et al. (2009) found, through their work on modelling hyperellipsoids, that the iterative procedure proposed by Hopkins (2004) was more reliable than the Newton-Raphson method. The procedure proposed by Hopkins (2004), however, requires the particles to be sufficiently rounded and could take many iterations to converge if the starting point is not close to the solution. Recall that in Section 2.2.1, it was highlighted that the concept of potential particles proposed by Houlsby (2009) could be used to create a convex polyhedron defined by an arbitrary set of planes. The equations in 2-D have been formulated so that it could be solved using the Newton-Raphson method. However, numerical convergence issues were also encountered (Harkness, 2009). Because the presence of Macaulay brackets in the 2^{nd} degree polynomial function results in a discontinuity in the second derivatives, Harkness (2009) proposed to increase the polynomial function to a 3^{rd} degree. Although convergence improved for rounded particles, it was found, at the beginning of this dissertation that, this problem persisted when very angular particles were used.

It is important to highlight that unrealistic results could emerge as a result of adopting certain numerical artifices in contact detection algorithms. For example, Kodam et al. (2009) highlighted that if multiple contact points are used to model a contact, the spring stiffness at each contact point should be adjusted correspondingly to avoid creating contacts which are too stiff or overdamped; the latter will happen if viscous damping forces are used in the contact law. In another example, Diederichs & Kaiser (1999) found through the modelling of jointed voussoir beams using the 2-D commercial DEM software, UDEC (Itasca, 2004), that the reaction forces are concentrated at the bottom corner of the abutments, when the abutment blocks were assigned as rigid (the blocks making up the beam were deformable). In retrospect, this is caused by the numerical artifice of locating the contact point at a penetrating vertex (Itasca, 2004). To put it another way, the method by which the contact point is calculated could be important in certain engineering applications.

2.2.3 Gaps in the literature and further discussion on contact detection algorithms

The literature survey shows that a contact detection algorithm is related closely to the data structure that is used to define the polyhedron. Algorithms based on establishing intersections between geometrical features, i.e. vertices, edges and faces, are more prone to errors because they rely on very careful housekeeping procedures to check for every contact scenario (Ghaboussi & Barbosa, 1990; Liu & Lemos, 2001). Moreover, the calculation procedures for the contact normals and overlap distances are ambiguous.

Several algorithms which are capable of calculating the contact normals at sharp corners or edges have been proposed in the literature, namely the common-plane method (Cundall, 1988; Nezami et al., 2004; Nezami et al., 2006) and the method of spheropolyhedron (Pournin & Liebling, 2005; Alonso-Marroquín, 2008; Galindo-Torres et al., 2009; Wang et al., 2011). However, as with the methods highlighted in the previous paragraph, careful housekeeping procedures are still required to distinguish between the different contact types when calculating the contact points (Zhao et al., 2006; Lawrence, 2009; Höhner et al., 2012; Galindo-Torres et al., 2009; Wang et al., 2011).

Contact detection algorithms between particles, whose shapes are defined as polynomial functions, are subjected to a clear mathematical framework. The consequence is that the contact point, the contact normal and the overlap distance of a contact are well defined. It is therefore worthwhile to develop a contact detection algorithm based on this approach. The first challenge is to define a mathematical function which can assume any convex shape. The concept of potential particles proposed by Houlsby (2009) is one such function. It is, nonetheless, worthwhile to explore other methods of defining the shape of a polyhedron, because it is not easy to establish the tolerance below which the degree of 'rounding' of a potential particle is acceptable. The second challenge is to formulate and solve the system of equations for contact detection robustly, because convergence issues have been reported using numerical solvers, such as the Levenberg-Marquardt method (Wellman et al., 2008) and the Newton-Raphson method (Peters et al., 2009; Harkness, 2009).

CHAPTER 3
PROPOSED ALGORITHMS: ROCK SLICING & CONTACT DETECTION

This chapter details the proposed algorithms which form the crux of this thesis, namely a rock slicing algorithm for block generation and a contact detection algorithm between polygonal (2-D) or polyhedral (3-D) convex particles in the distinct element method (DEM). The proposed rock slicing procedure sets out a novel way of identifying rock blocks using a linear programming approach, by defining the space occupied by a polygon or polyhedron using a set of linear inequalities**.** Unlike existing methods, information regarding vertices and edges are not involved in the rock slicing (also known as subdivision) procedure, and the algorithm needs to keep track only of the faces of each polyhedron. The second half of this chapter details a novel contact detection algorithm which is consistent with the conceptual development of the rock slicing algorithm in that the same polyhedron data structure is maintained; i.e. requiring only the faces of the polyhedron. The algorithm consists mainly of two stages; first to establish intersection, and, if there is intersection, calculate the contact point. Both these problems are cast as standard problems in the field of convex optimisation, for which there exist established solution procedures. The calculation of the contact normal has been enabled by the identification of another mathematical technique – the concept of "potential particles" (Houlsby, 2009). The contact detection algorithm has been reported in a more condensed form in Boon et al. (2012).

3.1 DEFINING THE POLYGON AND POLYHEDRON

In the proposed algorithms for rock slicing and contact detection, the interior region occupied by a convex polyhedron is defined solely using a set of linear inequalities (also known as halfspaces) (see Fig. 3.1). This way of defining the polyhedron is sufficient because the tasks of rock slicing and contact detection are formulated using a mathematical framework which does not require information on the vertices and edges.

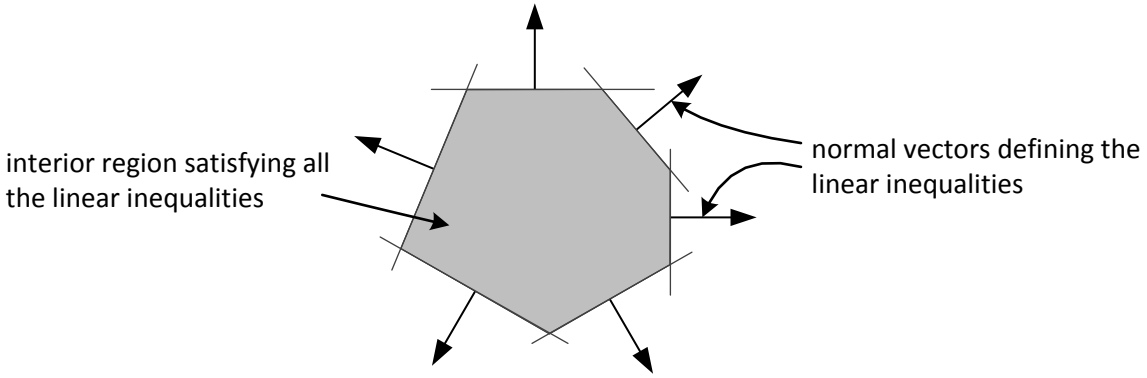

Fig. 3.1. A 2-D polygon defined using a set of five inequalities as shown in Eq. (3.1). The arrows are in the direction of the normal vectors. The interior region which satisfies all the inequalities is shaded.

For a convex particle defined by N planes, the space that it occupies can be defined using the following inequalities (see Fig. 3.1):

$$a_i x + b_i y + c_i z \le d_i, \quad i = 1,..., N \tag{3.1}$$

where (a_i, b_i, c_i) is the unit normal vector of the i^{th} plane, and d_i is the distance of the plane to the origin. For brevity, vector notation is used:

$$\mathbf{a}_i^{\mathrm{T}} \mathbf{x} \le d_i, \quad i = 1,..., N \tag{3.2}$$

where **a** and **x** are 3 × 1 vectors. In the rock slicing algorithm, the particles (or blocks) are defined entirely in the global coordinate system. That is, Eq. (3.2) is referenced to the global coordinate system. However, in the contact detection algorithm, transformations between the local and global reference systems are required. This is discussed later (Section 3.3.1).

3.2 ROCK SLICING ALGORITHM

The proposed rock slicing algorithm is based on the subdivision approach, where the starting point of the algorithm consists of an intact rock spanning the domain of the model (Section 2.1.2). This intact rock is then dissected sequentially, one at a time, by every rock joint in the field.

The rock slicing algorithm consists of several routines. The core of the algorithm is first explained in its simplest form, before extending the mathematics to include more advanced features. Depending on each problem, the more advanced version is not always necessary. The proposed algorithm generates convex blocks. Concave blocks can,

nevertheless, be generated through clustering two or more convex blocks (Section 2.1.2). This is discussed later in this chapter (Section 3.2.5). The algorithm for modelling persistent joints, i.e. joints with infinite extents, is explained first, while the algorithm to model non-persistent joints, i.e. joints with finite extents, is explained later (Section 3.2.3).

The rock slicing algorithm requires information on the orientations and positions of each discontinuity in the model. For non-persistent joints, the shape and size of the rock joint are also required (discussed later in Section 3.2.3). One can specify this information deterministically or using statistical models which assume that the discontinuities are planar and their roughness are attributed to their physical shear strength (Section 2.1.1).

In rock mechanics, the orientation of a joint is described in terms of the dip direction, θ_{dir} , and the dip angle, θ_{dip}, of the joint plane (see Fig. 3.2). The strike angle, θ_{strike}, is sometimes used in place of the dip direction, because it is simply perpendicular to the dip direction (see Fig. 3.2). Rather than working with these angles, the normal vector of the joint plane is used in the algorithm for ease of coding (see Fig. 3.3). The relationship of the normal vector to the aforementioned angles is as follows. Define $\mathbf{N}_{\text{plane}}$ as the plane normal vector and *d* the distance of the plane from the global origin. Define two auxiliary angles, χ:

$$\chi = (\pi / 2) - \theta_{\text{dip}} \tag{3.3}$$

and κ:

$$\left.\begin{aligned} \kappa &= \theta_{\text{dir}} + \pi \quad \text{for} \quad 0 \le \theta_{\text{dir}} < \pi \\ \kappa &= \theta_{\text{dir}} - \pi \quad \text{for} \quad \pi \le \theta_{\text{dir}} < 2\pi \end{aligned}\right\} \tag{3.4}$$

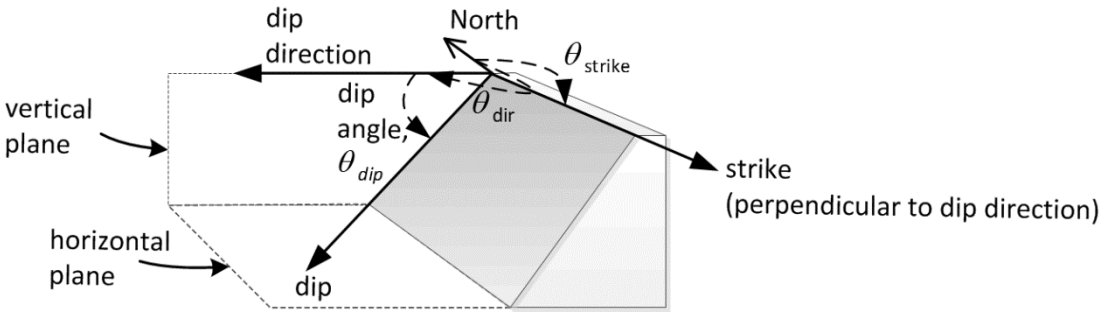

Fig. 3.2. Orientation of a rock joint in 3-D specified by its dip and dip direction (or strike). Note the convention of the right-hand rule; if the thumb points in the strike direction, the fingers should point down the dip.

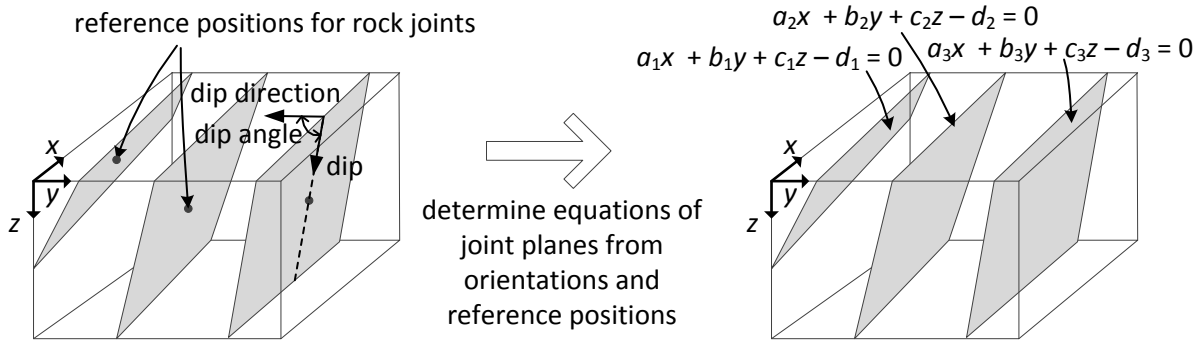

Fig. 3.3. An illustration showing that the positions and orientations of rock joints are converted to normal vectors

Then, $\mathbf{N}_{\text{plane}}$ can be calculated as:

$$\mathbf{N}_{\text{plane}} = (\cos\kappa\cos\chi, \sin\kappa\cos\chi, \sin\chi) \tag{3.5}$$

The distance, *d*, of the plane from the global origin can be calculated if any point lying in the plane, $\mathbf{x}_0$, is known:

$$d = \mathbf{N}_{\text{plane}}^{\text{T}}\mathbf{x}_0 \tag{3.6}$$

The derivation of this normal vector follows the sign convention proposed by Priest (1983) in which +**x** points North, +**y** points East and +**z** downwards. The joint planes can then be expressed in the form of Eq. (3.2), i.e. $\mathbf{N}_{\text{plane}}^{\text{T}}\mathbf{x} - d = 0$, in the rock slicing algorithm.

3.2.1 Establishing intersection and appending faces

In the subdivision approach, one needs to establish whether the existing blocks are intersected by the new discontinuity; this is the criterion for subdividing blocks (Section 2.1.2). To check whether there is intersection, a standard procedure for establishing feasibility in the field of convex optimisation is used, i.e. by checking whether or not an optimisation problem with the linear equality constraint, $\mathbf{a}_{\text{new}}^{\text{T}}\mathbf{x} - d_{\text{new}} = 0$, (defining the persistent joint plane) and the *N* linear inequality constraints, $\mathbf{a}_i^{\text{T}}\mathbf{x} - d_i \le 0$, (defining the interior region of the polyhedron) is feasible, i.e. the convex set is not empty. The problem is feasible if there exists a point lying on the linear equality constraint and inside the interior region defined by the linear inequalities (Boyd & Vandenberghe, 2004). To ascertain the

existence of such a point, a linear program is run to minimise the maximum infeasibility, whilst satisfying the equality constraint:

$$\left.\begin{array}{c} \text{minimise } s \\ \mathbf{a}_i^{\mathrm{T}}\mathbf{x} - d_i \le s, \quad i = 1,\ldots,N \\ \mathbf{a}_{\mathrm{new}}^{\mathrm{T}}\mathbf{x} - d_{\mathrm{new}} = 0 \end{array}\right\} \tag{3.7}$$

where N is the number of planes of the parent block, s is a slack variable which represents the maximum infeasibility, and the new discontinuity is introduced as an equality constraint in Eq. (3.7). If $s < 0$, there is intersection and the parent block is subdivided; the linear inequalities from the parent block are inherited by each child block and a linear inequality from the new discontinuity is appended to each child block (see Fig. 3.4) (with opposite signs for each child block). Note that this approach of establishing intersection and subdivision is different from existing algorithms which work out the exact intersections forming the new vertices of the subdivided polyhedra (Section 2.1.2). For example, let us consider that a parent block with N planes is subdivided into blocks A and B. Block A will inherit $\mathbf{a}_i^T\mathbf{x} \le d_i$, $i = 1,\ldots,N$ faces from its parent and have a new face, $\mathbf{a}_{\mathrm{new}}^T\mathbf{x} \le d_{\mathrm{new}}$, from the new discontinuity, whilst block B will have the inequalities $\mathbf{a}_i^T\mathbf{x} \le d_i$, $i = 1,\ldots,N$ and $-\mathbf{a}_{\mathrm{new}}^T\mathbf{x} \le d_{\mathrm{new}}$. Physical properties such as the friction angle and cohesion of the discontinuity are also stored with the new block face, with the possibility that each block

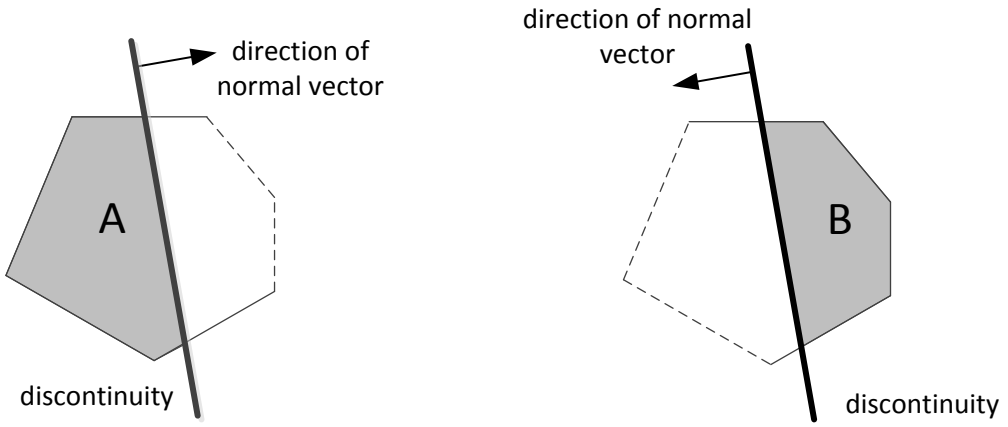

Fig. 3.4. The parent block in Fig. 3.1 is subdivided into a pair of child blocks (A and B). Opposite signs of the linear inequality of the new discontinuity is appended. Dashed lines are geometrically redundant for the shaded block.

face possesses different physical properties.

3.2.2 Checking for geometrically redundant planes

Upon subdivision, some of the linear inequalities inherited from the parent block could be geometrically redundant (dashed lines in Fig. 3.4, p. 32). Geometrically redundant inequalities can be removed without changing the interior region of the polyhedron. To check whether a linear inequality constraint $\mathbf{c}^{\mathrm{T}}\mathbf{x} \le d$ is geometrically redundant, we can solve the following linear program (Caron et al., 1989):

$$\left.\begin{array}{c} \text{maximise } \mathbf{c}^{\mathrm{T}}\mathbf{x} \\ \mathbf{a}_i^{\mathrm{T}}\mathbf{x} \le d_i, \quad i = 1,\ldots,N \end{array}\right\} \tag{3.8}$$

where $\mathbf{c}$ is one of the normal vectors, $\mathbf{a}_i$, of the faces defining the polyhedron. If $\left|\mathbf{c}^{\mathrm{T}}\mathbf{x} - d\right| > \varepsilon,$ where ε is a numerical tolerance close to zero, the linear inequality constraint is geometrically redundant. The linear program (Eq. (3.8)) must be performed in turn for each linear inequality defining the block. It is not necessary to check whether the new discontinuity is redundant because we know beforehand that it forms a new face with the subdivided block. To increase efficiency, instead of checking for geometrically redundant planes after every subdivision procedure, one can do this at the end of the rock slicing process after all the blocks have been subdivided by all the rock joints. The logic of the algorithm is not violated if these geometrically redundant planes are removed only at the end of the entire slicing process. The shape of a polygon or polyhedron, which is defined as the interior region satisfying all the linear inequalities, is not affected by the inequalities which are geometrically redundant (see Fig. 3.5).

The flow of the algorithm is illustrated in Fig. 3.6. Joint planes are appended as linear inequalities to existing blocks which they intersect. At the end of the rock slicing algorithm, geometrically redundant linear inequalities are removed. The updating and maintenance of the polyhedron data structure is straightforward since only the information on the block faces needs to be stored. An advantage is that the algorithm is less error prone during development and implementation in code.

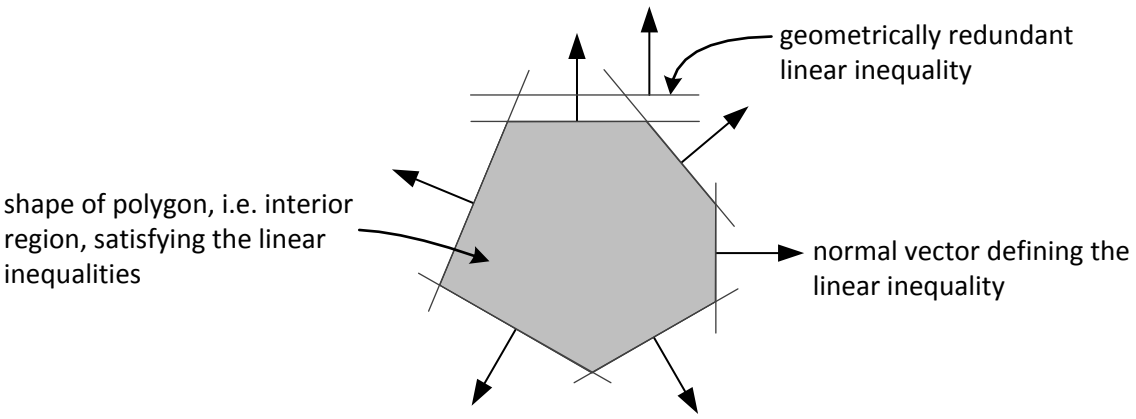

Fig. 3.5. An illustration of the 'shape' of a polygon (shaded region) not being affected by a geometrically redundant inequality

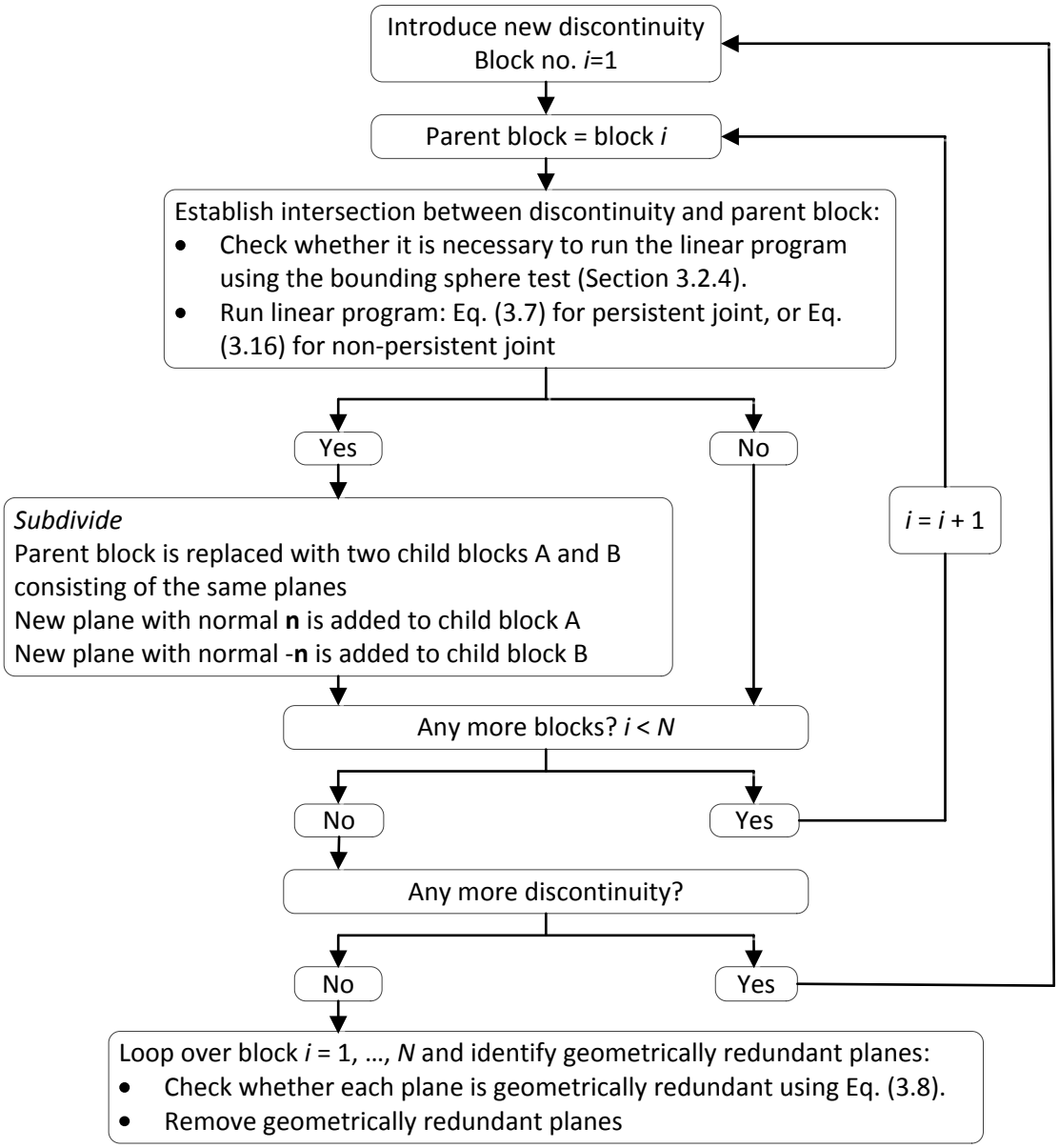

Fig. 3.6. Flow chart of the proposed rock slicing algorithm (non-persistent joints and bounding spheres are discussed later in Sections 3.2.3 and 3.2.4 respectively)

By comparison to existing algorithms in the literature, the data structure proposed in this algorithm is not sensitive to rounding errors. For instance, Fig. 3.7 shows that a joint plane just touching the vertex of a polyhedron may result in different outcomes due to rounding errors, i.e. whether or not the joint plane intersects the rock block. In block generation algorithms which employ a multi-level data structure, these rounding errors may cause the edges defining a face not to form a single closed loop (cf. Elmouttie et al., 2010). Instead, in the proposed algorithm, if the joint plane is found to intersect the block, it is appended to the list of faces defining the block shape, otherwise it is omitted. Either outcome does not give rise to a significantly different data structure since it is not necessary to calculate edges and vertices, or to maintain a compatible hierarchical tree. Since the subdivision approach is sequential, errors can be amplified. Hence, the increase in robustness from using a simpler data structure is an important advantage.

3.2.3 Taking into account the shape of the discontinuities

The previous analysis assumes that discontinuities are through-going in the domain of interest, i.e., persistent or infinite in extent. However, in reality, joints are non-persistent and are finite in extent (Section 2.1.1). Based on field investigations, it was found that most discontinuities are polygonal or elliptical in shape (Zhang & Einstein, 2010). If the boundaries of a discontinuity end against the face of another discontinuity, their shape must be polygonal. The polygonal boundaries of a discontinuity are defined in the α-β plane (see Fig. 3.8). They can be specified using the following linear inequalities (see Fig. 3.8):

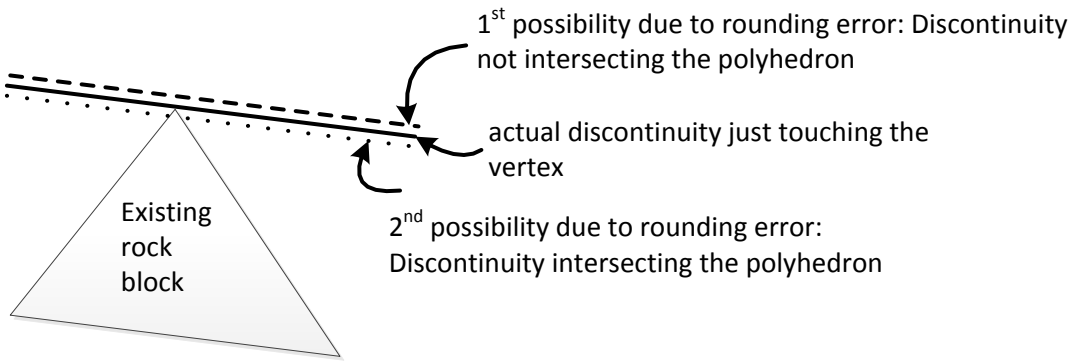

Fig. 3.7. Possible outcomes resulting from numerical rounding error which can affect the block data structure

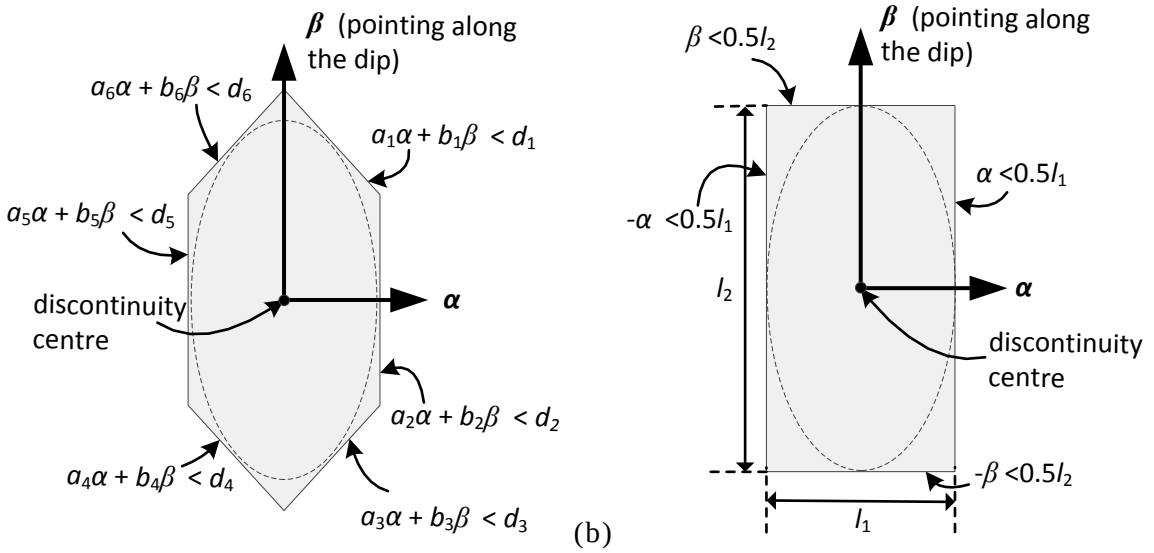

Fig. 3.8. Examples of how the extent of a rock joint can be delimited using linear inequalities. An ellipse can be approximated as a polygon consisting of N-lines, for instance as (a) a hexagon or (b) a rectangle

$$a_{i\text{local}}\alpha + b_{i\text{local}}\beta \le d_{i\text{local}}, \quad i = 1,...,M \tag{3.9}$$

where M is the number of lines defining the joint boundaries and $d_{i\text{local}}$ is the distance of the i^{th} line to the discontinuity centre (Fig. 3.8 (a)). Employing vector notation, this becomes:

$$\mathbf{a}_{i\text{local}}\boldsymbol{\alpha} \le d_{i\text{local}}, \quad i = 1,...,M \tag{3.10}$$

Note that, in the special case of rectangular-shaped joints, the input required from the user can be specified in a simpler form consisting of only the length and width of the joints (see Fig. 3.8 (b)). In the case of elliptical joints, the elliptical shape can be replaced with linear polygonal approximations. The simplest technique would be to use polygons circumscribing the ellipse (see Fig. 3.8). This is on the safe side because a larger joint area is considered. Alternatively, polygons with areas equivalent to the elliptical joints could be used, but their calculations are more cumbersome. Note that Eq. (3.10) is defined in terms of coordinates (α, β, γ), i.e. expressed with reference to a coordinate system whose origin is located at the discontinuity centre (e.g. centroid of the 2-D joint shape). The discontinuity centre could, in fact, be taken at any point on the polygon insofar as it is consistent with the equations defining the polygonal boundaries. The polygon in Eq. (3.10) is defined in such a way that the β-axis is oriented along the dip vector (see Fig. 3.9). The normal vector of the discontinuity is taken to be the local γ-axis (see Fig. 3.9). These inequalities have to be

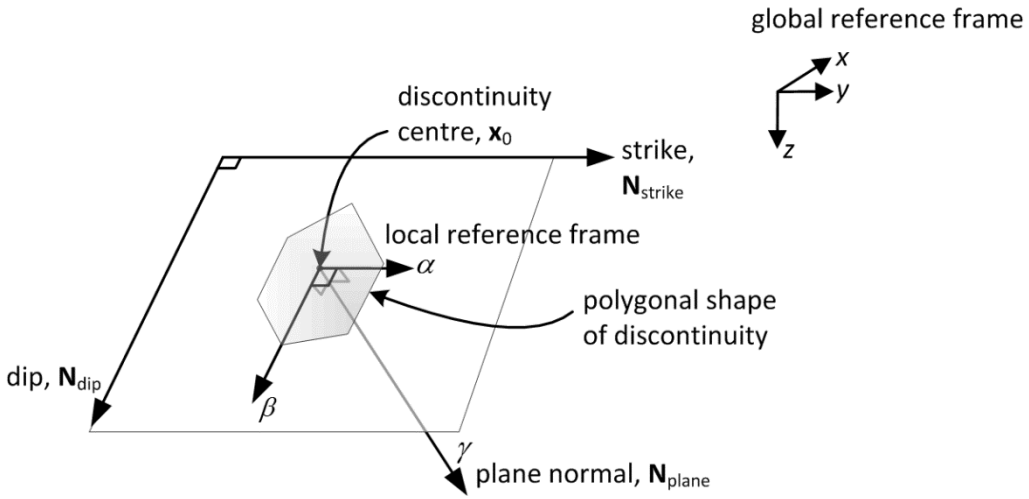

Fig. 3.9. In three-dimensional space, the discontinuity plane is bounded by lines forming a polygon.

transformed into global coordinates. The rotation matrix can be calculated as the geometrical transformation required to rotate the (α, β, γ) reference frame, in which the joints are defined, to the global (x, y, z) reference frame so that the α, β and γ axes become parallel to the strike, dip and normal vectors respectively (see Fig. 3.9).

To calculate the rotation matrix from local to global coordinates, first define the vectors $\mathbf{N}_{\text{strike}}$ and $\mathbf{N}_{\text{dip}}$ as:

$$\mathbf{N}_{\text{strike}} = (\cos\theta_{\text{strike}}, \sin\theta_{\text{strike}}, 0) \tag{3.11}$$

$$\mathbf{N}_{\text{dip}} = \mathbf{N}_{\text{plane}} \times \mathbf{N}_{\text{strike}} \tag{3.12}$$

after which $\mathbf{N}_{\text{dip}}$ is normalised. Recall that $\mathbf{N}_{\text{plane}}$ is the normal of the joint plane, and θ_{strike} is the strike angle which is orthogonal to the dip direction (see Fig. 3.2, p. 30). The rotation matrix can then be calculated as:

$$\mathbf{Q}_{\text{plane}} = \begin{bmatrix} N_{\text{strike\_x}} & N_{\text{dip\_x}} & N_{\text{plane\_x}} \\ N_{\text{strike\_y}} & N_{\text{dip\_y}} & N_{\text{plane\_y}} \\ N_{\text{strike\_z}} & N_{\text{dip\_z}} & N_{\text{plane\_z}} \end{bmatrix} \tag{3.13}$$

The coefficients for the linear inequalities with reference to the global reference frame for the M polygonal boundaries are therefore:

$$\mathbf{a}_{j\text{bound}} = \mathbf{Q}_{\text{plane}} \mathbf{a}_{j\text{local}}, \qquad j = 1,\ldots, M, \tag{3.14}$$

$$d_{j\text{bound}} = \mathbf{a}_{j\text{bound}}^{\text{T}} \mathbf{x}_0 + d_{j\text{local}}, \qquad j = 1,\ldots, M, \tag{3.15}$$

where $\mathbf{x}_0$ is the discontinuity centre or the origin of the joint plane.

In the slicing algorithm, it is assumed that these polygonal discontinuities will completely slice through any block that they reach (see Fig. 3.10); the cut needs to terminate at another discontinuity. In other words, non-persistent fractures or discontinuities inside any intact block are assumed to develop fully such that the block is completely sliced. After taking into account the shape of the discontinuity when establishing intersection, the linear program in Eq. (3.7) (p. 32) becomes:

$$\left.\begin{aligned} &\text{minimise } s \\ &\mathbf{a}_i^{\mathrm{T}}\mathbf{x} - d_i \le s, \quad i = 1,\ldots,N \\ &\mathbf{a}_{\mathrm{new}}^{\mathrm{T}}\mathbf{x} - d_{\mathrm{new}} = 0 \\ &\mathbf{a}_{j\mathrm{bound}}^{\mathrm{T}}\mathbf{x} - d_{j\mathrm{bound}} \le s, \quad j = 1,\ldots,M \end{aligned}\right\} \tag{3.16}$$

where $\mathbf{a}_{j\mathrm{bound}}^{\mathrm{T}}\mathbf{x} - d_{j\mathrm{bound}}$ defines the boundaries for the new discontinuity $\mathbf{a}_{\mathrm{new}}^{\mathrm{T}}\mathbf{x} - d_{\mathrm{new}} = 0$. If $s < 0$, there is intersection, and the parent block is subdivided. The geometrical interpretation of the linear program is to check whether or not a point satisfying all the linear equality and inequality constraints exists (see Fig. 3.11). As mentioned previously, this technique is used in convex optimisation to establish whether or not an optimisation problem with the specified constraints is feasible.

Note that, even with the linear inequalities delimiting the boundaries of the rock joints, the extent of a "slice" during the calculation is at least as large as the existing blocks. For instance, at the beginning of the slicing algorithm, the extent of the joint must be as large as the first block (entire domain). As more blocks are subdivided, the extent of the joints

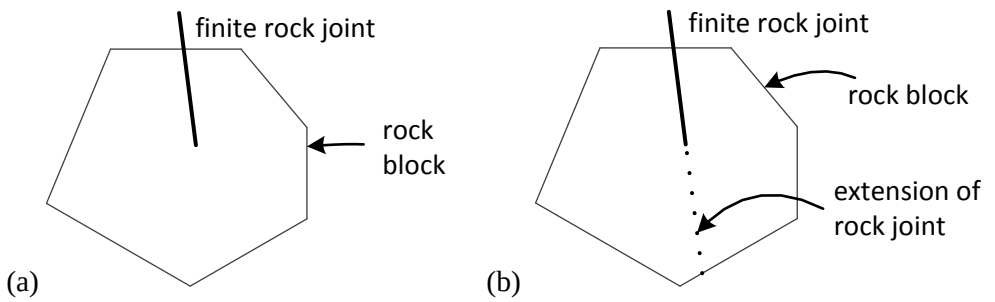

Fig. 3.10. (a) Assigned rock joint extent (b) Rock joint as modelled by the algorithm (the fracture is fully extended)

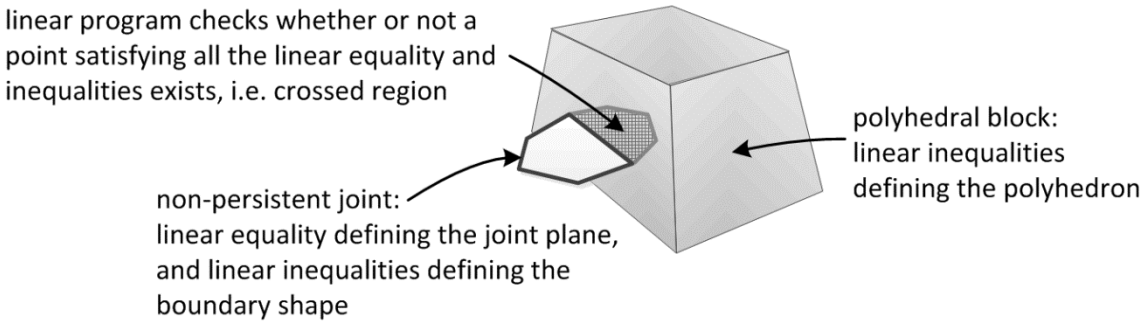

Fig. 3.11. Interpretation of linear program to establish intersection between a non-persistent rock joint and a polyhedral block.

reduces. To avoid creating cuts deeper than necessary, discontinuities with larger extents should be introduced before introducing discontinuities with smaller extents. This is discussed in further detail in Section 3.2.5.

3.2.4 Bounding spheres and conditioning of sizes

In the previous sections, the discussion has been limited to the essential features of the novel mathematical treatment of rock slicing, i.e. linear programming. Some peripheral features will now be discussed. In the previous sections, every rock joint has to be checked against every other polyhedron for intersection, i.e. to establish whether a polyhedron should be subdivided. When the number of rock joints is large and the joint extents are small relative to the size of the domain, this can be inefficient. Due to the inherent nature of algorithms based on sequential subdivision, as the number of already subdivided polyhedra increases, there are more polyhedra against which a rock joint has to be checked for intersection. Adopting a procedure typical of contact detection algorithms in the DEM, it is convenient to associate each polyhedron or rock joint with a simpler shape (such as a sphere) completely enclosing the block or joint, so that a faster check can be executed to decide whether it is necessary to run more complex intersection tests. Yu et al. (2009) introduced the use of prismatic bounding boxes in rock slicing algorithms. Here, the use of bounding spheres is proposed.

To work out the radius and centre of the bounding sphere, it is necessary to know the extents of the polyhedron. The extents of a polyhedron can be calculated by running a linear

program (Eq. (3.17)) along each principal axis $\mathbf{e}_i$ in the positive and negative directions, i.e. *x*, -*x*, *y*, -*y*, *z*, -*z* in 3-D or *y*, -*y*, *z*, -*z* in 2-D.

$$\left.\begin{aligned} &\text{maximise } \mathbf{e}^{\mathrm{T}}\mathbf{x} \\ &\mathbf{a}_i^{\mathrm{T}}\mathbf{x} \le d_i, \quad i = 1,...,N \end{aligned}\right\} \tag{3.17}$$

where $\mathbf{e}$ is the unit vector directed along the principal axis of interest. This will result in a pair of coordinates $\mathbf{x}_{\mathrm{p}} = (x_{\mathrm{p}}, y_{\mathrm{p}}, z_{\mathrm{p}})$ and $\mathbf{x}_{\mathrm{n}} = (x_{\mathrm{n}}, y_{\mathrm{n}}, z_{\mathrm{n}})$ which are the most positive and negative *x*, *y*, *z* coordinates respectively on the particle boundaries (see Fig. 3.12 for a 2-D illustration). The radius of the bounding sphere can be approximately calculated as $R = 0.5\left\|\mathbf{x}_{\mathrm{p}} - \mathbf{x}_{\mathrm{n}}\right\|$. The centre of the bounding sphere can be taken as the average of the extents, i.e. $0.5\times(x_{\mathrm{p}} + x_{\mathrm{n}}, y_{\mathrm{p}} + y_{\mathrm{n}}, z_{\mathrm{p}} + z_{\mathrm{n}})$. On the other hand, the bounding sphere for a rock joint can be approximated easily from its extents.

Before running the actual intersection test between a rock joint and a polyhedron, it is more efficient to first check whether their bounding spheres overlap (see Fig. 3.13 (a) for a 2-D illustration). If their bounding spheres do not overlap, it is not necessary to run the more expensive linear program (Eq.(3.16)). For a rock joint which is large in extent, its bounding sphere may span a large fraction of the domain, and most of the space inside the bounding

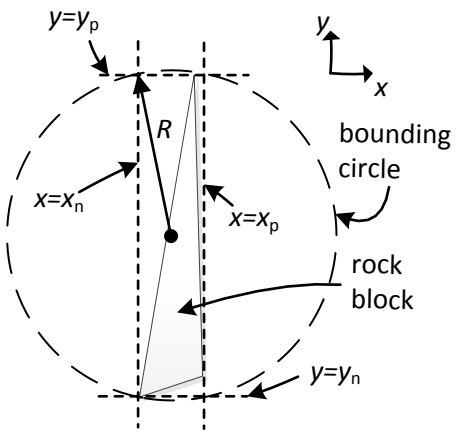

Fig. 3.12. Illustration of bounding circle in 2-D, circumscribing the polygon

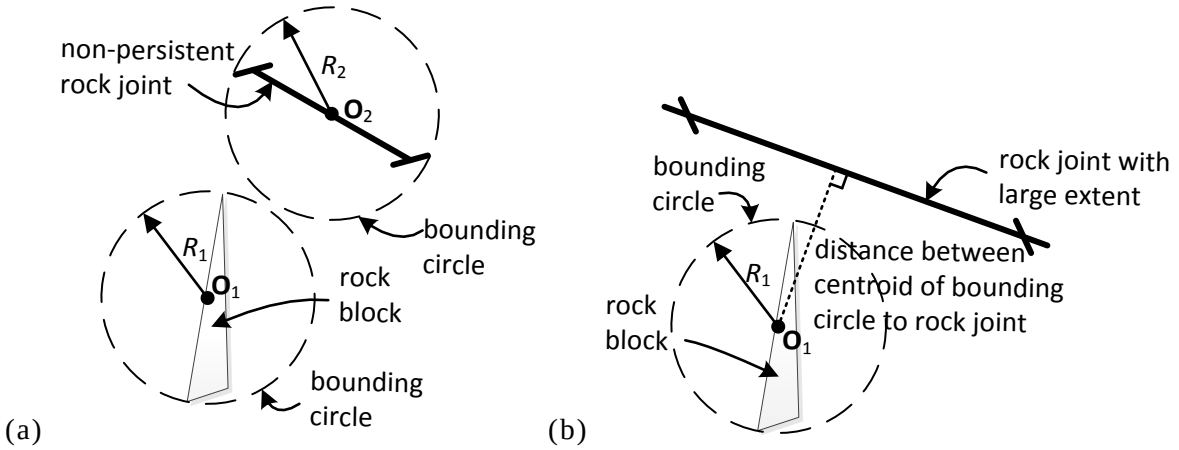

Fig. 3.13. Using bounding spheres to check for potential intersection. (a) non-persistent rock joints with small extents, $\text{Overlap} = (R_1 + R_2) - \|\mathbf{O}_1 - \mathbf{O}_2\|$, (b) persistent or joints with large extents

sphere is unoccupied. This is inefficient because rock blocks located far away will pass the test. To improve efficiency, one should also check whether the distance of the sphere centroid to the joint plane is less than the radius of the sphere (see Fig. 3.13 (b)). If the distance of the sphere centroid to the joint plane is larger than the sphere radius, it is not necessary to run the linear program (Eq.(3.16)).

Especially when rock joints are generated according to probabilistic distributions, it is desirable to control the smallest size of the polyhedra. This is because the maximum length of the time step of a DEM simulation is restricted by the size of the smallest polyhedron in the numerical model. Removing small polyhedra from the domain after they have been generated will create voids in the model; so if this approach is adopted, the tolerance has to be very small to avoid creating excessively large voids. An alternative approach is to ensure, during the slicing procedure, that the size of the subdivided child blocks is above an assigned tolerance. If the size of one of the child block is found to be too small after "slicing", the data structure of the parent block can be restored so that the block is not subdivided.

In principle, it would be possible to estimate the size of the blocks from the radius of their bounding spheres. However, this would not be a robust method since slices which subdivide a parent block into either needle or pancake shaped child blocks can satisfy the

tolerance more easily (see Fig. 3.14(a) and (b)), which in turn would lead to a model consisting of numerous highly elongated needle and pancake shaped blocks. Therefore, a better way to approximate the size of a block is by using its largest inscribed sphere (see Fig. 3.15). There are several ways to work out the radius of the largest inscribed sphere inside a polyhedron, one of which is to solve:

$$\left.\begin{array}{c} \text{minimise } t \\ \mathbf{a}_i^{\mathrm{T}}\mathbf{x} - d_i \le t, \quad i = 1,...,N \end{array}\right\} \tag{3.18}$$

with $\mathbf{a}_i$ being unit vectors, t the largest inscribed radius of a sphere in a polyhedron and the solution $\mathbf{x}$ is the Chebyshev centre of the polyhedron (Boyd & Vandenberghe, 2004). Geometrically, the Chebyshev centre represents the centre of the largest sphere inscribable in the polyhedron (see Fig. 3.15).

In some cases, it is also of interest to control the maximum aspect ratio of the polyhedra in the simulations, e.g. in order to reduce the occurrence of "outliers" with elongated shapes near an excavation. Therefore, to achieve a better "conditioned" blocky rock mass, one may wish to examine the aspect ratio of a subdivided block during the slicing process. The aspect ratio of a block can be approximated as the ratio of the radii of the bounding sphere to the inscribed one (see Fig. 3.15). A large ratio suggests that the block is either pancake or needle shaped. The sizes and aspect ratios of the child blocks after potential subdivision can be checked against their respective tolerances, before executing the subdivision. If one of the tolerances is not satisfied, subdivision procedure is not committed,

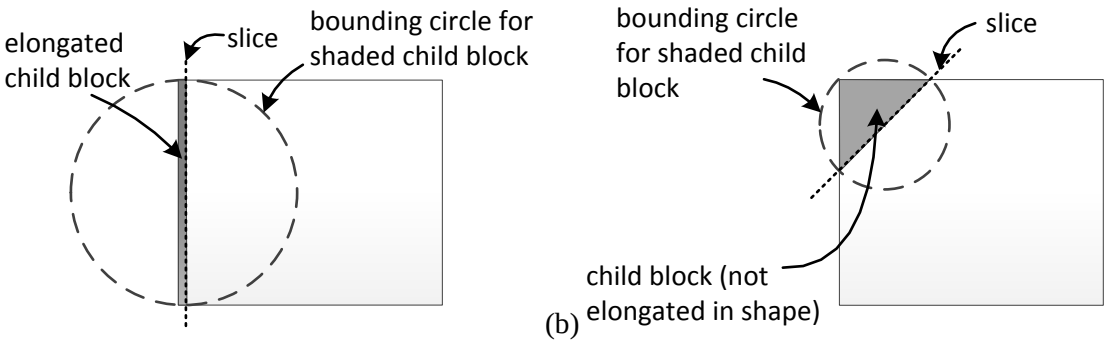

Fig. 3.14. Illustration in 2-D of why bounding circles (spheres in 3-D) are not suitable to evaluate block sizes: (a) an elongated block and (b) a non-elongated block.

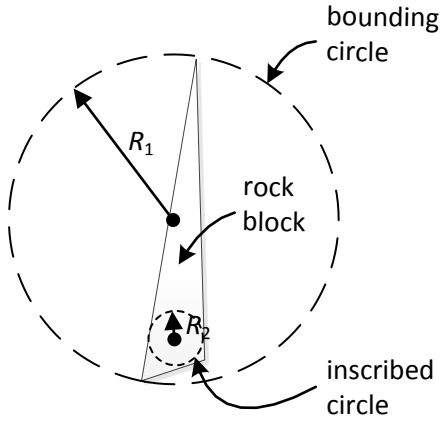

Fig. 3.15. Illustration of bounding and inscribed circles in 2-D. The largest inscribed circle is used to estimate the block size in the algorithm, and the ratio of the radii of the bounding to inscribed circles is used to identify pancake or needle-shaped blocks.

i.e. the original data structure of the parent block is restored.

3.2.5 Generation of block assemblies for discontinuum analysis

The blocks generated using the aforementioned algorithm is convex. If it is wished to model concave blocks, well-known procedures in the literature can be adopted (Section 2.1.2). A convenient way is to introduce a fictitious cut, otherwise known as a construction joint, so that subsequent slices can terminate at its face. Blocks which are subdivided by construction joints are either bonded by a bond of which the strength is set equal to the strength of the intact rock or clumped by a kinematic constraint preventing any relative movement between the two sides of the joint (Warburton, 1985). This method of generating concave blocks is illustrated in further detail in Chapter 4. Alternatively, if one desires to check the generated blocks against the actual patchwork of discontinuities and perform clustering as illustrated by Yu et al. (2009) (Section 2.1.2), this is also possible. This can be done at the end of the entire rock slicing algorithm. The algorithm proposed by Yu et al. (2009) requires information on the polyhedron vertices; a simple way to calculate the vertices is shown in Appendix B.

According to Baecher (1983) and Zadhesh et al. (2012), the extents of most joint sets could be statistically characterised using either a log-normal or an exponential distribution. That is to say, a particular joint set is likely to consist of joints with small and large extents. For algorithms based on the sequential subdivision approach, unless the assigned joint

extents are infinite, the sequence employed to introduce non-persistent joints will affect the generated block assembly. Each slicing sequence of the assigned joint pattern could be viewed as reproducing a particular geometry extracted from the prescribed probability distribution characterising the joint pattern of the analysed rock mass. However, to avoid creating 'slices' which are too large compared to the assigned joint extents, joints with larger extents should be introduced first. Because the first few slices inevitably have to span through the entire domain, one may wish to assign them as fictitious joints, i.e. to mimic the strength of intact rock (Section 2.1.2), depending on the actual joint extents relative to the modelling domain. To generate random joint patterns in the case of more than one joint set, joints should be introduced in a sequence such that joints belonging to different joint sets are alternated, in order to avoid the formation of long parallel blocks, i.e. pancake shaped blocks. This procedure is unnecessary for an interbedded rock mass, whose bedding planes are significantly larger in extent compared to the cross-joints; the bedding planes can be introduced first, before introducing the cross-joints.

Based on the recommendations of Hudson (2012) in a discussion as regards future developments on the modelling of fractures, it is desirable to introduce fractures following a sequence which is consistent with their mechanical genesis. Hudson (2012) illustrates this concept using Fig. 3.16 for a limestone rock mass. The proposed rock slicing algorithm is capable of modelling fractures following a sequence based on their mechanical genesis. Consider the example in Fig. 3.16. Fractures from joint set '1' are introduced first. Then fractures from joint set '2' are introduced so that they terminate against fractures from joint

Fig. 3.16. Possible sequence of fracturing in a limestone rock mass (image courtesy of Hudson (2013))

set '1'. Fractures from joint set '3' are then introduced, followed by those from joint set '4'.

At the end of the rock slicing procedure, each block is defined solely by its faces. Although the contact detection algorithm proposed later in this chapter does not require information on the vertices and edges, it is necessary to calculate the vertices to work out the block volume, mass and centroid for the purpose of DEM simulations. A simple way to calculate the vertices is shown in Appendix B. Previously, the planes defining each particle are defined with respect to the global reference system. To define the planes with respect to the local reference frame whose origin is at the particle centroid, $\mathbf{x}_0$ (see Fig. 3.17), the equations defining the planes can be updated as:

$$\mathbf{a}_{i\text{local}} = \mathbf{a}_{i\text{global}}, \quad i = 1,..., N, \tag{3.19}$$

$$d_{i\text{local}} = -\mathbf{a}_{i\text{global}}^{\mathrm{T}}\mathbf{x}_0 + d_{i\text{global}}, \qquad j = 1,..., N, \tag{3.20}$$

It is noteworthy that bounding boxes are commonly used in DEM codes to identify neighbouring particles before running the actual contact detection tests which are computationally more expensive (Cohen et al., 1995). The bounding boxes could be updated at each time-step using the procedures in Appendix C.

3.3 CONTACT DETECTION ALGORITHM

The proposed contact detection algorithm between a pair of convex polyhedra is presented in this section. A concave shaped polyhedron can be modelled as a cluster of two or more convex polyhedra. The proposed contact detection algorithm adopts the same conceptual framework as the block generation algorithm, i.e. the shape of a polyhedron is defined solely

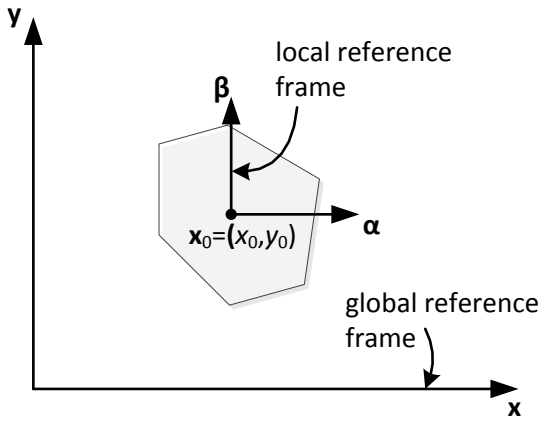

Fig. 3.17. Illustration of global reference frame and local reference frame in 2-D

using linear inequalities. The necessary mathematics is detailed here, namely the transformation of inequalities with respect to different reference systems, the linear program to establish intersection, the calculation of an appropriately defined centre as the contact point, the concept of "potential particles" to calculate the contact normal, and the calculation of the overlap distance.

3.3.1 Transforming the inequalities and changing reference systems

Note that, in a DEM model, the shape of each polyhedral particle is initially defined in terms of local coordinates; they are referred to as (α,β,γ) for clarity. The particle position and orientation, on the other hand, are defined with respect to the global reference frame (x,y,z). Consequently, for the purpose of contact detection between a pair of particles, whose shapes are defined with respect to their local reference frames, it is necessary to define the planes (linear inequalities) of both particles with respect to the same global coordinate system (see Fig. 3.18). Consider a vector $\boldsymbol{\alpha}=(\alpha,\beta,\gamma)$ which is rotated by θ (following the right-hand rule) about a vector with direction cosines (a,b,c) to $\mathbf{x}^* = (x^*, y^*, z^*)$. The rotated vector may be expressed by means of the rotation matrix (Kuipers, 2002):

$$\begin{bmatrix} x^* \\ y^* \\ z^* \end{bmatrix} = \begin{bmatrix} \cos\theta + a^2F & -c\sin\theta + abF & b\sin\theta + acF \\ c\sin\theta + abF & \cos\theta + b^2F & -a\sin\theta + bcF \\ -b\sin\theta + acF & a\sin\theta + bcF & \cos\theta + c^2F \end{bmatrix} \begin{bmatrix} \alpha \\ \beta \\ \gamma \end{bmatrix} \tag{3.21}$$

where $F = 2\sin^2(\theta/2) = 1-\cos\theta$.

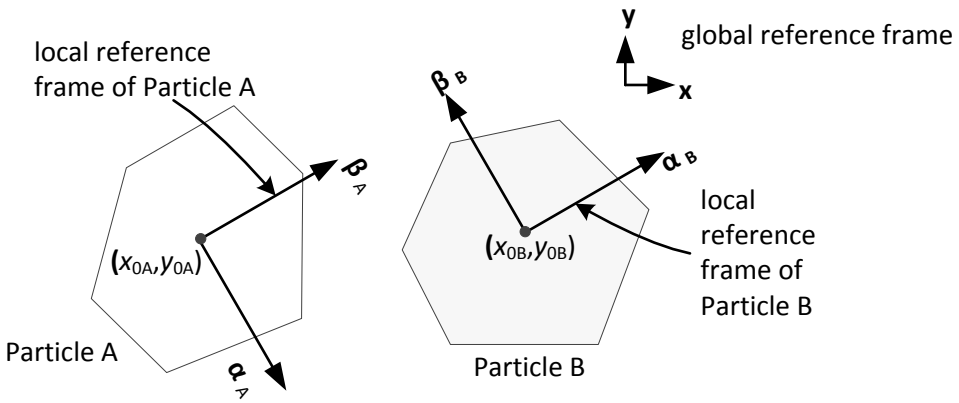

Fig. 3.18. A pair of particles considered for contact detection, with each particle having its own local reference frame according to which the particle faces have been defined. The local x and y axes are referred to as α and β for clarity.

Take for instance two particles, Particle A and Particle B. Suppose that their orientations are defined in terms of rotation matrices $\mathbf{Q}_\mathrm{A}$ and $\mathbf{Q}_\mathrm{B}$ respectively. Then, the linear inequalities previously defined in the local coordinates (α, β, γ) can be transformed into the global coordinates (x, y, z) using the following equations:

$$\mathbf{a}_{i\mathrm{A}} = \mathbf{Q}_\mathrm{A}\mathbf{a}_{i\mathrm{localA}}, \quad i = 1,..., N_\mathrm{A} \tag{3.22}$$

$$\mathbf{a}_{i\mathrm{B}} = \mathbf{Q}_\mathrm{B}\mathbf{a}_{i\mathrm{localB}}, \quad i = 1,..., N_\mathrm{B} \tag{3.23}$$

$$d_{i\mathrm{A}} = \mathbf{a}_{i\mathrm{A}}^\mathrm{T}\mathbf{x}_{0\mathrm{A}} + d_{i\mathrm{localA}}, \quad i = 1,..., N_\mathrm{A} \tag{3.24}$$

$$d_{i\mathrm{B}} = \mathbf{a}_{i\mathrm{B}}^\mathrm{T}\mathbf{x}_{0\mathrm{B}} + d_{i\mathrm{localB}}, \quad i = 1,..., N_\mathrm{B} \tag{3.25}$$

where $\mathbf{x}_{0\mathrm{A}}$ and $\mathbf{x}_{0\mathrm{B}}$ are the positions of particles A and B respectively in the global coordinate system.

Conversely, before any function evaluations, the global coordinates $\mathbf{x} = (x, y, z)$ must first be transformed back to the local coordinates $\boldsymbol{\alpha} = (\alpha, \beta, \gamma)$ (see Fig. 3.19). If the particle centre is at $\mathbf{x}_0 = (x_0, y_0, z_0)$ then first define:

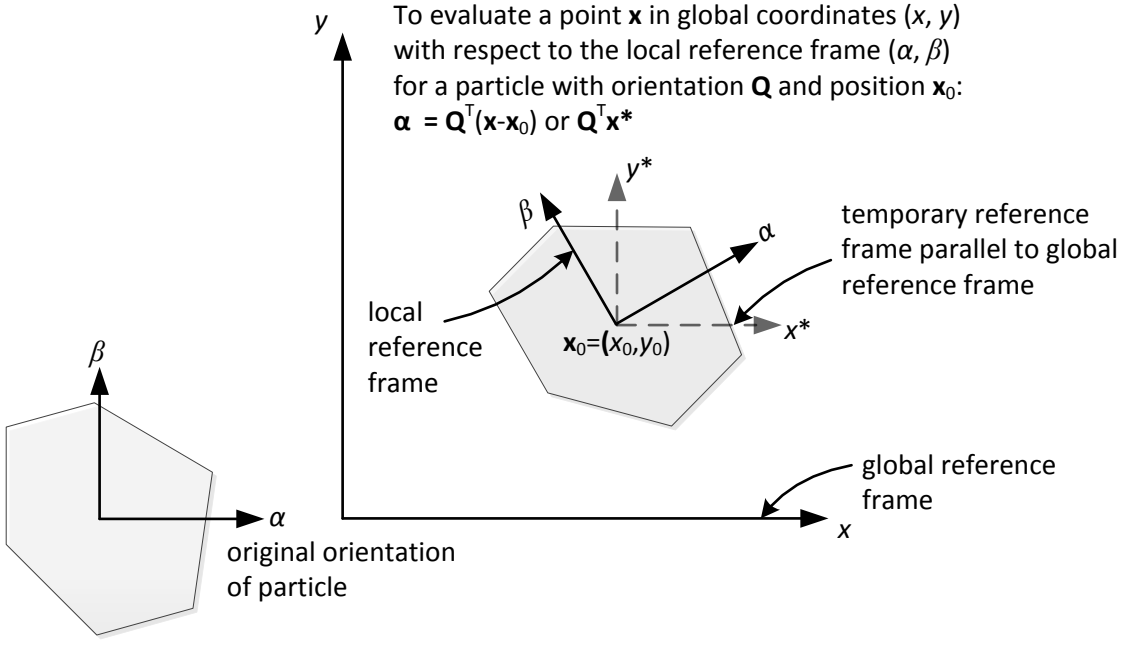

Fig. 3.19. Transformation between local and global reference frames of a particle. Refer to text for explanation.

$$\begin{bmatrix} x^* \\ y^* \\ z^* \end{bmatrix} = \begin{bmatrix} x \\ y \\ z \end{bmatrix} - \begin{bmatrix} x_0 \\ y_0 \\ z_0 \end{bmatrix} \tag{3.26}$$

If a particle whose shape is defined in terms of local coordinates $\boldsymbol{\alpha} = (\alpha, \beta, \gamma)$ has been rotated by θ (following the right-hand rule) about a vector with direction cosines (a, b, c) to $\mathbf{x}^* = (x^*, y^*, z^*)$, then the coordinates of the particle in the (α, β, γ) and (x^*, y^*, z^*) frames are related by $\boldsymbol{\alpha} = \mathbf{Q}^{\mathrm{T}}\mathbf{x}^*$. This is illustrated in Fig. 3.19 (p. 47).

3.3.2 Establishing intersection

Given a pair of polyhedra potentially in contact, we can establish whether there is actual intersection by checking if the linear inequalities from both polyhedra may form a feasible optimisation problem (see Fig. 3.20); the problem is feasible if there exists a point inside the interior region. We can determine this point by minimising the maximum infeasibility, by running the following linear program (Boyd & Vandenberghe, 2004):

$$\left.\begin{array}{c} \text{minimise } s \\ \text{where} \\ \mathbf{a}_i^{\mathrm{T}}\mathbf{x} - d_i \le s, \quad i = 1, \ldots, N_{\mathrm{A}} + N_{\mathrm{B}} \end{array}\right\} \tag{3.27}$$

There is intersection if s < -ε, where ε is a positive numerical tolerance for the overlap distance between two particles. This approach has for instance been applied in the field of

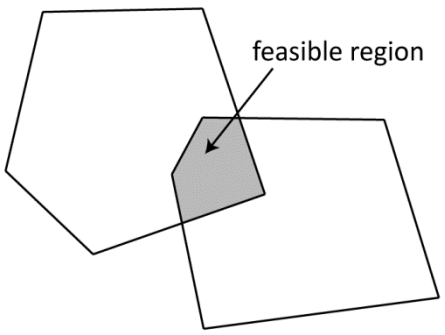

Fig. 3.20. The feasible region (shaded) which satisfies the linear inequalities for both particles (reprinted from Boon et al. (2012) with permission from Elsevier). The size of the overlap region is exaggerated for clarity. When there is no overlap, a feasible point cannot be found. The feasible point is used for the next stage of optimisation.

computer graphics (Seidel, 1991). One can either use a variety of methods to solve the linear program, e.g. the simplex method or the interior-point method. Because the overlap distance can be very small, it is found that the simplex method is well suited to the problem because it is numerically stable.

3.3.3 Finding the contact point

Once the existence of a contact is established, it is necessary to define an appropriate "contact point" which is the point at which the interaction forces are considered to act. To ensure that the DEM simulations are physically realistic, the contact point should follow the relative movement of the interacting particles, such that it is biased towards the region where the overlap is larger, but not too close to the boundary. A suitable point could be defined as the centroid of the overlapping volume (Smith et al., 2009; Feng & Owen, 2012). However, because working out the centroid of the overlapping volume is computationally expensive, an appropriately defined analytic centre of the linear inequalities is used as the contact point. The calculation of the analytic centre has replaced the calculation of the centre of gravity in many 'centering' algorithms because of its computational efficiency (Trafalis & Malyscheff, 2002; Baena & Castro, 2011). According to Boyd & Vandenberghe (2004), the analytic centre is defined by:

$$\text{maximise} \sum_{i=1}^{N_A+N_B} \log(d_i - \mathbf{a}_i^T \mathbf{x}) \tag{3.28}$$

The sum of the log-function is concave and its maximum is known as the analytic centre of the inequalities (see Fig. 3.21). The idea of the analytic centre stems from the concept of central path in the barrier method, which is a particular interior-point algorithm which has been widely used in linear programming. According to Boyd & Vandenberghe (2004), Eq. (3.28) can be given a simple mechanical interpretation in terms of potential forces, and can be viewed as the potential function associated with the total force field generated by the constraints (i.e. large negative forces generated). As a point approaches the boundary of the feasible set, it is strongly repelled by the forces generated by the constraints. In the case of Eq. (3.28), the optimal point gives the point which minimises the repelling forces.

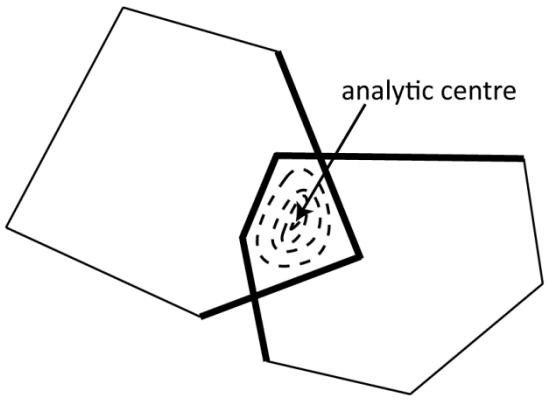

Fig. 3.21. The analytic centre for the inequalities defining both particles (after Boon et al. (2012) with permission from Elsevier). The size of the overlap region is exaggerated for clarity. Eq. (3.28) can also be written as minimising the negative sum of the log-function.

Geometrically, the analytic centre is the point which maximises the product of the distance between the planes $\prod_{i=1}^{N_A+N_B}(d_i - \mathbf{a}_i^T\mathbf{x})$ for $d_i - \mathbf{a}_i^T\mathbf{x} > 0$.

Eq. (3.28) is an unconstrained minimisation problem. In fact, algorithms written for linear programming can be easily adapted to calculate Eq. (3.28). Notice that a typical linear program has the following form:

$$\left.\begin{array}{c} \text{minimise } \mathbf{c}^T\mathbf{x} \\ \text{subject to} \\ d_i - \mathbf{a}_i^T\mathbf{x} \geq 0, \quad i = 1,\ldots, N \end{array}\right\} \tag{3.29}$$

where $\mathbf{c}^T\mathbf{x}$ is the so-called objective function. In interior-point methods, the inequality constraints are usually introduced implicitly in the objective function as:

$$\text{minimise } t\mathbf{c}^T\mathbf{x} - \sum_{i=1}^{N}\log(d_i - \mathbf{a}_i^T\mathbf{x}) \tag{3.30}$$

in which the original objective function $\mathbf{c}^T\mathbf{x}$ is multiplied by t. To solve the linear program in Eq. (3.29) using the log-barrier method, the problem Eq. (3.30) is solved repeatedly for a sequence of central points $\mathbf{x}^*(t)$ for $t > 0$, e.g. $t = 1, 10, 100 \ldots 10^6$, which finally converges to the optimal point. Note that the previous central point is used as the starting point to calculate the next central point. The path traced out by this method is known as the central path. Note that each central point is calculated using Newton's method. Therefore,

Eq. (3.30) is identical to Eq. (3.28) when $\mathbf{c}^T = 0$. The time to obtain the analytic centre is therefore expected to be much shorter than for a typical linear programming problem (solved using the log-barrier method) because we need only to calculate a single central point, i.e. it is not necessary to trace out the entire central path. Here, the log-barrier code provided by Boyd (2004) for linear programming (i.e. Eq. (3.30)) has been adapted to solve Eq. (3.28). Note that points outside the interior region are undefined by the log-function in Eq. (3.28). Hence, the point at every iteration has to be inside the interior region. The feasible point obtained previously upon establishing intersection from Eq. (3.27) can be used as the starting point in this problem (Eq. (3.28)). Boyd & Wegbreit (2007) claimed that, unlike primal-dual interior point methods, the log-barrier method has good warm-start properties. This is useful particularly when the contact point from the previous DEM time step is still inside the interior (overlap) region, and is expected to be close to the contact point in the current time step. Eq. (3.1) can be used to check whether the point is inside the overlap region. In this case, one can choose to skip the linear program. However, if the point falls too close to the boundaries, it is found here that first performing the linear program to minimise the maximum infeasibility (Eq. (3.27)) resulted in better convergence when calculating the analytic centre.

Note that the minimal set of planes defining the overlap region consists of the bold lines in Fig. 3.21 (p. 50). The thin lines (Fig. 3.21, p. 50) are geometrically redundant and can affect the location of the analytic centre as calculated in Eq. (3.28). Because it is time consuming to identify and remove all the redundant inequalities, the redundant inequalities are retained in Eq. (3.28); one needs to solve a linear program for every linear inequality to check if it is geometrically redundant (Caron et al., 1989). Including redundant inequalities in the calculation is acceptable because the essential property of the contact point remains unchanged, i.e. it is still located inside the interior region and it can follow closely the relative movement of the particles. Moreover, the effect of the redundant inequalities is not large because the gradient of the constraint (interpreted as the potential force) is relatively small compared to the constraints close to the analytic centre. Furthermore, including redundant inequalities ensures that the path traced out by the contact point is smooth during

transitions between contact types, e.g. from edge-edge to vertex-edge. Pruning redundant inequalities may cause the contact point to experience undesirable "jumps" during transitions between contact types because the number of inequalities for the calculation of the analytic centre (Eq. (3.28)) may suddenly change.

3.3.4 Establishing the contact normal

After calculating the contact point (Section 3.3.3), we need to calculate the contact normal and overlap distance. The calculation of the contact normal between a pair of polyhedral particles can be ambiguous when the interaction type is complex, such as edge-edge (Cundall, 1988). In this algorithm, an inner "potential particle" (related to the concepts described by Houlsby, 2009) entirely inside the polyhedral particle is defined so that the normal vector can be cheaply calculated, even at the particle edges and corners (see Fig. 3.22). The inner potential particle defined in the local coordinate system can be defined as:

$$f = \sum_{i=1}^{N} \left\langle a_i \alpha + b_i \beta + c_i \gamma - d_i + r \right\rangle^2 \tag{3.31}$$

where r is the radius of curvature of the corners and (a_i, b_i, c_i) are the normal vectors defining the particle faces. The Macaulay brackets $\langle\ \rangle$ are defined such that $\langle x \rangle = x$ and $\langle -x \rangle = 0$. The constant r also represents the distance of the inner particle surface to the actual particle surface. This value has to be larger than the largest expected overlap distance in the DEM simulation. In terms of local coordinates, the normal vector of the particle or the

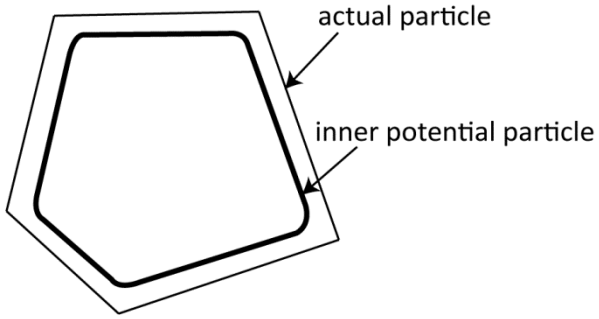

Fig. 3.22. A "potential particle" (cf. Houlsby, 2009) is defined inside the actual particle (reprinted from Boon et al. (2012) with permission from Elsevier). The normal vector of the particle at any point can be calculated from the first derivative of the potential particle.

gradient of f (Eq. (3.31)) can be calculated as:

$$\nabla f = \left(\frac{\partial f}{\partial \alpha}, \frac{\partial f}{\partial \beta}, \frac{\partial f}{\partial \gamma} \right) \tag{3.32}$$

where

$$\frac{\partial f}{\partial \alpha} = 2\sum_{i=1}^{N} a_i \left\langle a_i\alpha + b_i\beta + c_i\gamma - d_i + r \right\rangle \tag{3.33}$$

$$\frac{\partial f}{\partial \beta} = 2\sum_{i=1}^{N} b_i \left\langle a_i\alpha + b_i\beta + c_i\gamma - d_i + r \right\rangle \tag{3.34}$$

$$\frac{\partial f}{\partial \gamma} = 2\sum_{i=1}^{N} c_i \left\langle a_i\alpha + b_i\beta + c_i\gamma - d_i + r \right\rangle \tag{3.35}$$

The local coordinates (α, β, γ) in Eqs. (3.33), (3.34) and (3.35) can be calculated from global coordinates (x, y, z) (Section 3.3.1). The normal vector as calculated above has to be transformed into the global reference frame by $\nabla f_{\text{global}} = \mathbf{Q}\nabla f$ where $\mathbf{Q}$ can be calculated from Eq. (3.21).

To calculate the contact normal, the normal vector of each particle is first evaluated at the contact point, i.e. the analytic centre as calculated in Section 3.3.3. Then, the contact normal (from Particle A to Particle B) is taken as the average of the two unit vectors, i.e. $\mathbf{n}_{\text{AB}} = 0.5(\nabla f_{\text{A}} - \nabla f_{\text{B}})$ (see Fig. 3.23). Alternatively, one can use a weighted average of the two unit vectors based on the particle stiffnesses (cf. Houlsby, 2009).

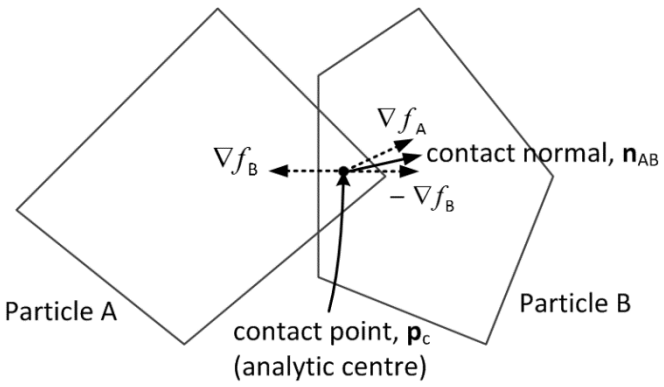

Fig. 3.23. Illustration of the calculation of contact normal. The overlap is exaggerated for clarity

3.3.5 Calculating the overlap distance

Once the contact point (Section 3.3.3) and contact normal (Section 3.3.4) are obtained, the overlap distance is calculated as the distance between the two particle surfaces along the contact normal (see Fig. 3.24). Consider two particles, Particle A and Particle B, which are overlapping such that the contact point is $\mathbf{p}_c$ and the contact normal, directed from Particle A to Particle B, is $\mathbf{n}_{AB}$. Define the line passing through $\mathbf{p}_c$ along the direction $\mathbf{n}_{AB}$ as $\mathbf{p}(t) = \mathbf{p}_c + t\mathbf{n}_{AB}$ where t is a scalar denoting the distance of the point from $\mathbf{p}_c$. This line intersects Particle A at $\mathbf{p}_A$ and Particle B at $\mathbf{p}_B$ at the boundaries of the overlapping region. The overlap distance is calculated as the distance between $\mathbf{p}_A$ and $\mathbf{p}_B$. An obvious way to calculate $\mathbf{p}_A$ is to first calculate the intersections of the line $\mathbf{p}(t) = \mathbf{p}_c + t\mathbf{n}_{AB}$ with the faces of Particle A whose normal vectors make positive dot products with $\mathbf{n}_{AB}$. For a face whose equation is expressed as $\mathbf{a}_A^T\mathbf{x} - d_A$ with respect to the global reference frame, the intersection with the line $\mathbf{p}(t) = \mathbf{p}_c + t\mathbf{n}_{AB}$ is:

$$\mathbf{p} = \mathbf{p}_c + \frac{d_A - \mathbf{a}_A \cdot \mathbf{p}_c}{\mathbf{a}_A \cdot \mathbf{n}_{AB}} \mathbf{n}_{AB} \tag{3.36}$$

Of the points which have been calculated, the point which is closest to $\mathbf{p}_c$ is the point on the surface of Particle A, i.e. $\mathbf{p}_A$. To calculate $\mathbf{p}_B$, the same procedure is repeated for Particle B but in the opposite direction, i.e. $\mathbf{p}(t) = \mathbf{p}_c - t\mathbf{n}_{AB}$.

Another method is to calculate $\mathbf{p}_A$ and $\mathbf{p}_B$ is to use bracketing algorithms,

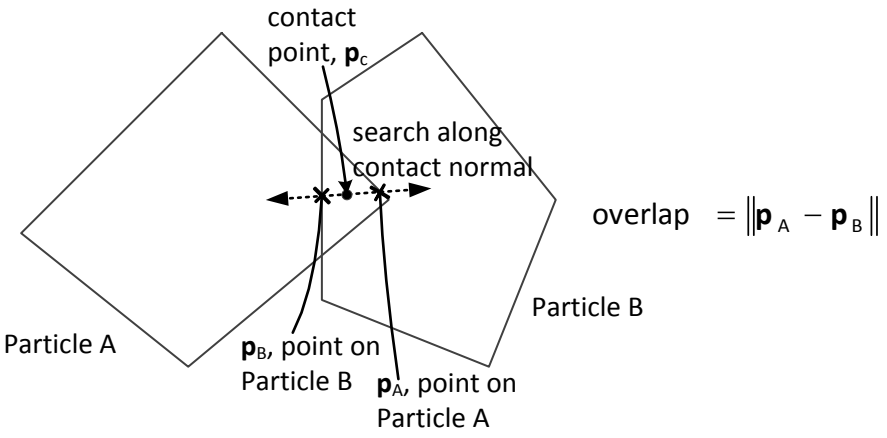

Fig. 3.24. Illustration of the calculation of overlap distance. The overlap is exaggerated for clarity

i.e. reducing the gap of an interval, which is defined by two endpoints and is known to contain the root. For a convex particle, the surface of the particle is known to exist between a point which is inside the particle and another point outside the particle. Now suppose that we are interested to calculate $\mathbf{p}_A$. One of the endpoints defining the interval could be taken as the contact point, $\mathbf{p}_c$; it is inside the particle. The other endpoint outside the particle can be sought easily by searching along the line $\mathbf{p}(t) = \mathbf{p}_c + t\mathbf{n}_{AB}$. For example, the first trial for t can be taken as the overlap distance in the previous time step. If the trial point $\mathbf{p}(t)$ is still inside the particle, the magnitude of t is increased until the trial point falls outside the particle. A suitable function to evaluate whether or not a point is inside a particle defined by N faces is (see Fig. 3.25):

$$g = \max(a_1^{\mathrm{T}} x - d_1, a_2^{\mathrm{T}} x - d_2, a_i^{\mathrm{T}} x - d_i, \ldots, a_N^{\mathrm{T}} x - d_N), \quad \text{for } i = 1,..., N \tag{3.37}$$

where $a_i^{\mathrm{T}} x - d_i$ is the equation of the i^{th} plane defining the polyhedron (Boyd & Vandenberghe, 2004). If $g > 0$, the point is outside the particle; and if $g < 0$, the point is inside the particle. The point is on the particle if $g = 0$. Once these two endpoints are established, the point $\mathbf{p}_A$ can be calculated easily through standard bracketing routines. The overlap distance is calculated as the distance between $\mathbf{p}_A$ and $\mathbf{p}_B$, as shown previously in Fig. 3.24 (p.54).

3.3.6 Rotating coordinates and scaling of constraints

When the log-barrier method encounters numerical difficulties, the two main reasons are that the starting point is poor or that the problem is badly scaled. It is found that first solving the linear program to minimise the maximum infeasibility can reduce numerical difficulties.

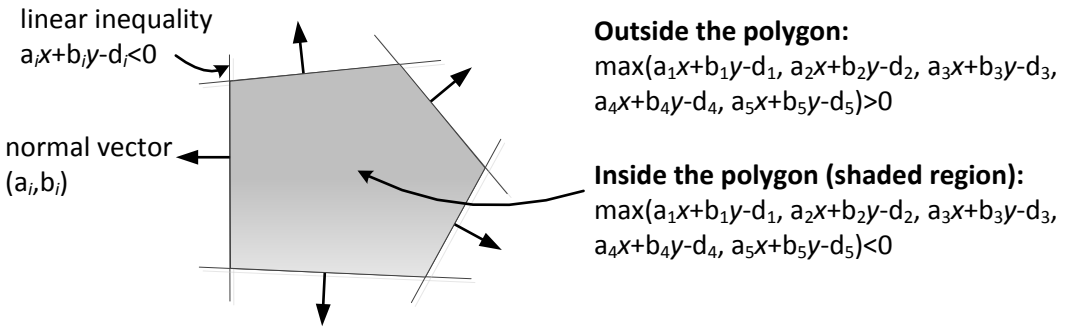

Fig. 3.25. Illustration of the method to evaluate whether a point is inside or outside the polygon in 2-D

When the problem is expected to be badly scaled, it is therefore necessary to rely on more powerful nonlinear programming solvers to calculate the analytic centre. When using optimisation software, it is helpful to introduce slack variables to ensure that the solver satisfies the inequalities in all iterations because points outside the overlap region are not defined in the log-function (Eq. (3.28)); most optimisation software honour bound constraints, e.g $u \geq x \geq l$, better (i.e., for every iteration) than equality or inequalitiy constraints , e.g $\mathbf{Ax} \geq \mathbf{b}$. Hence, the optimisation problem is recast as:

$$\left.\begin{aligned} &\text{minimise } -\sum_{i=1}^{N_\mathrm{A}+N_\mathrm{B}} \log(s_i) \\ &\text{subject to} \\ &d_i - \mathbf{a}_i^\mathrm{T}\mathbf{x} = s_i, \qquad i = 1,\ldots, N_\mathrm{A}+N_\mathrm{B} \\ &s_i \geq 0, \quad i = 1,\ldots, N_\mathrm{A}+N_\mathrm{B} \end{aligned}\right\} \tag{3.38}$$

where the slack variables s_i are a measure of how far away a point is from the constraint i. An interior point is a point inside the feasible region for which all slack variables s_i are positive.

For small overlap distances, the optimisation problem (Eq. (3.28)) can be badly scaled, especially when the contact length in one direction is significantly larger than in the other. This will be reflected in the slack variables s_i in Eq. (3.38), the largest of which could be several orders of magnitude larger than the smallest. It is therefore desirable to scale the constraints such that they operate within the same order of magnitude during the process of optimisation. Since the solution obtained at the previous time step is normally close to the new solution, the slack variables for the inequality constraints can be scaled by its initial value. This procedure is shown later in Eqs. (3.49) and (3.50) (refer to Gill et al. (1981) for scaling guidelines).

Secondly, the optimisation problem can be badly scaled if the solution of the optimisation problem shifts far from its starting point along some particular directions. Consider for instance a face-face interaction. The new contact point is likely to experience greater movement from its original position along the direction parallel to the particle faces

than along the direction of the contact normal. To overcome this, scaling can be done by shifting the reference frame to the starting point $\mathbf{x}_{\text{start}}$ and working in a new coordinate system whose axis is aligned with the contact normal $\mathbf{n}_{\text{plane}}$ calculated at the starting point. Then, the axis parallel to the contact normal can be scaled more than the other axes. Suppose that we wish to choose the newly transformed z-coordinate axis as the contact normal. To obtain the rotation matrix, we can perform the following calculations:

$$\mathbf{n}_{\text{z}} = (0,0,1) \tag{3.39}$$

$$\mathbf{n}_{\text{cross}} = \mathbf{n}_{\text{z}} \times \mathbf{n}_{\text{plane}} = (x_{\text{cross}}, y_{\text{cross}}, z_{\text{cross}}) \tag{3.40}$$

$$w_{\text{cross}} = 1 + \mathbf{n}_{\text{plane}} \cdot \mathbf{n}_{\text{z}} \tag{3.41}$$

$$l = \sqrt{w_{\text{cross}}^2 + x_{\text{cross}}^2 + y_{\text{cross}}^2 + z_{\text{cross}}^2} \tag{3.42}$$

Thereafter, define:

$$(w, x, y, z) = (w_{\text{cross}}/l, x_{\text{cross}}/l, y_{\text{cross}}/l, z_{\text{cross}}/l) \tag{3.43}$$

from which the rotation matrix $\mathbf{Q}_{\text{plane}}$ can be obtained as (Kuipers, 2002):

$$\mathbf{Q}_{\text{plane}} = \begin{bmatrix} w^2 + x^2 + y^2 + z^2 & 2xy - 2wz & 2xz + 2wy \\ 2xy + 2wz & w^2 - x^2 + y^2 - z^2 & 2yz - 2wx \\ 2xz - 2wy & 2yz + 2wx & w^2 - x^2 - y^2 + z^2 \end{bmatrix} \tag{3.44}$$

The linear inequalities with reference to the transformed axes are therefore:

$$\mathbf{a}_{i\text{A}} = \mathbf{Q}_{\text{plane}}^{\text{T}} \mathbf{Q}_{\text{A}} \mathbf{a}_{i\text{localA}}, \qquad i = 1,..., N_{\text{A}} \tag{3.45}$$

$$\mathbf{a}_{i\text{B}} = \mathbf{Q}_{\text{plane}}^{\text{T}} \mathbf{Q}_{\text{B}} \mathbf{a}_{i\text{localB}}, \qquad i = 1,..., N_{\text{B}} \tag{3.46}$$

$$d_{i\text{A}} = -(\mathbf{Q}_{\text{A}} \mathbf{a}_{i\text{localA}})^{\text{T}} (\mathbf{x}_{\text{start}} - \mathbf{x}_{0\text{A}}) + d_{i\text{localA}}, \qquad i = 1,..., N_{\text{A}} \tag{3.47}$$

$$d_{i\text{B}} = -(\mathbf{Q}_{\text{B}} \mathbf{a}_{i\text{localB}})^{\text{T}} (\mathbf{x}_{\text{start}} - \mathbf{x}_{0\text{B}}) + d_{i\text{localB}}, \qquad i = 1,..., N_{\text{B}} \tag{3.48}$$

where $\mathbf{x}_{\text{start}}$ is the starting point in global coordinates for the optimisation problem, while other variables retain the previous definition in Eqs. (3.14)-(3.25).

Finally, scaling constants **u** and **D** are introduced into Eq. (3.38), so that:

$$\left.\begin{array}{c} \text{minimise } f = -\sum_{i=1}^{N_A+N_B} \log(u_i s_i) \\ \text{subject to} \\ d_i - \mathbf{a}_i^T \mathbf{D}\mathbf{x} = u_i s_i, \qquad i = 1,..., N_A + N_B \\ s_i \geq 0, \qquad i = 1,..., N_A + N_B \end{array}\right\} \tag{3.49}$$

where

$$u_i = s_{i0}, \qquad i = 1,..., N_A + N_B \tag{3.50}$$

$$\mathbf{D} = \begin{pmatrix} 1 & 0 & 0 \\ 0 & 1 & 0 \\ 0 & 0 & h \end{pmatrix} \tag{3.51}$$

and s_{i0} is the initial value of the constraints $d_i - \mathbf{a}_i^T \mathbf{D}\mathbf{x}$ in Eq. (3.49) at the starting point $\mathbf{x} = (0,0,0)$ (with respect to the transformed axes after the operations in Eqs. (3.45)-(3.48) and h is a scaling constant that can be chosen as the overlap distance in the previous DEM time step. Note that the optimisation problem above is minimised over the transformed coordinates **x** and the slack variables **s**, with each being scaled respectively by the constants **D** and **u**. The scaling strategy assumes that the starting point (obtained from the previous DEM time step) is close to the current solution. The starting point for the minimisation is **x** = (0,0,0) and $s_i = 1$ for i = 1, ..., N_A + N_B. At the end of the optimisation process, the transformed coordinates **x** have to be transformed back into global coordinates:

$$\mathbf{x}_{\text{global}} = \mathbf{Q}_{\text{plane}}(\mathbf{D}\mathbf{x}_{\text{sol}}) + \mathbf{x}_{\text{start}} \tag{3.52}$$

Based on the formulation established in Eq. (3.49) consisting of coordinates **x** and slack variables **s**, the gradient of the objective function Eq. (3.49) is:

$$\nabla f = \begin{pmatrix} 0 \\ 0 \\ 0 \\ -1/s_1 \\ \vdots \\ -1/s_{N_A+N_B} \end{pmatrix} \tag{3.53}$$

where the first three entries are the derivatives with respect to the transformed coordinates $\mathbf{x}$ while the subsequent entries consist of the derivatives of the slack variables $\mathbf{s}$ for the linear inequalities. The Hessian of the objective function is:

$$\nabla^2 f = \begin{pmatrix} 0 & 0 & 0 & 0 & 0 & 0 \\ 0 & 0 & 0 & 0 & 0 & 0 \\ 0 & 0 & 0 & 0 & 0 & 0 \\ 0 & 0 & 0 & 1/s_1^2 & 0 & 0 \\ 0 & 0 & 0 & 0 & \ddots & 0 \\ 0 & 0 & 0 & 0 & 0 & 1/s_{N_A+N_B}^2 \end{pmatrix} \tag{3.54}$$

and the Jacobian, ∇g , of the equality constraints (Eq.(3.49)) can be calculated as:

$$\nabla g = \begin{pmatrix} -\mathbf{a}_1^T\mathbf{D} & -u_1 & 0 & 0 \\ \vdots & 0 & \ddots & 0 \\ -\mathbf{a}_{N_A+N_B}^T\mathbf{D} & 0 & 0 & -u_{N_A+N_B} \end{pmatrix} \tag{3.55}$$

where the i^{th} row represents the gradient of the i^{th} constraint. The derivatives of the objective function and constraints (Eqs. (3.53)-(3.55)) can be given as input into standard nonlinear program solvers such as KNITRO (Byrd et al., 2006) or IPOPT (Wächter & Biegler, 2006).

3.4 CONCLUDING REMARKS

Two algorithms have been proposed in this chapter. The first of the two is an algorithm to generate polyhedral blocks from planar rock joints. Based on the sequential subdivision approach, the identification of blocks has been reduced to a set of linear programming optimisation problems which can be efficiently solved using standard software for linear programming, such as CPLEX (2003). The algorithm can be summarised as follows: (i) check whether there is intersection between a non-persistent joint plane and a block; (ii) if there is intersection, append the joint plane to each of the subdivided child block; (iii) at the end of the rock slicing process, identify and remove the geometrically redundant planes which do not form a block face. The algorithm requires information only on the block faces. Unlike existing algorithms, this algorithm is not burdened by the need to maintain a complex multi-level hierarchical data structure throughout the process of subdivision, making bookkeeping of data structures significantly more straightforward.

The second proposed algorithm is a contact detection algorithm between polygonal or polyhedral particles. The problem of contact detection has been formulated such that it can be solved using standard convex optimisation procedures which are known to be robust and efficient. The calculation procedures to establish intersection (Section 3.3.2), to obtain the contact point (Section 3.3.3), the contact normal (Section 3.3.4) and the overlap distance (Section 3.3.5) have all been detailed, and they are unambiguous. Intersection between a pair of particles is established by solving a linear program. If there is intersection, the contact point is calculated from an appropriately defined centre which falls inside the overlap volume, i.e. the analytic centre of inequalities defining the pair of interacting polyhedra. The contact normal is calculated from the gradient vector of an inner "potential particle" whose corners are rounded (cf. Houlsby, 2009).

CHAPTER 4
VERIFICATION AND VALIDATION EXAMPLES

This chapter is mainly about the verification of robustness of the rock slicing and contact detection algorithms proposed in Chapter 3. Of the two algorithms, the rock slicing algorithm is first examined as to whether it is a useful engineering design tool, despite the advantage in terms of computer implementation of not requiring tedious bookkeeping procedures to update and maintain the polyhedron data structures (Chapter 3). The first example illustrates the general capabilities of the algorithm at generating typical features such as concave blocks, non-persistent joints and excavation profiles. The second example examines the capability of the algorithm at modelling joint patterns realistically. The generated block assemblies are compared with the commercial DEM software, UDEC (Itasca, 2004), based on the published results of Kim et al. (2007). In the next example, the scaling of the algorithm with the number of generated blocks is examined.

Then, the contact detection algorithm, which has been developed from the novel framework based on convex optimisation (Chapter 3), is examined. In the first test, different contact types between a pair of particles are examined in close detail. In the next test, two hundred particles are allowed to fall under gravity onto a base, allowing the particles to collide with each other in different ways. In the same test, the scaling of the algorithm with the number of particle faces is also examined. The next test addresses the question as to whether the calculation of analytic centre (Chapter 3) is computationally more efficient than calculating the more commonly known geometrical centroid.

The next few examples examine whether the proposed numerical tools are capable of modelling typical rock engineering problems, namely wedge sliding, roof falling, slope slumping, and buckling of a three-hinged beam. These tests include both stability and stiffness-type problems, and the DEM results are verified against analytical and numerical solutions in the literature (Hart et al., 1988; Itasca, 2007). Finally, comparisons are made with experimental model tests and FLAC (Itasca, 2000) simulations of multi-jointed beams reported by Talesnick et al. (2007) and Tsesarsky & Talesnick (2007) respectively.

4.1 REMARKS ON NUMERICAL IMPLEMENTATIONS

The C++/python open-source DEM code YADE (Kozicki & Donzé, 2008; Šmilauer, 2010; Šmilauer et al., 2010) was used to illustrate the capabilities of the proposed algorithms in Chapter 3. The rock slicing and contact detection algorithms (Chapter 3) were implemented into this code. Because YADE is a three-dimensional DEM code, the degrees of freedom of the rock blocks in 2-D simulations had to be restricted. The blocks were allowed only to translate in the *y*-*z* plane, and to rotate only about the *x*-axis. All the algorithms in YADE have been detailed in Šmilauer (2010), and are not reproduced in this thesis, unless a different algorithm is used. It is noteworthy, however, that in YADE the integration of equations of motion, both translation and rotational, was solved explicitly using the backward difference method. As with Hart et al. (1988) and Itasca (2007), although the moments of inertia along the three principal axes of a non-spherical body in 3-D are generally not equal, the rotational motion was solved as though they were equal. Only an approximate moment of inertia was used, and this was considered acceptable, since the work in this thesis is not concerned with simulating the trajectories of high-speed dynamic bodies. The moment of inertia was approximated by discretising the body into pyramids (with the block faces forming the pyramid bases) and treating the pyramids as lumped point masses, from which three principal moment of inertias can be approximated. The largest estimated principal moment of inertia was compared against the moment of inertia of a circumscribing sphere, and the larger of the two was used.

4.1.1 Contact detection algorithm

The DEM code was linked to two optimisation codes, CPLEX (CPLEX, 2003) and IPOPT (Wächter & Biegler, 2006). The linear program (Eq. (3.27), p. 48) to establish intersection was solved using CPLEX (2003) based on the simplex algorithm. Note that, the linear program (Eq. (3.16), p. 38) in the rock slicing algorithm was solved also using CPLEX. CPLEX is freely available to academics through the IBM academic initiative program. The analytic centre was calculated using two alternative methods, namely (Eq. (3.28), p. 49) solved using the log-barrier method (Boyd, 2004) or the nonlinear program (Eq.(3.49), p. 58)

solved using IPOPT . Every benchmark test is presented and discussed in separate section headings in this chapter, each of which may consist of the results of several simulations.

4.1.2 Contact constitutive model

The contact between a pair of rock bodies is referred to as a rock joint in rock engineering terminology. There are numerous publications on the laboratory study of the contact behaviour of a rock joint in both the normal and shear directions (Barton, 1973; Bandis et al., 1983; Grasselli & Egger, 2003; Asadollahi et al., 2010). Because rock joints sampled for laboratory investigations are planar, the quantities used to define their deformation characteristics have been in terms of stress and displacement rather than force or strain respectively. Stiffness, as a consequence, is also defined in terms of stress per unit displacement. In this thesis, a linear elastic model was used to model the contact in the normal direction, unless otherwise mentioned. For a linear elastic contact, the normal stress σ_n at a contact can be calculated as:

$$\sigma_{\mathrm{n}} = k_{\mathrm{n}} u_{\mathrm{n}} \tag{4.1}$$

from which the normal force F^{n} can be calculated as:

$$F^{\mathrm{n}} = \sigma_{\mathrm{n}} A_{\mathrm{c}} = k_{\mathrm{n}} u_{\mathrm{n}} A_{\mathrm{c}} \tag{4.2}$$

where u_{n} is the relative normal displacement (or DEM overlap) between a pair of rock blocks, k_{n} is the normal stiffness (units: GPa/m) and A_{c} is the area in contact (see Appendix D for calculation procedure). The normal force vector $\mathbf{F}^{\mathrm{n}}$ is given by:

$$\mathbf{F}^{\mathrm{n}} = F^{\mathrm{n}} \mathbf{n} \tag{4.3}$$

where **n** is the normal vector at a contact. Note that the calculation of contact area may not be required in some contact laws proposed in the literature. Among them, for example, are the contact laws proposed by Mirghasemi et al. (1997) and Lawrence (2009) for 2-D polygons and 3-D polyhedra respectively. Mirghasemi et al. (1997) suggested assigning the contact area as a constant, whose value can be chosen based on the particle size. Lawrence (2009) proposed that the contact area between a pair of 3-D polyhedra can be assigned as constants whose values are determined by the contact type, e.g. face-face or vertex-face.

The shear force at a contact was modelled as linear elastic perfectly plastic following the implementation of Hart et al. (1988) unless otherwise mentioned. In Hart et al. (1988), to account for the incremental rotation of the contact plane, the existing shear force vector $\mathbf{F}^s$ is corrected as:

$$\mathbf{F}^s_{i\_\text{rotated}} = \mathbf{F}^s_i - \mathbf{F}^s_i \times \mathbf{n}_{\text{old}} \times \mathbf{n} \tag{4.4}$$

where $\mathbf{n}_{\text{old}}$ and $\mathbf{n}$ are the previous and current contact normals respectively. The increment of shear force vector $\Delta\mathbf{F}^s$ before yield is calculated as:

$$\Delta\mathbf{F}^s = -k_s A_c \Delta\mathbf{u}_s \tag{4.5}$$

so that the total shear force vector $\mathbf{F}^s$ can be updated as:

$$\mathbf{F}^s_{i+1} = \mathbf{F}^s_{i\_\text{rotated}} + \Delta\mathbf{F}^s \tag{4.6}$$

where $\Delta\mathbf{u}_s$ is the relative shear displacement (refer to Hart et al. (1988) for calculation details). The magnitude of shear force is given by:

$$F^s = (\mathbf{F}^s\mathbf{F}^s)^{1/2} \tag{4.7}$$

The maximum absolute value of shear force $F^s_{\max}$ is governed by

$$F^s_{\max} = \mu F^n \tag{4.8}$$

where $\mu = \tan\phi$ and ϕ is the friction angle at the rock joint. If $F^s > F^s_{\max}$, the shear force is reduced to its plastic limiting value:

$$\mathbf{F}^s_{\max} = \mathbf{F}^s(F^s_{\max} / F^s) \tag{4.9}$$

The normal and shear forces are applied at the contact point.

4.2 EXAMPLES OF ROCK SLICING CAPABILITIES

This section highlights, through several simple illustrations, the capabilities of the rock slicing tool (Chapter 3) at modelling non-persistent joints, concave blocks and creating slope/excavation profiles using construction joints.

Fig. 4.1 shows that the result of the rock slicing algorithm in 2-D using the methodology described in Section 2.1.2 and Section 3.2.5. Some of the key elements when generating a jointed rock mass are highlighted in Fig. 4.1 (a)-(c). The famous Vaiont rock

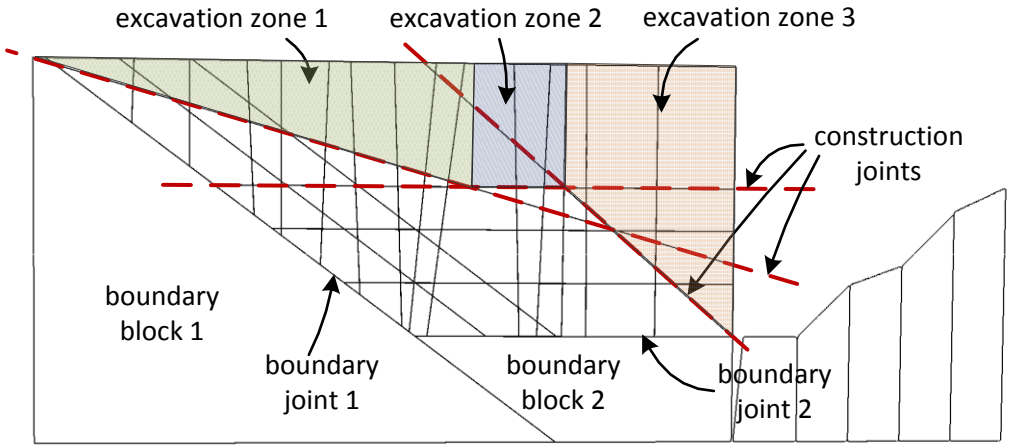

(a)

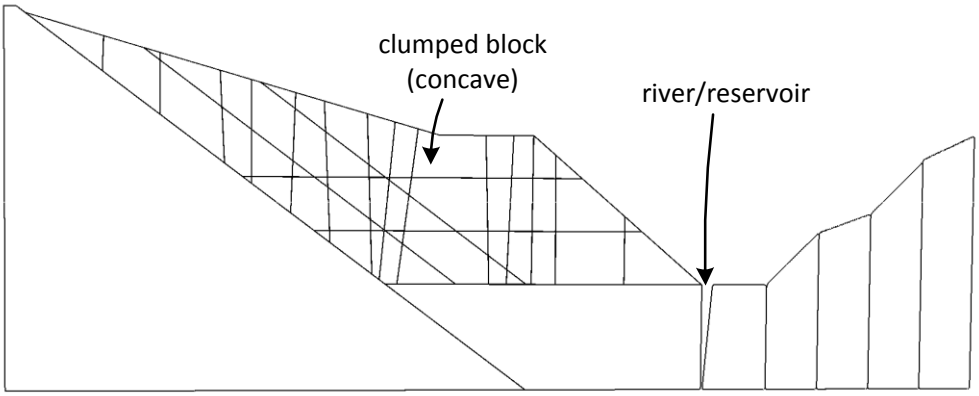

(b)

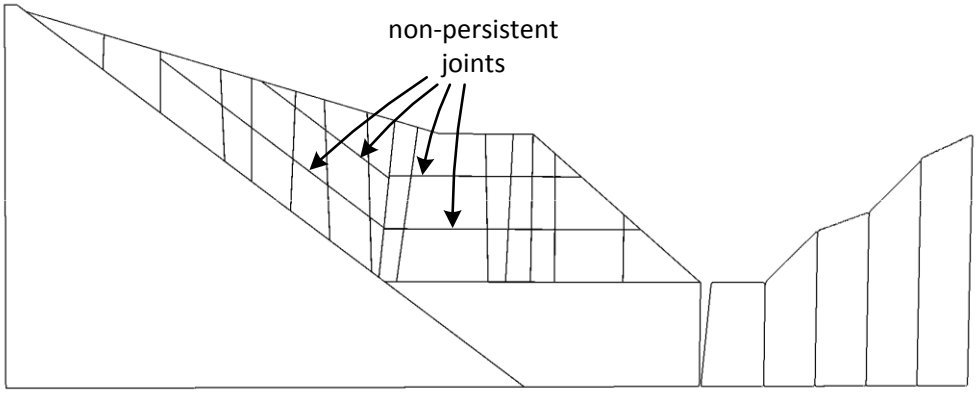

(c)

Fig. 4.1. Rock slope (2-D) generated from the rock slicing algorithm: (a) Construction joints were introduced to "outline" the free-surface of the rock slope. (b) Blocks whose centres are inside the excavation zone were removed, and blocks subdivided by construction joints are clumped together. (c) Example of use of non-persistent joints.

slope (Alonso & Pinyol, 2010; Müller, 1964) whose instability led to the catastrophic slide in 1963 was selected as an example. The middle section in Alonso & Pinyol (2010) was generated in Fig. 4.1 (p. 65).

Recall that the proposed algorithm is based on sequential subdivision; if a block is sliced by a rock joint, it is subdivided into a pair of child blocks. First, two 'boundary' joints defining the slide surface were introduced (see Fig. 4.1(a)). During the slicing calculation, the resulting child block which was located in the lower halfspace of the 'boundary' joint was automatically identified as a boundary block, so that it would not be subdivided by subsequent slices. Then, rock joints defining the rock mass were introduced. After the rock joints had been introduced, "constructions joints" (dotted red lines in Fig. 4.1 (a)) were introduced to outline the free surface of the slope, so that the blocks outside the slope profile could be removed. It can be noted that the construction joints outlining the slope profile have extended into the rock mass. These joints, however, should be fictitious because they are not part of the joint pattern. Following the procedure suggested by Warburton (1985) (Section 2.1.2 and Section 3.2.5), the blocks subdivided by construction joints were automatically clumped together to avoid creating artificial planes of weakness which may unduly affect the mechanical response of the jointed rock mass. The excavation area outside the slope profile was divided into three separate excavation zones (see Fig. 4.1 (a)). Any block falling within the specified excavation zones were then removed, as shown in Fig. 4.1 (b). Blocks which are located close to convex-shaped excavation openings or slope profiles are likely to be concave, and can be modelled based on this approach (Fig. 4.1 (b)). In some circumstances, it is desirable to control the extents of non-persistent joints to capture certain geometrical characteristics of the jointed rock mass (compare between Fig. 4.1 (b) and Fig. 4.1 (c)), to avoid subdividing certain blocks.

4.3 GENERATED BLOCK ASSEMBLY AND SUITABLE APPLICATIONS

In this verification example, the 2-D joint pattern assigned as input into UDEC (Itasca, 2004) by Kim et al. (2007) (see Fig. 4.2 (a)) was generated using the proposed rock slicing algorithm for comparison purposes. In Fig. 4.2 (b), the blocks generated by UDEC are

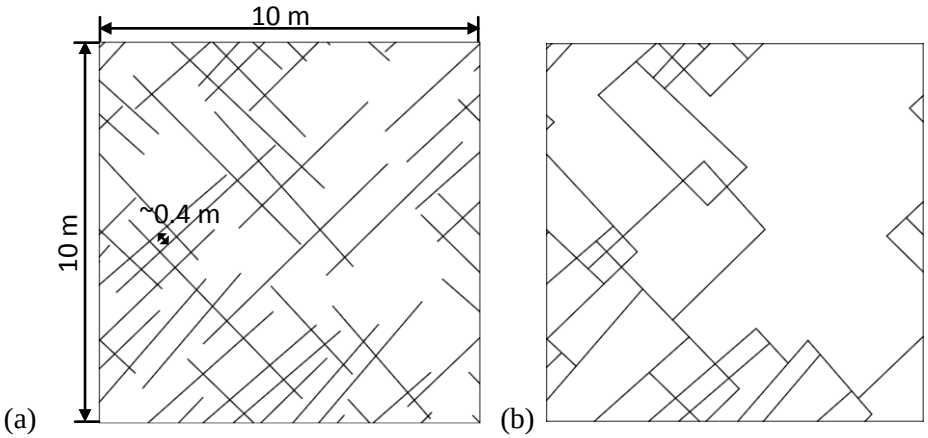

Fig. 4.2. Two dimensional joint pattern (a) input (b) generated model from UDEC (Itasca, 2004) (after Fig. 8 in Kim et al. (2007) with kind permission from Springer Science and Business Media)

plotted: it can be observed that dangling joints were removed. This is due to the fact that in a block analysis of a jointed rock mass carried out via DEM (Cundall, 1988) or DDA (Shi & Goodman, 1985), a rock joint has to either form a block face (contributing to block formation) or be removed completely. The block assembly generated using UDEC in Fig. 4.2 (b) can also be generated using the proposed rock slicing algorithm by adopting standard clustering procedures well-known in the literature (Section 2.1.2). The position and orientation of every joint in Fig. 4.2 (a) was determined and given as a deterministic input for the proposed rock slicing algorithm. Fig. 4.3 (a) shows the generated blocks having assumed joints of infinite extent; Fig. 4.3 (b) shows the generated blocks with non-persistent joints; Fig. 4.3 (c) shows the generated blocks having enforced a minimum block size of 0.4 m throughout the slicing procedure; this value was estimated from visual observation of the joint pattern (Fig. 4.2 (a)). The generated block assembly is adequately representative of the joint pattern. Note that suitably conditioning the size of the smallest block in the assembly may significantly reduce the simulation runtime of a DEM analysis since the critical timestep in the simulation is a function of the smallest block size.

To-date in the literature, block assemblies are generated based on fracture system models which are determined before the excavations are carried out. The engineer should be cautious against the degree of fracture propagation which is expected to take place during the

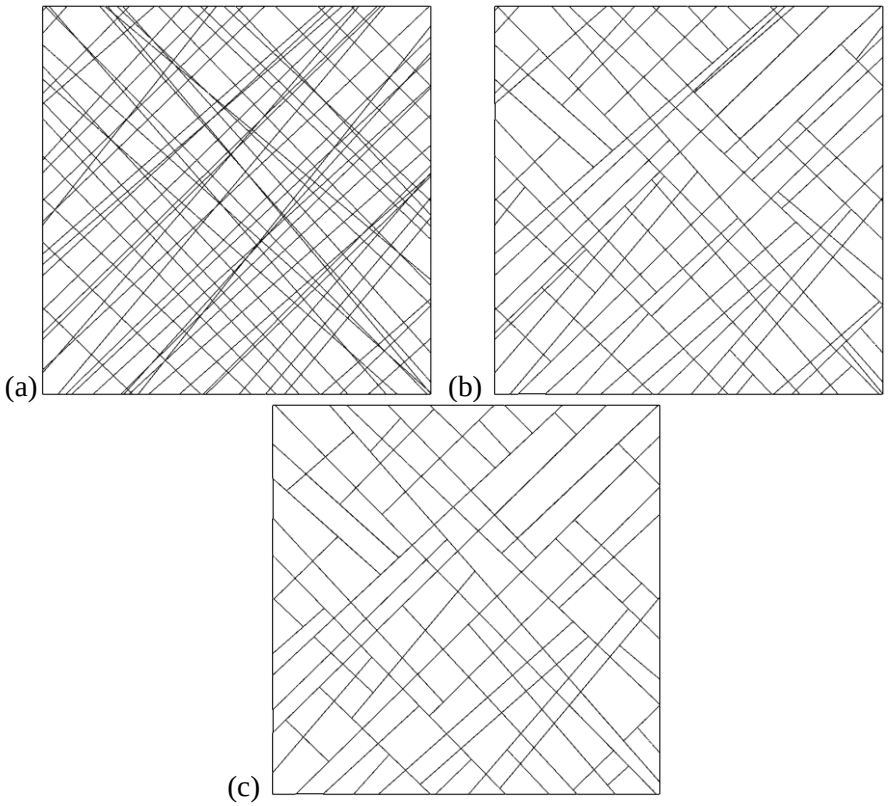

Fig. 4.3. Joint patterns generated using proposed rock slicing algorithm (a) fully-persistent, (b) non-persistent extents (c) non-persistent extents and enforcing minimum block size (inscribed circle) 0.4 m

process of excavation. The assumption of infinite joints as shown in Fig. 4.3 (a) is well-known to be overly conservative for stability considerations since the number of generated blocks is significantly larger than the actual case (Fig. 4.2 (a)). So, if a block generation code which is only capable of generating persistent joints is employed, a different measure of joint intensity should be used (Dershowitz & Herda, 1992). Conversely, the removal of dangling joints, as is done by UDEC (Fig. 4.2 (b)), increases the rock mass strength since there are fewer fractures than the actual case (Fig. 4.2 (a)), and could lead to an unsafe estimate of the stability of the excavation walls. However, if the intact rock is hard and dangling joints are unlikely to propagate, this could be a realistic estimate (cf. Kim et al., 2007). The number of blocks generated using the proposed rock slicing algorithm (Fig. 4.3 (c)) falls between the two extreme cases (Figs. 4.2 (b) and 4.3 (a)). The model in Fig. 4.3 (c) is, in fact, on the conservative side in terms of predicting block fall or sliding, i.e. that more support will be required.

Of the two block assemblies in Figs. 4.2 (b) (p. 67) and 4.3 (c) (p. 68), it is difficult to claim with certainty which model is closer to the joint pattern in Fig. 4.2 (a) (p. 67). Both are probable in a statistical sense. Note also that, on the one hand, we are concerned with generating a block assembly which is as close as possible to the joint pattern which is given as input. On the other hand, we are interested to generate a block assembly which is representative of the jointed rock mass in the field. The two concepts are distinct, and it is the latter that is the primary concern. Firstly, the joint pattern may have been simplified for input. Secondly, a particular joint pattern is merely a sample which is statistically probable in the field. With the assistance of the structural geologist, the engineer should always assess whether a generated block assembly is representative of the jointed rock mass for his stability analysis through in-situ monitoring as an excavation is carried out. Nonetheless, it is believed that, for engineering design purposes, a model which accounts for a statistically less favourable case within reasonable limits (Fig. 4.3 (c)) has more merits than a model in which a significant fraction of fractures are 'healed' (Fig. 4.2 (b)).

4.4 SCALING OF ROCK SLICING ALGORITHM

The scaling of the algorithm with the number of generated blocks in 3-D was investigated. The input is shown in Table 4.1. The number of generated blocks increases with the volume density of the discontinuity centres (Chapter 3). The extents of non-persistent joints were

Table 4.1: Input for algorithm scaling

Parameter	**Input**
Dimension of box sample	100 m × 100 m × 100 m
Orientation of joint set A	Dip direction = 122°, dip angle = 8°
Orientation of joint set B	Dip direction = 112°, dip angle = 80°
Orientation of joint set C	Dip direction = 9°, dip angle = 85°
Distribution of joint centres	Poisson's process
Joint extents (persistent case)	1000 m × 1000 m for all three joint sets
Joint extents (non-persistent case)	Square shape, lognormal distribution (mean = 5 m, standard deviation = 1 m) for all three joint sets
Minimum size (diameter of inscribed sphere)	0.4 m
Maximum aspect ratio (axes aligned box)	8000

assumed to follow a log-normal distribution. The additional efficiency derived from using bounding spheres was also investigated for both persistent and non-persistent joints.

Fig. 4.4 (a) shows the times required for block generation in the case that all three joint sets are persistent. The calculation was carried out on a standard desktop PC using one of the two cores of a Core-2-Duo CPU (3.1 GHz). It turned out that the computation time for block generation scales linearly with the number of generated blocks. The efficiency derived from using bounding spheres is not very significant (Chapter 3). The computational saving becomes more significant as the number of blocks increases.

Fig. 4.4 (b) shows the CPU time required for block generation in the case that all three joints sets are non-persistent. Without bounding spheres (crosses in Fig. 4.4 (b)), the computation time increases with the number of generated blocks in a non-linear manner. With bounding spheres (dots in Fig. 4.4 (b)), the computation time was found to scale

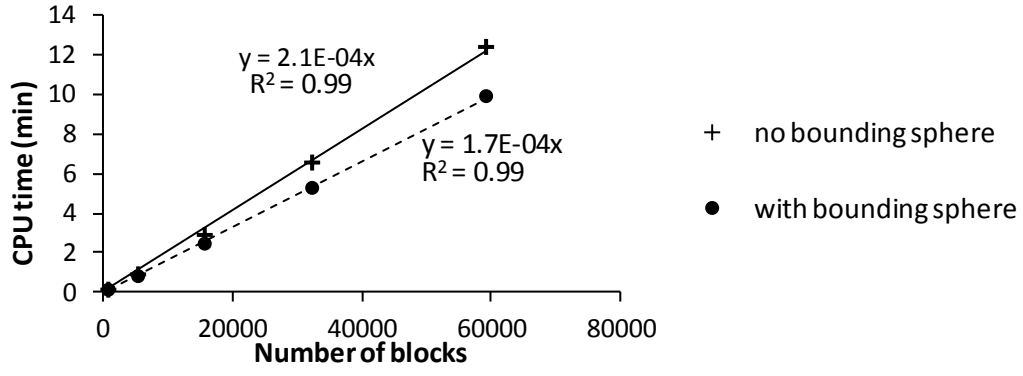

(a)

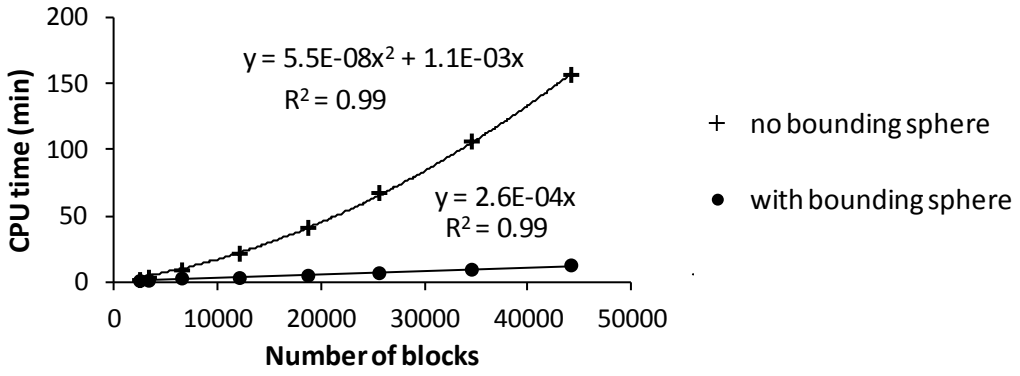

(b)

Fig. 4.4. Computation time versus number of generated blocks for (a) persistent joints, (b) non-persistent joints, with and without bounding spheres

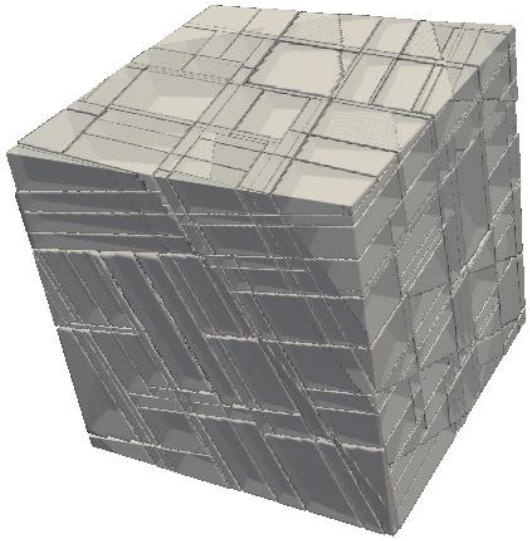

Fig. 4.5. Generated block assembly (2495 blocks) with three near-orthogonal joint sets (non-persistent joints). Opacity is reduced for better illustration.

linearly with the number of generated blocks. The efficiency derived from using bounding spheres is very significant; for more than 20000 blocks, the computation time for block generation is reduced more than 10 times. One of the joint patterns generated (number of blocks = 2495) is shown in Fig. 4.5.

The finding that the computation time scales favourably with the problem size is important because the complexity of engineering models tends to grow with time; algorithms which scale poorly with the problem size become obsolete quickly. Note that the use of prismatic bounding boxes, which is very similar to the method of bounding spheres (Chapter 3), had been proposed by Yu et al. (2009) and Zhang & Lei (2013), but the derived efficiency had not been investigated previously.

4.5 SIMPLE COLLISION TESTS

The following two simulations illustrate the capability of the contact detection algorithm to capture the contact evolution between a pair polyhedral particles after collision. High viscous damping was introduced at the contact to model realistic physical behaviour (Cundall & Strack, 1979). The size of the time-step was kept small because it was easier to interact (e.g. pause and run) with slower simulations. In the first simulation, a pair of

polyhedral particles was oriented to model a vertex-face contact, as shown in Fig. 4.6 (a). The yellow polyhedron was fixed in space, while the blue polyhedron was free to translate and rotate. The evolution of their interaction under gravity was recorded. The blue polyhedron first rotated about the colliding vertex (Fig. 4.6 (b)) before landing on one of its adjoining edges (Fig. 4.6 (c)). Subsequently, it rotated about the edge and leaned towards its centre of gravity, before coming to rest on its face (Fig. 4.6 (d)). A typical collision between polyhedra which involves transition from vertex-face, edge-face to face-face contact was successfully captured by the contact detection algorithm.

In the second simulation, a pair of cubes was oriented to model an edge-edge contact Fig. 4.7 (a). As in the first simulation, the blue cube was free to translate and rotate while the yellow cube was held fixed. Upon contact, the blue cube first rotated about the intersection of their edges and leaned towards its centre of gravity (Fig. 4.7 (b)). The edge of

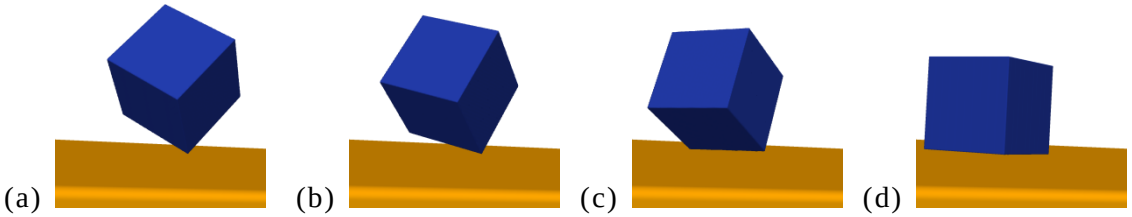

Fig. 4.6. A vertex-face contact between two polyhedra was modeled in (a). The snapshots show the polyhedra after (b) 50000, (c) 150000 time steps, and (d) 300000 time steps (very small step size). Images reprinted from Boon et al. (2012) with permission from Elsevier.

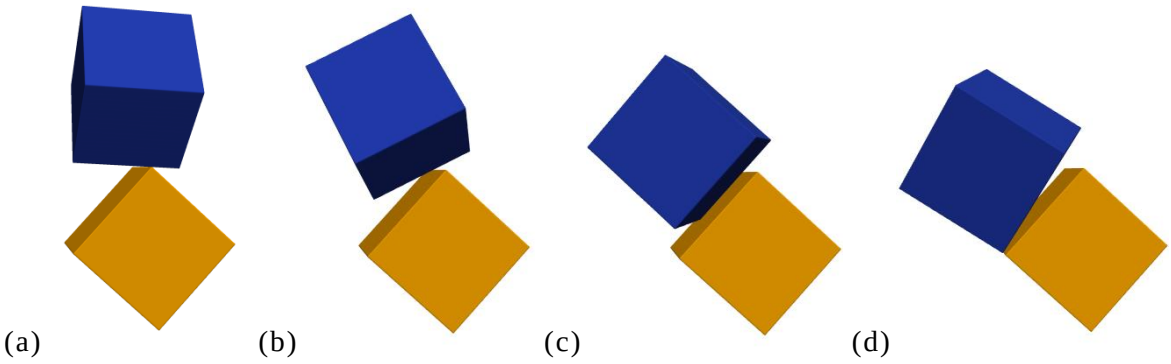

Fig. 4.7. An edge-edge contact between two cubes was modeled in (a). The snapshots show the cubes after (b) 100000, (c) 150000 time steps, and (d) 180000 time steps (very small step size). Images reprinted from Boon et al. (2012) with permission from Elsevier.

the blue cube then landed on one the faces of the yellow cube to which the intersecting edge belonged (Fig. 4.7 (c)). The blue block then landed on another edge before toppling off the yellow cube (Fig. 4.7 (d)). The results show that the contact detection algorithm is robust in modeling various contact orientations and can model interactions between polyhedral particles realistically.

4.6 PARTICLE FREE FALL AND SCALING OF CONTACT DETECTION ALGORITHM

In this section, the robustness of the algorithms was tested by simulating a variety of contact conditions for 3-D particles. First a loose packing of 200 polyhedra was generated (see Fig. 4.8). Each particle was given an initial random orientation. Then the particles were allowed to fall under gravity to impact on a surface. High viscous damping was introduced at the contact (Cundall & Strack, 1979). The time step was determined according to the suggestions given by Hart et al. (1988) to ensure numerical stability. This resulted in 7000 time steps for a total simulation time of 5.6 seconds. This exercise is suitable to test the robustness of the algorithms of contact detection since it involves particles colliding under free gravitational fall (dynamic conditions) and then bouncing against each other until they reach a final configuration at rest (quasi-static conditions). During the simulations, all types of contacts (e.g. face-face, edge-face, etc.) were encountered. Simulations involving free fall of particles have been used also by other researchers, e.g. Williams & O'Connor (1995),

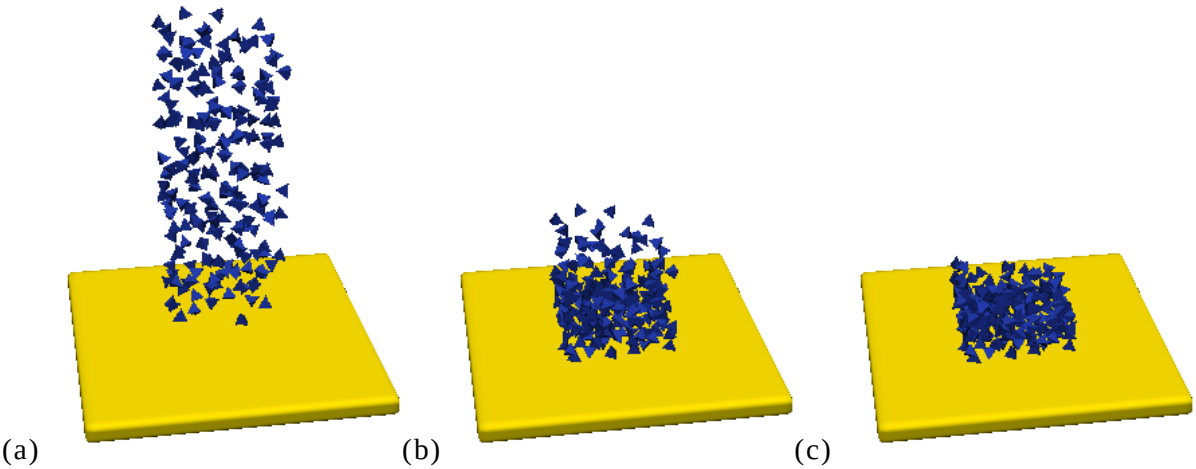

Fig. 4.8. Two hundred pyramidal particles falling under gravity: (a) loose packing as generated (b) after 4000 time steps (c) after 7000 time steps. Images reprinted from Boon et al. (2012) with permission from Elsevier.

Nezami et al. (2004) and Nezami et al. (2006) to test the robustness of their algorithms in terms of numerical convergence. Fig. 4.8 shows the simulation after 0, 4000 and 7000 time steps.

To assess the computation time with respect to the number of faces, the simulation was performed on a range of regular polyhedra, i.e., tetrahedron, cube, octahedron, dodecahedron and icosahedron. The simulation was run using one core of a 3.1 GHz Core 2 Duo Processor on a PC with 4GB RAM. Recall that for a pair of particles potentially in contact, a linear program (Eq. (3.27), p. 48) is first solved to establish whether there is actual intersection; and if there is intersection, the contact point is determined by calculating the analytic centre (Eq. (3.28), p. 49). In this example, the linear program was solved using the commercial software CPLEX based on the simplex algorithm, and the analytic centre was calculated using both the log-barrier method found in Boyd (2004) and using also the nonlinear programming software IPOPT. The two optimisation codes, i.e. CPLEX and IPOPT, were only initialised once, and were then used repeatedly for subsequent optimisation tasks.

Fig. 4.9 shows the computation time for a single contact problem averaged among all interactions over 7000 time steps. In these simulations, no numerical difficulties were encountered by any optimisation task. Notice that from our simulations, the computation time for the linear program (Eq. (3.27)) solved using CPLEX and the analytic centre (Eq. (3.28)) solved using the log-barrier method increases with the number of planes. The linear program solved using CPLEX is of O(N), where N is the number of planes involved. The speed of IPOPT to solve the nonlinear program (Eq. (3.49), p.58) is almost independent of number of planes. The computation time needed by the linear program and the log-barrier method are in the order of tens of micro-seconds (μs). The computation time used in linear programming can be reduced through warm-starting by providing the solution from the previous time-step (CPLEX, 2003). The log-barrier method can also be given an initial starting point. Although the computation time to solve the nonlinear program (Eq. (3.49)) using IPOPT is significantly slower, i.e. in the order of a few milli-seconds (ms), this procedure is necessary only when the log-barrier method fails to converge. In fact, in this

simulation, this procedure was redundant since the log-barrier method did not encounter numerical difficulties.

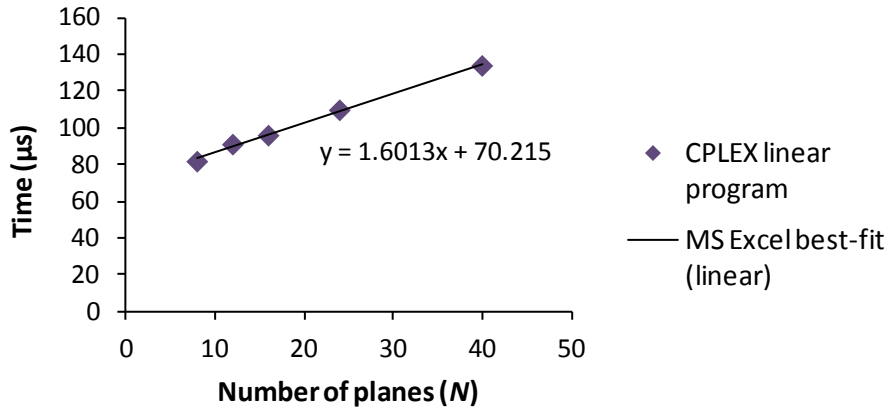

(a)

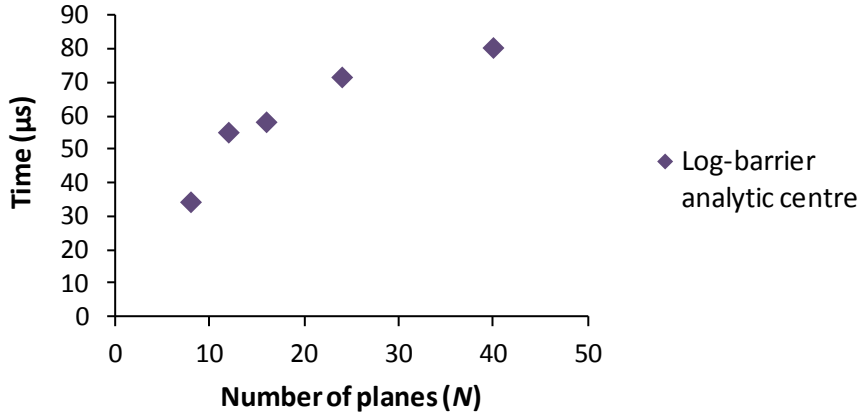

(b)

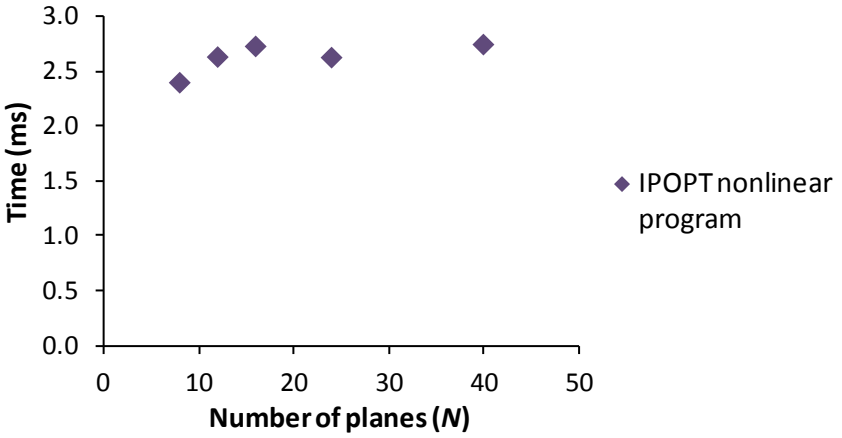

(c)

Fig. 4.9. The computation time per contact detection problem averaged among all interactions over 7000 time-steps (images reprinted from Boon et al. (2012) with permission from Elsevier). (a) CPLEX to establish intersection (Eq. (3.27)); (b) Log-barrier method to calculate analytic centre (Eq. (3.28)); (c) IPOPT to calculate analytic centre (Eq. (3.49))

4.7 BENCHMARK COMPUTATION TIME FOR ANALYTIC CENTRE AGAINST CENTROID OF OVERLAP VOLUME

The computation time of the analytic centre is compared against the standard calculation procedure of the centroid. The calculations were performed in an isolated environment in MATLAB (MathWorks, 2010). The procedure for the calculation of a polyhedron centroid made freely available by Kleder (2005) was used here, in which the polyhedron is subdivided into simplices and the weighted sum of their centroids is calculated. This calculation procedure requires the vertices of the polyhedron. The analytic centre was calculated by calling the MATLAB scripts provided by Boyd (2004).

Five regular polyhedra, i.e., tetrehedron, cube, octahedron, dodecahedron and icosahedron were generated for the purpose of this benchmark study. The calculations were repeated 2000 times and the average computation time was sought. Fig. 4.10 shows the computation time to calculate the analytic centre (red squares in Fig. 4.10) and the centroid of overlap volume (purple diamonds in Fig. 4.10) with the number of vertices. The starting point for the calculation of the analytic centre was assigned to the solver such that its distance to the centroid is 0.95 times the distance between the centroid and a vertex. The analytic centre is more efficient than the calculation of centroid for more than six vertices. Note that, during contact detection, if a point inside the interior region of the overlap is not

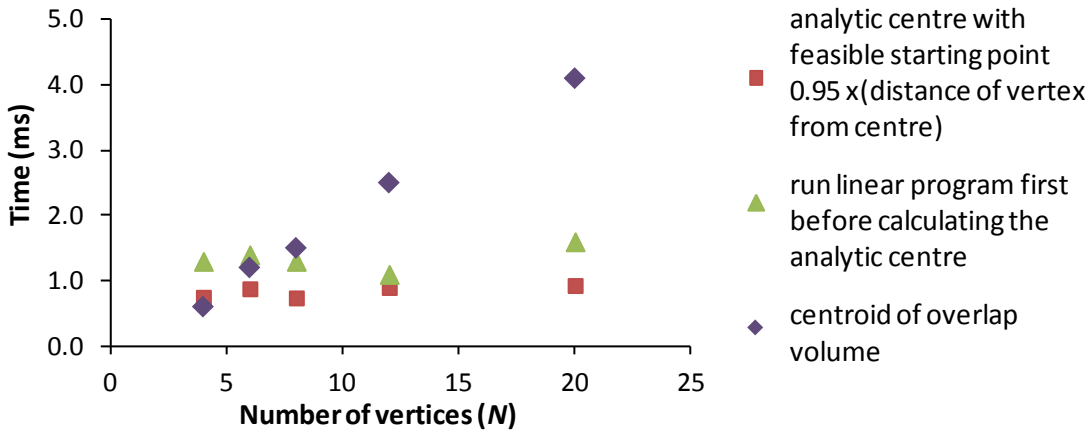

Fig. 4.10. Comparison of computation time to calculate the analytic centre and the centroid of overlap volume for several regular polyhedra

known, it is necessary to first run a linear program to obtain a starting point before calculating the analytic centre. The combined computation time for these two calculations (running a linear program to obtain a starting point and the calculation of the analytic centre) is also plotted in Fig. 4.10 (green triangles). This is still more efficient than calculating the centroid of overlap volume for more than eight vertices. In the context of contact detection in the DEM, although not considered here, additional efficiency can be derived from using the analytic centre because its calculation does not require one to work out the vertices which form the overlap volume; working out all the intersections between a pair of overlapping polyhedra is computationally expensive.

4.8 STABILITY OF A SLIDING WEDGE

In this simulation, the contact detection algorithm is used to simulate a sliding wedge problem in rock engineering (see Fig. 4.11). The model consists of four rigid blocks. Three blocks are fixed with only one wedge being allowed to move under gravity. The following discontinuities (rock joints) are present:

A: dip = 40° dip direction = 130°

B: dip = 60° dip direction = 220°

The three-dimensional rock model in Fig. 4.11 was generated using the proposed rock slicing algorithm.

The critical friction angle at which the free wedge starts sliding was sought. This

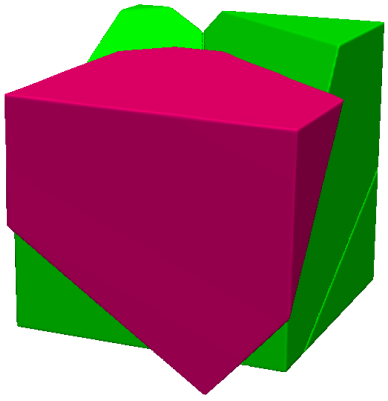

Fig. 4.11. Three-dimensional sliding wedge example with two rock joints (image reprinted from Boon et al. (2012) with permission from Elsevier)

problem was also simulated by Hart et al. (1988). The same parameters used in Hart et al. (1988) were adopted. The normal and shear stiffnesses of the joints were both set to 10 MPa/m and the rock density was 2000 kg/m^3. An elastic perfectly-plastic model with the Mohr-Coulomb yielding surface was assumed for the joint behaviour. The analytical solution for this problem is given in Hoek & Bray (1974). This problem is statically determinate and independent of the size of the blocks. Hence, the joint stiffness and density do not affect the solution (cf. Itasca, 2007). To simulate the problem numerically, a high coefficient of friction was first assigned to the discontinuities. Once the wedge reached static equilibrium, the friction was reduced by a small fraction. This process was repeated until static equilibrium was lost and the wedge started sliding. The critical friction angle at which sliding occurred in the simulation was 33.23°. The difference is minor compared to the analytical solution (33.36°) and the DEM solutions (35.0° and 33.19°) reported by Hart et al. (1988) and Itasca (2007). Note that the contact detection algorithm used in Hart et al. (1988) has been implemented into the commercial DEM software, 3DEC (Itasca, 2007). The physical behaviour was successfully captured by the proposed contact detection algorithm. Problems which are largely governed by stability alone are less likely to result in large differences due to different contact algorithms.

4.9 STABILITY OF A ROOF WEDGE

This simulation concerns the stability of a rock wedge in the roof of an excavation (see Fig. 4.12), for which a closed-form solution was proposed by Goodman et al. (1982). Discontinuity orientations and *in situ* stresses were adopted from the example in Hart et al. (1988). Three discontinuities dipping at 60° were introduced with dip directions of 30°, 150° and 270°. The normal and shear stiffnesses were both 10 MPa/m and the rock density was 2000 kg/m^3. The height of the wedge is 1 m. *In situ* stresses were applied by introducing boundary stresses, with the two horizontal principal stresses being -0.05 MPa and the vertical principal stress being zero. A high friction angle was first assigned to the discontinuities. Once the model reached equilibrium under the boundary stresses after some time-steps, the blocks surrounding the wedge were fixed. Then, as in the previous example, the friction angle of the discontinuities was gradually reduced until instability took place.

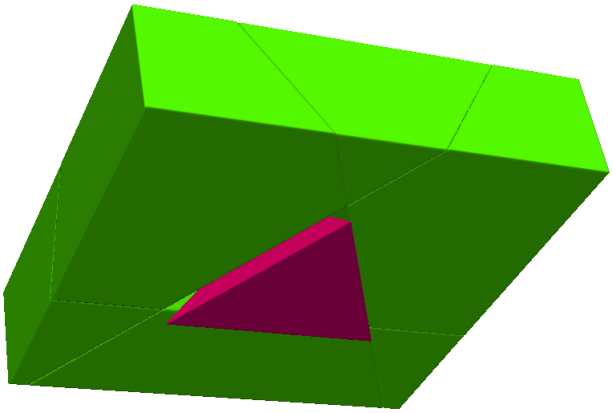

Fig. 4.12. Three-dimensional roof wedge example bounded by three rock joints (image reprinted from Boon et al. (2012) with permission from Elsevier)

The closed-form solution yields a friction angle of 34.41° while the critical friction angle found in the DEM simulation was 34.81°. The DEM results reported in Hart et al. (1988) and Itasca (2007) are 34.37° and 34.40° respectively. This small difference is due to the way *in situ* stresses were introduced. In Hart et al. (1988) and Itasca (2007), the blocks surrounding the wedge were fixed and the contact forces between the three wedge faces were set in accordance with the *in situ* stress state, i.e. resolved in the direction of the discontinuity. No joint deformations were introduced. In this model instead, deformations at the joints were introduced during the application of boundary stresses.

4.10 ROCK SLUMPING

In this example a three dimensional-representation of a rock slope in sedimentary rock is simulated to show that failure modes involving rotations of rock blocks can be captured correctly by the contact detection algorithm (see Fig. 4.13). This example was previously simulated by Hart et al. (1988) in 3-D and Starfield & Cundall (1988) in 2-D to show that jointed rock slopes can fail due to slumping even though discontinuities do not daylight the slope face. According to Starfield & Cundall (1988), this was a case study where failure was counter-intuitive; an engineer designed a cut slope such that its face was parallel to the bedding to avoid translational sliding failure along the discontinuities. However, it transpired that the slope failed because of slumping. In this simulation, as in previous examples, a high friction angle was first assigned at the discontinuities. It was then

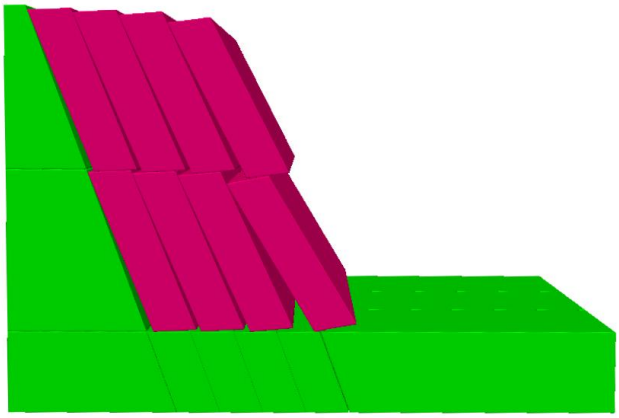

Fig. 4.13. Rock slope failing through rotations (image reprinted from Boon et al. (2012) with permission from Elsevier)

gradually reduced until failure. As shown in Fig. 4.13, rotational failure was successfully captured in the DEM simulation. The smooth transition between contact types such as face-face, face-edge and edge-edge was modeled successfully.

4.11 BUCKLING OF A THREE HINGED-BEAM

This example shows how solutions to rock engineering problems may vary when different choices of contact points are implemented. Whilst the DEM code YADE is a 3-D DEM code, the simulations here were run in 2-D by restricting the degrees of freedom of the rock blocks. The movement of the blocks were allowed only to translate in the *y*-*z* plane, and to rotate only about the *x*-axis. The problem of a three-hinged beam presented in Goodman (1989, Chapter 7, problem 22) is used as a comparison exercise. The roof of an underground opening is intersected by soft joints at the midspan and abutment. The problem therefore can be schematically idealised as two rigid blocks with deforming joints (Goodman, 1989). The blocks are flanked by abutment blocks at both sides. Due to the weight of the blocks, a three-hinged structure is formed (Fig. 4.14); hinges are formed at the lower vertices touching the abutment and at the upper vertices at the midspan. Note that the solution provided by Goodman (1989) is incomplete: although the displacements caused by the rotations of the blocks are correctly calculated, his solution does not consider the influence of structural stiffness on stability.

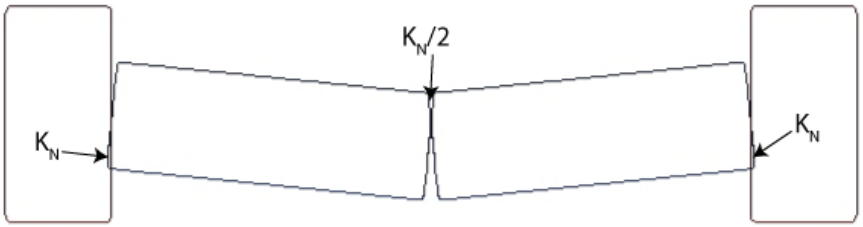

Fig. 4.14. Three-hinged beam example (irregularities along the particle edges are an artifact of the graphical rendering package and are not present in the underlying model). Image reprinted from Boon et al. (2012) with permission from Elsevier.

In the DEM simulations here, two choices of contact points were implemented for comparison, namely (i) the analytic centre and (ii) the centroid of the overlap area (in 2-D). The overlap distances in the DEM calculations were obtained from performing line searches along the direction of the contact normal evaluated at the contact point. The DEM simulations were also compared against a closed-form solution that was derived based on the assumption that horizontal thrusts were acting at the centroid of the overlap (see Appendix E). In this closed-form solution, several simplifying assumptions were made, all of which were also used in the DEM simulations to allow comparison. First, the influence of contact area is assumed to be negligible, by employing a constant joint stiffness (unit: N/m) independent of contact area. Second, the abutment is assumed to be non-compliant, and therefore the joint stiffness (K_N in Fig. 4.14) at the abutment (100 MN/m) was taken to be twice the net joint stiffness at the midspan (50 MN/m). The dimension of each block is 138 mm $\times$ 46 mm. The load-rotation response curve for each calculation method is plotted in Fig. 4.15 (a). Failure occurs when the stiffness of the system becomes zero, corresponding to the peak of the curves shown in Fig. 4.15 (a). This failure occurs for a smaller deflection than the geometrical solution suggested by Goodman (1989), i.e. 0.32 radians. In his solution, the three-hinged beam fails when the hinges are aligned horizontally, i.e., the lever arm of the resisting moment becomes zero. As shown in Fig. 4.15 (a), different load-rotation response curves were obtained for the two choices of the DEM contact points. This difference can be attributed to differences in the size of the lever arm and overlap distance which contribute to the restoring moment. The DEM calculation using the centroid of the overlap area as the contact point is almost identical to the closed-

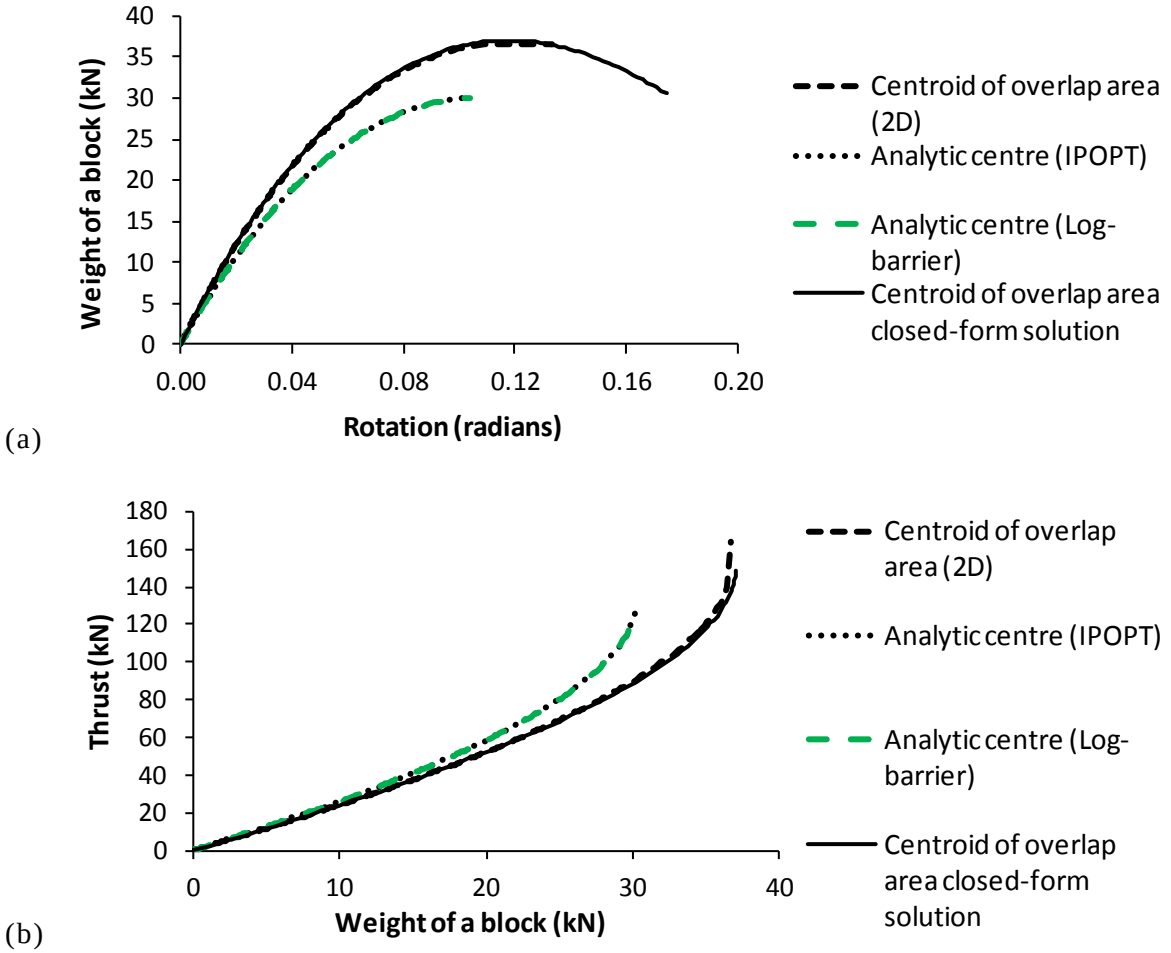

Fig. 4.15. The response of a three-hinged beam based on different choices of contact points used in DEM simulations (a) vertical load versus rotation (image reprinted from Boon et al. (2012) with permission from Elsevier) (b) horizontal thrust versus vertical load

form solution derived in Appendix E. The DEM result obtained by using the analytic centre as the contact point failed at a lower block weight than using the centroid of the overlap area as the contact point (see Fig. 4.15 (a)). Fig. 4.15 (b) shows the response of the three-hinged beam plotted in terms of the horizontal thrust versus the block weight. As the block weight increases, the overturning moment acting on the block increases. The horizontal thrust increases correspondingly with the block weight so that the restoring moment matches the overturning moment.

Fig. 4.15 (a) and (b) also compare the DEM solutions in which the analytic centre was calculated using the log-barrier method (Boyd, 2004) with the solutions obtained using the nonlinear program solved using IPOPT (Wächter & Biegler, 2006). The results of these

two optimisation techniques are almost identical. Subsequent DEM verification examples in this chapter were solely calculated using the log-barrier method (Boyd, 2004).

4.12 JOINTED BEAMS

In many underground excavations through layered rock structures, it was observed that the strata above the opening tend to separate upon deflection such that their weights are transferred to the abutments, instead of loading the layers underneath (Fayol, 1885). This observation led many investigators to analyse the stability of a multi-layered roof structure as a single layer voussoir beam. Recent studies from numerical and laboratory-scale analyses show that capturing the effects of discontinuities is important because it affects the rotations of blocks which can contribute towards the development of stable arching (Tsesarsky & Hatzor, 2006; Talesnick et al, 2007; Tsesarsky & Talesnick et al, 2007). A well instrumented laboratory-scale experiment on a single layer jointed beam has been published by Talesnick et al. (2007). This physical model test was carried out in a centrifuge, and the horizontal thrust and deflection of the beam were measured as gravity was increased. The tests were conducted on two block dimensions, 46 mm × 46 mm × 46 mm (see Fig. 4.16(a)) and 46 mm × 23 mm × 46 mm (see Fig. 4.16(b)). In Talesnick et al. (2007), they were referred to as the full-block model and half-block model respectively. The density of the blocks and the friction angle between the block interfaces were determined to be 1207 kg/m^3 and 40° respectively. Tsesarsky & Talesnick (2007) also carried out numerical simulations to compare with their experimental measurements, using the finite difference commercial software, FLAC (Itasca, 2000), and discontinuous deformation analysis (DDA) (Shi, 1988). In their FLAC models, each block (including the abutment blocks) was discretised with 25 × 25 finite difference zones and the discontinuities were introduced as numerical interfaces. Comparison with the results of DDA simulations was not carried out here because the contact stiffness in DDA has no physical significance, although it could be tinkered to influence the deformability of the models (Tsesarsky & Talesnick, 2007); the contact stiffness in DDA is used to enforce the no-penetration rule between blocks. In this section, the experimental and FLAC results are used as benchmark tests.

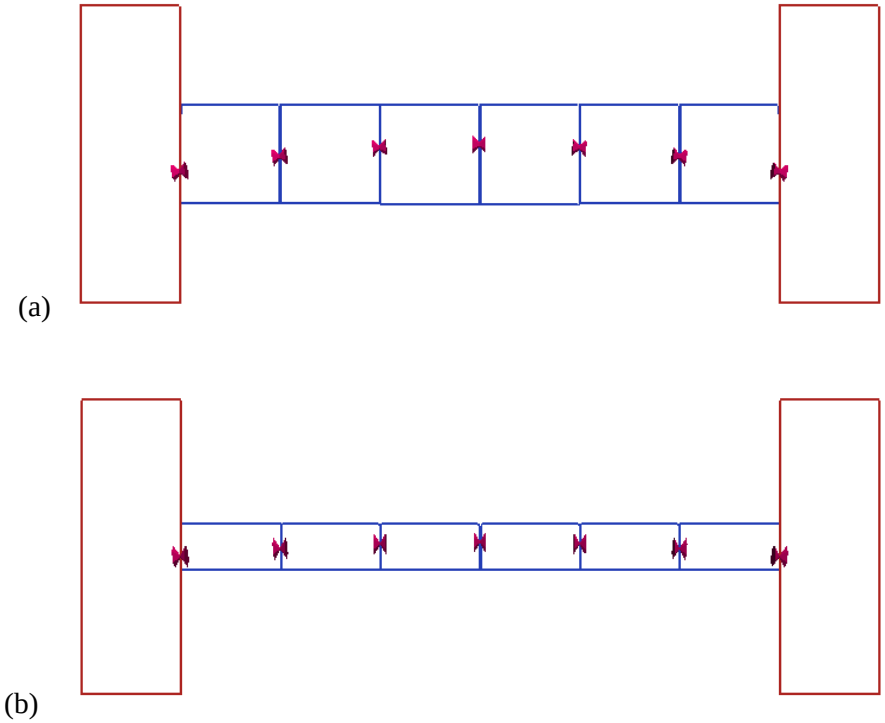

Fig. 4.16. Configurations of (a) the full-block model and (b) the half-block model at gravity accelerations of 40 g. The tip of a pair of adjoining cones marks the location of the contact point, while the cones are oriented along the direction of the total force at the contacts

4.12.1 Details of numerical setup

In this numerical study, the DEM with rigid particles and compliant joints was used. This is in contrast to the numerical setup used by the investigators, in which the blocks were deformable. An initial horizontal force of approximately 60 N was applied at 1 g. The gravity was gradually increased, and the horizontal thrust and displacements experienced by the beam were recorded. This was repeated up to the maximum gravity acceleration tested in the centrifuge (40 g for the full-block model and 90 g for the half-block model). Fig. 4.16 (a) and (b) show the configurations of the blocks in the full-block and half-block model respectively. The contact points (Fig. 4.16) between blocks form a distinct line of thrust across the beam.

The stress-displacement behaviour of a rock joint in both normal and shear directions can be determined experimentally from normal compression and direct shear tests

respectively. Therefore, it is common to implement the results obtained from these laboratory-scale tests into a DEM calculation to model the load-deformation response of a rock joint. The contact laws proposed by Tsesarsky & Talesnick (2007) (derived from experiments) were implemented here so that the results calculated using the algorithms in Chapter 3 can be compared directly with their numerical simulations. To model the experimental behaviour of stress-dependent stiffness, they proposed two contact models in the normal direction (see Fig. 4.17). In the first model, the stiffness was modelled as a linear function of stress, whereas in the second model the stiffness was modelled as a power function of stress. The former was later implemented by Tsesarsky & Talesnick (2007) into FLAC to compare with the experimental data. The following equations (Tsesarsky & Talesnick, 2007) were proposed for the linear stiffness model:

$$k_{\mathrm{n}} = \frac{\mathrm{d}\sigma_{\mathrm{n}}}{\mathrm{d}u_{\mathrm{n}}} = 4\times10^{9} + 7.4\times10^{4}\sigma_{\mathrm{n}} \quad \text{(units: Pa)} \tag{4.10}$$

$$k_{\mathrm{s}} = 1\times10^{8} + 9.7\times10^{4}\sigma_{\mathrm{n}} \tag{4.11}$$

Integrating Eq. (4.10), we obtain:

$$\sigma_{\mathrm{n}} = 0.5405\times10^{5}(\mathrm{e}^{7.4\times10^{4}u_{\mathrm{n}}} - 1) \tag{4.12}$$

The power model proposed by Tsesarsky & Talesnick (2007) in the normal direction is:

$$k_{\mathrm{n}} = \frac{\mathrm{d}\sigma_{\mathrm{n}}}{\mathrm{d}u_{\mathrm{n}}} = 2.1\times10^{6}\sigma_{\mathrm{n}}{}^{0.75} \tag{4.13}$$

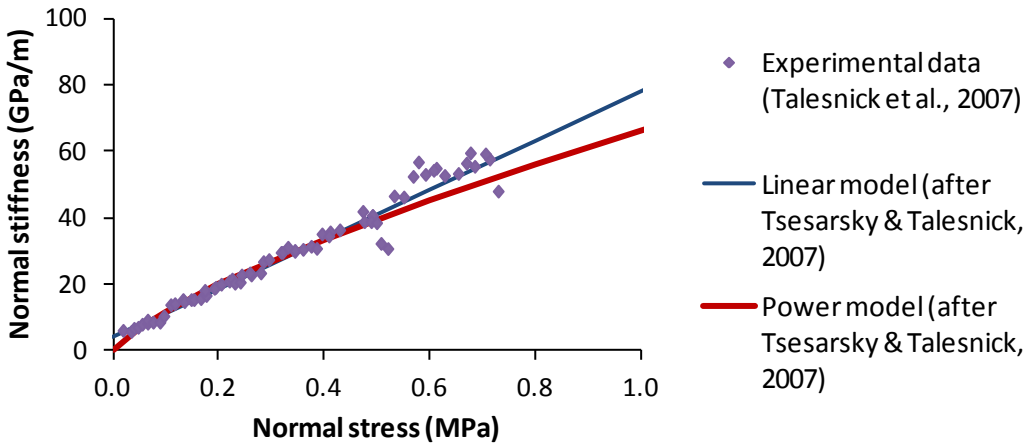

Fig. 4.17. Interface normal stiffness plotted against stress for the experimental data (Talesnick et al., 2007) and proposed relationships (linear model – Eq. (4.10) and power model – Eq. (4.13))

Because the linear model fits better the experimental data (see Fig. 4.17), the power model was not used by Tsesersky & Talesnick (2007) and also not used here. Comparisons with the investigators' numerical simulations and experimental measurements are detailed in Section 4.12.2 and Section 4.12.3 respectively.

4.12.2 Comparison against numerical simulations (Tsesarsky & Talesnick, 2007)

DEM simulations were run using the same joint properties used in the FLAC simulations (see Table 4.2). Two of the simulations used constant stiffness contact models. The linear stiffness model in Table 4.2 refers to the contact law (Eqs. (4.10) and (4.11)) proposed by Tsesarsky & Talesnick (2007). The horizontal thrusts obtained from our DEM simulations in comparison with the FLAC simulations by Tsesarsky & Talesnick (2007) are shown in Figs. 4.18 and 4.19 for the full-block and half-block models respectively. Figs. 4.20 - 4.22 show the deflection profiles for each of the three models in Table 4.2 in comparison with the aforementioned FLAC simulations.

Table 4.2. DEM simulations compared with FLAC simulations published by Tsesarsky & Talesnick (2007)

No.	Model	k_n (GPa/m)	k_s (GPa/m)
1	full-block	10	1
2	full-block	linear model - Eq. (4.12)	linear model - Eq. (4.11)
3	half-block	10	1

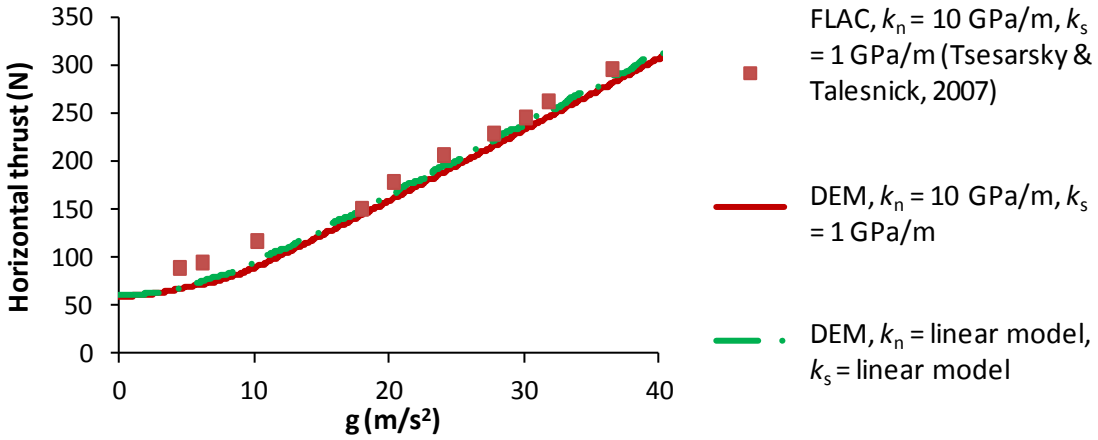

Fig. 4.18. Comparison of thrust build-up of the full-block model between DEM simulations and FLAC simulations (red squares) carried out by Tsesarsky & Talesnick (2007). Linear model = Eqs. (4.11) and (4.12).

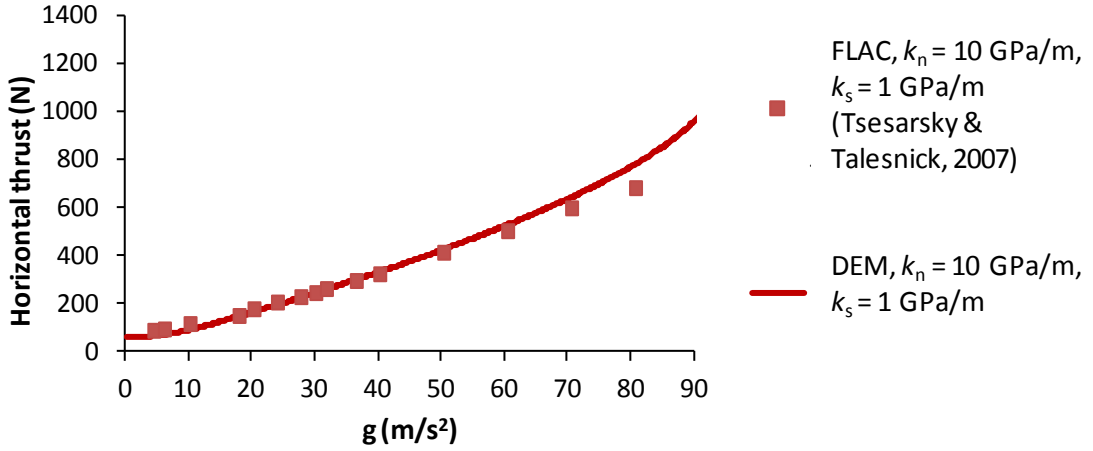

Fig. 4.19. Comparison of thrust build-up of the half-block model between DEM simulations and FLAC simulations (red squares) carried out by Tsesarsky & Talesnick (2007).

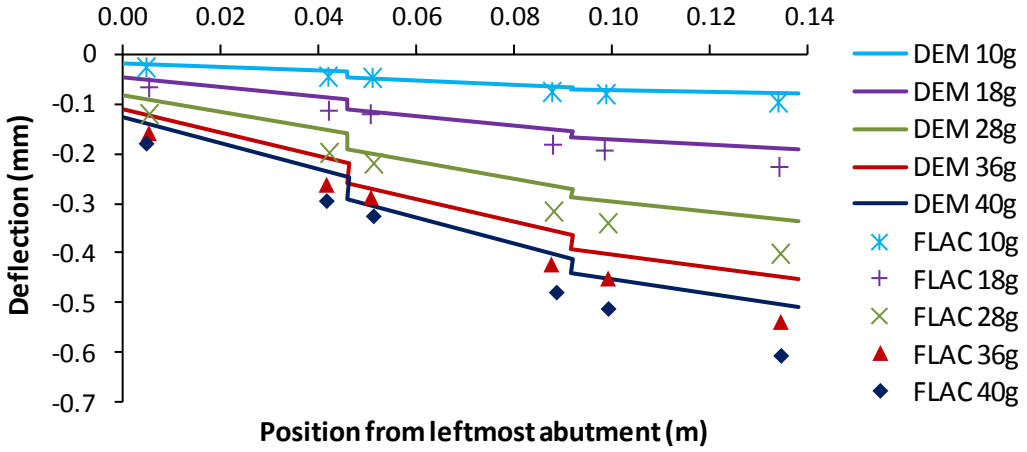

Fig. 4.20. DEM displacement profile for the full-block model, k_n = 10 GPa/m and k_s = 1 GPa/m in comparison with FLAC simulations by Tsesarsky & Talesnick (2007)

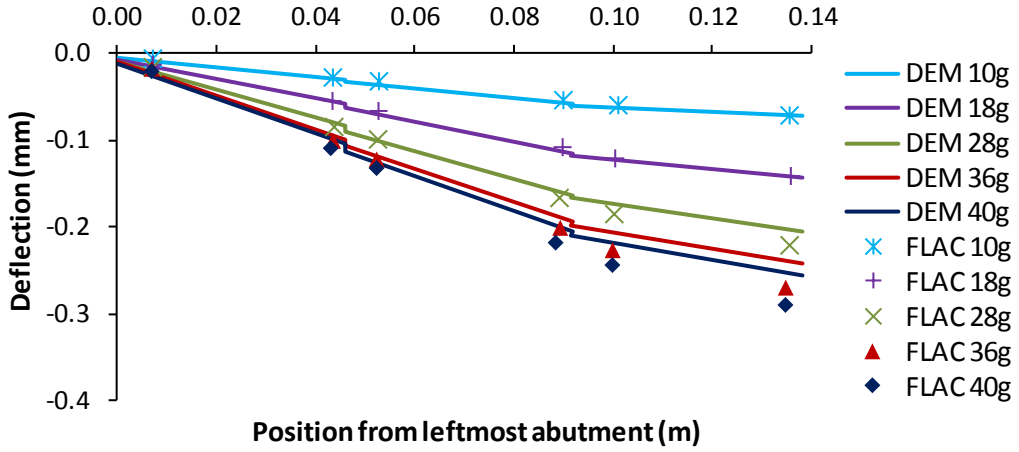

Fig. 4.21. DEM displacement profile for the full-block model, k_n = linear model (Eq. (4.12)) and k_s = linear model (Eq. (4.11)) in comparison with FLAC simulations by Tsesarsky & Talesnick (2007)

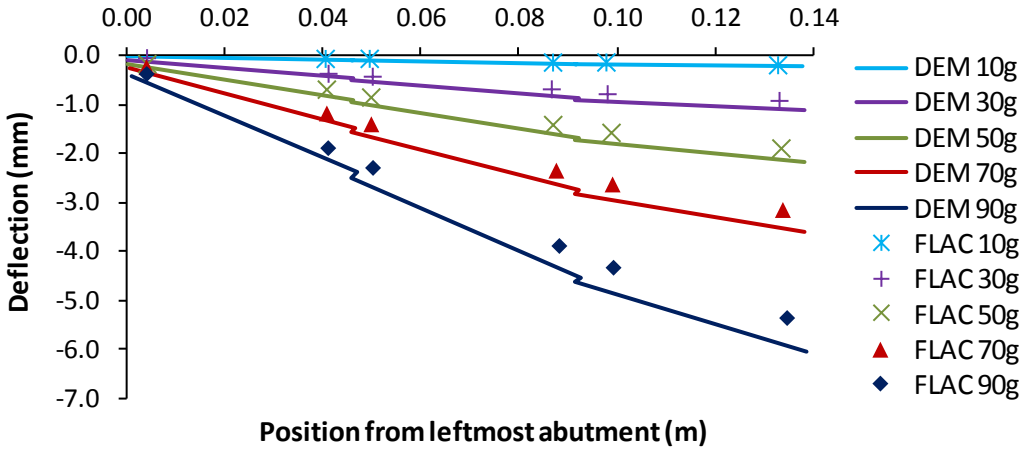

Fig. 4.22. DEM displacement profile for the half-block model, k_n = 10 GPa/m and k_s = 1 GPa/m in comparison with FLAC simulations by Tsesarsky & Talesnick (2007)

Both the horizontal thrusts (Figs. 4.18 and 4.19) and deflection profiles (Figs. 4.20 – 4.22) obtained by the DEM simulations compare well with the results obtained by FLAC. The horizontal thrusts of the jointed beams were found to increase with gravity loading (see Figs. 4.18 and 4.19). Increased deflections, a sign of instability, were observed at loading levels exceeding 70g for the half-block model (see Fig. 4.22). This was noted also by Tsesarsky & Talesnick (2007) in their FLAC simulations where increased deflections were observed at 70g and instability was observed at 90g.

4.12.3 Comparison against experimental measurements (Talesnick et al., 2007)

4.12.3.1 Comparison using contact models proposed by Tsesarsky & Talesnick (2007)

Here, the results of the previous DEM simulations using the linear stiffness contact models (Eqs. (4.10) and (4.11)) are compared against experimental measurements published by Talesnick et al. (2007). Recall that, previously in Section 4.12.2, the DEM models have been verified against the FLAC simulations published by Tsesarsky & Talesnick (2007). Therefore, the conclusions obtained here in comparison with experimental measurements are similar to those obtained by Tsesarsky & Talesnick (2007) using FLAC. The horizontal thrusts for the full-block and half-block models are shown in Figs. 4.23 and 4.24 respectively. The thrusts obtained from the DEM simulations using the stress-dependent contact models are ~40% lower than the experimental measurements (Figs. 4.23 and 4.24).

Figs. 4.25 and 4.26 compare the deflections of the jointed beams. The displacements at both midspans and abutments were under-predicted (Figs. 4.25 and 4.26).

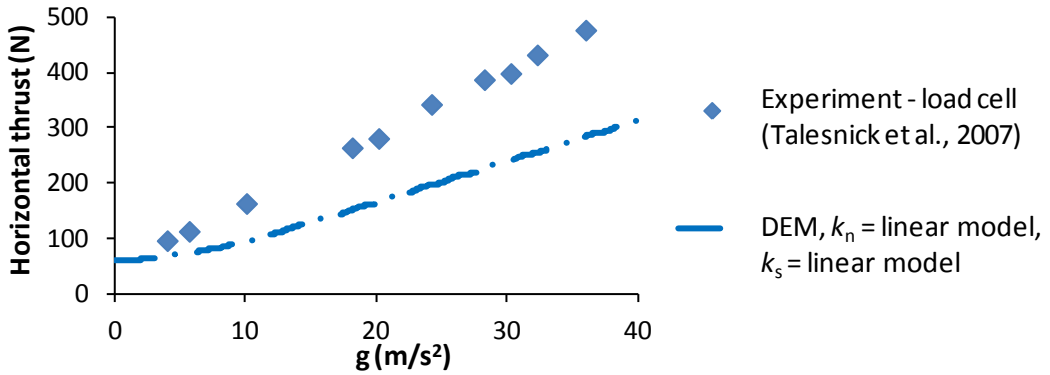

Fig. 4.23. Comparison of thrust build-up of the full-block model between DEM simulations and experiments (blue diamonds) carried out by Talesnick et al. (2007).

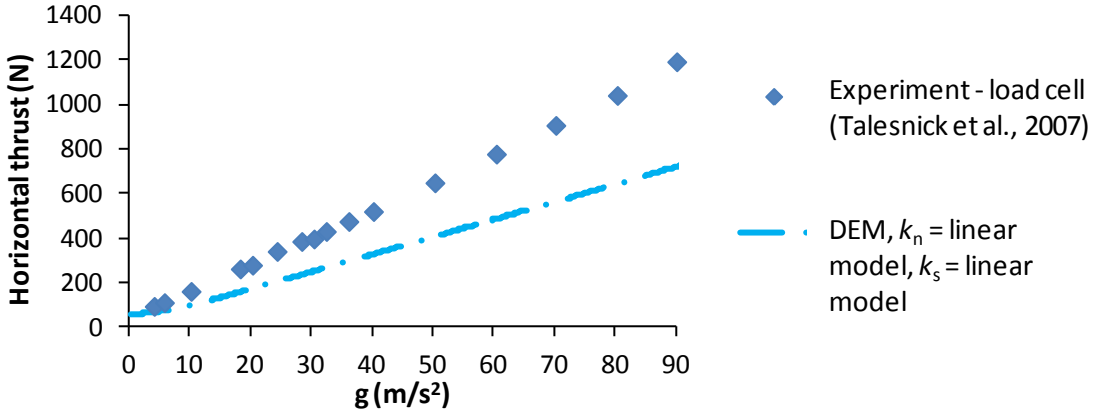

Fig. 4.24. Comparison of thrust build-up of the half-block model between DEM simulations and experiments (blue diamonds) carried out by Talesnick et al. (2007).

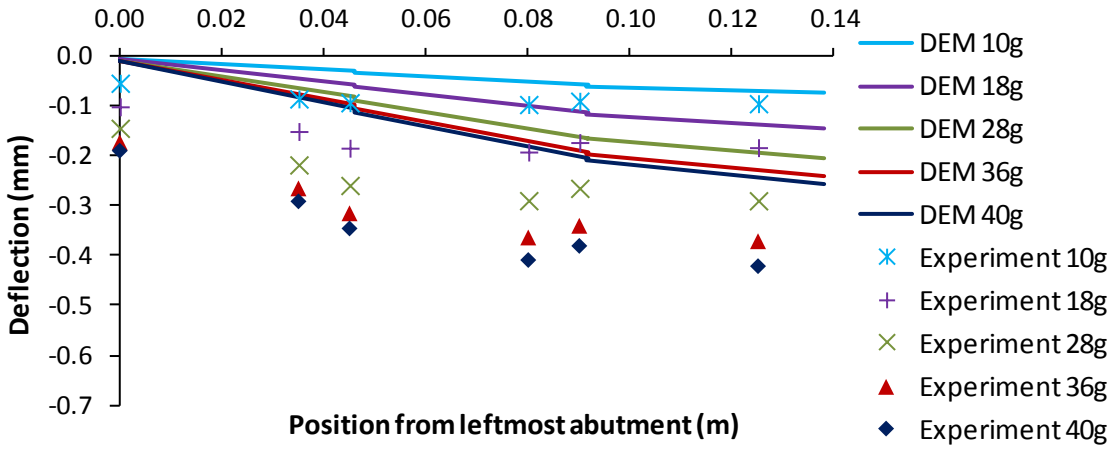

Fig. 4.25. DEM displacement profile for the full-block model, k_n = linear model (Eq. (4.12)) and k_s = linear model (Eq. (4.11)) in comparison with experiments (Talesnick et al., 2007). Experimental deflections were measured from LVDT (Test 180-E).

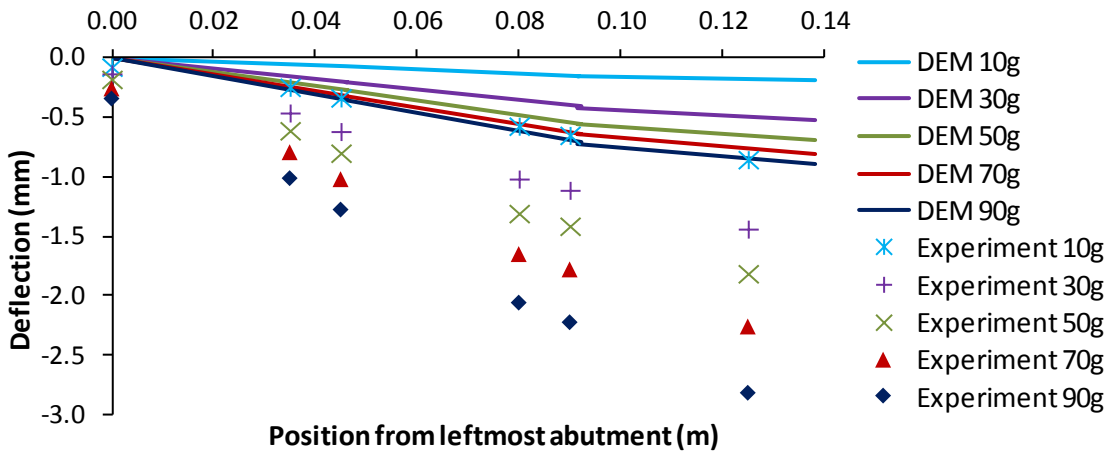

Fig. 4.26. DEM displacement profile for the half-block model, k_n = linear model (Eq. (4.12)) and k_s = linear model (Eq. (4.11)) in comparison with experiments carried out by Talesnick et al. (2007). Experimental deflections were measured from LVDT (Test 180-3).

There are two possible explanations for the discrepancies between the DEM analyses and experimental measurements. The first is that the numerical analyses (including FLAC) could be incapable of predicting physical reality. The second is that the contact models proposed by Tsesarsky & Talesnick (2007) (Eqs. (4.10) and (4.11)) are not sufficiently accurate.

4.12.3.2 More accurate contact models

To improve predictions, the experimental data published in Talesnick et al. (2007) and Talesnick (2007) were reinterpreted to derive more refined normal and shear contact models.

4.12.3.2.1 Proposed contact models

From the stress-displacement data (Fig. 4.27) of a uniaxial compression test on a three-block column published by Talesnick et al. (2007), the stress-displacement relationship for the joint contact law can be obtained. This approach is more direct than working out the stiffness values from the slope of the curve as was done Tsesarsky & Talesnick (2007) (Eq. (4.11)). It is believed that this approach of deriving the stress-displacement relationship directly was not undertaken by the investigators because assigning the stiffness of an interface is more convenient in FLAC.

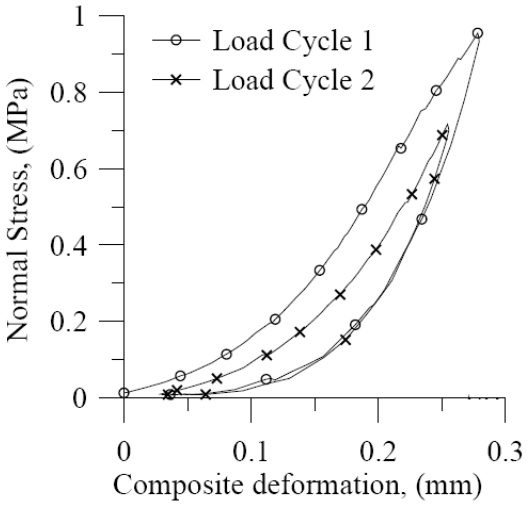

Fig. 4.27. Stress-deformation of load-unload cycles for uniaxial compression of a three-block column (reproduced from Fig. 14 in Talesnick et al. (2007) with kind permission from Springer Science and Business Media)

In the three-block column (see Fig. 4.28), there are six block interfaces in total, or three rock joints; a rock joint consists of a pair of mating block interfaces (or material boundaries). By assuming that the intact block material behaves in a linear elastic manner, the deformations of the intact material were calculated based on the Young's modulus reported in Talesnick et al. (2007), i.e. 5600 MPa. The deformations comprising of only the block interfaces were then deduced by taking off the deformations of the intact material from the total measured deformations. Fig. 4.29 shows the procedure that was used to deduce the stress-displacement relationship at a rock joint. Note that in FLAC and DEM calculations, the use of contact stiffness refers to a joint, i.e. a pair of mating interfaces. Because the three-block column consists of three rock joints (including the topmost and bottommost interfaces), the remaining deformations should be divided by three to obtain the deformations contributed by a rock joint (see Fig. 4.28). As shown in Fig. 4.29, the stiffness relationship proposed by Tsesarsky & Talesnick (2007) in Eq. (4.10) is less accurate; their model is close to the case for which the remaining deformations are divided by six. As a first estimate, the normal stiffness for the linear model in Eq. (4.10) is halved, so that:

$$\sigma_{\mathrm{n}} = 0.5405\times10^{5}(\mathrm{e}^{3.7\times10^{4}u_{\mathrm{n}}} - 1) \tag{4.14}$$

From Fig. 4.29, it is obvious that the stress-displacement response given by Eq. (4.14) matches the experimental measurements well.

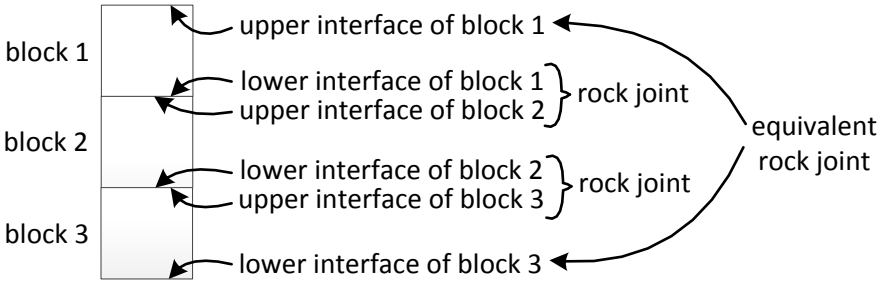

Fig. 4.28. Illustration of the number of interfaces and rock joints for a three-block column. There are 'six interface springs' or 'three rock joint springs' in this setup.

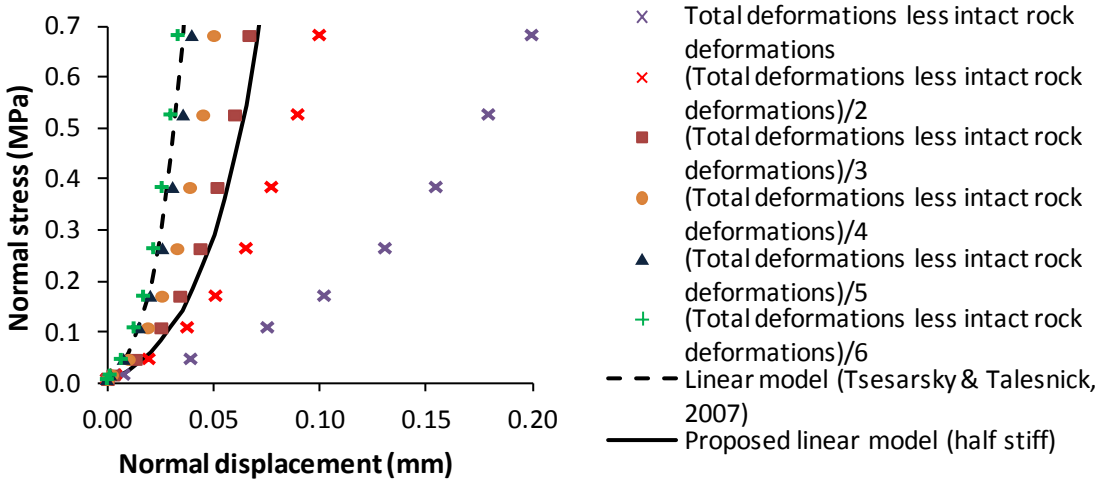

Fig. 4.29. Normal stress-displacement relationships of contact models plotted against experimental measurements. Experimental fit was derived from Load Cycle 2 in Fig. 4.27 after deducting the deformations of the intact rock material (three blocks).

Based on experimental shear evidence published in Talesnick (2007), the joint shear stiffness measured in the centrifuge decreases with shear displacement (see Fig. 4.30 (a)). Because the linear model (Eq. (4.11)) proposed by Tsesarsky & Talesnick (2007) models only the *initial* shear stiffness, it does not capture the shear stiffness degradation behaviour in the centrifuge. Eq. (4.11) would lead to an underestimation of shear displacements because the determination of shear stiffness does not take into account the shear history which can cause a substantial decrease in stiffness. It is possible to model the instantaneous shear stiffness as:

$$k_s = \left(1 - \frac{u_s}{u_{peak}}\right) k_{s\_initial}, \qquad u_s < u_{peak} \tag{4.15}$$

where $k_{s\_initial}$ is the initial shear stiffness, u_s is the shear displacement, and u_{peak} is the peak displacement, i.e. the displacement at which the shear stress reaches its peak and levels off.

Note that when $u_s \geq u_{peak}$, the stiffness is zero, and there is no resistance to shear (fully plastic) (see Fig. 4.30 (a) and (b)). The peak displacement u_{peak} can be modeled using:

$$u_{peak} = 2\times10^{-6}\sigma_n^{0.213} \tag{4.16}$$

while the initial shear stiffness $k_{s\_initial}$ can be modeled as:

$$k_{s\_initial} = 1.9\times10^{6}\sigma_n^{0.7} \tag{4.17}$$

Eq. (4.17) is plotted in Fig. 4.31 against the experimental values and model proposed by Tsesarsky & Talesnick (2007). For high normal stresses, the initial shear stiffness predicted

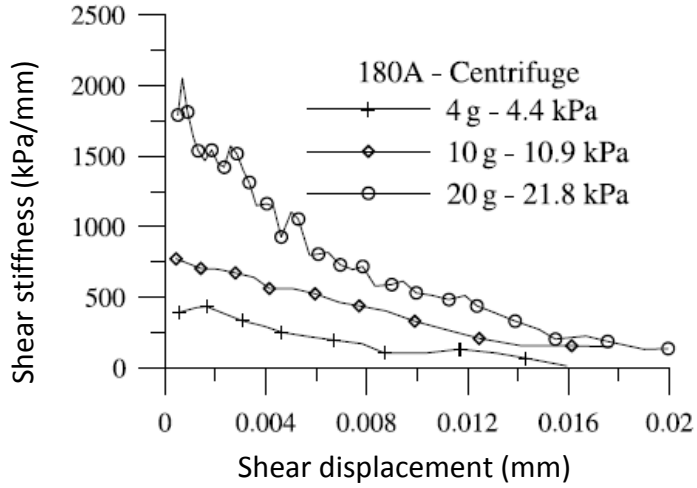

(a)

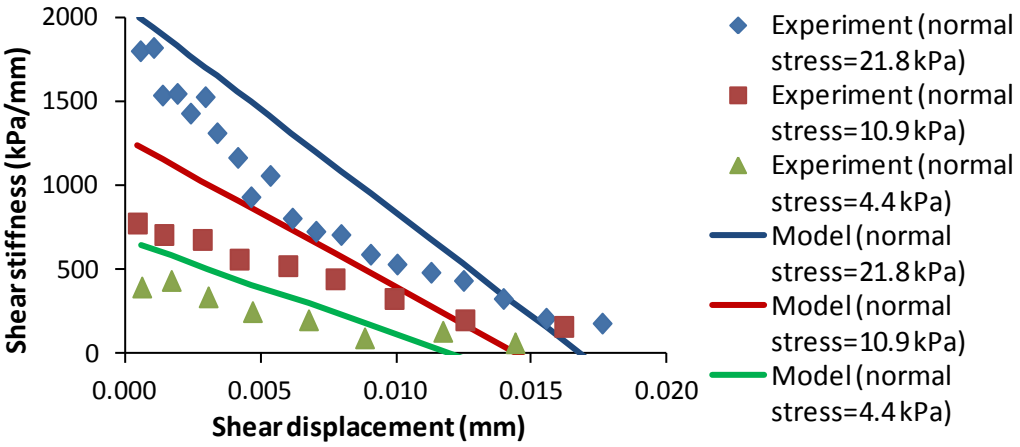

(b)

Fig. 4.30. Shear stiffness as a function of shear displacement at different normal stress. The experimental shear stiffness was taken from the 2nd loading cycle: (a) experimental data (after Fig. 5(c) in Talesnick (2007) with kind permission from Springer Science and Business Media), (b) proposed model (Eq. (4.15)) plotted against experimental data deduced from (a)

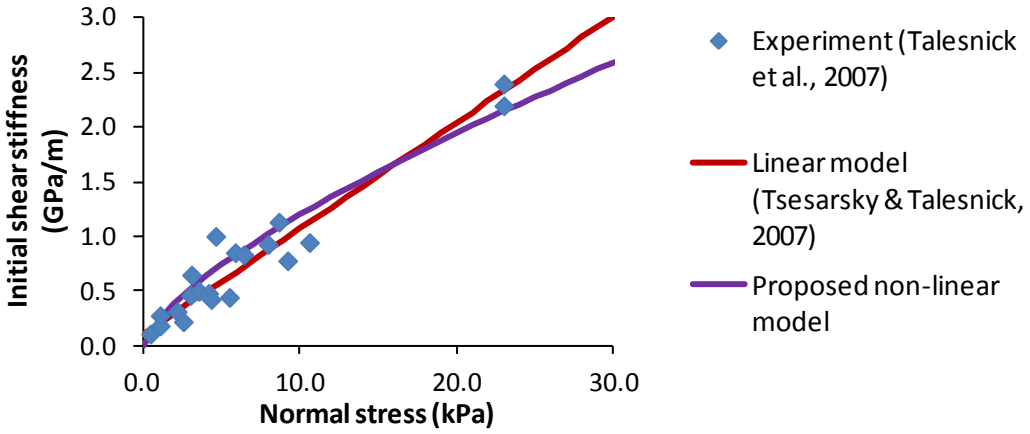

Fig. 4.31. Initial shear stiffness as a function of normal stress. The proposed model Eq. (4.17) is plotted against experimental values and model (Eq. (4.11)) proposed by Tsesarsky & Talesnick (2007)

using Eq. (4.17) is lower compared to the linear model (Eq. (4.11), p.85) proposed by Tsesarsky & Talesnick (2007). The model predictions for the instantaneous shear stiffness juxtaposed against experimental measurements are shown in Fig. 4.30 (b).

Because of the complex stress path, it is possible that this model (Eq. (4.15)) can give zero stiffness before yielding occurs; for example, if the normal stress increases as the joint shears, the joint may experience $u_s > u_{peak}$ although the shear stress is still less than $\mu\sigma_n$ where μ is the friction coefficient. This behaviour is not physically consistent. Instead of modeling stiffness degradation, it is numerically more robust to model this behavior as strain hardening or continuously yielding so that:

$$\mu = \mu_0(1-e^{-u_s/u_{peak}}) \tag{4.18}$$

where μ_0 is the maximum friction coefficient, i.e. 40°. In this shear model, the friction coefficient increases from nil with shear displacement and the elastic shear stiffness is simply $k_{s\_initial}$. The predicted shear stress as predicted by Eq. (4.18) is juxtaposed against laboratory measurements (Fig. 4.32 (a)), and the model was found to predict the laboratory measurements well (see Fig. 4.32 (b)). The stress-update algorithm in Appendix F was used to calculate the shear stresses during the DEM calculations. Note that Figs. 4.30 and 4.32 are two different interpretations derived from the same set of experimental data in Talesnick (2007).

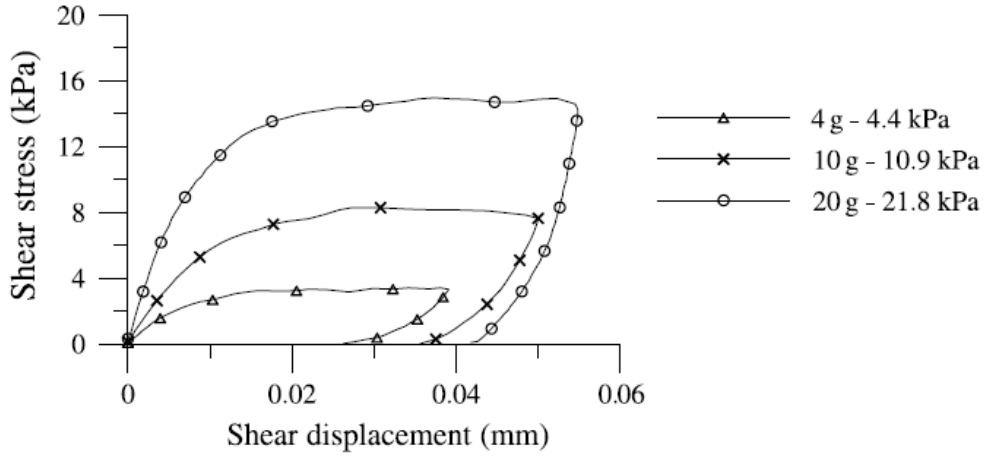

(a)

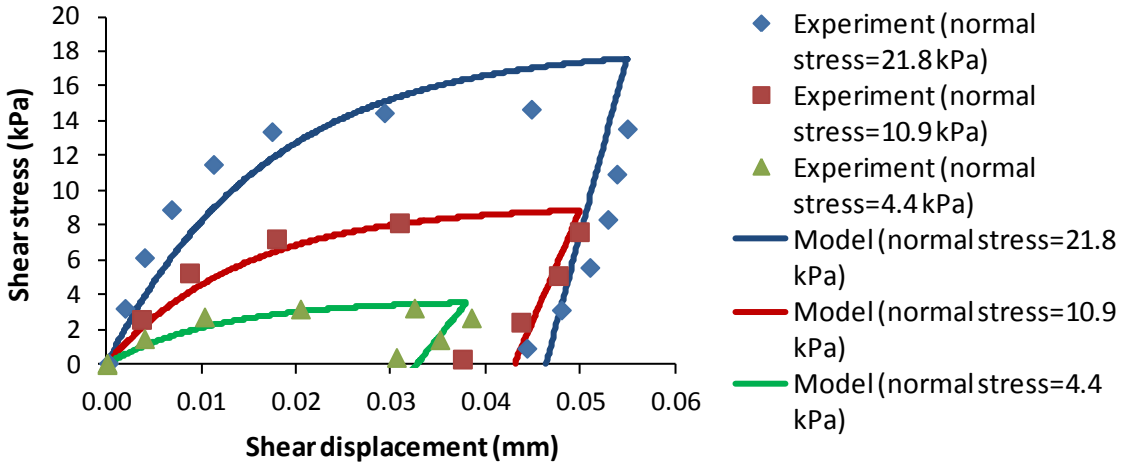

(b)

Fig. 4.32. Shear stress versus shear displacement at different normal stress: (a) experimental data (reproduced from Fig. 4b in Talesnick (2007) with kind permission from Springer Science and Business Media) (b) proposed model (Eq. (4.18)) and experimental data deduced from (a).

It is reassuring that the reinterpretation of experimental data shows that the actual contacts in both the normal and shear directions are more compliant than the original contact models (Eqs. (4.10) and (4.11)). Since the displacements of the jointed beams were underpredicted previously, the increase in compliance should improve the predictions.

4.12.3.2.2 Results of proposed contact models

The results of the DEM calculations using the proposed contact models in comparison with the experimental measurements are presented here. The parameters and models that were used in each figure are summarised in Table 4.3. First, only the proposed contact model in the normal direction was updated (Eq. (4.14), p. 91), while keeping the shear stiffness model (Eq. (4.11), p.85) proposed by Tsesarsky & Talesnick (2007). In another comparison, the

proposed contact models were used in both normal and shear directions (Eqs. (4.14) and (4.18), pp. 91 and 94).

There is little improvement in terms of horizontal thrust prediction, despite using the more rigorous contact models (see Figs. 4.33 and 4.34). The predicted horizontal thrusts from the DEM simulations are lower compared to the values measured from the load cell. It is interesting to note that the results of the numerical simulations are closer to the force estimations made by Tsesarsky & Talesnick et al. (2007) based on the strain gauge readings reported in Talesnick et al. (2007) (see Fig. 4.33). The reason for the discrepancy between the load cell readings and the stress values derived from the strain gauges was not known

Table 4.3. Summary of models in DEM calculations to compare with experimental data published by Talesnick et al. (2007)

Figure No.	**Experiment reference, data downloadable from website (Talesnick, 2006)**	k_n	k_s
4.35	full-block, 180-E	linear model (half stiff) Eq. (4.14)	linear model proposed by Tsesarsky & Talesnick (2007) Eq. (4.11)
4.36	half-block, 180-3	linear model (half stiff) Eq. (4.14)	linear model proposed by Tsesarsky & Talesnick (2007) Eq. (4.11)
4.37 (a), (b), (c)	full-block, 180-C1, 180-D, 180-E (same experiment setup)	linear model (half stiff) Eq. (4.14)	continously yielding model - Eqs. (4.17) & (4.18)
4.38	half-block, 180-3	linear model (half stiff) Eq. (4.14)	continuously yielding model - Eqs. (4.17) & (4.18)

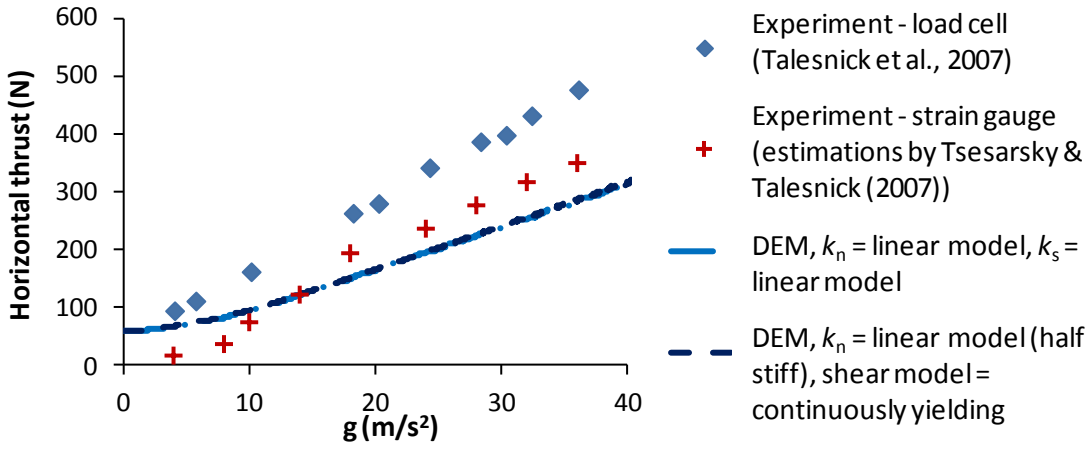

Fig. 4.33. Comparison of thrust build-up of the full-block model between DEM simulations and experiments (blue diamonds) carried out by Talesnick et al. (2007).

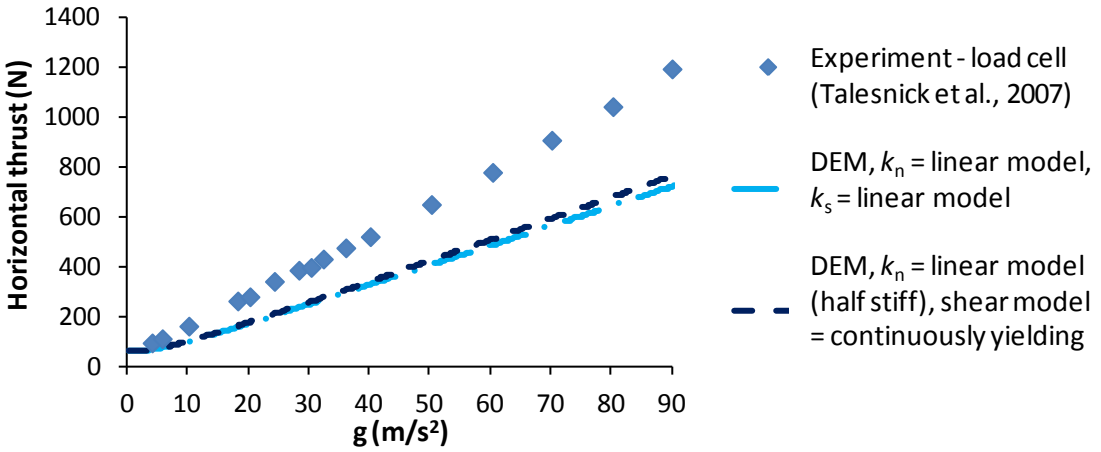

Fig. 4.34. Comparison of thrust build-up of the half-block model between DEM simulations and experiments (blue diamonds) carried out by Talesnick et al. (2007).

(Talesnick et al., 2007). But it is noteworthy that the initial stress values derived from the strain gauges were lower than the initial horizontal force of 60 N.

Using the more accurate contact model in the normal direction (Eq. (4.14)), the predicted deflections of the DEM simulations agree better with the experimental measurements (see Figs. 4.35 and 4.36) by comparison to the results obtained using the model proposed by Tsesarsky & Talesnick (2007) (Eq. (4.10)). Using also the more refined shear contact model in Eq. (4.18) (p. 94), the calculated shear displacements at the abutment (Figs. 4.37 and 4.38) are slightly larger compared to those in Figs. 4.35 and 4.36 simulated using the simpler model in Eq. (4.11) (p. 85). The difference, however, is marginal. Note that the centrifuge data were downloaded online from Talesnick (2006). Notice that three sets of centrifuge data are presented for the full-block model (Fig. 4.37 (a), (b) and (c)), while only one for the half-block model (Fig. 4.38). This is because only one set of experimental data for the half-block model is reported in Talesnick (2006). The three sets of centrifuge tests for the full-block model (Fig. 4.37 (a), (b) and (c)) were of the same experimental setup repeated using the same set of blocks (Talesnick et al., 2007).

Note that for both the full-block and half-block models, the displacements at the abutment were under-predicted by the DEM simulations (Figs. 4.37 and 4.38). Poor predictions of shear displacements by the advanced shear model (Eqs. (4.17) and (4.18)) are largely due to the lack of experimental shear data for model calibration at higher normal

stresses under which the experiments were conducted; the shear tests for stiffness calibration was carried out up to a normal stress of 0.023 MPa (see Fig. 4.31, p.94), in contrast to centrifuge tests for which the approximated normal stresses were up to 0.5 MPa for the full-block model and 1.0 MPa for the half-block model.

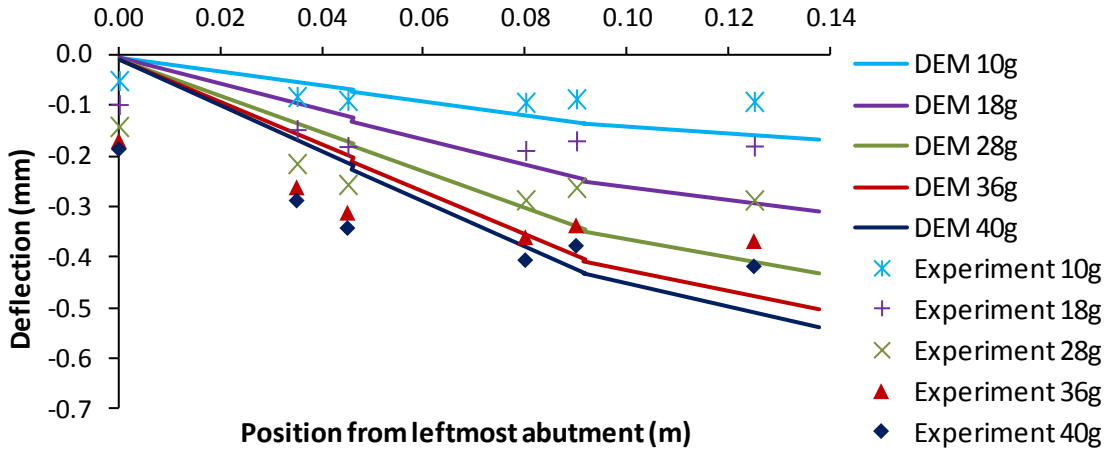

Fig. 4.35. DEM displacement profile for the full-block model, k_n = linear model with half stiffness Eq. (4.14) and k_s = linear model Eq. (4.11) in comparison with experiments carried out by Talesnick et al. (2007). Experimental deflections were measured from LVDT (Test 180-E).

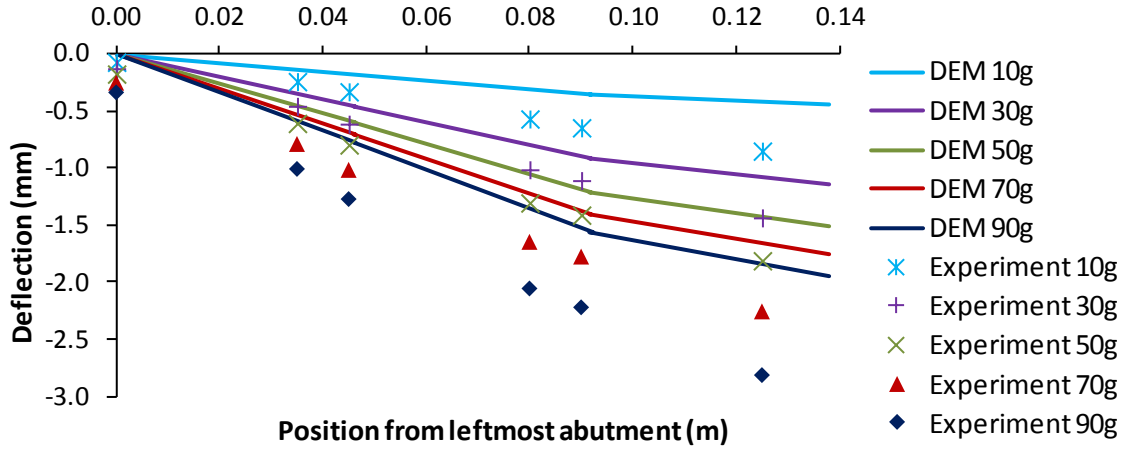

Fig. 4.36. DEM displacement profile for the half-block model, k_n = linear model with half stiffness Eq. (4.14) and k_s = linear model Eq. (4.11) in comparison with experiments carried out by Talesnick et al. (2007). Experimental deflections were measured from LVDT (Test 180-3).

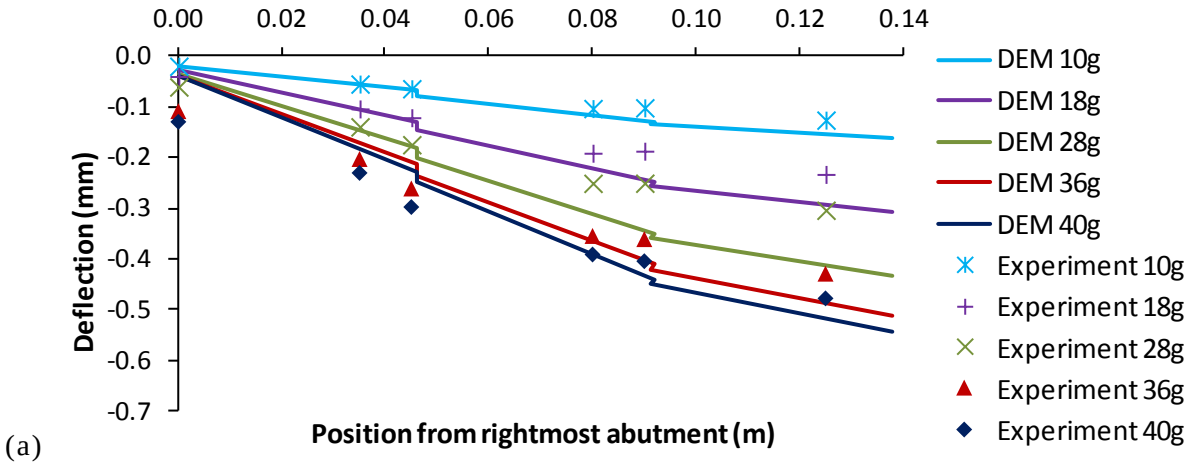

(a)

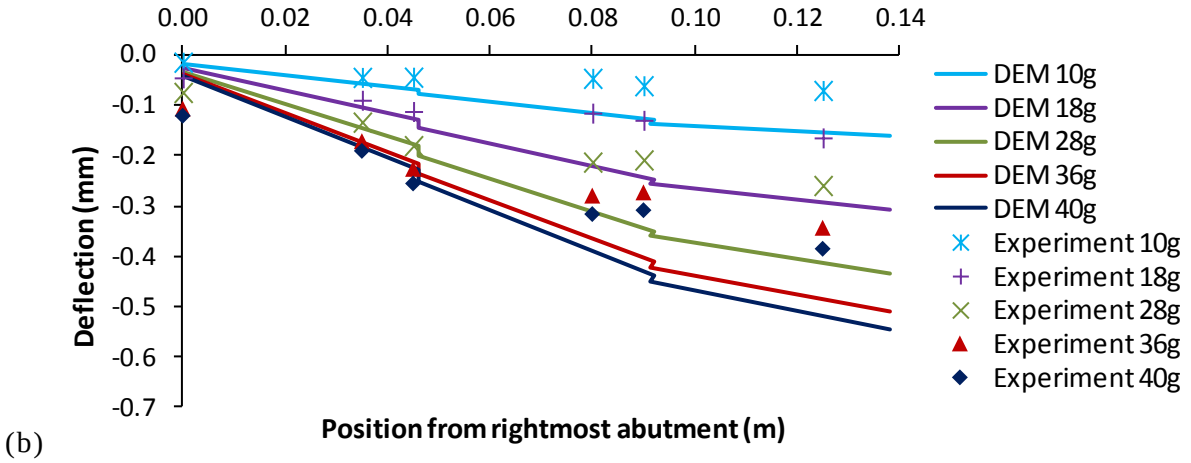

(b)

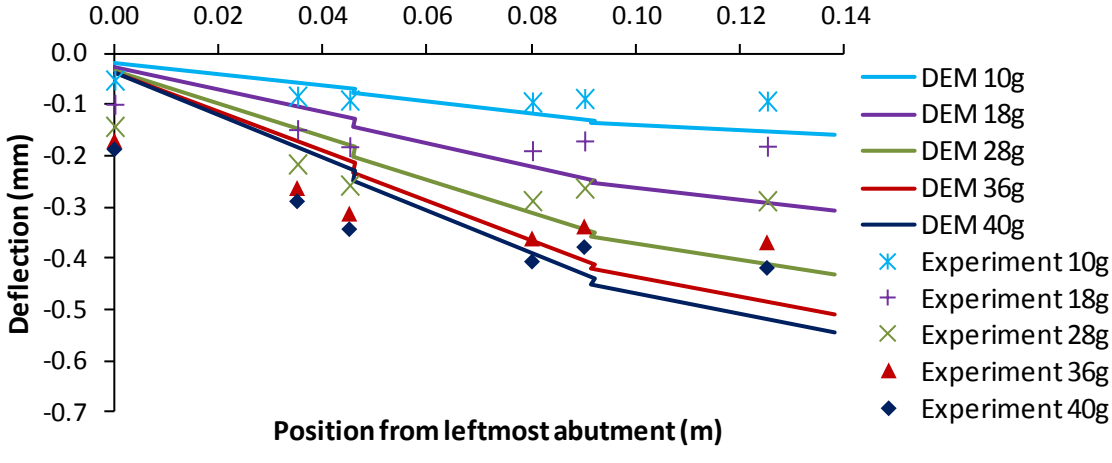

(c)

Fig. 4.37. DEM displacement profile for the full-block model, k_n = linear model with half stiffness Eq. (4.14) and k_s = continuously yielding model Eq. (4.18) in comparison with experiments carried out by Talesnick et al. (2007). Experimental deflections were measured from LVDT: (a) 180-C1, (b) 180-D, (c) 180-E

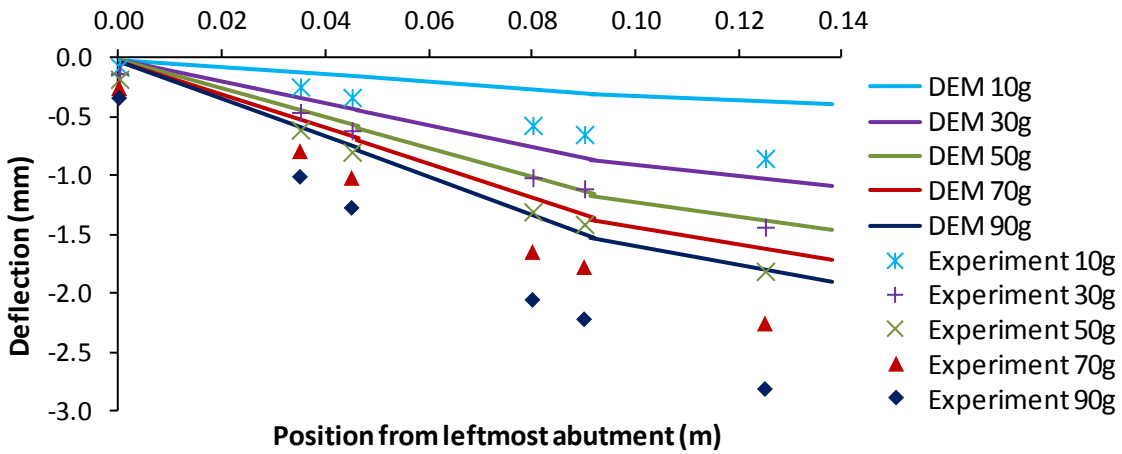

Fig. 4.38. DEM displacement profile for the half-block model, k_n = linear model with half stiffness Eq. (4.14) and k_s = continuously yielding model Eq. (4.18) in comparison with experiments carried out by Talesnick et al. (2007). Experimental deflections were measured from LVDT (Test 180-3).

Overall, the predictions obtained by the DEM calculations using the proposed contact models (Eqs. (4.14) and (4.18)) improved significantly. This is particularly obvious for the full-block model (compare Fig. 4.25, p. 89, with Fig. 4.37, p. 99). Note that the discrepancies observed previously between the DEM and FLAC analyses (Figs. 4.20 – 4.22, pp. 87 - 88) using the same contact constitutive models are much smaller by comparison to the discrepancies due to using less accurate contact constitutive models; the DEM predictions improved significantly when more accurate contact constitutive models were used. Therefore, in the attempt at predicting physical reality, it is reasonable to believe that the errors due to simplifying contacts in a geometrical sense, using the proposed contact detection algorithm (Chapter 3), is secondary by comparison to the errors due to using inaccurate contact constitutive models.

4.13 CONCLUDING REMARKS

This chapter has been about the verification of the algorithms proposed in Chapter 3. The proposed rock slicing algorithm was shown to be able to model non-persistent joints, concave blocks, excavation profiles and realistic joint patterns. In an example, the generated block assembly using the proposed algorithm was found to introduce more blocks than the commercial DEM code, UDEC (Itasca, 2004). Dangling joints had been approximately extended by the proposed algorithm, but they had been 'healed' in UDEC. The block

generation algorithm was also found to scale linearly with the number of generated blocks, when used together with bounding spheres. Through several collision tests, the DEM simulations indicate that the contact detection algorithm is robust in terms of detecting different contact types, e.g., vertex-edge, vertex-face, vertex-vertex, edge-edge, edge-face, etc. A range of typical rock structures was simulated in 3-D to examine the performance of the numerical tools in stability and stiffness-related problems and also in capturing the correct failure mechanism, *viz*., wedge sliding, roof falling, slumping of a rock slope and buckling of a three-hinged beam. The results of the DEM simulations compare well with analytical solutions and with the results reported by the commercial DEM code, 3DEC (Itasca, 2007). This suggests that the algorithms in Chapter 3 are robust and capable of modelling typical rock engineering problems. It is also worth highlighting that, for a jointed beam problem, the results of these numerical tools compared well with the results calculated using the commercial finite difference code FLAC (Tsesarsky & Talesnick, 2007); the former consists of 6 rigid particles with compliant contacts, while the later consists of 3750 elements (25 × 25 finite difference zones for each particle). Furthermore, by implementing more accurate rock joint contact models, the models were able to give closer predictions to the experimental data published by Talesnick et al. (2007) compared to the original numerical calculations presented in Talesnick & Tsesarsky (2007). That is to say, interaction rules between particles implemented on a local basis were successfully manifested in the system. This observation is important because it shows that the proposed numerical tools are capable of predicting, to some degree of success, problems consisting of multiple blocks by implementing contact models derived from small-scale laboratory tests. The remaining puzzle as to whether or not these numerical tools are equally robust when modelling large assemblies of blocks is examined in the next chapter.

CHAPTER 5
NUMERICAL MODELLING OF UNDERGROUND OPENINGS

This chapter shows how the numerical procedures proposed in Chapter 3 can be useful tools for engineers to design rock support for underground openings in moderately jointed rock masses. First, common failure patterns arising from a broad range of joint patterns are presented and discussed. The modelling of support for a hypothetical case is then illustrated in subsequent sections, showing how rock engineers can make use of these numerical tools to examine the influence of various design parameters. Because of the wide range of failure patterns which could be encountered in practice, it is unlikely that the conclusions obtained from the simulations are universal. Nevertheless, the design procedures adopted in this hypothetical case can be a useful guideline according to which the numerical tools can be used to help make support design decisions. This chapter also shows interesting comparisons between the predicted support loads obtained by the DEM calculations and closed-form solutions proposed in the literature.

5.1 INTRODUCTION TO UNDERGROUND OPENINGS IN JOINTED ROCK MASSES

In a rock tunnelling project, the engineer is normally tasked to design support systems economically while procuring a safety margin. The design must prevent any rock blocks from loosening and falling. The main support measures for jointed rock masses are rock bolts and lining (Hoek et al., 1995). Depending on local practice, the details of the installation may vary, such as the use of pretension in rock bolts and the types of lining support.

The stability of underground excavations in rocks is governed by numerous factors; for instance, the rock mass and rock joint properties, in-situ stresses and geometry of the excavation. The choice and extent of support depends largely on the failure mechanism. In most cases, it is helpful to anticipate the failure pattern of the unsupported opening so that effective support measures can be undertaken. For jointed rock masses intersected by

discontinuities, the design philosophy is different between sparsely and moderately jointed rock masses. For underground excavations in sparsely jointed rock masses with large joint spacing, stability is governed by key blocks whose shapes permit free kinematic movement into the opening. Failure involves either sliding or falling of key blocks. The study of key blocks by rock engineers has led to established analytical design procedures using stereographic projection techniques and block theory (Goodman, 1995). The engineer can identify key blocks from rock joint surveys, and secure them using pre-tensioned rock bolts.

However, designs based on key blocks are not suitable for underground excavations in moderately to heavily jointed rock masses. Sliding of large wedge structures is not normally encountered, as maintained by Bawden (1993). In contrast, failure usually involves ravelling or loosening of rock mass material into the excavation opening; the failed material usually consists of numerous rock blocks. The complexity of the problem has led rock engineers to develop, for the purpose of routine design, rock mass classifications based on past field data, such as the RMR system (Bieniawski, 1983) and the Q-system (Barton et al., 1974). Depending on the cost and the importance of the project, the distinct element method is sometimes used to verify the support measures recommended by the rock mass classifications. In fact, the use of DEM for design verification is becoming more widespread (Ghee et al., 2011). In this chapter, the distinct element method takes on a more active role and is used to design rock support from the beginning of the design phase.

5.2 UNSUPPORTED OPENINGS

Several unsupported openings were modelled to explore the various failure mechanisms that could occur for an underground opening in a jointed rock mass. Jointed rock masses consisting of three joint sets (in *y*-*z*) were modelled in this exercise. The opening diameter and cover depth in the simulations were 10 m and 50 m respectively, and in-situ stresses were hydrostatic. The simulations here were run in 2-D by restricting the degrees of freedom of the rock blocks, as was done in some simulations in the previous chapter; the blocks were allowed to translate only in the *y*-*z* plane, and to rotate only about the *x*-axis. Table 5.1 lists the summary of the failure patterns for different joint orientations and joint

friction angles. In previous academic studies of failure patterns of jointed rock masses, most investigators, e.g. Yeung & Leong (1997), Solak & Schubert (2004) and Solak (2009), modelled only two joint sets. With more than two joint sets, the degree of freedom with which the rock blocks can move into the excavated opening is significantly larger, and more than one failure pattern may occur.

Table 5.1: Failure patterns for different joint orientations and friction angles

No.	Joint orientations			Friction angle	Failure Mechanism 1	Failure Mechanism 2
	A	B	C			
1	60˚E	40˚E	80˚W	35˚	Roof fall – wedge subtended by joint sets with largest acute relative angle	N/A
2	10˚E	30˚W	50˚W	35˚	Roof fall – wedge subtended by joint sets with largest acute relative angle	Toppling at opposite side wall – along most shallow joint set
3	80˚E	5˚E	65˚W	35˚	Roof fall – wedge subtended by joint sets with largest acute relative angle	Sliding at opposite sidewall – wedge subtended by other joint sets
4	20˚W	60˚W	80˚W	35˚	Roof fall – wedge subtended by joint sets with largest acute relative angle	Roof fall – random blocks sliding along the steepest joint set
5	40˚E	20˚E	50˚W	35˚	Roof fall – blocks sliding along steepest joint set	Sliding at sidewall – blocks sliding along most shallow joint set
6	55˚E	25˚E	45˚W	35˚	Roof fall – blocks sliding along second steepest joint set	N/A
7	60˚E	80˚E	40˚W	35˚	Roof fall – minor block falling without distinct pattern	Sliding at sidewall – blocks sliding along most shallow joint set
8	75˚E	55˚E	65˚W	35˚	Roof fall – wedge subtended by joint sets with largest acute relative angle	Sliding propagates along two opposite directions after wedge falls
9	60˚E	85˚E	80˚W	25˚	Roof fall – minor block fall without distinct pattern	N/A
10	5˚E	55˚E	15˚W	30˚	Roof fall – blocks sliding along steepest joint set	Toppling at sidewall along second steepest joint set
11	85˚E	75˚E	65˚W	25˚	Roof fall – wedge subtended by joint sets with largest acute relative angle	N/A
12	85˚E	75˚E	65˚W	35˚	Roof fall – minor block fall without distinct pattern	N/A
13	85˚E	75˚E	55˚W	30˚	Roof fall – wedge subtended by joint sets with largest acute relative angle	Sliding propagates along two opposite directions after wedge falls
14	85˚E	75˚E	55˚W	35˚	Roof fall – minor block fall without distinct pattern	Sliding at sidewall – blocks sliding along most shallow joint set
15	85˚E	75˚E	45˚W	30˚	Roof fall – minor block fall without distinct pattern	Sliding at sidewall – blocks sliding along most shallow joint set
16	85˚E	75˚E	45˚W	35˚	Roof fall – minor block fall without distinct pattern	Sliding at sidewall – blocks sliding along most shallow joint set
17	85˚E	75˚E	35˚W	35˚	Roof fall – minor block fall without distinct pattern	Sliding at sidewall – blocks sliding along most shallow joint set
18	75˚E	25˚W	75˚W	35˚	Roof fall – block fall without distinct pattern	Sliding at sidewall – minor block fall along most shallow joint set
19	75˚E	25˚W	55˚W	35˚	Roof fall – wedge subtended by joint sets with largest acute relative angle	Sliding propagates along two opposite directions after wedge falls
20	75˚E	25˚W	45˚W	35˚	Roof fall – blocks sliding along steepest joint set	Sliding at sidewall – minor block fall along most shallow joint set
21	75˚E	25˚E	25˚W	35˚	Roof fall – blocks sliding along steepest joint set	Sliding at sidewall – minor block fall along most shallow joint set
22	75˚E	45˚E	25˚W	35˚	Roof fall – blocks sliding along steepest joint set	Sliding at sidewall – blocks sliding along second steepest joint set
23	75˚E	85˚E	25˚W	35˚	Roof fall – minor block fall without distinct pattern	Sliding at sidewall – blocks sliding along most shallow joint set
24	85˚E	70˚E	45˚E	25˚	Roof fall – wedge subtended by joint sets with largest acute relative angle	N/A

Fig. 5.1 (a) shows the loosening of rock material at the roof. This is the more typical case of opening failure based on the experience from mining operations; in the Stability Graph Method (Potvin, 1988), an empirical method used for cable-bolt design, susceptibility to roof falls has been specially rated based on gravity-induced effects and joint inclinations. However, for certain joint patterns, stability of the sidewall could be more critical than the roof. Fig. 5.1 (b) shows the loosening of material at the sidewall. From all the cases simulated, none of the rock masses failed uniformly around the opening and a certain degree of anisotropy is present. It is, therefore, important that the engineer does not make presumptions with regard to the exact localised failure pattern. Failure does not always occur along the steepest joint set (compare Fig. 5.2 (a) and (b)), nor does failure occur along just any particular two joint sets; it is possible for all the joint sets to participate in failure (see the outline of the falling material in Fig. 5.3).

It is difficult to qualitatively characterise the failure patterns using specific descriptions. Take for instance the roof failure in Fig. 5.2 (a). It is arguable that the failed material is bounded by joint sets which subtend the largest acute relative angle; it is reasonable also to claim that the failed material is sliding along the steepest joint set. Hence, for practical purposes, the qualitative description of failure patterns (e.g. in Table 5.1) should not be taken too rigidly. A pedantic approach towards the qualitative study of failure patterns is unhelpful and can cause confusion.

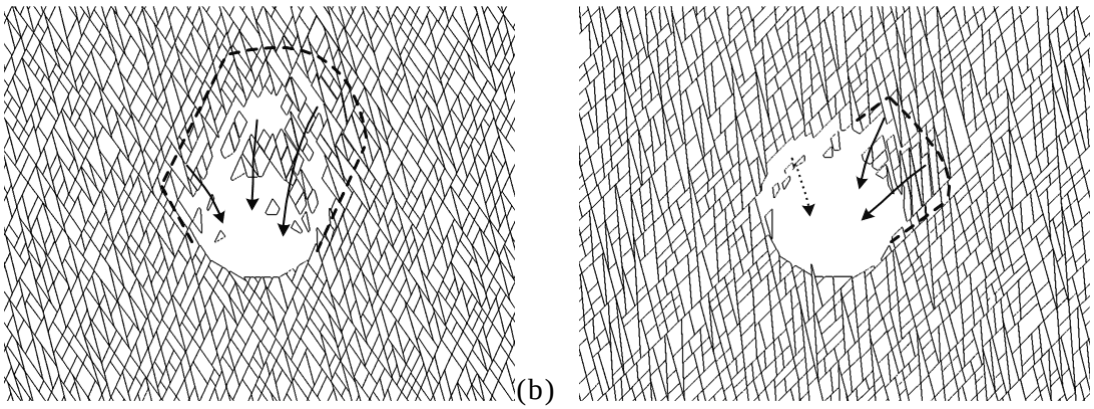

Fig. 5.1. Failure pattern at (a) roof and (b) sidewall. Joint patterns: (a) 75°E, 55°E, 65°W, ϕ = 35° (b) 75°E, 85°E, 45°W, ϕ = 35°

(a) 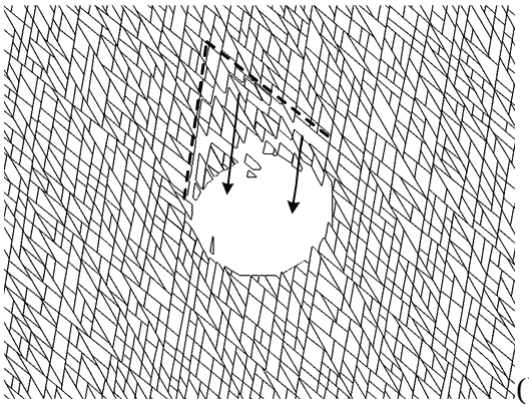 (b) 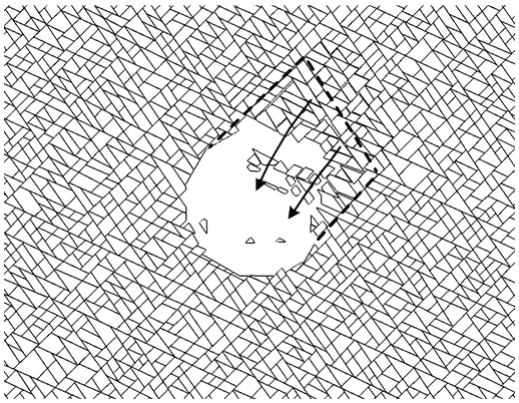

Fig. 5.2. Examples of failure in which sliding occurs along (a) the steepest joint set and (b) the second steepest joint set. Joint patterns: (a) 60°E, 40°E, 80°W, ϕ = 35° (b) 55°E, 25°E, 45°W, ϕ = 35°

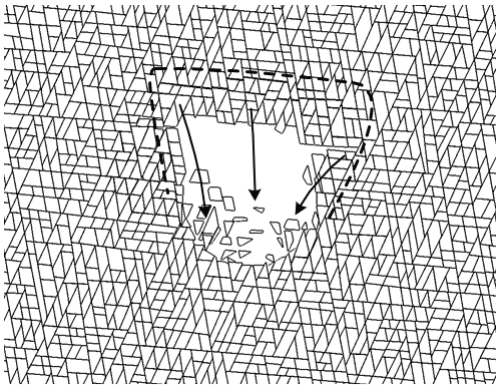

Fig. 5.3. Examples of failure in which all joint sets are involved. Joint patterns: 80°E, 5°E, 65°W, ϕ = 35°

Another observation in this exercise is that, for the majority of joint patterns, more than one failure pattern took place. They could be approximately categorised into three types of cases. In the first case, two failure patterns occurred simultaneously and to approximately the same extent; for example, roof fall and sidewall failure (see Fig. 5.4(a)). In the second case, the behaviour of the unsupported opening was dominated by a failure pattern, while other minor gravity-induced rock falls were present (see Fig. 5.4(b)). In the third case, initial falling or sliding of material led to more complex failure mechanisms. For instance, in Fig. 5.5 (a), the boundaries of the roof fall can be defined using a wedge shape; in this simulation, as the roof wedge slid off, the roof began to collapse from both sides of the wedge. In Fig. 5.5 (b), the failure mode evolved into a toppling mechanism, with material caving-in into the opening.

(a) 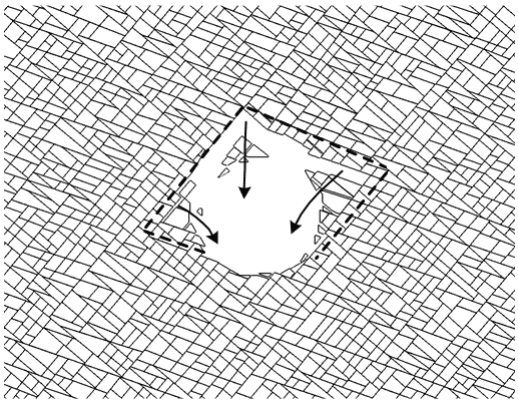 (b) 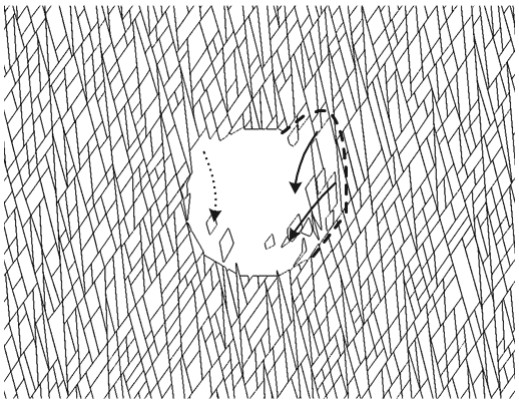

Fig. 5.4. Two failure patterns occurring simultaneously (a) Sliding along the steepest joint set led to failure at the roof and eastern side wall, and sliding along the shallowest joint set led to failure at the western sidewall. Joint pattern: 40°E, 20°E, 50°W, ϕ = 35°, (b) Sliding along the most shallow joint set led to sidewall failure, and there are minor rock falls from the roof. Joint pattern: 75°E, 85°E, 55°W, ϕ = 35°.

(a) 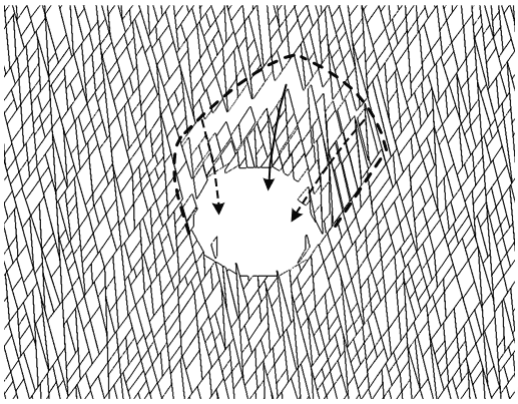 (b) 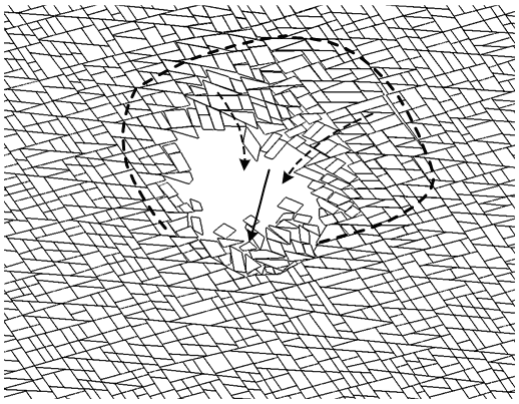

Fig. 5.5. Evolution of failure patterns (a) Joint pattern: 75°E, 85°E, 55°W, ϕ = 30°, (b) Joint pattern: 5°E, 55°E, 15°W, ϕ = 30°. The first failure mode is denoted by the solid arrow, which in-turn evolved or propagated into more complex failure modes denoted by the dashed arrows.

When the orientations of two of the three joint sets were fixed, and the third set was varied, it was found that one of the failure patterns could be affected (compare between Fig. 5.6 (a) and Fig. 5.6 (b)).

Because the failure patterns are sensitive to the joint patterns, moderately to densely jointed rock masses have been supported in practice using systematic bolting around the tunnel opening. That is to say, the characterisation of "exact" failure patterns is unlikely to be successful in practical situations, and rock engineers have in the past decided to support a large circumference of the opening. This is in contrast to sparsely jointed rock masses,

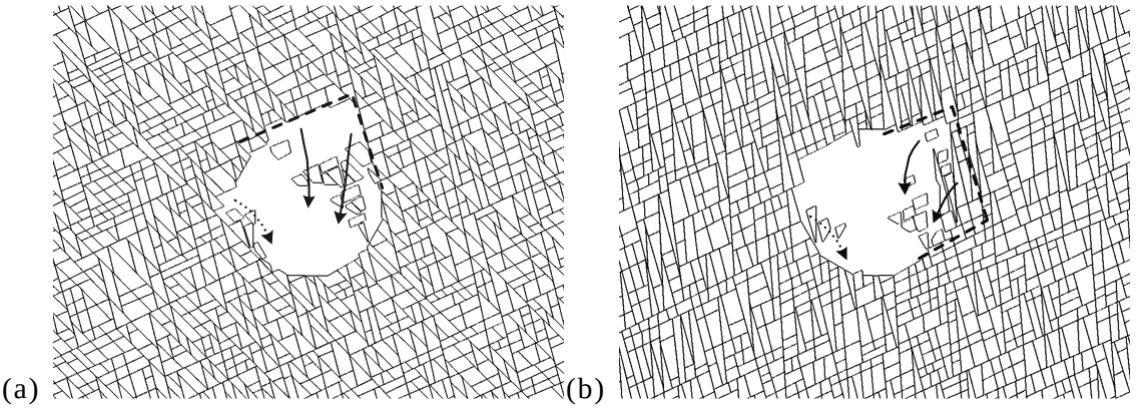

Fig. 5.6. Different failure patterns for two joint patterns with similar joint sets (a) Joint pattern: 75°E, 45°E, 25°W, ϕ = 35°, (b) Joint pattern: 75°E, 85°E, 25°W, ϕ = 35°

where spot bolting is used to support specific rock wedges whose location relative to the opening can be sought through stereographic projections in the design stage and confirmed later during the construction stage through site observations (Goodman, 1995).

5.3 NUMERICAL IMPLEMENTATION OF SUPPORT STRUCTURES

It is not the purpose of this chapter to propose novel rock support methods using rock bolts and linings, but to illustrate that the numerical tools proposed in Chapter 3 can be used to analyse rock support methods in a DEM calculation for support design. Although a particular approach is implemented in this study, the same design procedure (or logic) could be used with other rock support methods.

5.3.1 Flow of support subroutines in the DEM code

As with the block generation and contact detection algorithms, support subroutines have been written for this study to model support structures in the academic DEM code YADE. These subroutines are called before the motion integration of blocks every time step (see Fig. 5.7). At any given time-step in a DEM calculation, blocks occupy a certain position in space, and contact forces between overlapping blocks are calculated. In a similar manner, based on the positions of the rock blocks at the current time-step, forces arising from the interactions with the support structures are calculated. Finally, following conventional DEM calculation procedures, the inertial forces on every block are calculated from the contact and support forces, so that the positions and velocities of the blocks can be updated.

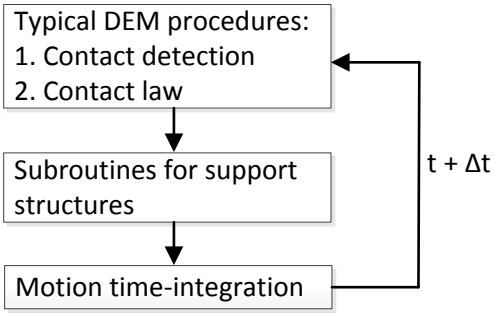

Fig. 5.7. The location of support subroutines in a DEM code

5.3.2 Survey of rock bolt algorithms in the literature

Because a DEM calculation follows the evolving configuration of a system over time, it is natural to model reinforced rock blocks just as if they are unreinforced, while adding into the numerical simulation bolt forces which act along the deformed bolt configurations. There exist several rock bolt algorithms in the literature. Although there are variations among the algorithms which have been proposed, they share a similar feature; that is, forces resulting from the axial extensions of rock bolts are modelled so that there is restraint against the displacement of any block relative to its neighbour. Most of the algorithms assume that the restraint afforded by a bolt is predominantly resisted by its axial forces, and its shear resistance is ignored. In these algorithms, the shearing motion between mating rock blocks, i.e. a rock joint, is resisted by the friction generated by the bolt axial forces. Because the axial direction of the rock bolt changes locally with the relative displacements of rock blocks, the direction of the axial force can also give rise to resistance for a shearing motion (see Fig. 5.8).

For every pair of mating rock blocks through which the rock bolt intersects at the time of installation, a spring is used to model the axial restraint afforded by the bolt. A spring consists of a pair of anchor points, each of which is assigned to opposite mating rock blocks. An anchor point is defined in the local reference frame of the rock block (to which it is referenced), so that it follows the motion of the rock block in global coordinates (see Fig. 5.8). A tensile force is calculated and applied for every pair of adjoining anchor points based on their elongation.

In the literature, however, there are different ways in which the anchor points for a rock bolt are assigned. A simple way is to assign an anchor point midway between the two

end points in a rock block through which the rock bolt passes (see Fig. 5.8 (a)). This approach was proposed by Garga & Wang (1993), and is similar to the algorithms used in Shi (1988) and Kim et al. (1999), in that the anchor points are not intentionally placed close to the joints.

Another alternative is to assign the anchor points at the discontinuity interface

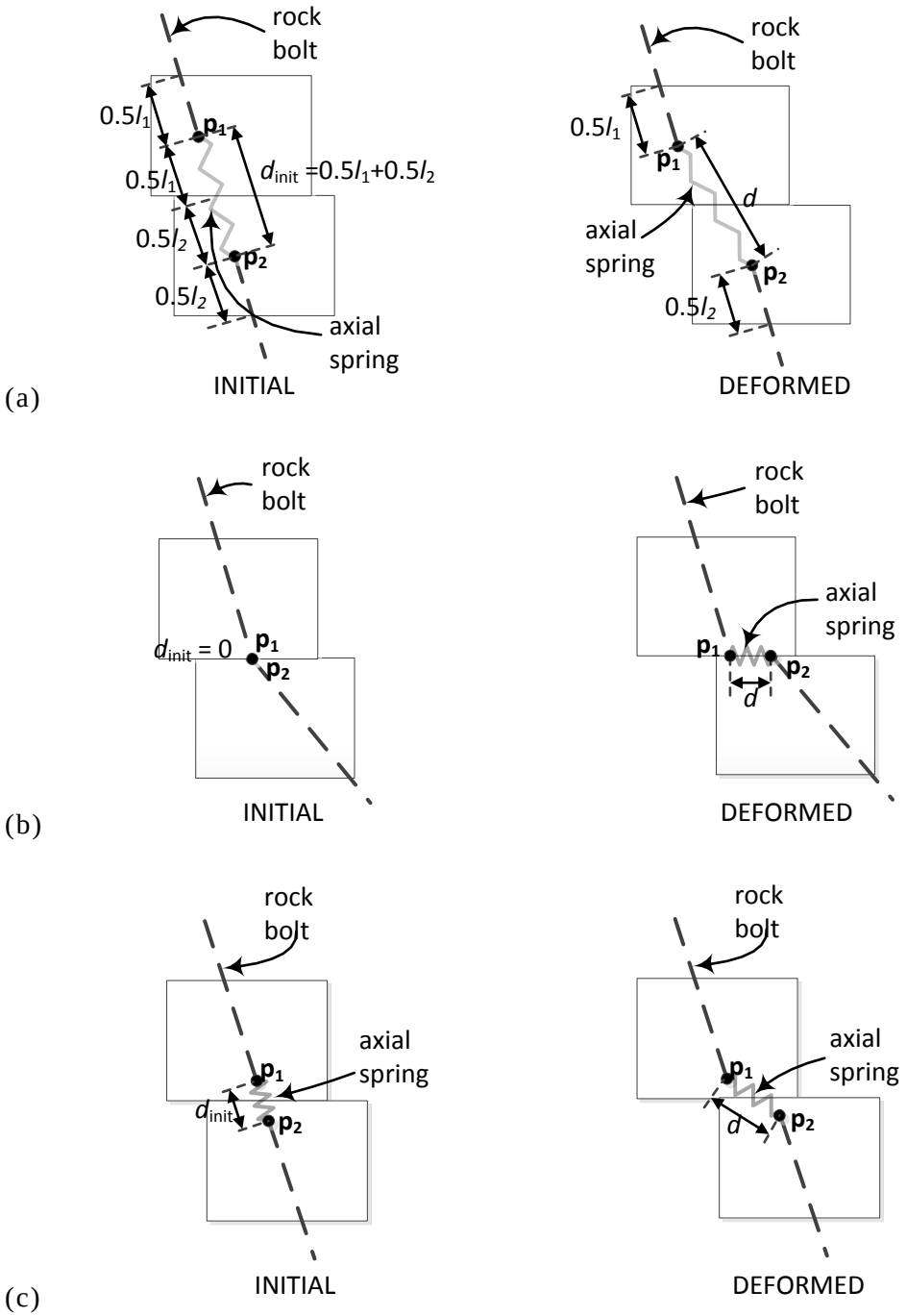

Fig. 5.8. Rock bolt algorithms. Choices of anchor point located (a) midway inside the rock block, (b) at the rock joint interface, (c) at an offset distance. The initial and deformed configurations of a rock bolt intersecting a pair of mating rock blocks are shown.

(Moosavi & Grayeli, 2006) (see Fig. 5.8 (b)). The consequence is that, on shear displacement, the axial forces of the rock bolt are directed parallel along the mating joint. This is more suitable for cable-type bolts with very low bending stiffness or for rock material with very high strength, in which case crushing of rock material near the discontinuity interface does not take place. The increase of normal force at a rock joint due to the shearing of the anchor could not be captured by this numerical implementation.

Among the many methods, the model proposed by Lorig (1985) is most commonly used because it has been implemented into the commercial code UDEC (Itasca, 2004). The model proposed by Lorig (1985) for fully-bonded rock bolts consists of two springs located at the discontinuity interface; the first spring is oriented parallel to the reinforcement axis to model the axial resistance of the bolts, while the second spring is perpendicular to this axis to model the shear resistance contributed by the bolts. Upon displacement, the shear resistance parallel to the discontinuity is contributed by both axial and shear forces from the bolt. The anchor points are located one to two diameters away from the discontinuity interface into each of the mating rock blocks (see for example Fig. 5.8 (c), although the figure shows only axial springs).

5.3.3 Numerical model for rock bolts

In this study, an algorithm which can model only the effects of axial forces of a rock bolt was implemented. The axial forces of the rock bolts were assumed to be dominant compared to the shear forces. In the algorithm, for every pair of rock joint which it intersects, a pair of anchor points is allocated to the mating rock blocks. Each of the anchor points is located at an arbitrary distance (one to two diameters) away from the rock joint into the intact rock material. A schematic of the bolt is shown in Fig. 5.8 (c). It has been observed experimentally that there is crushing of rock material at the bolts as the rock joint shears (Lorig, 1985). These anchor points are fixed with respect to the local reference frame of the rock blocks (to which they are referenced). During a simulation, a force is applied to every pair of rock blocks making up the reinforced rock joint. The force, **f**, is applied at the anchor points, $\mathbf{p_1}$ and $\mathbf{p_2}$ (Fig. 5.8 (c)), and is oriented in the direction which connects them. The magnitude of the force, **f**, is based on their elongation:

$$\hat{\mathbf{f}} = \frac{(\mathbf{p}_2 - \mathbf{p}_1)}{\|\mathbf{p}_2 - \mathbf{p}_1\|} \tag{5.1}$$

$$\mathbf{f} = K_a(\|\mathbf{p}_2 - \mathbf{p}_1\| - d_{init})\hat{\mathbf{f}} \tag{5.2}$$

where d_{init} is the initial distance between $\mathbf{p_1}$ and $\mathbf{p_2}$.

5.3.4 Survey of lining algorithms in the literature

In the literature, different methods have been used in the DEM to model lining support for an underground opening. A simple way to model the effect of lining support for a circular opening is to replace the opening with a large circular particle (Jiang & Yin, 2012) (see Fig. 5.9 (a)). The advantage is that the ground pressure on the lining can be calculated cheaply without additional programming modifications to the DEM code. This method, however, does not give information concerning the structural forces, i.e. axial, shear and moment, which are often of interest to the tunnel engineer. Another method is to model the lining as a closed-chain of geometrical entities (e.g. circular particles), between which a strong bond exists to resist shear forces and moments (Funatsu et al., 2008) (see Fig. 5.9 (b)). In this method, the values for the bond stiffness are difficult to determine.

Rather than using simple bond models (Funatsu et al., 2008), the physical relationship between adjoining geometrical entities can be modelled using a linear beam model so that the structural properties of the lining in terms of elastic modulus and second moment of area can be used directly (see Fig. 5.9 (c)). The same principle that is used in structural mechanics for a framed structure can be used to calculate the internal forces of the lining based on the displacements and orientations of the geometrical entities (Case & Chilver, 1971). The geometrical entities are represented as nodes, i.e. a circular DEM particle with zero radius but with a lumped mass, so that the overlap distance with the rock blocks can be calculated cheaply. The forces at the lining-rock interface are modelled through the contact forces between the nodes and rock blocks. Unlike the simple bond models, in which the geometrical entities are connected physically, the geometrical entities in the beam model are spaced apart. This beam algorithm was suggested by Chryssanthakis et al. (1997) and has been implemented in the commercial code UDEC (Itasca, 2004).

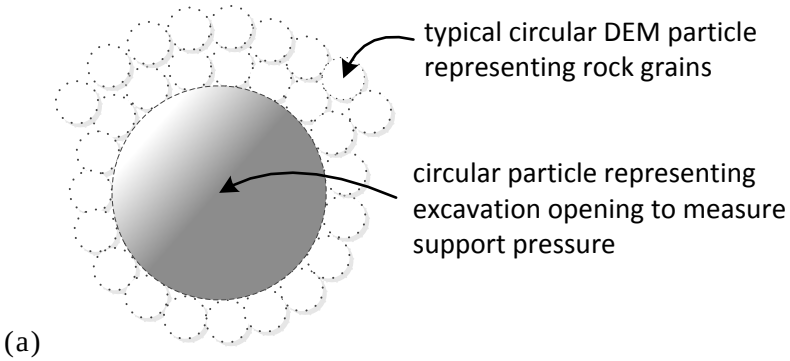

(a)

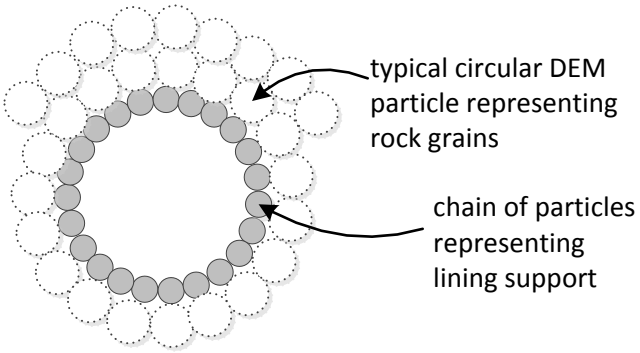

(b)

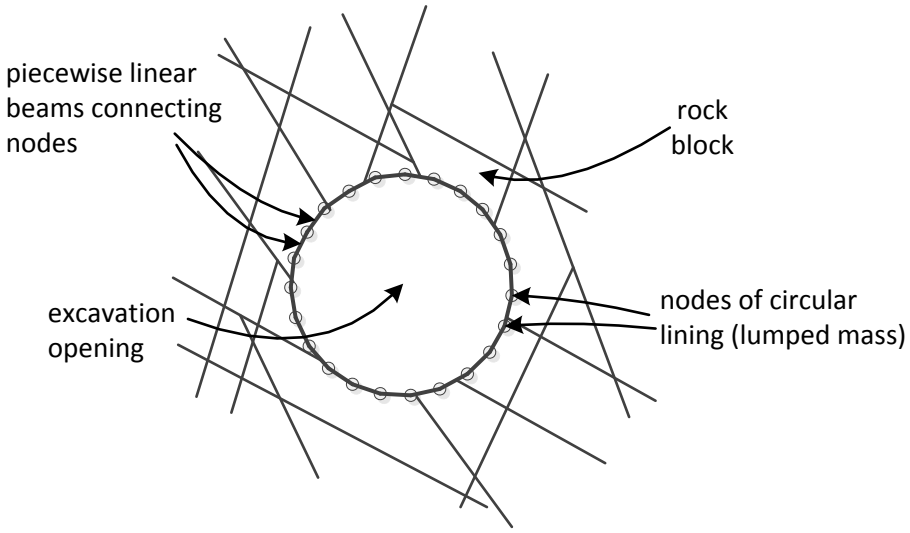

(c)

Fig. 5.9. Different approaches to model a tunnel lining using (a) a circular particle, (b) a chain of geometrical entities or (c) nodes connected using piecewise linear beams

5.3.5 Numerical model for the lining

The algorithm proposed by Chryssanthakis et al. (1997) was implemented in this study. The lining was modelled as a series of nodal points around the excavation opening (see Fig. 5.9(c)). Each nodal point was assigned a lumped mass and was subject also to motion-time integration like any other DEM particle. Fig. 5.10 shows how the contact forces between the lining nodes and rock blocks can be derived from the depth of penetration of the nodes into

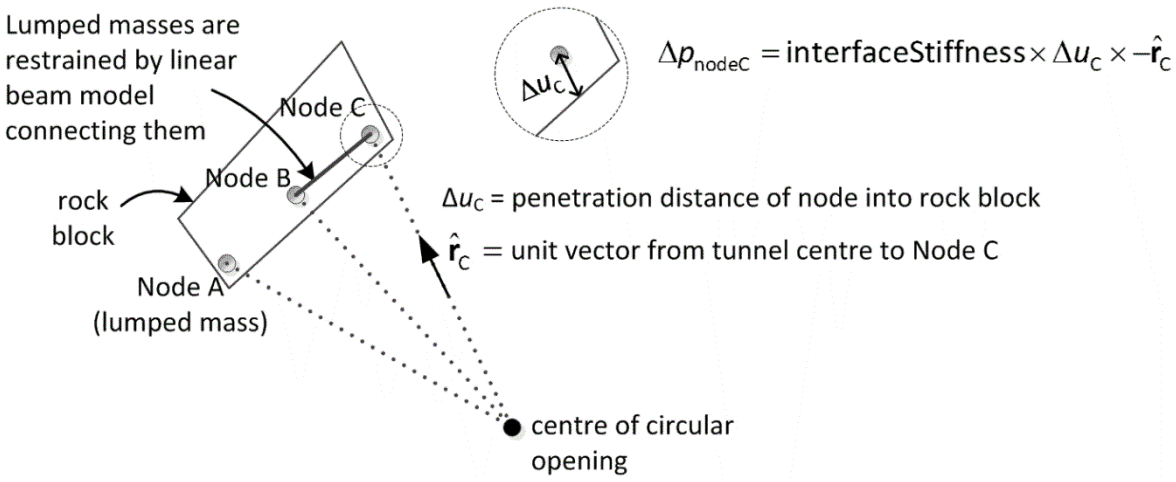

Fig. 5.10. Nodes forming a segment of lining. External contact forces on the nodes are calculated from the overlaps with rock blocks. Forces in the beam (with the assigned Young's modulus, second moment area and cross-sectional area of the lining) between nodes are calculated as Case & Chilver (1971).

the rock blocks. The contact forces on the nodes (or lumped masses) are calculated in the same manner like any other DEM particle.

These lumped masses were connected using linear beam models which restrain the nodes from moving freely due to external contact forces with the rock blocks (see Fig. 5.10). Although more accuracy can be obtained using piecewise curved-beams rather than piecewise linear beams, the error introduced from this approximation was assumed to be small compared to the DEM idealisation that rock joints are planar; in reality natural rock joints are wavy and can be folded depending on the geology. The method of approximating a non-linear geometrical shape through the interpolation of piecewise linear models is commonplace in engineering numerical analyses, as long as the level of discretisation is sufficiently fine. Because of the inherent numerical artifact that a gap exists between nodes, the spacing between nodes was kept smaller than the rock joint spacing; it is possible for rock blocks to fall between the nodes if the block size is smaller than the node spacing.

Because the beams were assumed to be elastic, standard calculation procedures for framed structures in structural analysis can be used to work out the internal forces of each beam segment (Case & Chilver, 1971). That is, it is possible either to calculate the internal forces for every beam segment one-at-a-time using its local stiffness matrix (derived from the elastic modulus and second moment of area), or to calculate the internal forces for the

entire framed structure after assembling the global stiffness matrix. The former approach was taken. That is, the displacements of the two end nodes (nodal mass) are first transformed from global coordinates to local coordinates of the beam. Then the internal forces (axial N, shear V and moment M in local coordinates) of the beam are calculated from the local stiffness matrix (Case & Chilver, 1971). The internal forces are then transformed back to the global reference frame. After the internal forces at the two ends of the beam are calculated, these forces are applied to the end nodes in the opposite direction.

5.4 DESIGN OF A ROCK SUPPORT SYSTEM FOR UNDERGROUND OPENINGS

This section shows how the numerical tools in Chapter 3 can be used together with the rock support algorithms (Section 5.3) to help an engineer make practical design decisions. The open-source DEM code, YADE (Kozicki & Donzé, 2008), was used.

5.4.1 Simulation setup and installation of support

After the rock blocks were generated, the in-situ stresses were initialised, i.e. gravity was applied and horizontal forces were applied at the "boundary blocks". The major and minor principal stresses were assumed to be oriented in the vertical and horizontal directions. The contact models detailed previously in Section 4.1.2 were used here. During this generation stage, the friction angles between rock joints were assigned as the minimum friction angle required for stability; this value can be calculated from the Mohr failure criterion based on the joint orientations and K_0. This ensures that the generated stresses are homogeneous within the domain and stress concentrations do not exist. For example, under hydrostatic stresses, the minimum friction angle is 0°. The DEM models were cycled with local damping (Cundall, 1987) to facilitate rapid convergence to quasi-static equilibrium (Hart et al., 1988; Bym et al., 2012). In the models here, local damping was switched off when the unbalanced forces were sufficiently low, and the boundary blocks were fixed in space. Viscous contact damping (Cundall & Strack, 1979) was then activated, with a damping ratio $\xi = 0.1$. Viscous damping was preferred over local damping in modelling energy dissipation mechanisms (which was not accounted explicitly), because it is physically more meaningful. A schematic of the numerical model is shown in Fig. 5.11. Then, the blocks in the

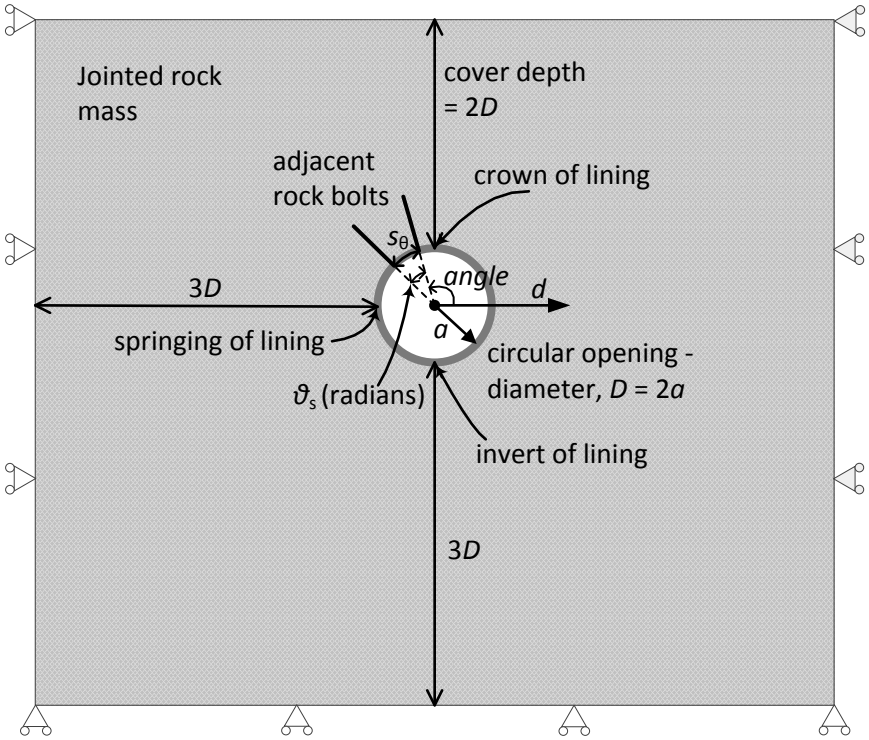

Fig. 5.11. Schematic of supported opening after the horizontal stresses are generated (dimension of DEM model in the out-of-plane direction = 1 m)

excavation opening were removed and support was installed simultaneously, i.e. wished-in-place. The reference (initial) positions of the rock bolt and lining nodes were then assigned. Note that the immediate installation of support structure is in contrast to the actual 3-D scenario; support has to be installed behind the excavation face with a distance lag (also known as the round length). Nevertheless, this assumption of wished-in-place support is acceptable insofar as to illustrate the usefulness of the numerical tools proposed in this thesis, and does not affect the quality of the numerical calculations.

5.4.2 Hypothetical case without support

A hypothetical case is selected to illustrate the use of these numerical tools to model underground openings in jointed rock masses with support structures. The unsupported opening is shown in Fig. 5.12. A series of simulations were run to show how the engineer can use these numerical tools to design the support system. The study begins with support consisting of only rock bolts, and of only lining, before the two support measures are combined. The values adopted for the parameters in the numerical simulations are shown in Table 5.2. In practice, these values can be determined experimentally or from field survey.

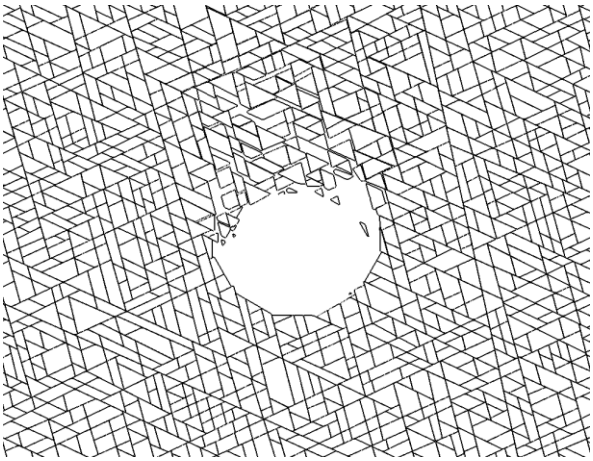

Fig. 5.12. Hypothetical case without support showing unsupported collapse mechanism. Joint pattern 75°E, 25°E, 25°W

Table 5.2: Parameters used in the numerical model

Parameters	Values
Cover depth	20 m
Diameter of opening	10 m
Rock joint normal stiffness, k_n	5 GPa/m
Rock joint shear stiffness, k_s	0.5 GPa/m
Bolt axial stiffness, K_a	0.2 GN/m
Joint friction angle, ϕ	35°
Lining friction angle, ϕ_L	30 °
Lining interface stiffness, K_L	1 GPa/m
Lining elastic modulus, E_L	25 GPa
Joint orientations: Joint set 1 Joint set 2 Joint set 2	 dip direction = East, dip angle = 75° dip direction = East, dip angle = 25° dip direction = West, dip angle = 25°
Standard deviation of dip angle for each joint set	1°
Joint centre intensity (number of joint centres per unit area in 2-D) for each joint set	1 joint/m^2
Minimum block size (minimum radius of largest inscribed circle in slicing algorithm)	0.5 m
Density of rock material	2700 kg/m^3

5.4.3 Results with rock bolt support only

5.4.3.1 Influence of numerical algorithms, spacing and length

In the design of rock bolts, length and spacing are the chief parameters of concern, because they are directly related to the cost of support. From literature survey, the length and spacing

of rock bolts to date has been estimated based on empirical rock mass classifications. DEM software has been used mainly to verify support designs. This section shows how the length and spacing of the rock bolts can be determined more directly using these numerical tools.

First, a particular rock bolt specification has to be used as the starting point for the iterative design procedure. From Stillborg (1994), for a 20 mm diameter steel bar with an ultimate tensile strength of 18 tonnes, the axial stiffness obtained by pulling two blocks of concrete apart is approximately 0.1 GN/m. This test is more representative of field conditions for a rock mass intersected with discontinuities. In this exercise, a more conservative bolt diameter was used as a first estimate, i.e. 28 mm, and the axial stiffness was assumed to correspond approximately to 0.2 GN/m. In practice, this value should be obtained from the bolt manufacturer. Some bolt suppliers may specify only the grade and Young's modulus of the steel. But for a jointed rock mass, the axial stiffness of a bolt across a rock joint is the more important parameter. As a starting point, a dense support system is modelled, i.e. long rock bolts with small spacing (see Fig. 5.13). The initial trial consists of 21 bolts, each 7 m long, with spacing of 11.25° around the crown and springing.

Based on the rock bolt algorithm in Section 5.3, the forces between adjoining rock blocks are governed by the relative displacements between the pair of adjoining nodes located across each joint. Here, two variations of node positions were explored. In the first, the nodes are placed 1.2 diameters away from each joint (see Fig. 5.8 (c), p. 110). In the second, the nodes are placed midway between the two points at which the rock bolt

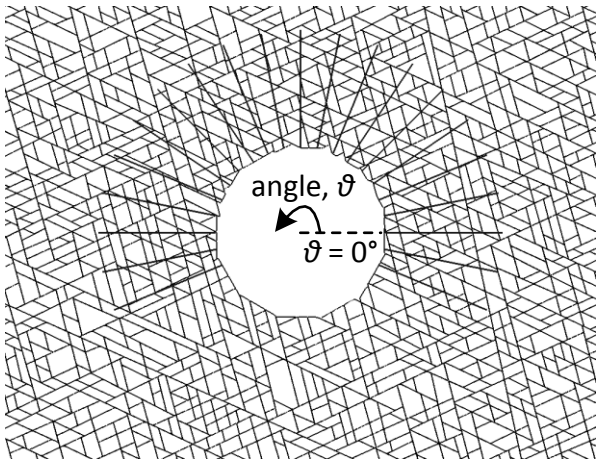

Fig. 5.13. Long and dense bolt pattern (length 7 m, spacing 11.25°).

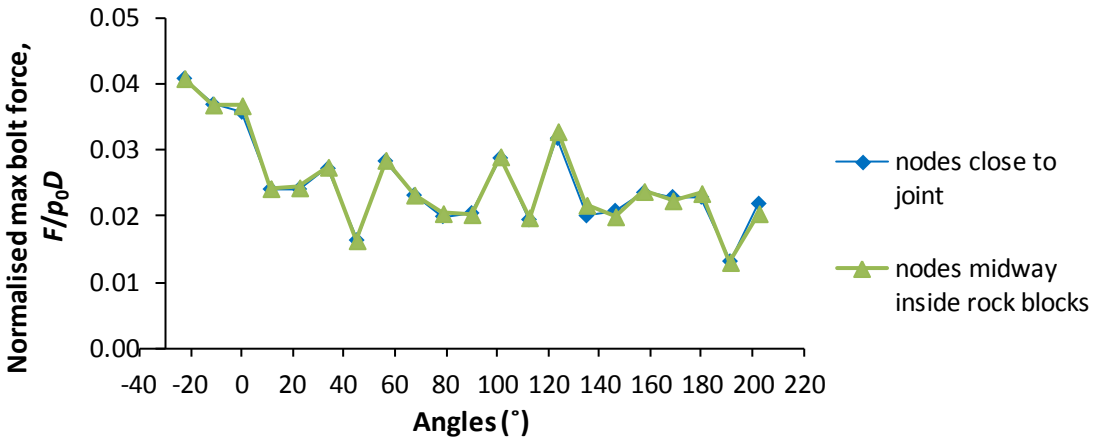

Fig. 5.14. Comparison of maximum bolt forces between two rock bolt algorithms

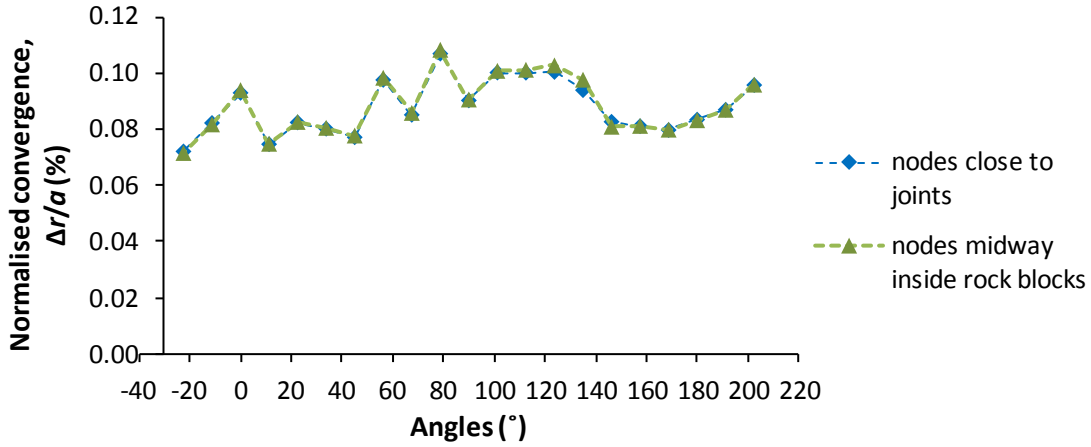

Fig. 5.15. Comparison of displacements between two rock bolt node choices

intersects the rock block (see Fig. 5.8 (a), p. 110). Figs. 5.14 and 5.15 compare the results of the two numerical implementations in terms of maximum bolt forces and displacements for the bolt configuration shown in Fig. 5.13. The bolt forces are normalised by the ground pressure at the tunnel centre, p_0, and the tunnel diameter, D (see Fig. 5.11, p. 116, for notation). From Figs. 5.14 and 5.15, the results calculated by the two variations of node position are close – one almost traces the other, the largest percentage difference being 8.1 % and 4.0% for the bolt forces and displacements respectively. From now on, the node positions are placed close to the joints, i.e. with an offset distance of 1.2 diameters away from each joint.

The distribution of axial forces in each rock bolt normalised by its maximum value are plotted against the distance of the bolt from the tunnel centre in Fig. 5.16.

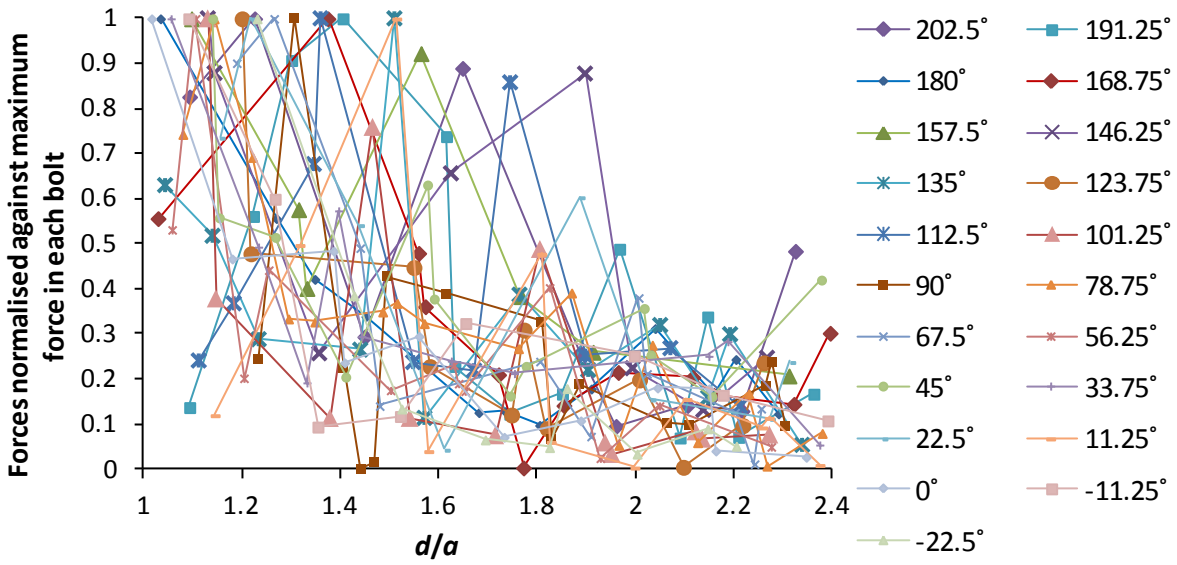

Fig. 5.16. Forces along each bolt normalised against its maximum force versus the ratio of radial distance from the centre of the opening to the opening radius. Note that *d* is the distance from the tunnel centre

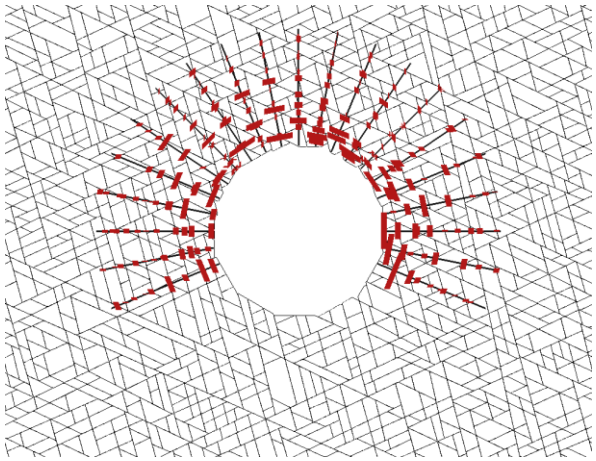

Fig. 5.17. Long and dense bolt pattern (length 7 m, spacing 11.25°). The magnitudes of bolt axial forces (red bars) are all drawn using the same scale

Figs. 5.16 and 5.17 show that most of the forces follow a consistent pattern; the curve reaches a peak and then tails off away from the excavation opening. As shown in Fig. 5.16, the bolt forces are roughly constant beyond 1.8 times the tunnel radius (4 m) from the tunnel centre.

In the next trial (see Fig. 5.18), 4 m long bolts were adopted and the bolts below the horizontal axis were removed. The bolt forces and displacements increased only marginally. An exercise of increasing the bolt spacing was then conducted with spacing increased to 15°

and 22.25° (see Figs. 5.19 and 5.20). As shown in Figs. 5.21 and 5.22, the bolt forces and displacements increased slightly when the spacing increased from 11.25° to 15°. From 15° to 22.25° spacing, the bolt forces and displacements increased significantly. Significant ravelling of rock blocks occurred between the rock bolts (see Fig. 5.20), indicating that the bolt spacing of 22.5° and greater is unsafe. Fig. 5.23 shows the trend of the bolt forces and displacements at the crown with bolt spacing.

An interesting observation is that the maximum bolt forces, F, when normalised by the product of characteristic ground pressure, p_0, and bolt spacing, $a\theta_b$, for different bolt spacings are roughly similar (see Fig. 5.24). For the ideal case in which the rock bolts are uniformly distributed and the far-field stresses isotropic, the product of pressure and bolt spacing ($p_0 a\theta_b$) can be interpreted as the upper bound load per bolt.

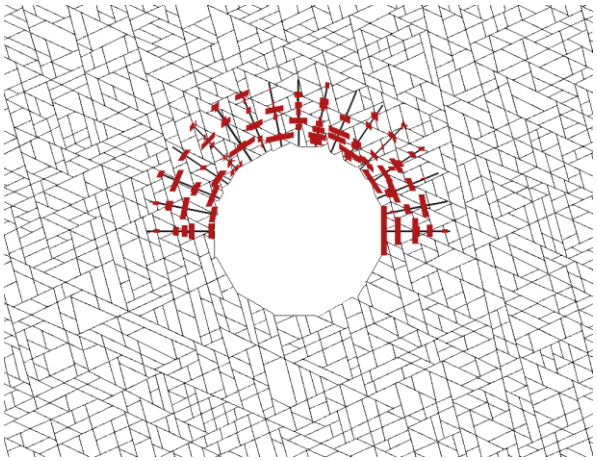

Fig. 5.18. Second trial. Bolt configuration: length 4m, spacing 11.25°.

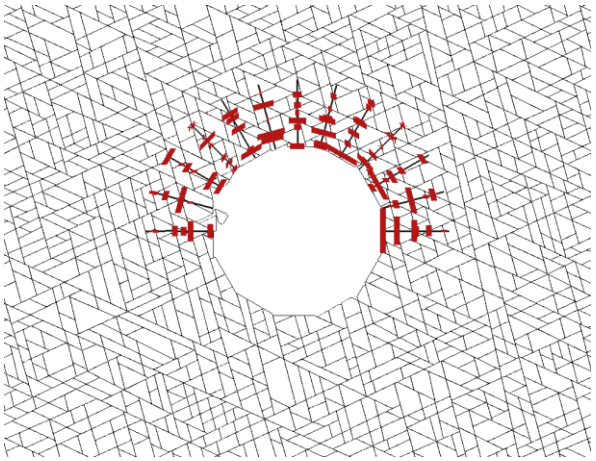

Fig. 5.19. Third trial. Bolt configuration: length 4m, spacing 15°.

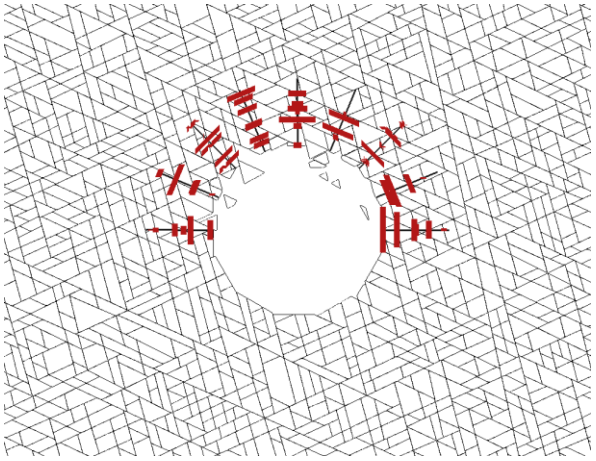

Fig. 5.20. Many loose blocks falling between the rock bolts for bolt configuration: length 4m, spacing 22.5°.

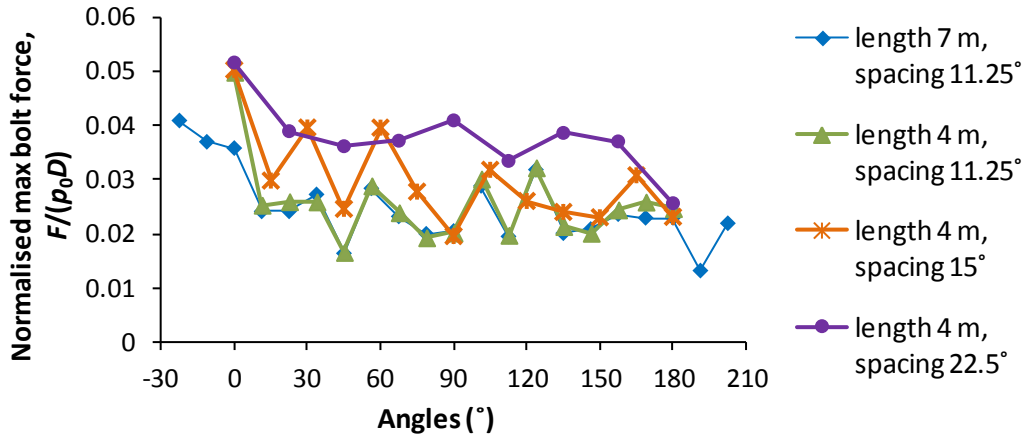

Fig. 5.21. Maximum bolt forces for different bolt length and spacing.

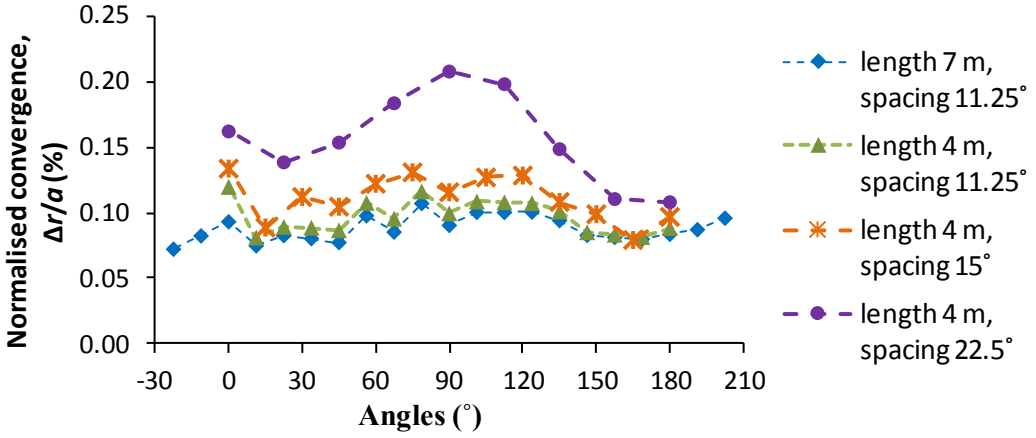

Fig. 5.22. Displacements for different bolt length and spacing

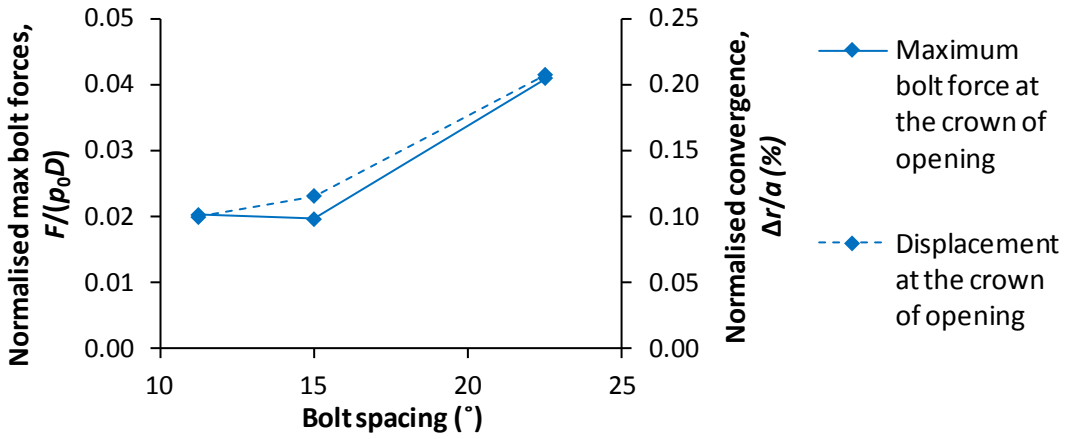

Fig. 5.23. Bolt forces and displacements at the crown with bolt spacing (bolt length = 4m)

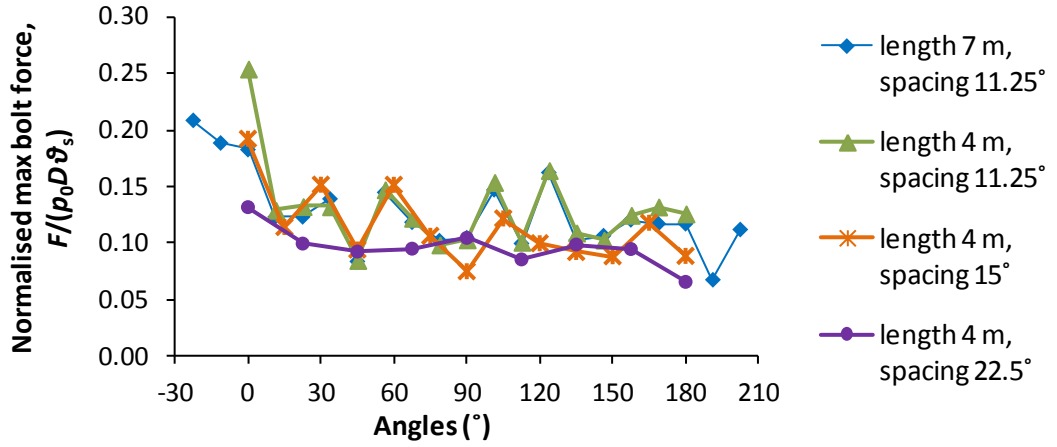

Fig. 5.24. Maximum bolt forces normalised against tangential spacing for different bolt length and spacing

5.4.3.2 Influence of pretension

Although grouted rock bolts without pretension are recommended in more recent rock mass classifications, it is commonplace in some parts of the world to introduce pretension in rock bolts (Liu et al., 2009). The influence of pretension can be examined using the proposed numerical tools. From the results in Fig. 5.25, pretension was able to reduce the displacements. For bolt pretension of 100 kN and 150 kN, the displacements around the opening was found to be more uniform; the differential displacements between the crown and the springing were smaller. Nevertheless, in terms of overall displacements, the influence of pretension was found to be minor. Using pretension also led to an increase of bolt forces (see Fig. 5.26); this in turn may lead to the need for bolts with higher yield limits.

Note that pretension is not found in the rock bolt recommendations for rock mass classifications such as the RMR system (Bieniawski, 1983) and the more recent version of Q-system (Barton, 2002).

A suitable bolt configuration from the above analysis was considered to be 4 m length and 15° spacing. Pretension was not necessary because of its limited benefit in this particular excavation example. To examine this conjecture, simulations were run with larger bolt spacing (22.5°), but with longer length or with higher pretension. For bolt spacing of 22.5°, increasing the bolt length from 4 m to 7 m did not significantly change the displacements (see Fig. 5.27); and although introducing pre-tension of 150 kN resulted in smaller displacements, the bolt forces increased substantially (see Fig. 5.27) so that bolts with higher yield limits would have to be used. Moreover, the ravelling of rock blocks between bolts persisted as shown in Fig. 5.28. In other words, pretension was only capable of controlling displacements locally around the bolt. In this example, a larger bolt spacing

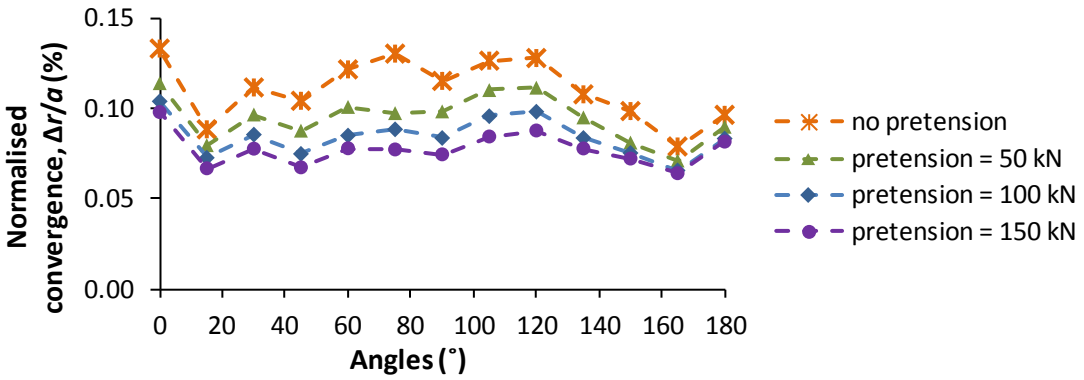

Fig. 5.25. Normalised displacement for different magnitudes of pretension

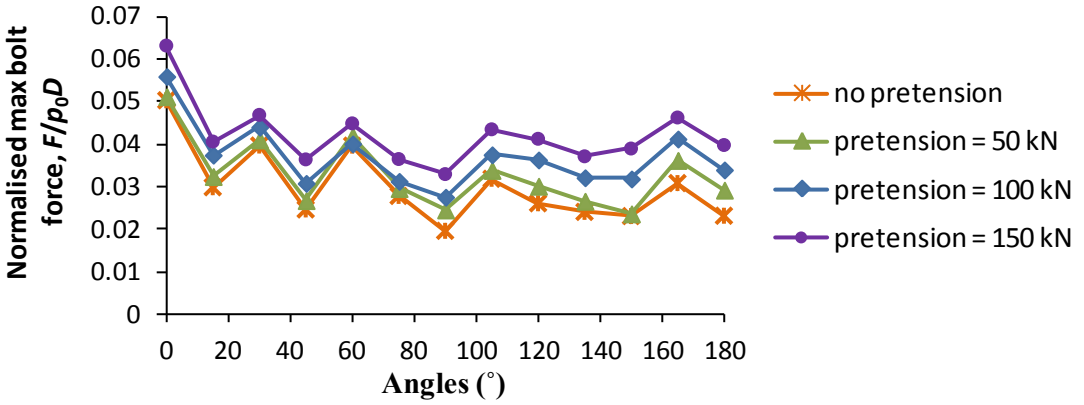

Fig. 5.26. Maximum bolt forces for different magnitudes of pretension

(22.5°) but longer length (7 m) or with pretension was less effective compared to a bolt pattern with smaller spacing (15°) but shorter length (4 m). Less steel was used in the latter.

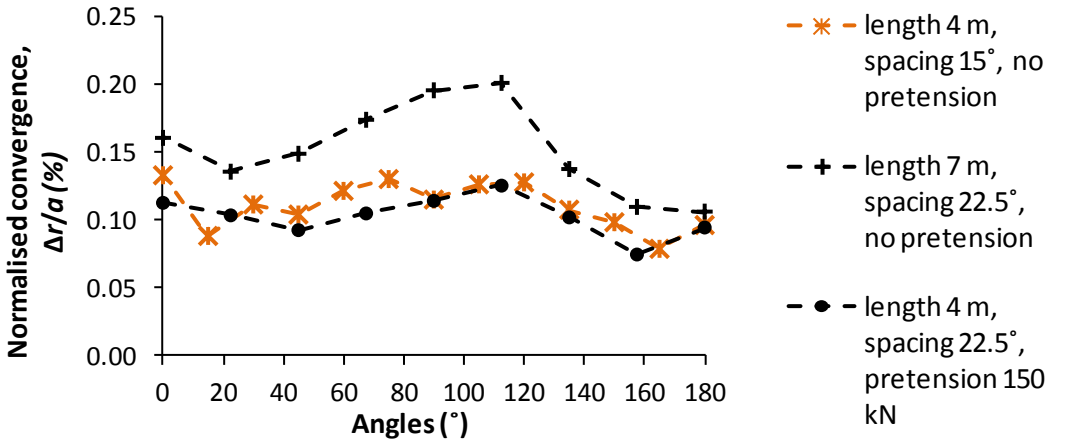

(a)

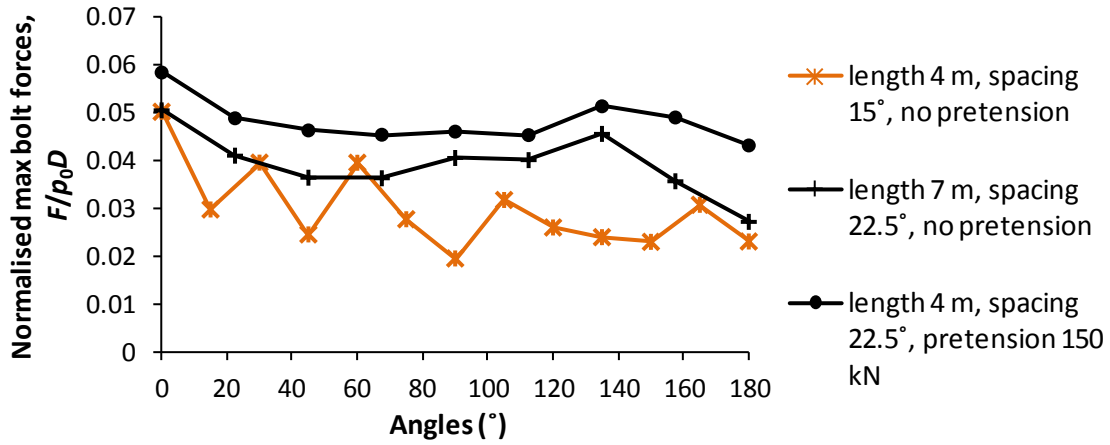

(b)

Fig. 5.27. Comparison of (a) displacements and (b) maximum bolt forces for non-optimal spacing with longer bolts and with pre-tension

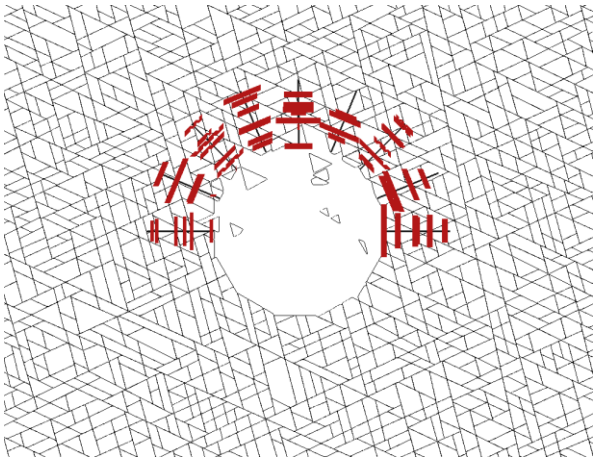

Fig. 5.28. Use of 150 kN pretension for bolt configuration: length 4m, spacing 22.5°

5.4.4 Verification of rock bolt support against elastic solution

The DEM calculations with rock bolt support are verified against the elastic solution proposed by Carranza-Torres (2009) for a circular opening in a rock mass subjected to isotropic stress. In Carranza-Torres (2009), the axial stresses of the bolts are assumed to be smeared into the rock mass uniformly in both the circumferential and longitudinal directions. The conditions of axisymmetry of geometry and loading are assumed in Carranza-Torres (2009), and the solution is formulated as a differential equation in terms of the radial displacements. There is another analytical approach by which the rock bolt stresses can be estimated. This approach is known as the shear-lag method, in which equations of equilibrium are derived for a single rock bolt (Li & Stillborg, 1999; Bobet, 2009). This method, however, has several shortcomings which have been discussed in detail by Bobet & Einstein (2011). This method is not used in this verification exercise mainly because (i) the interaction between adjacent bolts has not been considered in its derivation and (ii) the calculation requires as input the shear resistance at the interface between the rock bolt and rock mass; this parameter is often not known a priori.

Based on the analytical solution proposed by Carranza-Torres (2009), assuming that the opening is wished-in-place and that the rock bolts are installed without pretension, the relative stiffness of this ground-structure interaction problem can be defined using the following dimensionless variable, β:

$$\beta = \left(\frac{1}{s_\theta s_l} \right) \frac{K_\mathrm{a} s_\mathrm{mean}}{2G} \tag{5.3}$$

where s_θ (units: m) and s_l (units: m) are the rock bolt spacing in the tangential and longitudinal directions measured along the tunnel perimeter, and s_mean is the mean joint spacing which is characteristic of the rock mass. The rock bolt radial stresses and the opening convergence can be calculated from the general solution of the differential equation and from the boundary conditions (Carranza-Torres, 2009). To use the closed-form equations in Carranza-Torres (2009), the shear modulus, G, of the jointed media has to be estimated (Eq. (5.3)).

There are numerous ways by which the elastic constants of the generated model can be approximated. A recent review of the analytical and empirical solutions proposed in the literature can be found in Zhang (2010). The analytical solution in Goodman (1989) is used here as a first estimate, since this method is conceptually straightforward and could be used as a benchmark for other methods (Duncan & Goodman, 1968; Kulhawy, 1978). In Goodman (1989), for a jointed rock mass with uniform joint spacing s_{mean}, its elastic modulus E is approximated as:

$$\frac{1}{E} = \frac{1}{E_i} + \frac{1}{k_n s_{mean}} \tag{5.4}$$

and the shear modulus G as:

$$\frac{1}{G} = \frac{1}{G_i} + \frac{1}{k_s s_{mean}} \tag{5.5}$$

where E_i and G_i are the Young's modulus and shear modulus of the intact rock material. Since rigid rock blocks are used in the models here, the Young's modulus E can be approximated as:

$$E = k_n s_{mean} \tag{5.6}$$

and the shear modulus as:

$$G = k_s s_{mean} \tag{5.7}$$

Alternatively, if the Poisson's ratio v is known, the shear modulus can be calculated from the elastic modulus based on elasticity theory:

$$G = \frac{E}{2(1+v)} \tag{5.8}$$

Substituting Eq. (5.6) into Eq. (5.8), we obtain:

$$G = \frac{k_n s_{mean}}{2(1+v)} \tag{5.9}$$

A typical Poisson's ratio of 0.2 for rock masses is adopted here.

A simple way to approximate the mean joint spacing, s_{mean}, is to draw a straight line and divide its length by the number of times it is intersected. This method is analogous to

the characterising of scanlines in the field using the joint frequency (Priest & Hudson, 1976). Based on this procedure, a mean spacing of 0.77 m was adopted for this study.

The aforementioned approaches of approximating the Young's and shear moduli are for idealised joint patterns. It is, therefore, of value to use another method to determine the elastic properties of the actual block assembly that was used for the DEM calculations. A possible solution is to run a numerical "laboratory test" on the modelling domain. Like common laboratory tests for geomaterials, a nonlinear stress-strain response will take place, and a data point or several points from the numerical laboratory test have to be selected to calculate the elastic constants; for instance, whether the engineer should use the tangent or secant stiffness depends on his experience and judgement of that particular engineering problem (Davis & Selvadurai, 1996). In this exercise, an oedometer (consolidation) test was run on the DEM modelling domain without gravity. A vertical stress p_0 = 662 kPa equal to the stresses experienced at the tunnel centre was applied on the top boundary while the sample was constrained horizontally. Unlike actual laboratory oedometer tests, the lateral pressure can be measured in a DEM calculation, making possible the determination of two elastic constants. From Hooke's law,

$$\sigma_1 = (\lambda + 2G)\varepsilon_1 + \lambda\varepsilon_3 \tag{5.10}$$

$$\sigma_3 = \lambda\varepsilon_1 + (\lambda + 2G)\varepsilon_3 \tag{5.11}$$

where λ is Lame's constant, and with $\varepsilon_3 = 0$, the shear modulus G can be calculated as:

$$G = \frac{(\sigma_1 - \sigma_3)}{2\varepsilon_1} \tag{5.12}$$

Based on Hooke's law (with $\varepsilon_2 = 0$ and $\varepsilon_3 = 0$), the Poisson's ratio, ν, can be calculated from:

$$\frac{\sigma_3}{\sigma_1} = \frac{\nu}{1-\nu} \tag{5.13}$$

Note that there are other ways by which the rock mass deformability could be determined from DEM simulations (Staub et al., 2002).

The shear moduli approximated using the three aforementioned approaches are summarised in Table 5.3. Note that the estimated shear moduli using Eqs. (5.7) and (5.9)

Table 5.3: Estimated shear moduli using different approaches

Ref. No.	Method of estimation	Poisson's ratio, v	Shear modulus, G (GPa)
G1	$G = k_s s_{mean}$	0.2 (assumed)	0.385
G2	$G = k_n s_{mean}/(2(1+v))$	0.2 (assumed)	1.604
G3	Oedometer test on the full domain (Fig. 5.11), φ=35˚, $G = (\sigma_1-\sigma_3)/2\varepsilon_1$	0.37 (obtained)	0.527
G4	Oedometer test on the full domain (Fig. 5.11), φ=89˚, $G = (\sigma_1-\sigma_3)/2\varepsilon_1$	0.37 (obtained)	0.529
G5	Oedometer test on reduced sample size of 20 m x 20 m, φ=35˚, $G = (\sigma_1-\sigma_3)/2\varepsilon_1$	0.36 (obtained)	0.542
G6	Oedometer test on reduced sample size of 10 m x 10 m , φ=35˚, $G = (\sigma_1-\sigma_3)/2\varepsilon_1$	0.36 (obtained)	0.536

differ by approximately 400%. There are two possible reasons for this discrepancy. First, these methods are derived for idealised joint patterns and could be inaccurate if applied to random joint patterns. The second possible reason is that the adopted normal to shear stiffness ratio (k_n:k_s = 10) is not physically attainable in reality, as is implied in Eqs. (5.7) and (5.9). Note that using a Poisson's ratio approaching the limit of 0.5 still results in a discrepancy of approximately 300%. A k_n:k_s ratio of 10 or larger has been adopted commonly in the literature for modelling rock joints (Shen & Barton, 1997; Eberhardt et al., 2004; Jiang et al., 2006; Hammah et al., 2008). This ratio is consistent with the experimental work by Bandis et al. (1983) which indicates that the k_n:k_s ratios of rock joints are typically in the range of 1 to 130, and decrease with the normal stress. Also, Oda et al. (1993) concluded from their numerical analyses of a storage cavern that a k_n:k_s ratio of greater than 10 was necessary to model the anisotropic stress field, which resulted in better comparison with field measurements. It is, nevertheless, reassuring that the shear moduli, approximated using Eq. (5.12) based on the DEM oedometer tests, fall between the values given by Eqs. (5.7) and (5.9).

Another noteworthy observation is that the Poisson's ratios obtained from the oedometer tests are high (v = 0.36 - 0.37) (see Table 5.3). This is believed to be a consequence of adopting a high k_n:k_s ratio for modelling the rock joints. Note that in the

literature on the bonded particle method (BPM), i.e. a DEM approach of modelling intact rock as a cemented granular material, it is well known that the Poisson's ratio of a particle assembly increases with the interparticle contact stiffness ratio, k_n:k_s (Potyondy & Cundall, 2004; Cho et al., 2007; Kazerani & Zhao, 2010).

The oedometer tests were repeated with different sample sizes of the modelling domain (i.e. Fig. 5.11, p. 116). Scale effects have been shown to be important in Ivars et al. (2011). However, as with Staub et al. (2002), the deformability properties did not show obvious trends with the sizes of the sampling domain that was investigated (see Table 5.3). But this observation could be restricted to the particular joint pattern that was adopted in this study.

The closed-form equations in Carranza-Torres (2009) were derived for continuous and homogeneous rock. To use the equations on a heterogeneous jointed rock mass, the equivalent input parameters have to be approximated. This is discussed in Appendix G. Figs. 5.29 – 5.31 show the results of DEM calculations juxtaposed against the elastic solution proposed by Carranza-Torres (2009) using the different approximated shear moduli and Poisson's ratios (Table 5.3). For small rock bolt spacing (11.25°), the results obtained from the DEM solutions compare well with the elastic solution (see Fig. 5.29). Some scatter for jointed discontinuous material is inevitable. The discrepancy increases for larger spacing (15° and 22.5°), and is expected because plastic displacements were likely to have had occurred for less support; the bolt forces obtained by the DEM calculations are higher than the forces predicted by the elastic solution. The favourable comparison suggests that the numerical tools in Chapter 3 are reliable at predicting the global response of large block assemblies and also the interactions with structural components. This verification exercise is important because it corresponds more closely to the actual problems on which the tools would be applied by practising engineers. This is an important milestone by comparison to the simpler verification models presented in Chapter 4. Verification against elastic solutions is considered to be more robust by comparison to field validation because the uncertainties in the field could cause different combinations of parameters to converge to the same solution (cf. Einstein et al., 2010).

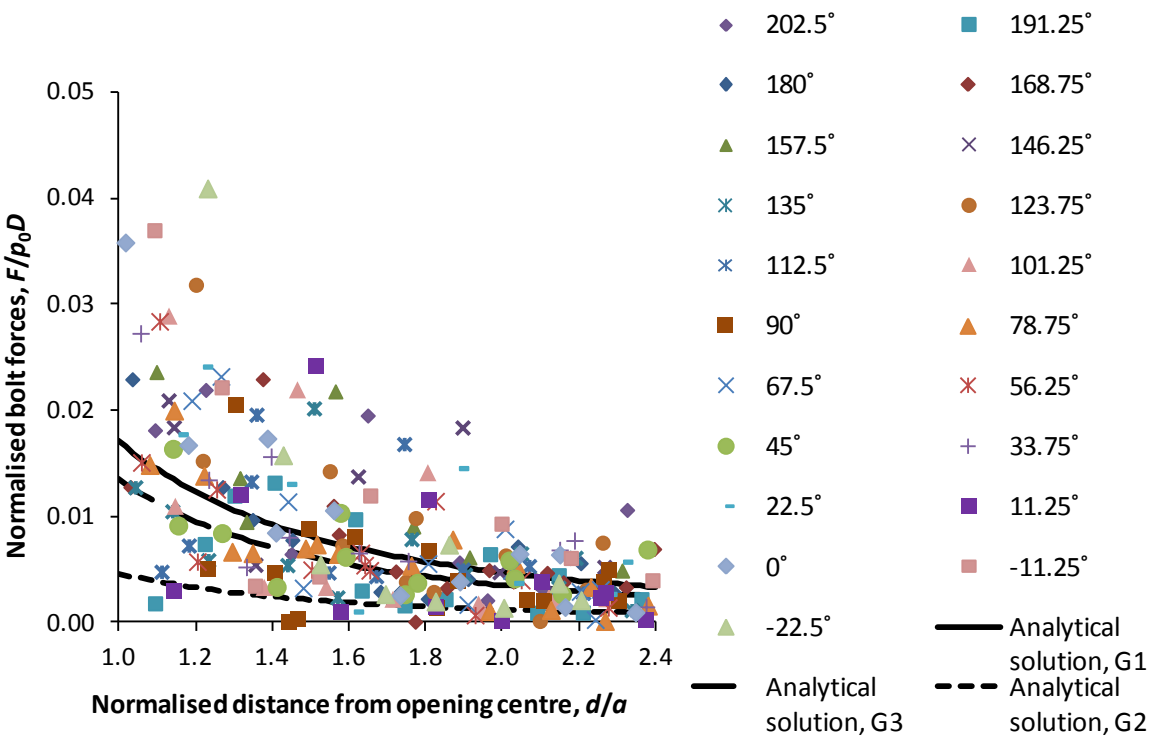

Fig. 5.29. Comparison of DEM calculations against analytical solutions proposed by Carranza-Torres (2009) for bolt configuration: 7 m length, 11.25° spacing. Shear moduli were estimated using approaches summarised in Table 5.3 (p. 129).

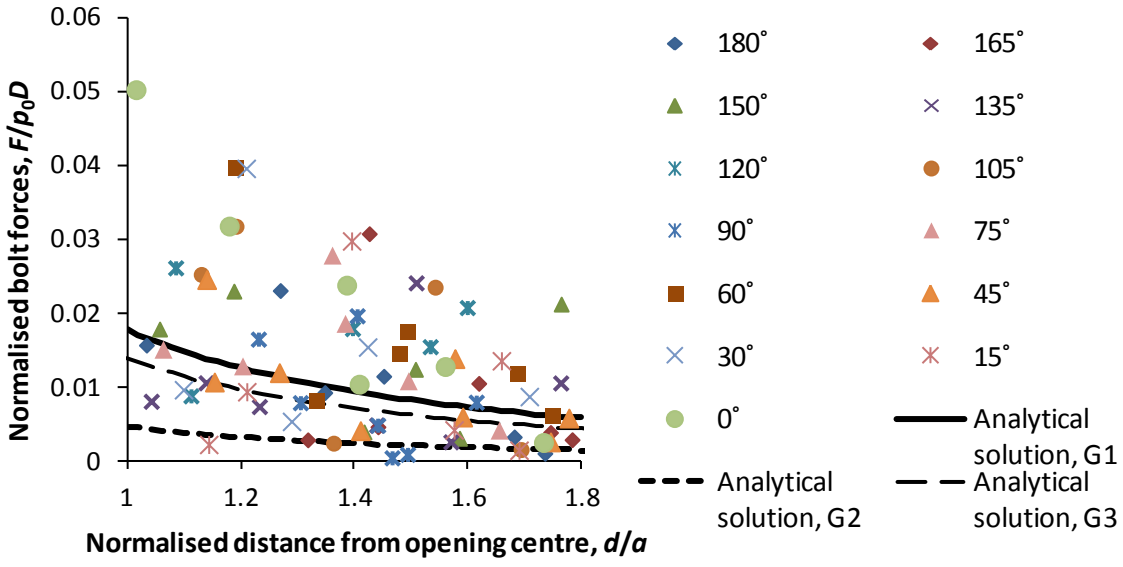

Fig. 5.30. Comparison of DEM calculations against analytical solutions proposed by Carranza-Torres (2009) for bolt configuration: 4 m length, 15° spacing. Shear moduli were estimated using approaches summarised in Table 5.3 (p. 129).

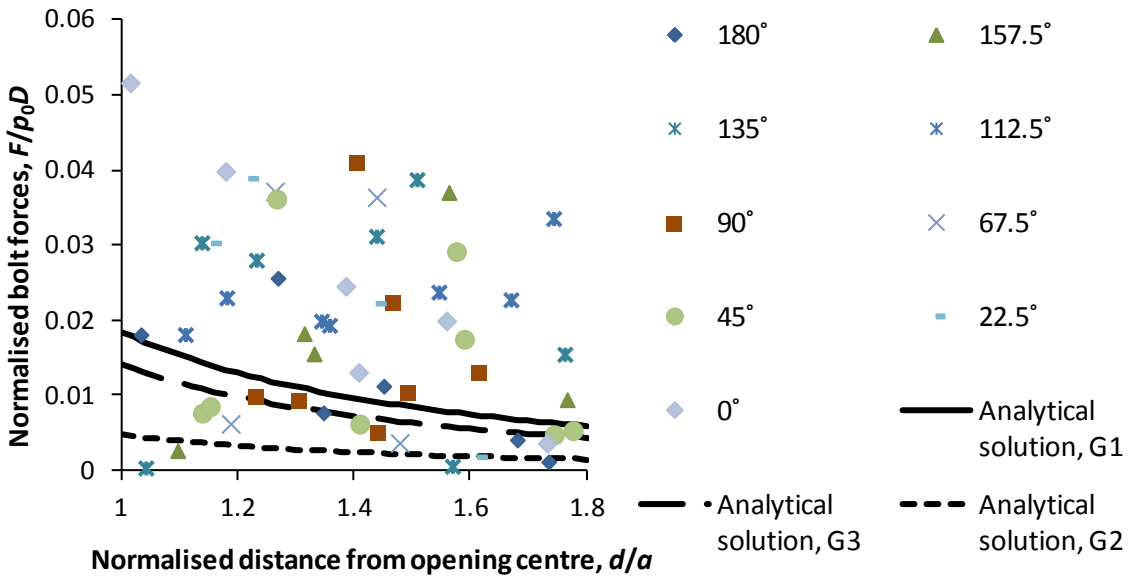

Fig. 5.31. Comparison of DEM calculations against analytical solutions proposed by Carranza-Torres (2009) for bolt configuration: 4 m length, 22.5° spacing. Shear moduli were estimated using approaches summarised in Table 5.3 (p. 129).

5.4.5 A comment on the variability of ground properties and rock bolt forces

The previous results show significant scatter of bolt forces. The most obvious source for the scatter is because the ground is not homogeneous; the geometrical properties of rock joints, i.e. spacing, orientation and extent, are irregular. A simple way to visualise the scatter of maximum bolt forces is through a force-frequency histogram. Also, it is important to appreciate that the results of the previous analyses do not predict precisely the actual bolt forces in the field, because a joint pattern generated numerically from statistical input is analogous to a random sample. For a rock mass intersected by a large number of rock joints, it is impossible to determine every single rock joint from geological survey; the rock joints are characterised using probabilistic distributions for design purposes. This is in contrast to sparsely jointed rock masses where the exact spatial coordinates and orientations of the joints might be deterministically measured, in which case the most critical cross-section of the underground excavation could be adopted for numerical modelling. To put it another way, a joint pattern generated from statistical input data is only one of the many possible engineering outcomes. To address the inherent uncertainty in this calculation, the engineer can repeat the simulations using a different "sample" generated from the same statistical input. Depending on the in-situ stress ratio, the number of joint sets and their relative

spacing and extents, the assumption of an equivalent isotropic medium may be acceptable for engineering purposes, in which case one can fairly assume that the forces experienced in the bolts are independent and non-correlated. The data from different numerical "samples" can be merged to increase the sample size, i.e. the number of bolts. A large sample size can estimate the distribution of the "population" better.

Fig. 5.32 (a), (b) and (c) show the histograms of maximum bolt forces for three different "samples" of joint patterns. The merged data can be analysed using statistical tools as shown in Fig. 5.33. Note that the fitting of statistical distributions should be conducted on the raw data rather than on the histograms. In most situations, the distribution can be modelled as a normal distribution. In this example, the mean of the normalised maximum bolt forces is 0.03 and the standard deviation is 0.009.

Instead of merging the data, the bolt forces from different simulations can be

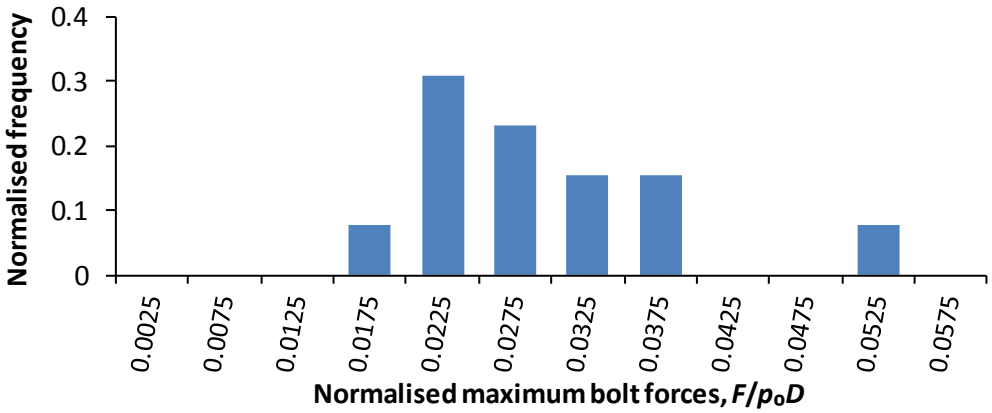

(a)

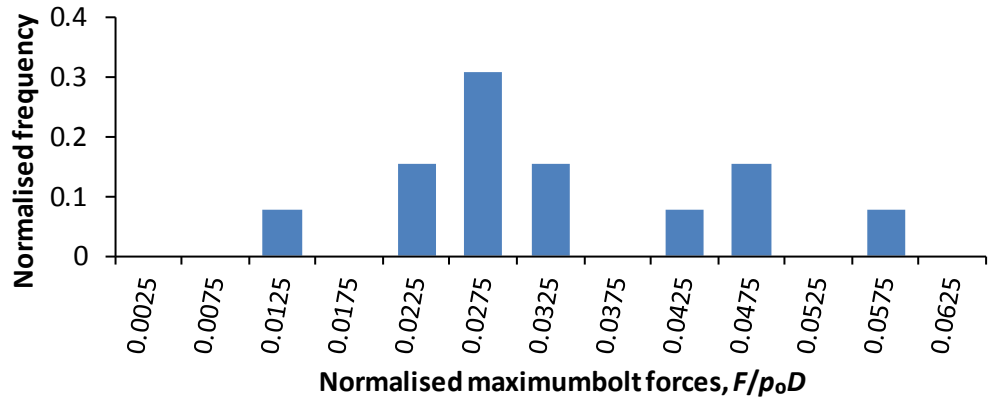

(b)

Fig. 5.32. Histogram of frequency distribution for the max bolt forces (a) reference sample (mean = 0.030, standard deviation = 0.008), (b) sample A (mean = 0.032, standard deviation = 0.012), (c) sample B (mean = 0.028, standard deviation = 0.007)

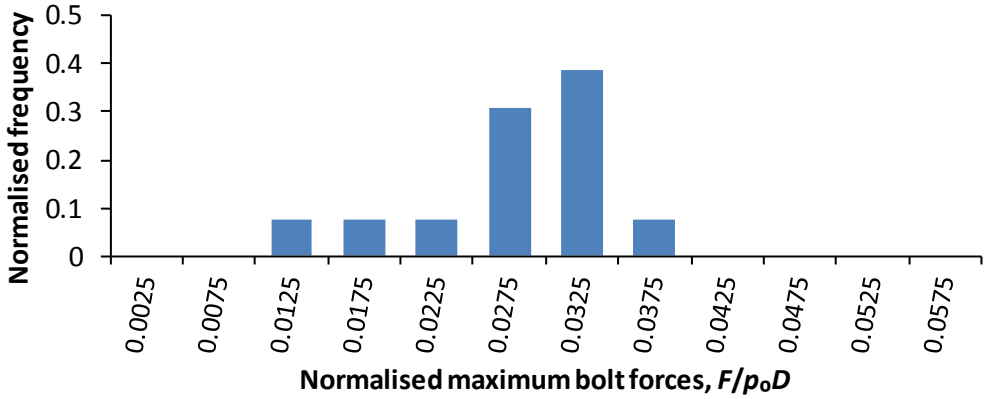

(c)

Fig. 5.32 (cont.)

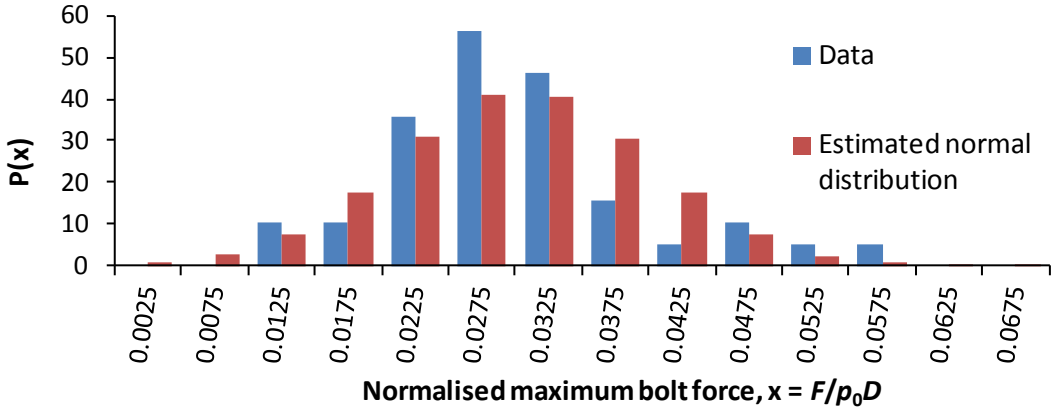

Fig. 5.33. Probability distribution of merged samples of maximum bolt forces, and estimated normal distribution with mean = 0.03 and standard deviation = 0.009.

analysed separately. One way is to calculate the confidence intervals for each statistical distribution. Alternatively, if a probability distribution is a function of a parameter χ, this parameter can be treated as a random variable and updated recursively using techniques such as Bayesian estimations (Montgomery & Runger, 2010). Bayesian estimation techniques can also take into account prior information of the ground obtained from previous projects in which the local geology is expected to be similar.

The use of the discussed mathematical techniques should not over-ride the significance of geology. For example, the geometry of the fractures in a granitic rock mass is different from the fracture geometry in limestone strata (cf. Hudson & Harrison, 1997).

5.4.6 Results with lining support only

For underground openings of which the main concern is the falling of rock blocks, lining is rarely used as the only support structure. It is normally used as secondary support together

with rock bolts. Nevertheless, in this section, parametric analysis was undertaken with lining support only (e.g. shotcrete) to show the influence of certain parameters which are not addressed routinely in design and in the literature; for example, the influence of rock-lining interface compliance and lining bending stiffness. An understanding of the influence of bending stiffness can help the engineer to design the lining cross-section. If reinforced concrete is used, an understanding of the effect of bending stiffness also helps the engineer to evaluate the consequence of cracking. Cracking is normally followed by a reduction in bending stiffness.

The results show that openings supported with compliant support (through a soft rock-lining interface) experienced displacement patterns which are smooth and continuous (see Fig. 5.34). The bending moment and shear force diagrams of the lining are reminiscent of soft ground tunnelling. The bending moment evolves smoothly around the tunnel, and is sagging at the crown and hogging at the invert under gravity loading (see Fig. 5.35). Here,

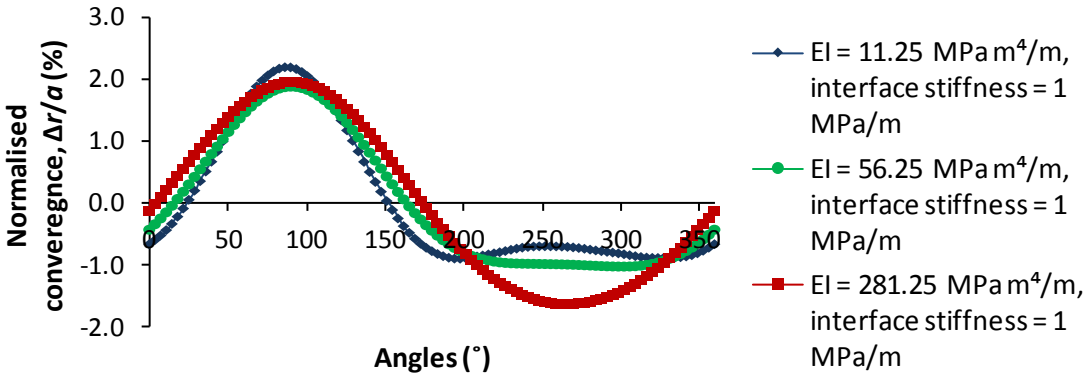

Fig. 5.34. Normalised displacement of a lining with soft contact interface for different bending stiffness

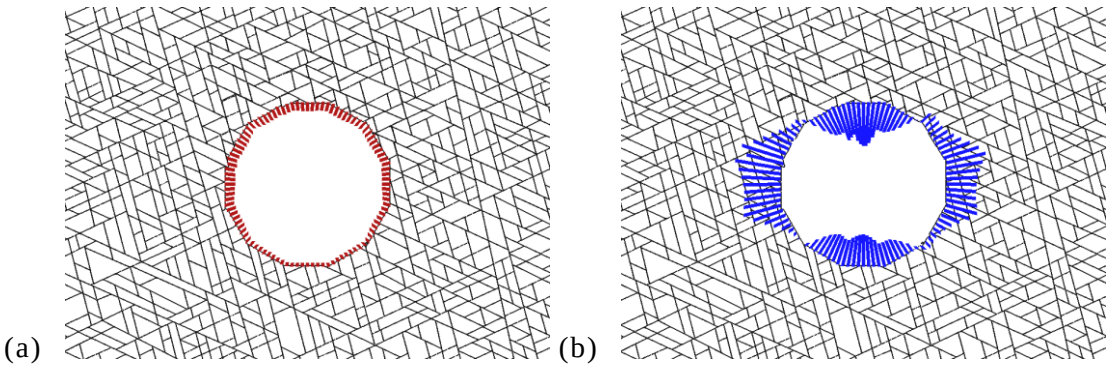

Fig. 5.35. (a) Hoop, (b) bending moment, (c) shear force diagram of lining for 1 MPa/m rock-lining interface and bending stiffness 56.25 MPam^4/m (note that the lining thickness is not displayed in the figures)

(c) 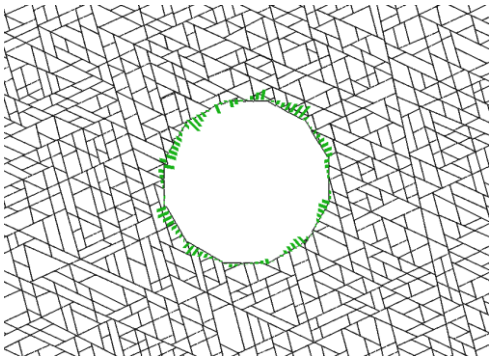

Fig. 5.35. (cont.)

displacements converging into the opening are taken as positive. Negative displacements were observed, mainly at the invert, suggesting that the lining deformed outward from its original configuration. This is possible because of the very compliant lining-rock interface, which permits the penetration of the lining nodes into the rock blocks. The higher is the bending stiffness, the greater is the penetration into the rock mass at the invert of the tunnel (see Fig. 5.34, p. 135).

For a stiff lining-rock interface, the openings experienced smaller displacements and the deformation mechanisms were different; every segment of the lining was forced to converge into the opening. Because the lining could no longer deform through "flattening" or "squashing" as in Fig. 5.34, the displacements did not follow an ordered deformation pattern about the tunnel axis. Rather, displacements and forces experienced local fluctuations (see Figs. 5.36 and 5.37). The fluctuations observed in opening convergence diminished with higher lining bending stiffness (Fig. 5.36). The negative displacements in

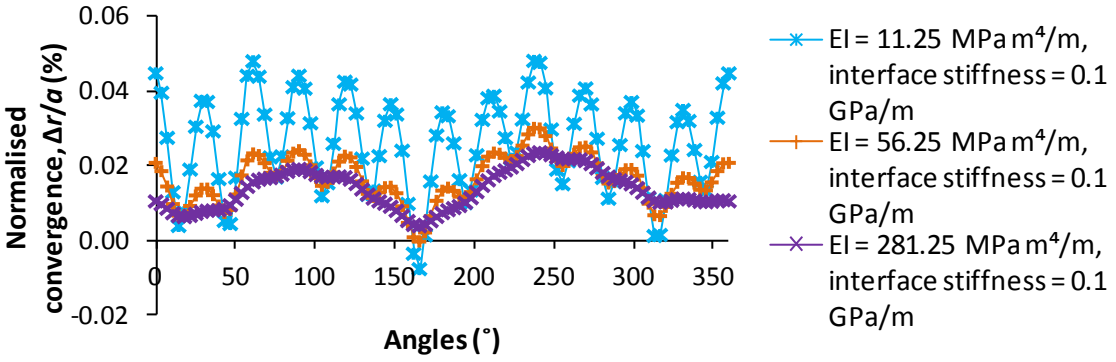

Fig. 5.36. Normalised displacement of a lining with hard contact interface for different bending stiffness

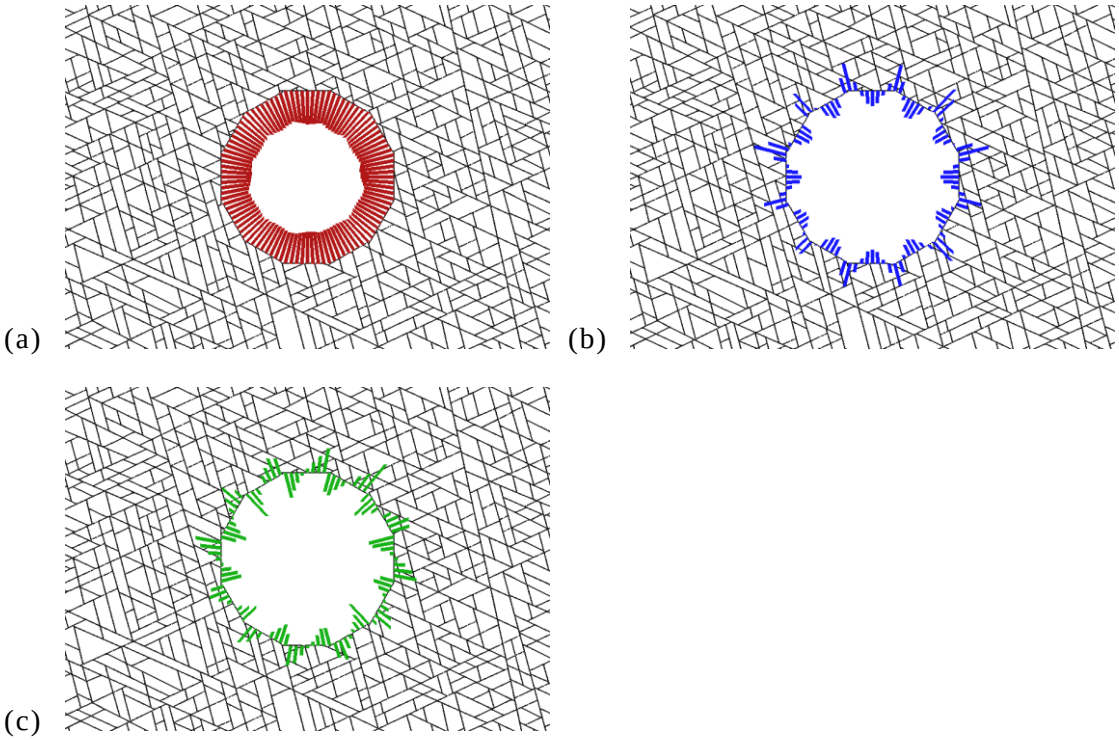

Fig. 5.37. (a) Hoop, (b) bending moment, (c) shear force diagram of lining for 0.1 GPa/m rock-lining interface and bending stiffness 56.25 MPam^4/m (note that the lining thickness is not displayed in the figures)

Fig. 5.36 were caused by local interface gaps between the rock lining and rock material. The use of grout is therefore warranted in practical situations to fill the voids at rock-lining interfaces, since the results suggest that interface imperfections generate stress/strain concentrations.

The results show that the interface stiffness between rock and lining is an important parameter which can significantly influence the convergence of an excavation opening. The influence of this parameter is investigated in more detail later in Section 5.4.7.

Figs. 5.38 (b) and 5.39 (b) show that, when the bending stiffness was reduced, the lining experienced smaller bending moments for both soft and hard rock-lining interfaces. Here, bending moments which are sagging inward into the opening are taken as negative. The result that the support load is proportional to the support stiffness is consistent with common engineering knowledge. The same trend was obtained by Steiner & Meier (1996) for openings subjected to anisotropic in-situ stresses using the closed-form equations proposed by Einstein & Schwartz (1979) for tunnel design. From the DEM analyses shown in Fig. 5.39 (a), the hoop forces were found to increase also with bending stiffness. This

finding is logical because a higher bending stiffness will impose larger constraints on lining deformations. This finding also agrees with the analyses conducted by Son & Cording (2007) using UDEC (Itasca, 2004) for an elastic rock mass without discontinuities.

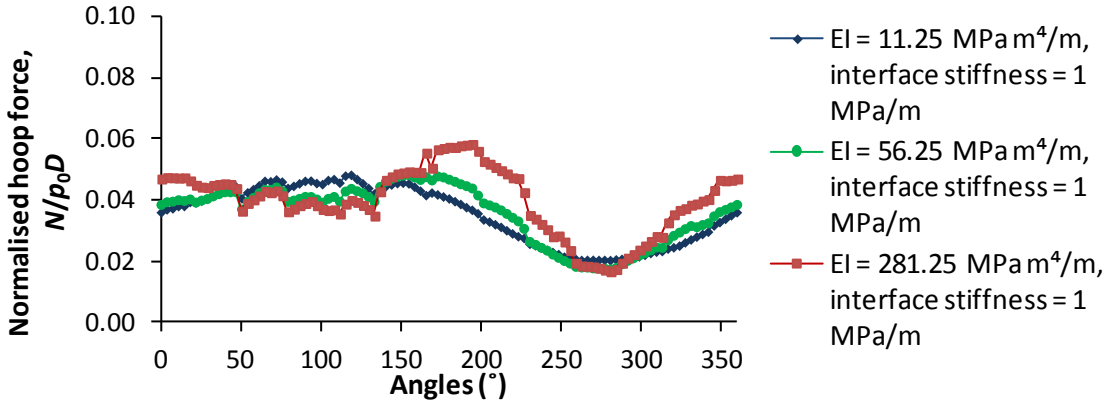

(a)

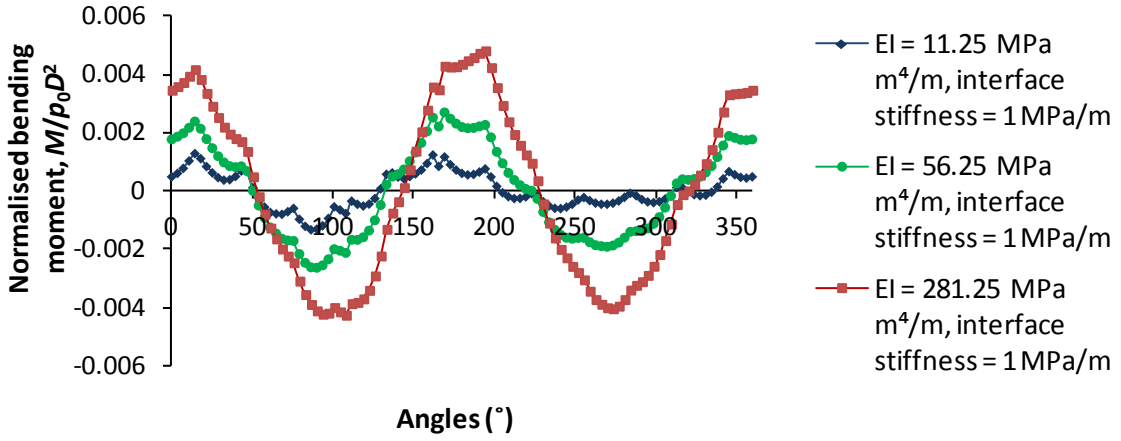

(b)

Fig. 5.38. (a) Hoop force and (b) bending moment of a lining with soft contact interface for different bending stiffness

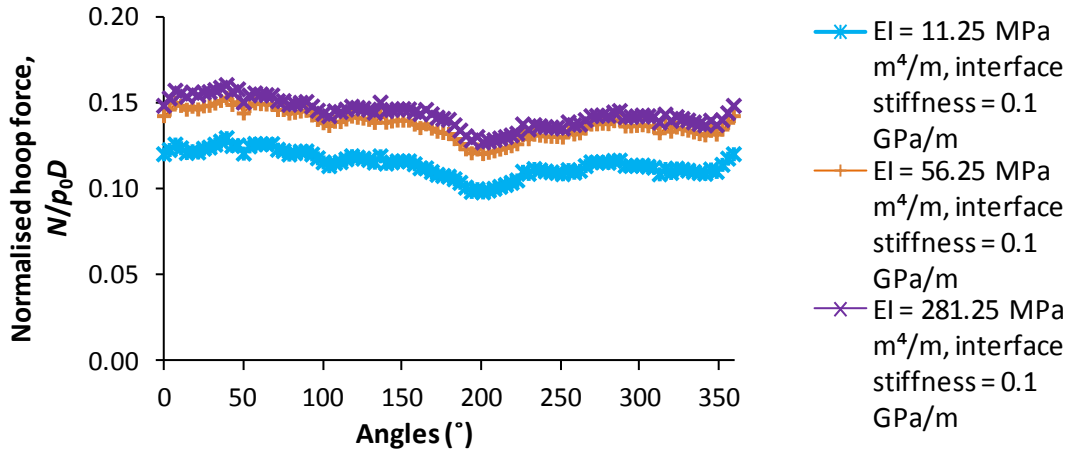

(a)

Fig. 5.39. (a) Hoop force and (b) bending moment of a lining with hard contact interface for different bending stiffness

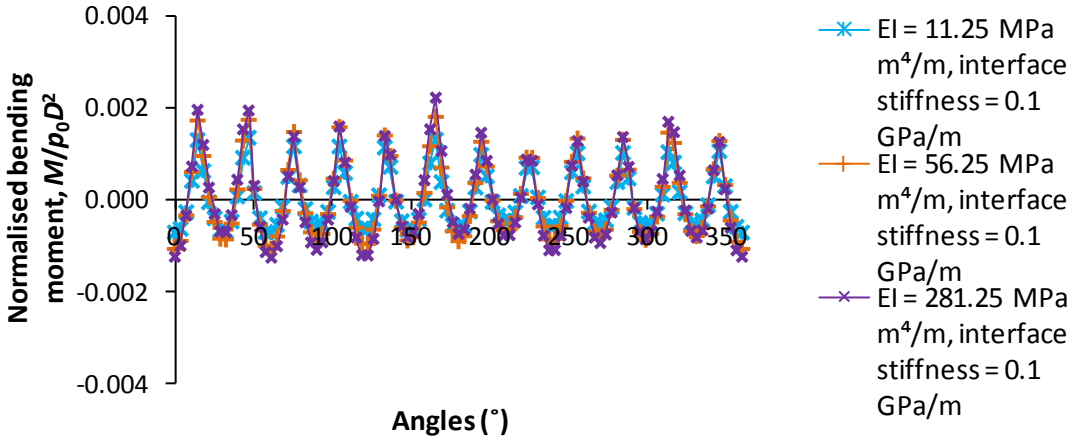

(b)

Fig. 5.39. (cont.)

The bending moments shown in Fig. 5.39 (b) contain repeating fluctuating patterns. This was found to be caused by approximating the circular opening as a polygon which is composed of straight segments (see Fig. 5.37 (b), p. 137). Twelve straight segments were used in the DEM models here. Using more straight segments will reduce the amplitude of the fluctuations but might increase its frequency. This numerical artifact does not manifest for large displacements, and the calculated bending moments are smooth (see Fig. 5.38 (b), p. 138). Note that localised fluctuating bending moments were also found in Vardakos et al. (2007), Chryssanthakis et al. (1997) and Bhasin et al. (1996). Here, an attempt to approximate a smoothed bending moment pattern from the original data was undertaken.

The bending moment pattern in Fig. 5.37 (b) (p. 137) is reminiscent of a framed structure subjected to uniformly distributed loads acting along its straight segments. From the bending moments obtained using the DEM calculations, the pressures acting on an equivalent circular lining were approximated using the procedures detailed in Appendix I. Based on the approximated pressure distribution, the bending moments of the lining were then calculated using the solutions for a ring structure detailed in Timoshenko & Young (1965). The smoothed bending moments juxtaposed against the original bending moments presented previously in Fig. 5.39 (b) are shown in Fig. 5.40 (a) and (b) for bending stiffness values of 281.25 MPa/m^4 and 11.25 MPa/m^4 respectively. Fig. 5.41 shows the bending moments in Fig. 5.39 (b) after smoothing.

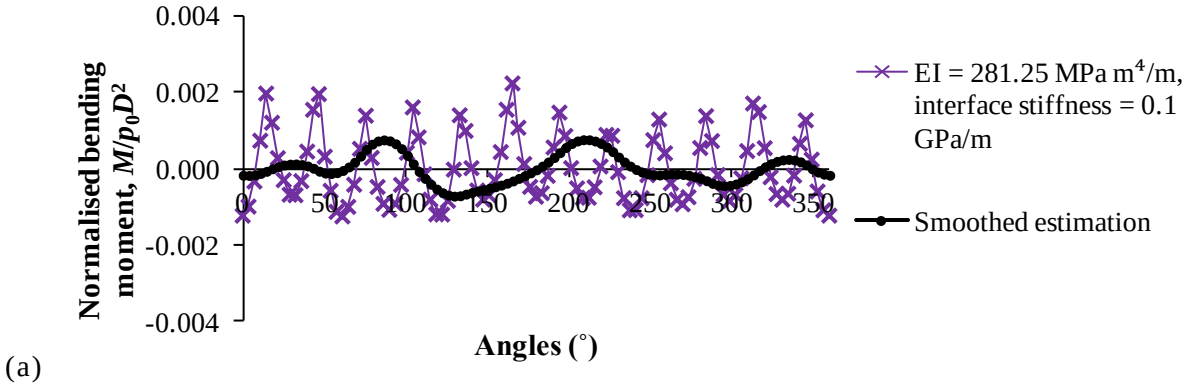

(a)

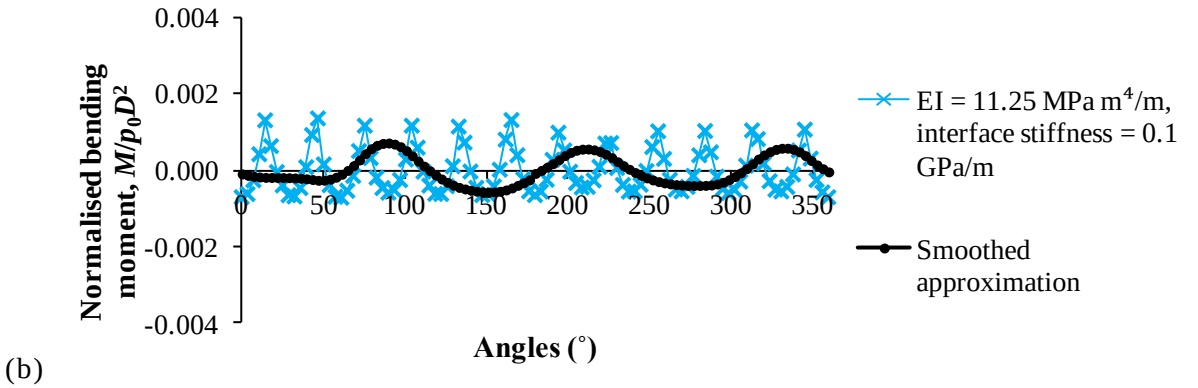

(b)

Fig. 5.40. Smoothing of bending moments using procedures in Appendix I for bending stiffness (a) 281.25 MPa m^4/m, (b) 11.25 MPa m^4/m (correction for the fluctuating bending moments caused by the polygonal approximation of a circular opening)

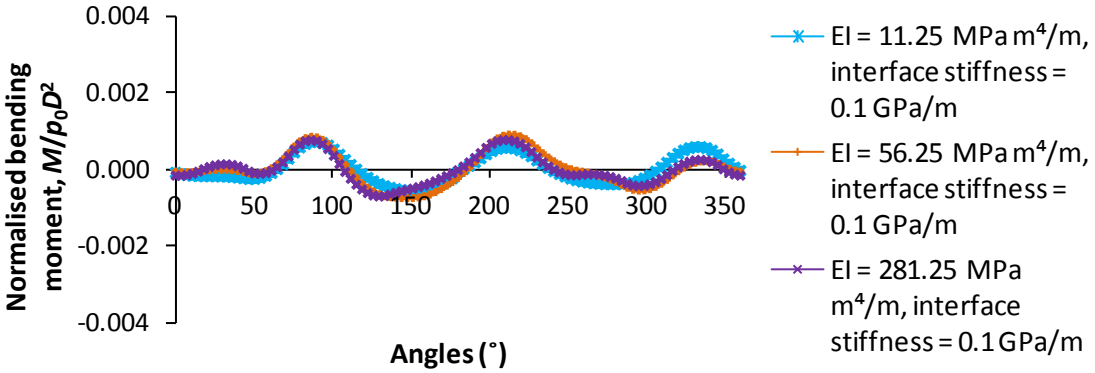

Fig. 5.41. Smoothed approximation of bending moments using methods in Appendix I

Note that in the DEM models presented previously, the boundary stresses were hydrostatic. For the case of isotropic pressure, the expected bending moment is nil. The scales of the vertical axes, with which the figures are drawn, could give a misleading impression that the bending moments are significant. To assess the magnitudes of bending moments obtained in the DEM models, the bending moments of a ring structure subjected to a vertical pressure of p_0 was used as a benchmark case (see Fig. 5.42 (a) and (b)), the solution of which can be found in Young et al. (2011).

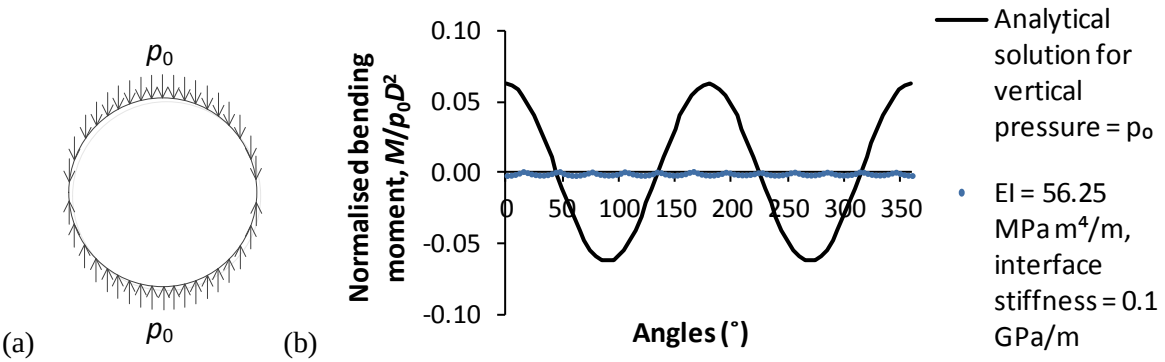

Fig. 5.42. Benchmark case for the magnitude of bending moments (a) illustration, (b) bending moment diagram for the benchmark case in comparison with one of the curves previously presented in Fig. 5.39 (b).

5.4.7 Verification of lining support against elastic solution

As was done for openings with rock bolt support, the DEM calculations for lining support were also verified analytically. The elastic solution for this boundary value problem with isotropic stresses can be derived from cavity expansion theory for an elastic medium, and by assuming that the opening is supported by a thin-walled cylinder (Crandall et al., 1978). This classic solution, however, will underestimate the convergence of the opening, even if the plastic displacements that take place in the simulations are negligible. Recall that, in the algorithm that is used to model the tunnel lining, the pressure on a lining node is derived from its penetration distance into a rock block (see Fig. 5.43). The elastic solution, therefore, needs to account for the deformability introduced at the lining interface in the DEM calculation, i.e. the overlap distance between the lining nodes and rock blocks.

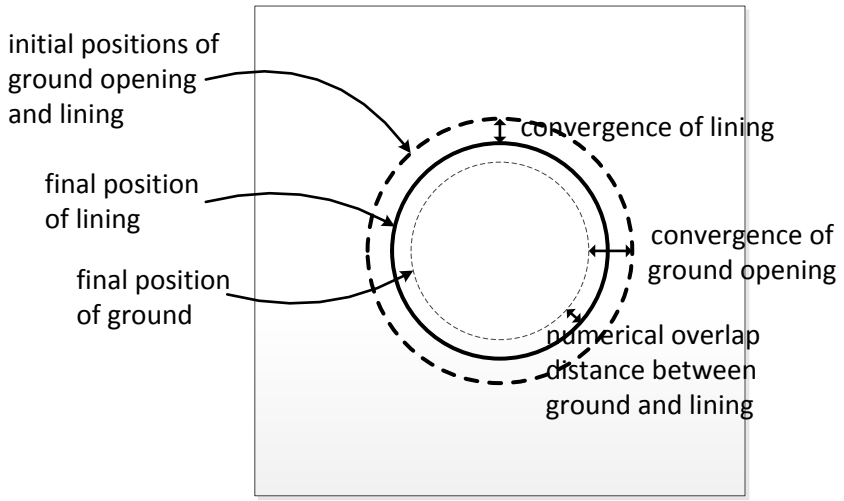

Fig. 5.43. Schematic showing the significance of lining-rock interface compliance

After accounting for the effect of interface stiffness, the hoop forces in the lining can be calculated as (see Appendix H for derivation):

$$N = \frac{p_0 E_L t K_L a}{2K_L G a + \frac{2E_L t G}{a} + E_L t K_L} \tag{5.14}$$

where E_L is the elastic modulus of the lining, K_L is the stiffness at the rock-lining interface, t is the lining thickness, a is the opening radius, G is the ground shear modulus and p_0 is the ground characteristic pressure. The shear modulus of the jointed rock mass in the DEM calculation was approximated using the same methods in Section 5.4.4 (Table 5.3, p. 129). Fig. 5.44 (a), (b) and (c) show the axial (hoop) forces registered at each lining beam element (in the DEM calculations) in comparison with the elastic solutions for three different lining-

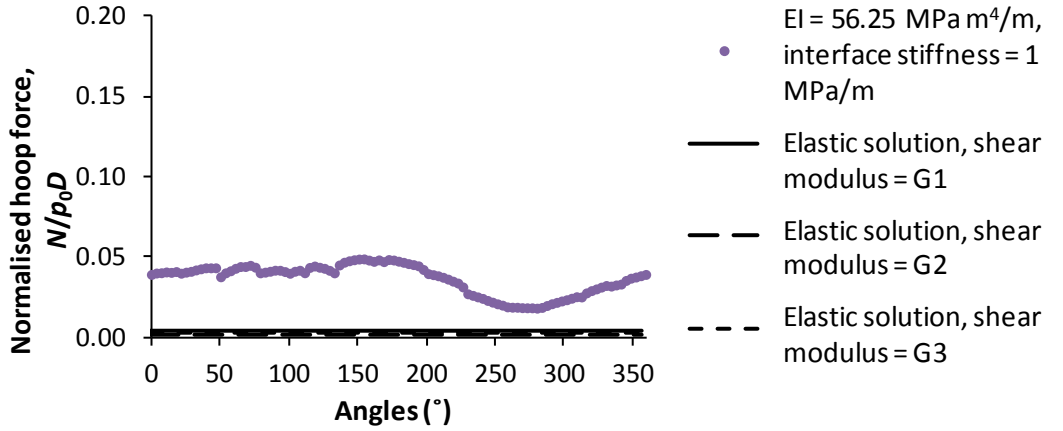

(a)

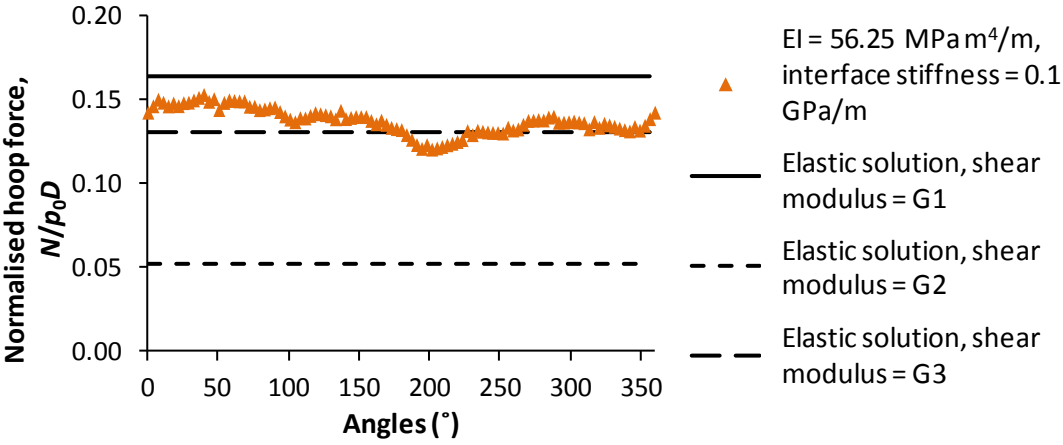

(b)

Fig. 5.44. Comparison between the elastic solution (Eq. (5.13)) for the lining hoop force and the beam forces registered between the lining nodes in DEM calculations for different lining-rock interface stiffnesses (a) 1 MPa/m, (b) 0.1 GPa/m, (c) 1 GPa/m. Shear moduli were estimated using approaches summarised in Table 5.3 (p. 129).

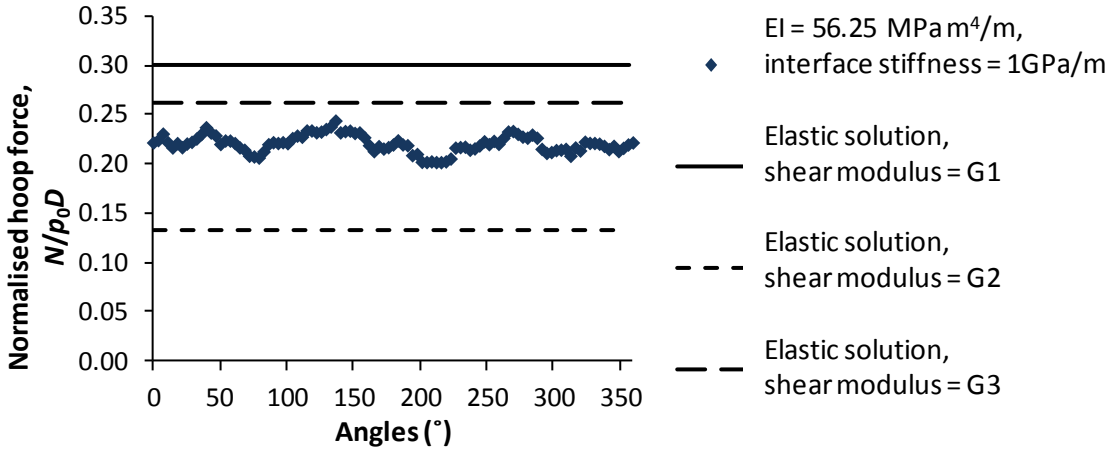

(c)

Fig. 5.44. (cont.)

rock interface stiffnesses, namely 1 MPa/m, 0.1 GPa/m and 1 GPa/m respectively.

The averaged values are plotted and compared for a wider range of interface stiffness in Fig. 5.45. The comparison is encouraging, in that the DEM solutions for large interface stiffness are bounded between the elastic solutions based on the estimated shear moduli (Table 5.3, p. 129). For low interface stiffness, the hoop forces calculated by the DEM simulations are higher than the elastic solutions. This is reasonable because, for soft interface stiffness, plastic displacements between the rock blocks may have taken place, thereby increasing the pressure on the lining.

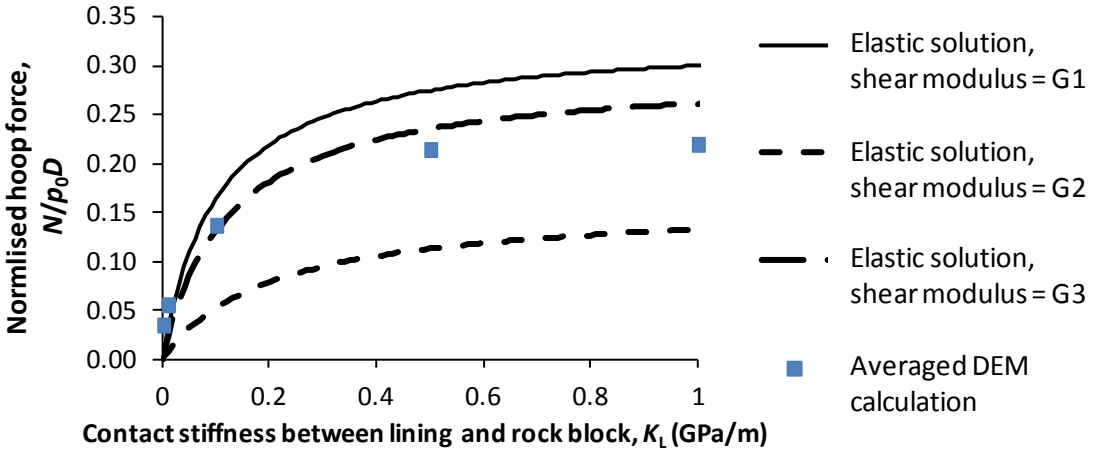

Fig. 5.45. Comparison between the averaged results of DEM calculations and the elastic solution (Eq. (5.13)) on the lining hoop forces for different lining-rock interface stiffnesses. Refer to Table 5.3 (p. 129) for shear moduli.

5.4.8 Results with both rock bolt and lining support

5.4.8.1 Influence of lining thickness with rock bolt support

It is of interest to the engineer to design the thickness of the lining based on engineering judgement without resorting entirely to empirical experience. The optimal lining thickness can be determined by comparing the effect of different lining thickness on the bolt forces and tunnel convergence. In general, a suitable support system should keep the bolt and lining forces below yield. As shown in Figs. 5.46 and 5.47, the opening convergence and bolt forces decreased, as the lining thickness increased. The hoop forces and bending moments of the lining increased correspondingly with the lining thickness (see Figs. 5.48 and 5.49). In this example, the benefit of introducing 10 cm lining to an unlined opening is significant, reducing ground convergence by almost half (see Fig. 5.47). A subsequent increase in lining thickness reduced the opening convergence, but to a lesser extent. From a cost-benefit viewpoint, a 10 cm lining can be considered as favourable in this example, unless a smaller convergence is desired.

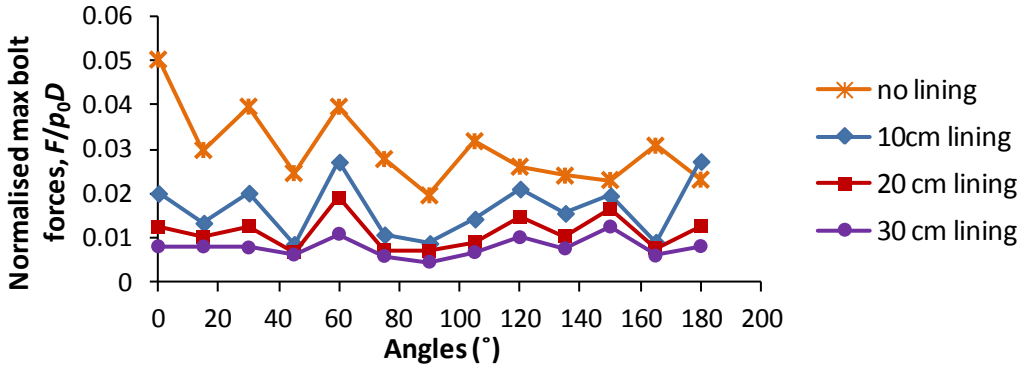

Fig. 5.46. Bolt forces for different lining thickness (4 m bolt length, 15° spacing)

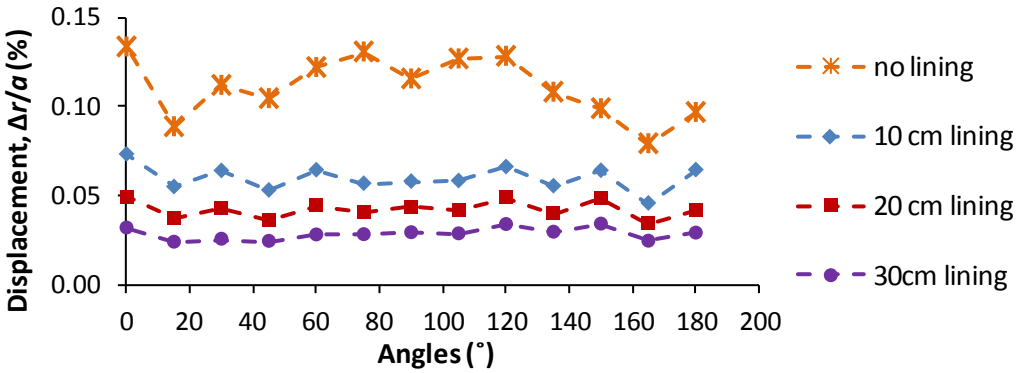

Fig. 5.47. Displacements for different lining thickness (4 m bolt length, 15° spacing)

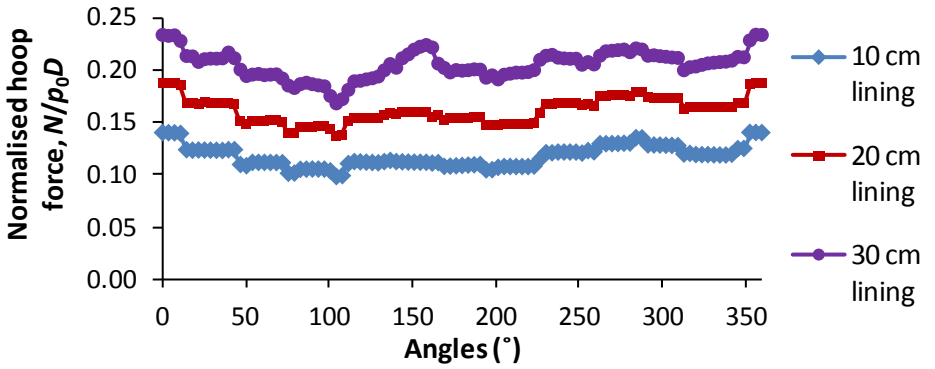

Fig. 5.48. Lining hoop forces for different thickness (4 m bolt length, 15° spacing)

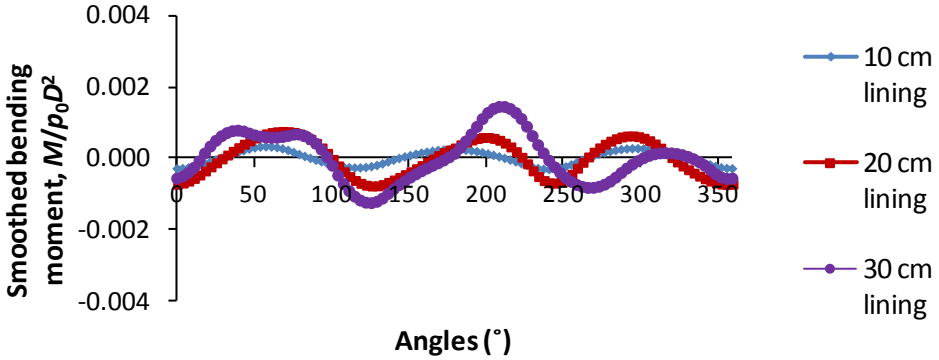

Fig. 5.49. Lining bending moments for different thickness of lining (4 m bolt length, 15° spacing) (smoothed approximation using procedures in Appendix I)

5.4.8.2 Interaction diagram as a design tool

The design of support consisting of both rock bolts and lining is not straightforward, since there are two ways by which the ground convergence can be controlled, either by installing more rock bolts or by increasing the lining thickness. The design procedure discussed in the previous section attempts to find an optimal lining thickness, beginning from a particular rock bolt configuration. Conversely, it is possible also to start with a target lining thickness and work out the optimal rock bolt pattern. If either of the two procedures is repeated for different combinations of lining thickness and rock bolt spacing, the results can be visualised using an interaction diagram, with contours of tunnel convergence, as shown in Fig. 5.50. The diagram (Fig. 5.50) has the normalised lining axial stiffness along the bottom horizontal axis, and the lining thicknesses, which are used to derive the stiffness values, along the top horizontal axis. Likewise, the normalised bolt axial stiffness is on the left vertical axis, and the corresponding rock bolt spacing is on the right. Cases in which failure had occurred are marked with red circles (Fig. 5.50). From this interaction diagram, the engineer can judiciously make an economical design decision, by gauging the effectiveness of introducing

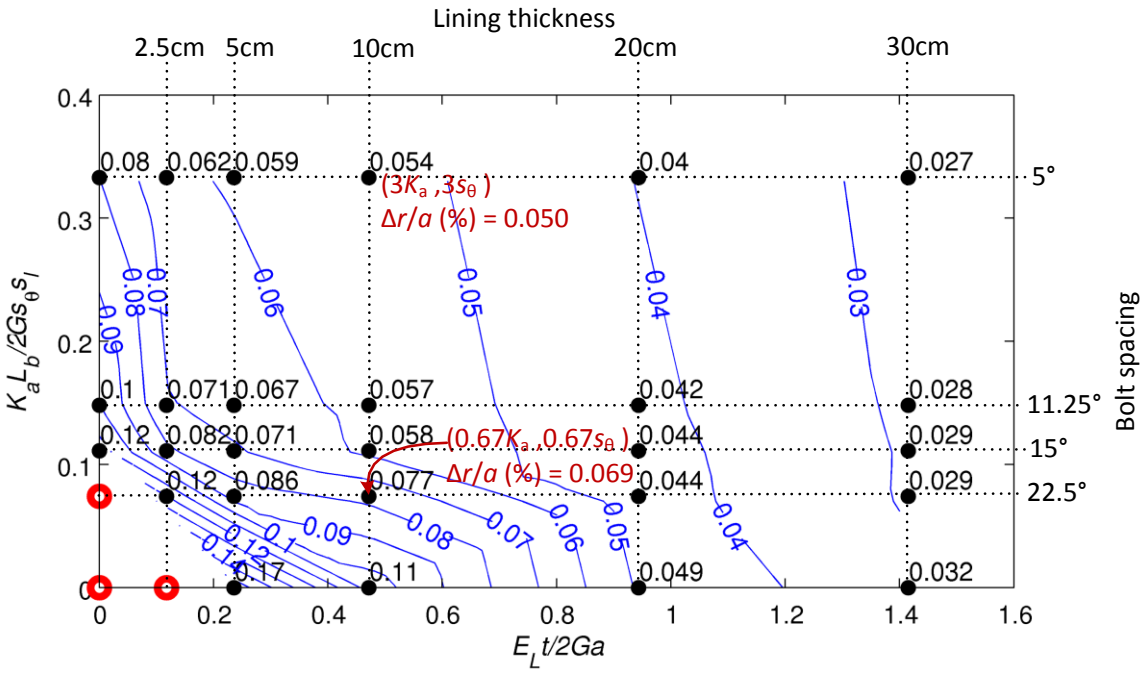

Fig. 5.50. Interaction diagram showing contours of convergence $\Delta r/a$ (%) at the crown for different combinations of lining thickness (horizontal axis) and bolt spacing (vertical axis). Red circles denote failure.

an "increment" of rock bolt support or lining support. Although, in this thesis, this technique is illustrated for the case in which the opening is wished-in-place, it can be replicated for cases in which the support is installed after a presupposed traction loss at the opening, so that the effects of tunnel face advancement are considered (Vardakos et al., 2007). The interaction diagram in this example (Fig. 5.50) suggests that for lining thickness of 20 cm and greater, the support contribution of rock bolts are marginal and the ground convergence will be resisted mainly by the lining. In this example, the lining thickness is selected to be 10 cm and the rock bolt spacing to be 15° because there is a good compromise between their relative contributions to resisting tunnel convergence. Note that the concept of the interaction diagram could also be used to examine the influence of other variables.

5.4.8.3 Influence of rock bolt stiffness (steel grade or diameter of rock bolt)

Like any other composite material, the load distribution between the materials depends on their relative stiffness. Therefore, if the stiffness for the rock bolts is reduced, the bolt forces will reduce correspondingly (see Fig. 5.51 (a)); and the loads (hoop forces and bending moments) on the lining will in turn increase, as shown in Figs. 5.52 and 5.53. In this

example, the introduced changes in bolt stiffness (⅔ K_a and $3K_a$) influenced the tunnel convergence and lining loads only very slightly.

An estimate for changing the stiffness values can be obtained from the interaction diagram plotted in terms of dimensionless groups. Note that the dimensionless bolt axial stiffness depends on both the bolt spacing and bolt stiffness, and it is possible for two different bolt configurations to have the same dimensionless value. The results which are obtained from using these two different bolt stiffness values (⅔ K_a and $3K_a$) are plotted in the interaction diagram in Fig. 5.50 (p. 146, annotated in red). The final design should,

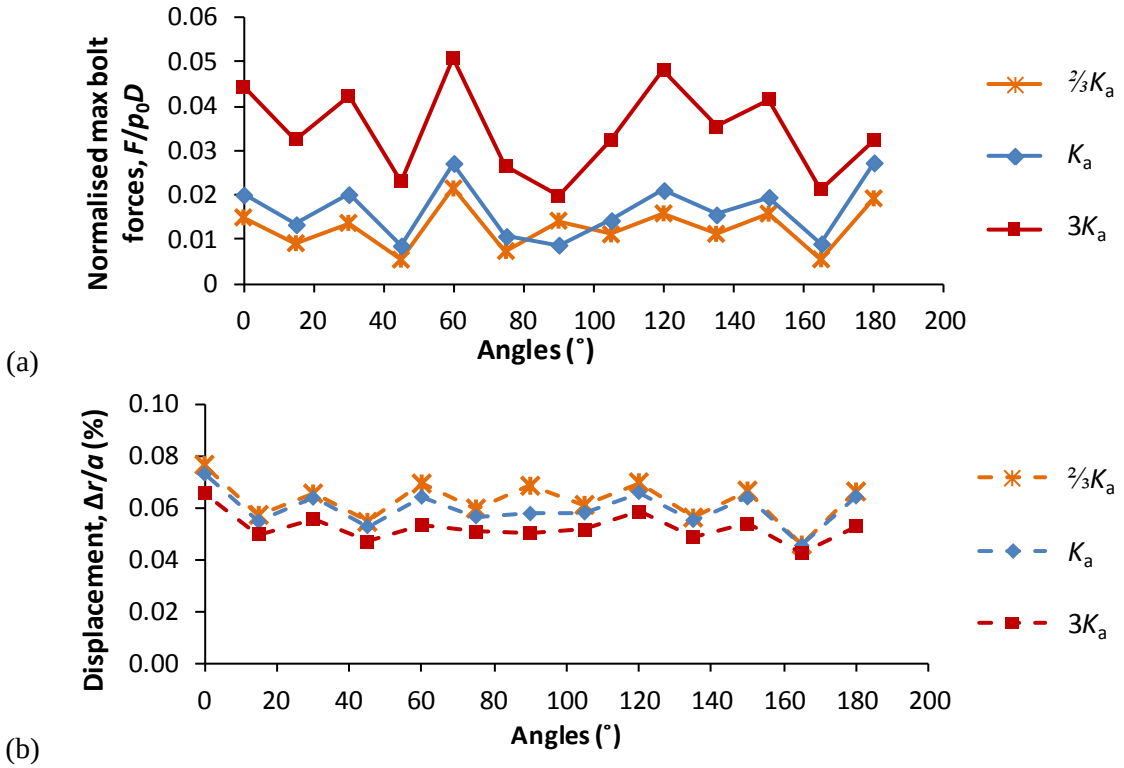

Fig. 5.51. Bolt (a) forces (b) displacements for different bolt axial stiffness (4m bolt length, 15° bolt spacing, 10 cm lining)

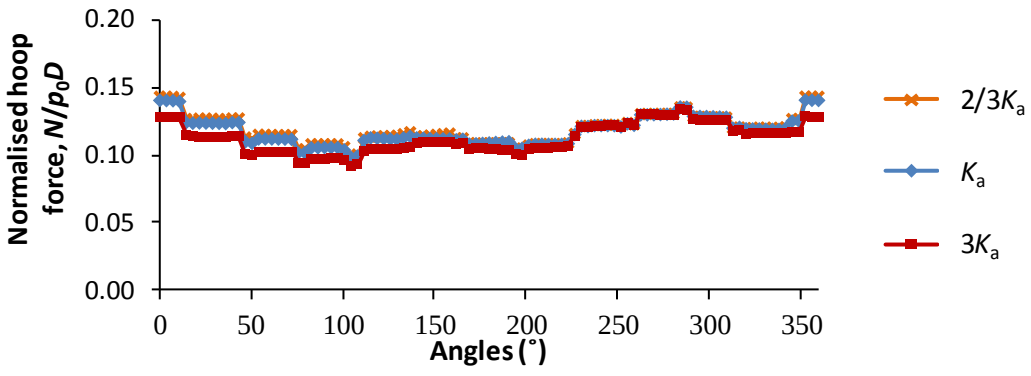

Fig. 5.52. Lining hoop forces for different bolt axial stiffness (4m bolt length, 15° bolt spacing, 10 cm lining)

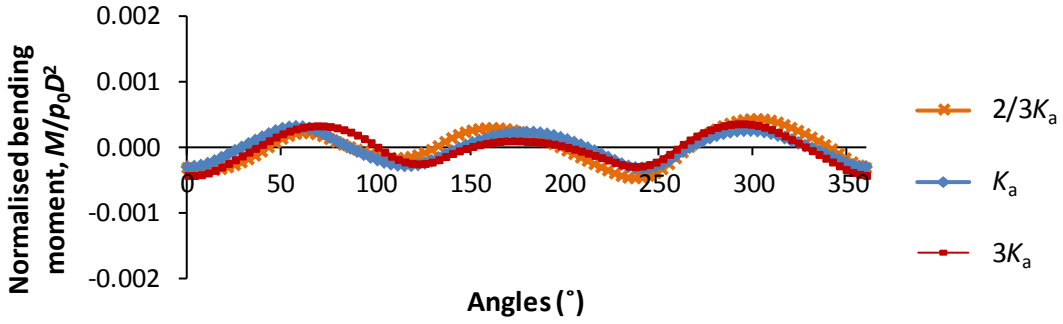

Fig. 5.53. Lining bending moments for different bolt axial stiffness (4m bolt length, 15° bolt spacing, 10 cm lining) (smoothed approximation using method in Appendix I)

nonetheless, be verified against actual numerical simulations because the errors arising from using this method of estimation can be significant, particularly at support levels for which the ground convergence is sensitive to support contributions, i.e. a smaller gap between convergence contour lines in the interaction diagram (Fig. 5.50, p.146).

5.4.8.4 Influence of in-situ stresses

The numerical tools can also be used to examine the effects of uncertainties or local variations of geology obtained from site investigations. For example, variation of in-situ stresses, variation in cover depth, or local weak faults. In cases where the water table is anticipated to submerge the opening during heavy rainfall, inflow of water should be taken into consideration. Figs. 5.54 – 5.56 show the influence of in-situ stresses on the rock bolts and lining respectively. The trend for displacements is clear. For the horizontal-to-vertical stress ratio, K_0 = 0.5, the crown experienced larger displacements compared to the springing (see Fig. 5.54 (b)). In contrast, for K_0 = 1.5, the springing experienced larger displacements. For the case of anisotropic in-situ stresses in this example, the bolt axial forces (Fig. 5.54 (a)) were close to those of the hydrostatic case. It is important to emphasise that this observation on the bolt forces is not universal and may be true only for this particular numerical setup/model. The results of the lining hoop forces are interesting. For K_0 = 1.5, the portion of lining parallel in the direction of higher ground stresses experienced larger hoop forces (see Fig. 5.55). The results indicate that the models are capable of capturing the influence of in-situ stresses. Note, however, that the principal stresses in rock masses do not necessarily align along the vertical and horizontal directions (Hudson & Harrison, 1997).

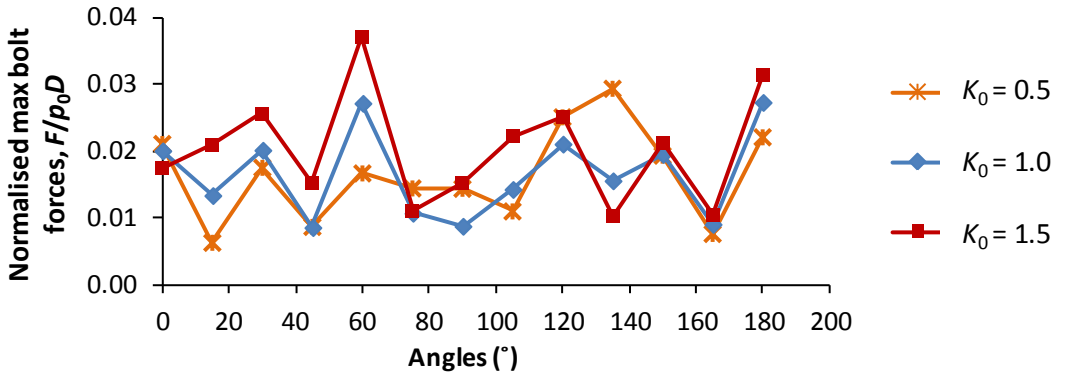

(a)

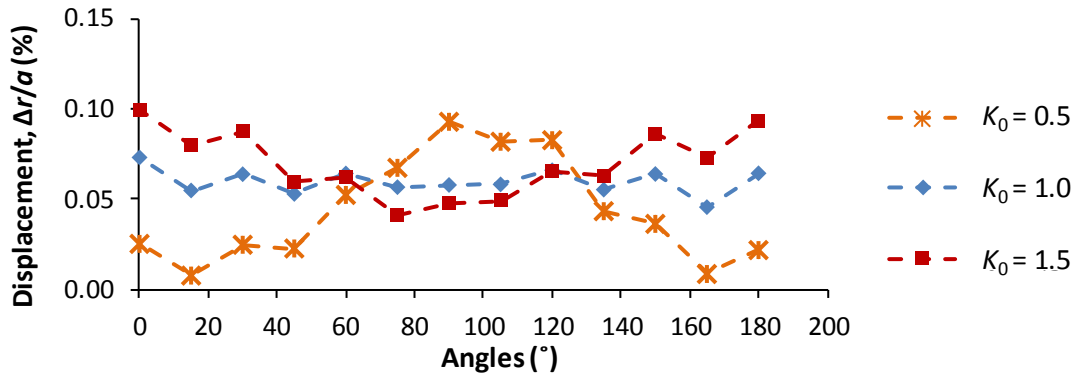

(b)

Fig. 5.54. Bolt (a) forces and (b) displacements for different in-situ stresses K_0 (4m bolt length, 15° bolt spacing, 10 cm lining)

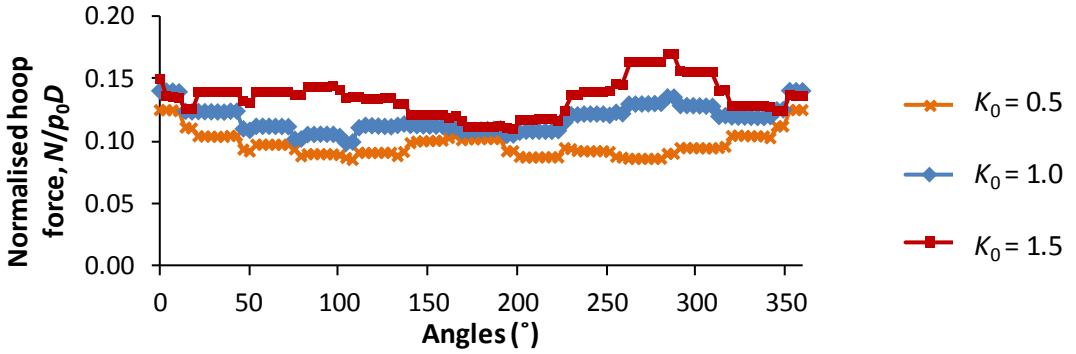

Fig. 5.55. Lining hoop forces for different in-situ stresses (4m bolt length, 15° bolt spacing, 10 cm lining)

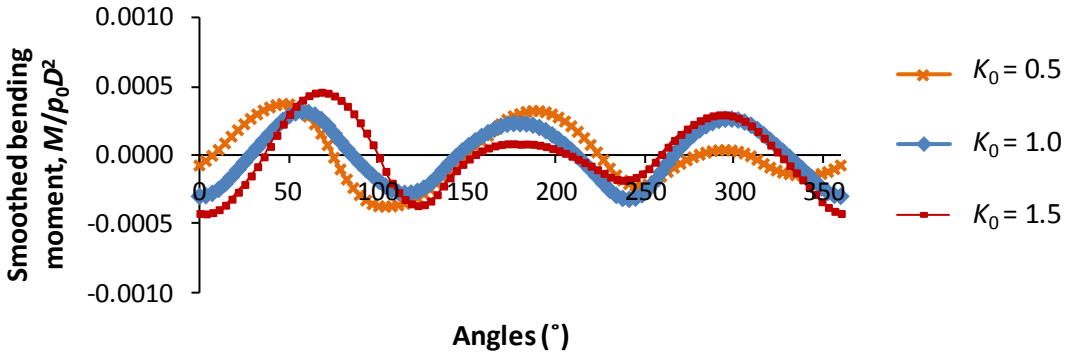

Fig. 5.56. Lining bending moment for different in-situ stresses (4m bolt length, 15° bolt spacing, 10 cm lining) (smoothed approximation using procedures in Appendix I)

5.5 CONCLUDING REMARKS

This chapter has shown that the numerical tools proposed in Chapter 3 can be used to model underground openings in jointed rock masses. When used together with rock support algorithms, the tools can be used to examine important parameters for tunnel design, such as the rock bolt length and spacing, and the lining thickness. DEM simulations of openings with rock bolt support only or lining support only were verified against elastic solutions proposed in the literature. The comparison is encouraging, suggesting that these numerical tools are robust. Because of the large number of variables which could affect the performance of an actual underground excavation, the conclusions derived from the simulations are unlikely to be universal. The chapter also demonstrates how the tools could assist engineers in designing tunnel support. The procedure begins with an estimated bolt diameter. Using the supposed bolt stiffness (for this particular diameter), simulations can be carried out to find the optimal length and spacing. Different lining thicknesses can then be modelled together with this optimal bolt spacing, and the most economic thickness which gives rise to acceptable stresses and displacements is selected. To examine more rigorously the relative benefit of introducing more rock bolts or increasing the lining thickness, the concept of an interaction diagram was illustrated. Together with the numerical tools proposed in Chapter 3 (and the rock support algorithms), the interaction diagram can facilitate the engineer to select the optimal bolt spacing and lining thickness. For this bolt and lining support configuration, if a different bolt diameter is considered more suitable, the simulations should be repeated with the updated bolt stiffness. Finally, checks against stress variability or other adverse conditions should be undertaken to ensure that the design is robust under these circumstances. Overall, the numerical tools were shown to be capable of examining the influence of various parameters governing the performance of supported underground openings – this is of greater practical interest by comparison to the simpler models examined in Chapter 4.

CHAPTER 6
A CASE STUDY: VAIONT ROCK SLIDE

In the previous chapter, the numerical tools were used to model a generic rock engineering problem. In this chapter, a study of a well-known case history is undertaken. The purpose is to show that the numerical tools are capable of modelling specific geological detail and obtaining insights concerning the performance of a practical problem through parametric analyses of geometrical and physical parameters. In many projects, the performance of the supposed geotechnical structure could be influenced by numerous parameters: it is of interest to the engineer to identify the important parameters through parametric analyses, so that resources can be allocated judiciously for site investigation. Here the 1963 Vaiont rock slide is studied, from which useful insights concerning the stability of this rock slope are obtained. Parametric analyses were carried out in 2-D to investigate the influence of variables which have not been studied previously in detail. Finally, the results of 3-D simulations are presented, showing that these models are capable of capturing three-dimensional geological detail, the influence of which can be important in rock slope stability.

6.1 INTRODUCTION AND LITERATURE REVIEW OF THE CASE HISTORY

6.1.1 Background of the case history

The Vaiont Dam was constructed in Italy in 1925. The dam was sited at the downstream of the Vaiont River. The location was chosen because of the solid Dogger formation and sound Jurassic limestones of the Calcare del Vaiont (Semenza & Ghirotti, 2000). The dam spans a very deep narrow gorge in the Vaiont Valley and has a height of 265 m and chord length of 160 m. It was designed for a water storage level of 722.5 m a.s.l. The base of the river was approximately 465 m a.s.l. (see Figs. 6.1 and 6.2). On 9 October 1963, when the resevoir level was about 700 m above sea level, an estimated rock mass volume of 200 - 300 million m^3 slid off from the toe of Mount Toc into the reservoir at an estimated speed of 30 m/s (around 110 km/ hour). The slide happened close to the dam and extended to as far

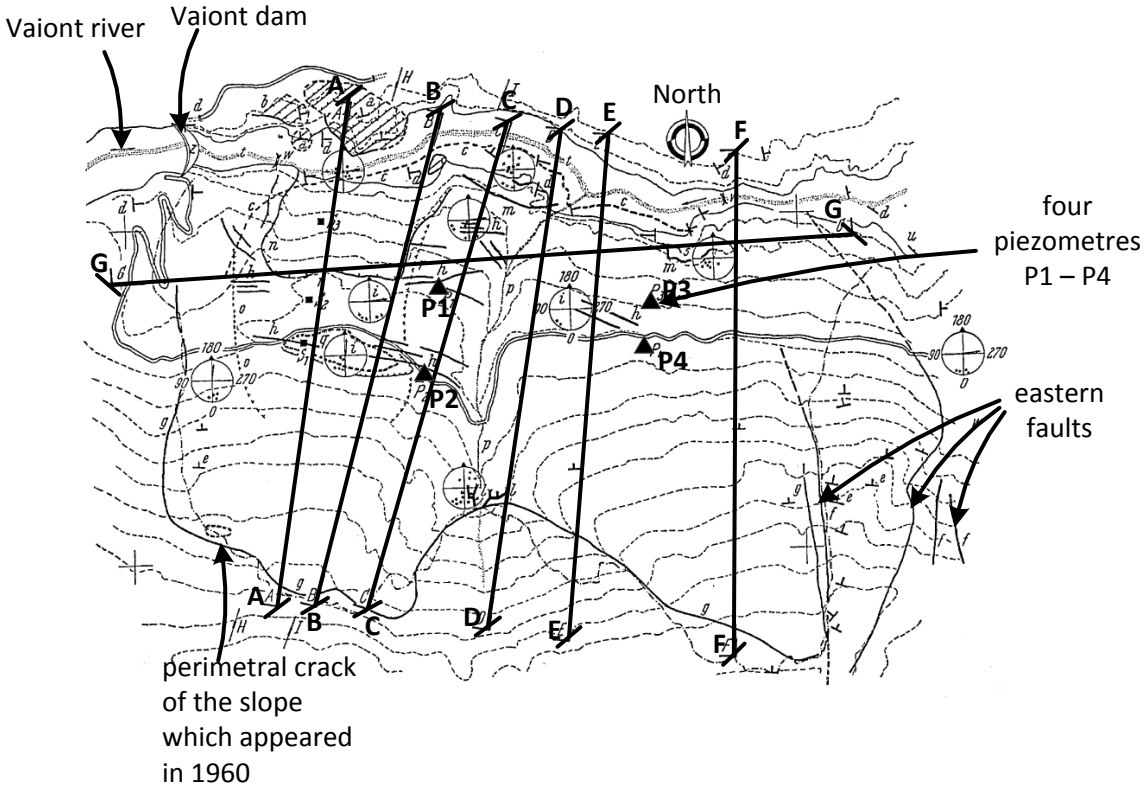

Fig. 6.1. Plan view of Vaiont slope (modified after Fig. 5 in Broili, 1967, with kind permission from Springer Science and Business Media).

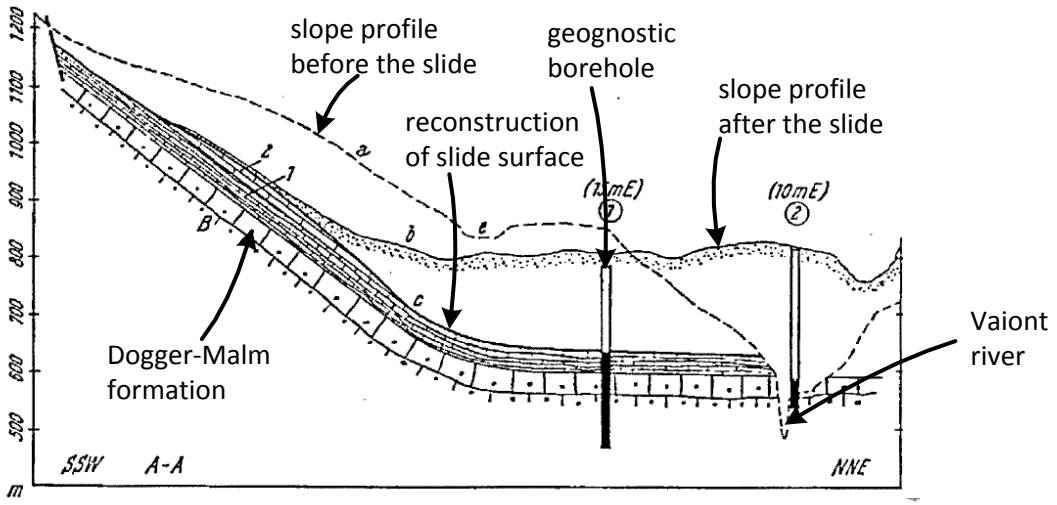

Fig. 6.2. Western end of slope, viewed from the East, section A-A of Fig. 6.1 (modified after Fig. 9 in Broili, 1967, with kind permission from Springer Science and Business Media). For annotation see Fig. 6.3 (p. 155).

as 1800 m upstream (East-West direction in Fig. 6.1). The slide surface reached an elevation of 1400 m a.sl. and as far as 1600 m away from the shores of the lake (Jaeger, 1972).

This catastrophic event was a structural success because the dam was not damaged by the rock slide. But water from the reservoir overtopped the dam and flooded the Piave

Valley. The small town of Longarone was destroyed and 2500 lives were lost. There are numerous publications on the rock slide, and interested readers are encouraged to refer to the original publications of the investigators (Müller, 1964; Müller, 1968; Müller; 1987; Broili, 1967; Belloni & Stefani, 1987; Hendron & Patton, 1985; Semenza & Ghirotti, 2000).

6.1.2 The warning signs and mitigation measures prior to the slide

In 1959, prior to the catastrophic slide on 9 October 1963, geological investigations were undertaken, and several relics of an ancient landslide were visually identified (Semenza & Ghirotti, 2000). The elevation of the ancient failure surface was thought to be at approximately 600 m a.s.l. These observations led to field investigations including boreholes, seismic surveys and daily measurements on the slope movement. The reservoir water level was raised nonetheless. By the end of October 1960, when the lake level reached more than 600 m a.s.l., the movement rate was 30 mm/day, and a continuous crack 1 m wide and 2.5 km long appeared. This observation confirmed the ancient landslide was likely to be reactivated. On 4 November 1960, when the lake level was at about 650 m a.s.l., approximately 0.7 million m^3 of material at the western end of the slope slid into the lake. The water level was then lowered to 600 m.

Müller, the engineer entrusted to study the problem, thought that it was not possible to arrest the slide completely, but its velocity could be reduced. He suggested to increase the reservoir level in a controlled manner. In October 1961, after the construction of a bypass tunnel was completed, the level of the lake was gradually increased. In December 1962, it reached a level of 700 m a.s.l, 50 m higher than the first filling. The velocity of the movement, however, was only 15 mm/day, which was less than the velocity at the first resevoir filling. The lake level was gradually lowered and reached 650 m a.s.l. in March 1963. Müller formulated a hypothesis that the slope movements were due to the saturation of materials. During the first filling, the material was inundated by water for the first time, and therefore the slope underwent larger movements. According to his hypothesis, subsequent filling of the reservoir would be less severe compared to the previous filling. The next raising of the water level began in April 1963. Low velocity was initially registered. At the end of August 1963, a level of 710 m was reached and the velocity of the

movements was 20 mm/day. The lake was lowered in September, with the purpose of slowing the slope movement, but the velocity underwent a rapid increase till the large slide on 9 October 1963.

6.1.3 Geological features

The key feature of the slope of Mount Toc is its "chair" shaped structure. The chair shape of the slope can be viewed clearly from the dam which is to the west of the slope (see Fig. 6.1, p. 152, for the position of the dam relative to the slope). The cross-section of the western end of the slope is shown in Fig. 6.2 (p. 152). The failed slope can be characterised using an M-shape geometry (see Fig. 6.1, p. 152, for plan view), and a non-circular, chair-shaped slip surface (see Fig. 6.2, p.152). The rock strata consist of several limestone formations. The slide material consists of the Lower Cretaceous and Malm formations, which slid over the underlying Dogger-Malm formation (see Fig. 6.3 for geological description). It is important to highlight that clay was found along much of the sliding surface (Hendron & Patton, 1985), contrary to initial publications on the rock slide by Müller (1964). According to Hendron & Patton (1985), the clay layers are stratigraphically continuous, and are 1 to 2 cm thick on average, but vary from 0.5 to 10 cm or greater. The eastern end of the slide is bounded by geological faults (see Fig. 6.1, p. 152). Detachment of the failed mass from the eastern fault has been found by numerous investigators (Broili, 1967; Hendron & Patton, 1985). The cross-section of the rupture surface perpendicular to the sliding direction is characterised by a bowl-shape structure (see Fig. 6.3). On the eastern end of this section, there is angular discordance in terms of geological strata, which is characterised by the breaking of rock mass across bedding planes (Broili, 1967; Hendron & Patton, 1985) (see Fig. 6.3). According to Hendron & Patton (1985), the east end of this rupture surface is ladder-shaped.

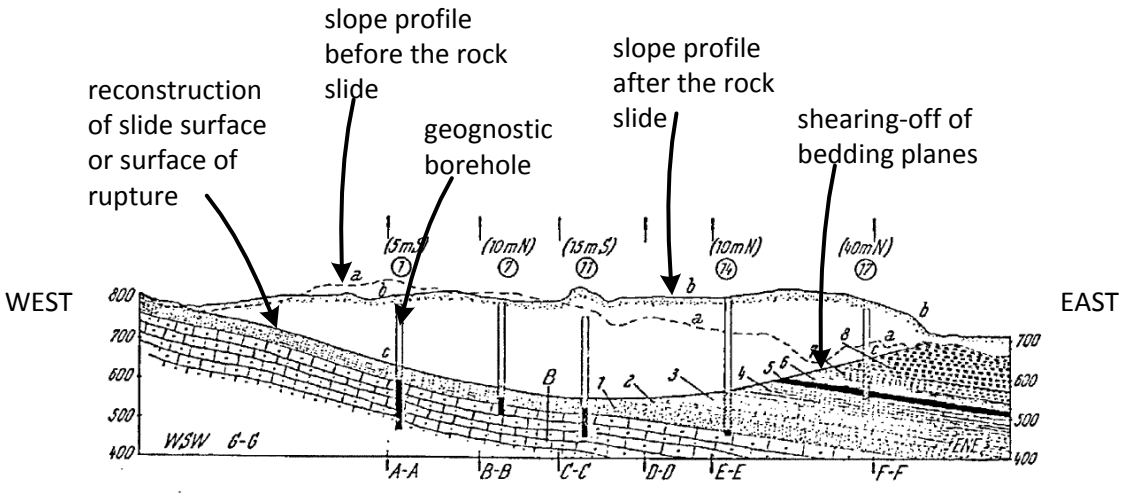

Fig. 6.3. West-East section of slide surface. Section G-G in Fig. 6.1 (modified after Fig. 11 in Broili, 1967, with kind permission from Springer Science and Business Media). B - Oolitic limestone (not involved in the slide); 1 – grey limestone bearing nodules or beds of dark chert; 2 – compact limestone, often greyish or reddish with nodular structure; 3 – greyish to blue limestone bearing nodules or beds of chert, intercalated with marly limestone; 4 – greenish or pink limestone bearing nodules or beds of chert, intercalated with marly limestone; 5 – brecciated limestone, intercalated with marly limestone; 6 – greyish or pink, sometimes marly limestone; 7 – greyish and brecciated limestone bearing nodules or beds of chert; 8 – greyish and reddish limestone, bearing nodules of chert; a – topographic surface before the slide; b – topographic surface after the slide; c – reconstructed surface of rupture and sliding; e – depression of the "seat" area.

6.1.4 Summary of literature review and interesting observations

A review of the literature was carried out. The strength parameters suggested by the literature for the slide surface and rock mass are summarised in Tables 6.1 – 6.3. Table 6.1 lists the strength parameters which were deduced from laboratory experiments; Table 6.2 lists the estimated strength parameters adopted by the investigators for their stability or velocity analyses; Table 6.3 shows the strength parameters calculated by various investigators from back analyses.

A noteworthy observation from the literature review is that, from two-dimensional analytical and numerical calculations by numerous investigators, the estimated critical sliding friction angles were significantly higher than the residual friction angle of the wet clay layer measured at the slide surface, $\phi_{calculated}$ = 17 - 23° against $\phi_{measured}$ = 6 - 10° (compare between Table 6.1 and Table 6.3). Hendron & Patton (1987) suggested that this discrepancy is due to three-dimensional effects, since the additional side resistance afforded

by the eastern boundary of the slope cannot be captured in 2-D analyses. On the other hand, Alonso & Pinyol (2010) showed that the slide surface friction angle at failure could reach values as low as 12° based on a simplified model consisting of a pair of interacting wedges; the active and passive wedges were separated by an inclined shear plane located at the bend of the chair-shaped slope. The analysis was carried out on a less critical 2-D cross-section because they considered it to be more representative of the slope. However, it can be argued that the choice of a less critical section was an indirect admission of the significance of three-dimensional effects; the more stable adjacent sections were assumed to be able to provide additional resistance to the more critical sections. Moreover, the assumption of the boundaries between the active and passive wedges (i.e. inclination of the shear plane), and also the friction angle along the shear plane may be non-conservative.

Another interesting phenomenon is the velocity of the slide, which was estimated as approximately 30 m/s (around 110 km/hour). In most slope failures, the slope would self-stabilise as more mass accumulates at the toe during the slide. Instead, the failed mass slid 300-400 m across the deep gorge and rose more than 100 m on the opposite bank (Jaeger, 1979). The high slide velocity has been explained in terms of strength loss along the slide surface; the first explanation offered in the literature is that frictional loss was caused by thermo-poro-mechanical effects at the clay layer due to heating (Voight & Faust, 1982; Vardoulakis, 2002), while the second is that high shearing rates under wet conditions can lead to frictional loss (Tika & Hutchinson, 1999; Ferri et al., 2011). The latter hypothesis has been experimentally confirmed by Ferri et al. (2011) who demonstrated that shear softening under wet conditions does not involve thermal pressurisation, and that heating and thermo-poro-mechanical effects could occur only under dry conditions.

Table 6.1: Experimental data on the Vaiont case study

Source of Data	Authors	Test description	Slide surface friction angle (°)	Rock cohesion (MPa)	Rock friction angle (°)
EXPERIMENTS	Nonveiller (1967)	Crushed debris containing sand, clay or silt with angular fragments of limestone	N/A	0 - 0.098	22.4 - 42.5
		Clay material	5.6 - 6.8 (c= 0.00981 - 0.149 MPa)		
	Hendron & Patton (1985)	Wet	6 - 10	N/A	N/A
	Tika & Hutchinson (1999)	Wet, peak friction angle	30	N/A	N/A
		Wet, residual friction angle	9.7 - 10.6	N/A	N/A
		Wet, v > 0.075 m/s	4.4	N/A	N/A
	Ferri et al. (2011)	Room humidity, $v < 5\times10^{-5}$ m/s	25.17	N/A	N/A
		Room humidity, v = 1.31 m/s	6.8	N/A	N/A
		Wet, $v < 5\times10^{-5}$ m/s	9.65	N/A	N/A
		Wet, v > 0.70 m/s	0	N/A	N/A

v = shear velocity

Table 6.2: Strength parameters adopted by investigators for calculations

Authors	Slide surface friction angle (°)	Rock cohesion (MPa)	Rock friction angle (°)	Purpose
Müller (1968, p. 43)	40.0 (clay absent)			Stability analysis
Chowdhury (1978)	28			Sensitivity analysis on horizontal stresses
Voight & Faust (1982)	13.28 (Model 1) 26.57 (Model 2-4)			Thermo-poro-mechanical analysis for velocity calculation
Hendron & Patton (1987)	12 (clay)	0	40 (Inter-slice) 30 (Inter-slice) 36 (East wall) 30 (Inter-slice) 25 (East wall)	Stability analysis (Spencer method but satisfying only force equilibrium) Dynamic analysis
Nonveiller (1987)	22.4			Thermo-poro-mechanical analysis for velocity calculation
Veveakis et al. (2007)	22.2 (peak) 10.2 (residual)			Thermo-poro-mechanical analysis for creep calculation
Alonso & Pinyol (2010)	12 12	0.55-1.25 0.787	38 - 40 38.5	Estimated of strength values
Pinyol & Alonso (2010)	12	0.762	38	Thermo-poro-mechanical analysis for velocity calculation

Table 6.3: Strength parameters obtained from back calculations

Authors	Slide surface friction angle (°)	Interslice/ rock		Water level (m)	Type of calculation
		Cohesion (MPa)	Friction angle (°)		
Mencl (1966a)	18.75	0.49	30	700	Prandtl Wedge (2 inclined shear planes)
Mencl (1966b)	17.5	0	30	700	Prandtl Wedge different from Mencl (1966a)
Kenney (1967)	22.2			700	Janbu's generalised method
Nonveiller (1967)	17.6 20.6			700 700	Spencer Spencer (Assumed φ = 15° at the "seat")
Müller (1968)	22.5 21.9 20.8			700 700 Phreatic water table	Petterson Janbu's generalised method Spencer
Lo (1972)	25 13	0 0	25 13	Phreatic water table 700	Wedge analysis (Assumed φ = 28° at the "back")
Corbyn (1982)	18.43			700	Dynamic analysis
Nonveiller (1987)	22.4			700	Spencer
Vardoulakis (2002)	22.3			Phreatic water table	Taylor's friction circle method
Sitar et al. (2006)	8 - 14 (number of blocks = 2, with different joint orientation) 15 (number of blocks = 3-23) 16 (number of blocks = 105) 20	0	40 (static) 32 (dynamic)	0 0 0 Pore-pressure/overburden-pressure = 0.3	Discontinuous deformation analysis (DDA)
Crosta et al. (2007)	c=141.5-168.5kPa, φ=18.9-22.5° c=163.0-206. kPa, φ=16.3-20.7°	1.0	40 30	Different reservoir levels and different rainfall conditions	Finite element analysis c -φ strength reduction
Veveakis et al. (2007)	22.3			Phreatic water table	Limit analysis to calculate stresses Sliding block to calculate φ from stresses
Alonso & Pinyol (2010)	12 (assumed) 12 (assumed)	0.7623 0.564	38 40	710 710	Wedge analysis
Paronuzzi et al. (2013)	17.5 - 27	Not mentioned	Not mentioned	700	Finite element analyses

6.2 ASSUMPTIONS OF PARAMETER VALUES

Based on the literature review presented in the previous section, a numerical model which is sufficiently representative of the Vaiont slope was constructed. Several simplifying assumptions, however, had to be made in the discontinuum model, because it would be computationally unaffordable to replicate every fracture in the rock mass. As with the discontinuum calculation carried out by Sitar et al. (2005) using the method of discontinuous deformation analysis (DDA), the western end of the slope was chosen for the 2-D analysis. The western end is geometrically representative of the slope, which is well-known to be chair-shaped, and has been established by numerous investigators to be more critical than the middle section (also chair-shaped). The eastern section was not considered for 2-D analysis because field surveys by investigators suggested that the slope did not slide along the

bedding planes; the bedding planes were found to be broken-off by the slide (see Fig. 6.3, p. 155). The numerical model is illustrated in Fig. 6.4, and different strength and stiffness values were adopted to model independently the rock mass and slide surface. The following discusses the values that were adopted in the central analysis of this case study. Parametric analyses were later carried out to evaluate the sensitivity of the slope response to these parameters.

6.2.1 Rock joints and joint pattern

The rock mass making up the Vaiont slope is heavily jointed with spacing in the range of tens of centimeters (Broili, 1967). Therefore, the simulated rock joints in the numerical model do not represent the actual joint pattern or joint continuity (see Fig. 6.4). Instead, the shear strength modelled at a rock block contact in the DEM model represents the shear strength of the rock mass, which can be considered as a weighted average of the shear strength of the intact rock and the actual rock joints which have non-persistent extents and random spatial distributions. This assumption is consistent with the work of other investigators, who used the method of slices in their slope stability calculations, in which a friction angle between slices (i.e. the rock mass) has to be assumed. The joint pattern that was adopted for this numerical study was not arbitrary. Like Sitar et al. (2005), the joint pattern adopted, i.e. with bedding planes and vertical cross joints, is representative of the geological structure of the Vaiont slope. Broili (1967, p. 60) maintained that most of the

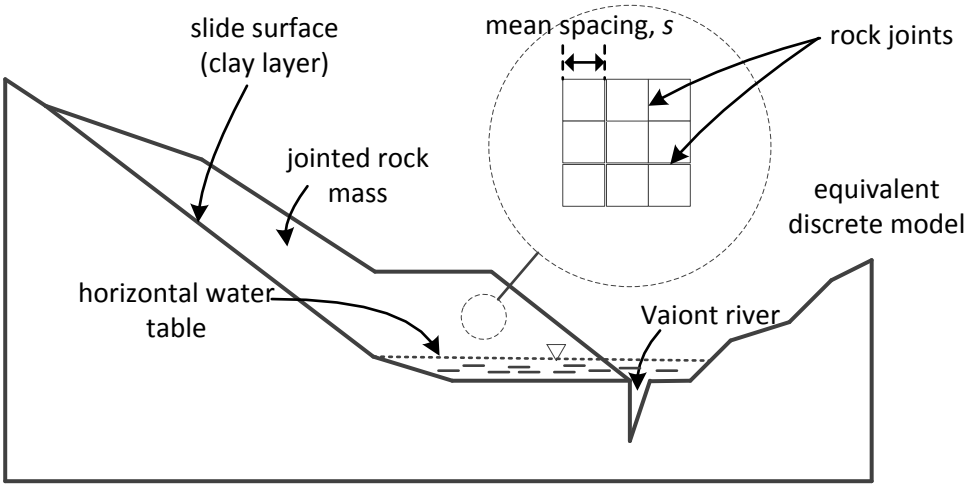

Fig. 6.4. Schematic diagram of the numerical model. Different stiffness and strength parameters are used for the slide surface and jointed rock mass.

major joints in the Vaiont area were vertical, whilst numerous folded structures were found to be present. The choice of cross joint orientations is investigated later in Section 6.4.8.3. The contact properties adopted at these "rock joints" are discussed in the following.

6.2.1.1 Strength parameters: friction angle, cohesion and tensile strength

Various researchers have proposed different rock strength parameters for the Vaiont slope. Both Müller (1968) and Hendron & Patton (1987) maintained that the friction angle φ = 40° (and cohesion c = 0) would be the value estimated a-priori for slope stability calculations. This value is incidentally the upper bound among those proposed in the literature. The lower friction angles suggested by other researchers may be influenced by back-calculations for sliding friction angles. Alonso & Pinyol (2010) derived the rock mass strength to be of friction angle φ = 38.5° and cohesion c = 0.787 MPa from Hoek-Brown estimates (uniaxial compressive strength of intact material, σ_c = 50 MPa; Geological Strength Index, GSI = 50; material constant, m_i = 9 (marls, soft limestones); disturbance factor, D = 0.5 (Hoek et al., 2002)) at a normal stress of 2 MPa; this level of stress was considered representative of the rock slope. Their estimated residual strength values were friction angle φ = 38.5° and cohesion c = 0 MPa. On the other hand, Crosta et al. (2007) estimated the rock mass friction angle, φ, and cohesion, c, to be 40° and 1 MPa respectively. Because the failure friction angles at the slide surface calculated from back analyses in the literature have been higher than experimental measurements, the higher credible rock mass strength values proposed in the literature were adopted in the central analysis, i.e. rock mass friction angle φ = 40.0°, cohesion c = 0.787 MPa, tensile strength σ_t = 0.076 MPa, and residual values of φ = 40.0°, c = 0.0 MPa, σ_t = 0.0 MPa (see Fig. 6.5). The residual friction angle values were assumed to be the same as the peak friction angle values 40°. The tensile strength was estimated from Hoek-Brown parameters proposed by Alonso & Pinyol (2010) using the software RocLab (Rocscience Inc., 2007). Both the residual cohesive and tensile strength values were considered to be nil once their peak strengths were exceeded to mimic the fragile breaking-off of rock bridges across discontinuities. A model similar to Fig. 6.5 was adopted by Eberhardt et al. (2004) in their DEM analyses of the Randa rock slide in the Swiss Alps.

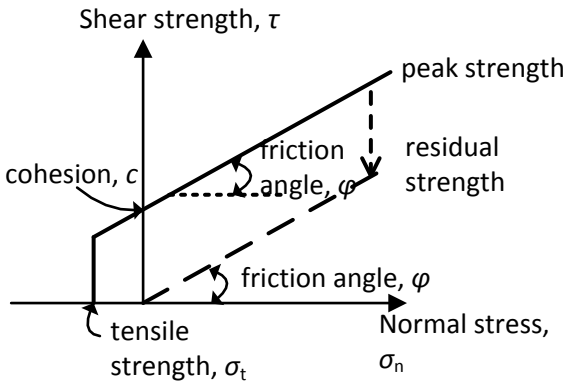

Fig. 6.5. Shear strength model at a numerical rock joint contact

6.2.1.2 Deformability parameters: normal and shear stiffness

Because the Vaiont rock slope is heavily jointed with respect to the scale of the slope, it was impractical to model the actual joint spacing. When viewed as an equivalent intact rock mass, the elastic modulus of the rock mass can be estimated from the software RocLab (Rocscience Inc, 2007) using the Hoek-Brown parameters suggested by Alonso & Pinyol (2010), i.e. strength of intact material = 50 MPa, Hoek Geological Strength Index (GSI) = 50, m_i = 9 (marls, soft limestones). The shear modulus can, in turn, be estimated from the deformation modulus and a typical value of Poisson's ratio for limestone. It is important to note that limestone, even when intact, is a highly variable material that exhibits a wide range of Young's modulus, i.e. 3 – 82 MPa and Poisson's ratio 0.08 – 0.39 (Ramamurthy, 2007). Moreover, the estimation of the deformation moduli for a jointed structure is typically not very accurate. Although the values adopted here may deviate from the actual deformability of the rock slope, these values can be legitimately used as a central value about which parametric analyses could be carried out. For this purpose, the Young's modulus and shear modulus of the jointed rock mass were taken to be 7680 MPa and 3072 MPa respectively; the latter was calculated using Poisson's ratio of 0.25 (which is within reasonable bounds mentioned previously). Because the distinct element method does not model the rock mass as a continuum, the rock mass deformation modulus cannot be used directly. The deformation of the rock mass in this numerical model is captured through joint deformations (rigid blocks were used in this model). The joint stiffness in the DEM was scaled according

to the mean joint spacing, s_{mean}, to match the rock mass deformation properties using the following equations (Goodman, 1989):

$$k_n = \frac{E}{s_{mean}} \tag{6.1}$$

$$k_s = \frac{G}{s_{mean}} \tag{6.2}$$

with k_n and k_s being the normal and shear joint stiffness per unit area. Table 6.4 shows the stiffness values adopted with the mean spacing. This technique of scaling the contact stiffness with joint spacing is conceptually illustrated in Fig. 6.6.

This procedure of adjusting the stiffness values according to the mean joint spacing allows the geometrical influence of the chosen number of blocks and deformability to be separated, albeit in a crude manner. This is particularly important since the actual joint spacing and stiffness are not replicated exactly in the DEM model. Without this procedure,

Table 6.4: Normal and shear stiffnesses used in the model for different mean joint spacing

mean joint spacing (m)	normal stiffness (GPa/m)	shear stiffness (GPa/m)
300	0.0256	0.01024
150	0.0512	0.02048
120	0.064	0.0256
80	0.096	0.0384
60	0.128	0.0512
40	0.192	0.0768
30	0.256	0.1024
20	0.384	0.1536

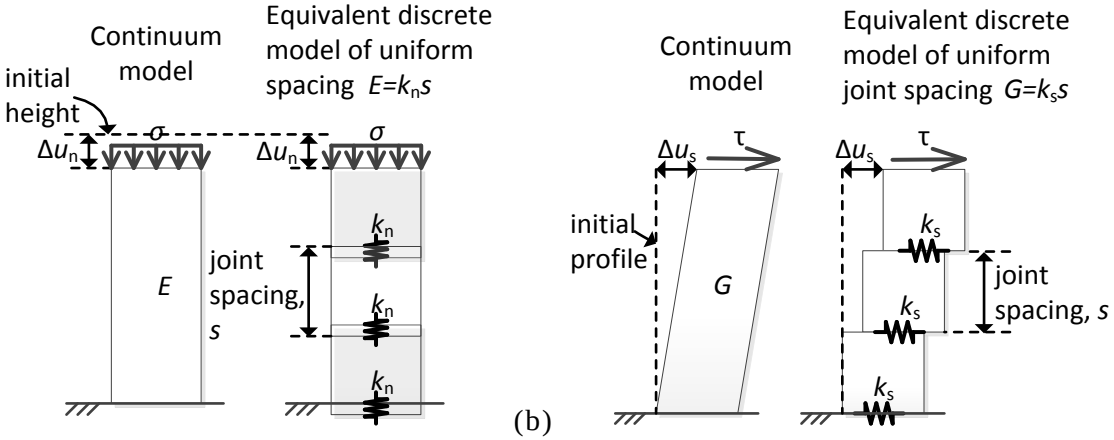

Fig. 6.6. Method to scale deformability of a continuum body using discrete bodies

increasing the number of discontinuities will increase the rock mass deformability, i.e. more springs are added. At the same time, the kinematic freedom of the rock slope is affected by the number of discontinuities adopted (the higher the number, the larger the kinematic freedom). The increase of freedom in terms of permitted kinematic movements with number of blocks can be regarded as an artifact of numerical discretisation.

6.2.2 Pore pressures

Piezometer readings were recorded prior to the slide (see Fig. 6.1). The piezometers were open perforated pipes which measured only average water pressures crossed by the tube, and did not reach the slide surface. The pore pressures at the slide surface can therefore only be deduced because they were not measured directly. Before 1962, high water pressures were initially recorded by one of the three piezometers. After that, all three piezometers suggested that the water pressures were hydrostatic. Hendron & Patton (1985) hypothesised that the ends of the piezometers at the clay layer was sheared off as the slope crept forward due to poor installation, and the readings recorded referred to the pore pressure in the surrounding rock mass rather than along the slide surface. However, the water level was assumed here to be horizontal, as in Alonso & Pinyol (2010). The reservoir water level when the slide occurred was approximately 700 m a.s.l., while the maximum recorded water level before the slide took place was 710 m a.s.l. Based on rainfall data, Hendron & Patton (1985) found that the amount of rainfall was also important. The rainfall data was analysed based on intervals of 7, 15, 30 and 45 days preceding the slope movement. Hendron & Patton (1985) processed the rainfall data based on different intervals so that different rainfall infiltration rates can be examined. A pair of rainfall and reservoir water level values was sought every time the slope moved. For all rainfall data intervals, it was found that there is an obvious trend that, for high rainfalls, the slope could move at a lower reservoir water level. According to Alonso & Pinyol (2010), the equivalent maximum water level which takes into account the effect of rainfall (based on a 30-day interval) is 710 m a.s.l. or approximately 90 m above the slide surface for the western section of the rock slope.

6.2.3 Slide surface with clay layer

Many investigators have found that the friction angle of the slide surface from back analyses is much higher than the residual friction angle obtained from ring shear tests on remoulded specimens. However, because Vaiont was a case of landslide reactivation and had experienced large prior shear displacements, Hendron & Patton (1985) suggested that the residual friction angle was likely to be the relevant strength parameter along the slide surface. In other words, concerning the residual friction angle, there is disagreement between the back calculated values from slope stability analyses and experimentally determined values. The possibility of strength recovery was indirectly suggested by some researchers to support the results of their back analyses (Vardoulakis, 2002). Here a shear softening model is used to model the shear behaviour of the clay from the fully-softened friction angle to the residual friction angle, based on published experimental data by Tika & Hutchinson (1999) (see dashed lines in Fig. 6.7). Brittle failure causing shear softening was also suggested by Kilburn & Petley (2003) to be one of the mechanisms which had taken place during the Vaiont slope failure.

The normal stiffness at the slide surface was kept at 2 GPa/m in the simulations throughout this chapter (unless otherwise mentioned). This value for the normal stiffness was selected so that it was always higher than all the shear stiffness values adopted for parametric analyses, because this is more physically realistic. The shear stiffness used in the

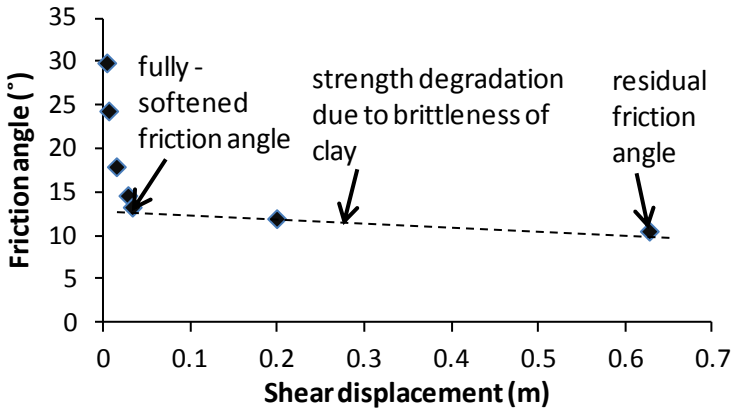

Fig. 6.7. Ring shear tests on remoulded clay specimens retrieved from the slide surface (values adopted from Vardoulakis, 2002; originally by Tika & Hutchinson, 1999)

central analysis was 0.1 GPa/m. The shear stiffness values deduced from the results of ring shear tests (stress-displacement curves) presented in Tika & Hutchinson (1999) and Ferri et al. (2011) are in the same order of magnitude (~10^8 Pa). The thickness of their samples was between 18-20 mm, while the thickness of clay layers observed in the field varied between 1 – 20 cm (Ferri et al., 2011).

6.3 NUMERICAL IMPLEMENTATION

This section details the numerical implementation of the parameters (Section 6.2). Table 6.5 shows the material properties which were used in the central analysis. As with Chapters 4 and 5, the open-source DEM code, YADE (Kozicki & Donzé, 2008), was used together with the tools proposed in Chapter 3.

6.3.1 Generation of the model

The approach of fixing the boundaries of the slope model, and applying gravity before the actual numerical computation was adopted (Bhasin & Kenya, 2003; Kveldsvik et al., 2009a). That is, after the slope geometry (consisting of the slope profile and rock joints) was generated, the slope was allowed to settle under gravity (9.81 m/s^2) with high local damping (cf. Cundall (1987) and Šmilauer (2010)). During the generation stage, the same friction angle was assigned to both the slide surface and the rock joints (ϕ = 40°). The simulations were allowed to cycle until the slope was stationary and the ratio of out-of-balance inertial

Table 6.5: Properties of materials used in the central 2-D DEM analysis

Properties	**Values**
Normal rock joint stiffness	0.192 GPa/m
Shear rock joint stiffness	0.0768 GPa/m
Rock joint friction angle (peak and residual)	40°
Rock joint cohesion (peak)	0.787 MPa
Rock joint cohesion (residual)	0 MPa
Rock joint tensile strength (peak)	0.076 MPa
Rock joint tensile strength (residual)	0 MPa
Unit weight (adopted from Alonso & Pinyol, 2010)	23.5 kN/m^3
Water table	90 m above horizontal slide surface

forces and the contact forces were sufficiently low (less than 0.5%), so that the slope could be considered as quasi-static for practical purposes. Then, local damping was switched off, and viscous contact damping was switched on. At this stage, breakages of cohesive and tensile bonds between rock joints, as well as shear softening at the slide were permitted. The numerical implementations of the contact law and viscous damping are discussed in Sections 6.3.3 and 6.3.6 respectively.

6.3.2 Strength reduction

A strength reduction approach is used to determine the value of the slide surface friction angle at which the landslide took place, hereafter called *critical*. Two strength reduction methods were considered, from which one was adopted. It is convenient to refer the two methods as Method A and Method B respectively.

In Method A, the friction angle is reduced by a very small amount at each time step. Displacements increase gradually with strength reduction (executed at every time step). The critical friction angle can be determined from the results (displacement - friction angle curve). Failure is assumed to occur when a sharp increase of displacement takes place. It is necessary to establish that the rate of strength reduction is low enough for force redistribution to take place and that the simulation is not dominated by dynamic effects. It is worthwhile mentioning that this approach of gradually reducing the slope strength circumvents some of the problems related to numerical convergence which arise for other approaches of strength reduction.

In Method B (Dawson et al., 1999; Hammah, 2007), strength reduction is conducted by taking larger strength reduction steps. But unlike Method A, every time a strength reduction step is taken, the simulation is cycled until a static solution is established or until no further progress could be made, i.e. certain tolerance criteria are met in terms of unbalanced forces, displacement increments, kinetic energy or number of iterations. Then, the next strength reduction step is taken. Failure is deemed to take place when the increase in displacements is significantly larger than the increments recorded in previous strength reduction steps. A common problem associated with using a displacement tolerance criterion for strength reduction is that the slope can move very slowly for long iterations but

with a displacement increment still above the specified tolerance. This would imply long computational time. Secondly, the tolerance criteria, i.e. unbalanced forces, displacements or energy tolerances, are often arbitrary, and the critical friction angle identified may depend on the adopted tolerance. Thirdly, it is not always straightforward to ascertain whether the increment in slope displacements at a strength reduction step is large enough to be considered as failure; in some situations, the increment in displacements may appear to be large, but "not large enough" compared to displacement increments recorded in previous strength reduction steps. The alternative choice of defining a critical cumulative displacement as suggested by Diederichs et al. (2007) could be equally ambiguous in terms of identifying failure, depending on the slope response. Fourthly, the satisfaction of tolerance criterion could be due to fortuitous oscillations. If a strength reduction approach based on Method B is adopted, special care has to be taken to address these issues. There is another way of finding the critical sliding friction angle, namely carrying out multiple simulations at different friction angles and measuring their displacements. However, in this method, the abrupt and large decrease in friction angle from a high value (at which the slope is stable for generation) may induce dynamic effects.

Method A is adopted in this numerical study, i.e. the slide surface friction angle is reduced by a very small amount at every time step, i.e. at constant rate.

6.3.3 Contact law for rock joints and slide surface

6.3.3.1 Shear behaviour

A linear elastic-perfectly plastic contact law was used to model the shear behaviour of rock joints. When cohesive bonds are present, the maximum allowable shear strength F^{s}_{max} is modelled as:

$$F^{s}_{max} = cA_{c} + \mu F^{n} \tag{6.3}$$

where c and $\mu = \tan\phi$ are the joint cohesion and friction coefficient respectively. When this limit is reached or exceeded, the maximum allowable shear strength becomes:

$$F^{s}_{max} = \mu F^{n} \tag{6.4}$$

At residual strength, cohesion is assumed to be completely lost (see Fig. 6.5, p. 161).

6.3.3.2 Normal behaviour

The stress-displacement behaviour in the normal direction was modelled as linear elastic (see Fig. 6.8). It is easier to calculate the tensile forces between particles through an "offset overlap distance" than with an actual non-overlapping gap. Suppose that the actual overlap distance at the contact is u_n, then the normal force can be calculated as:

$$F^{\mathrm{n}} = k_{\mathrm{n}} A_{\mathrm{c}} (u_{\mathrm{n}} - \delta_0) \tag{6.5}$$

When $u_{\mathrm{n}} \geq \delta_0$, the contact is compressive. When $0 < u_{\mathrm{n}} < \delta_0$, the contact is under tension. Since the joint stiffness is assumed to be linear elastic, the maximum tensile force can be expressed as:

$$F_{\max}^{\mathrm{tensile}} = k_{\mathrm{n}} A_{\mathrm{c}} \delta_0 \tag{6.6}$$

from which δ_0 can be calculated if the tensile strength is known.

6.3.4 Shear softening at the slide surface

An elastic-plastic contact law with shear softening was used to model the slide surface. This was derived from the experimental data obtained by Tika & Hutchinson (1999), as discussed in Section 6.2.3 (see also Fig. 6.7, p. 164). Based on the modified data presented by Vardoulakis (2002) for his calculations, the effect of shear softening was modelled using the following expression:

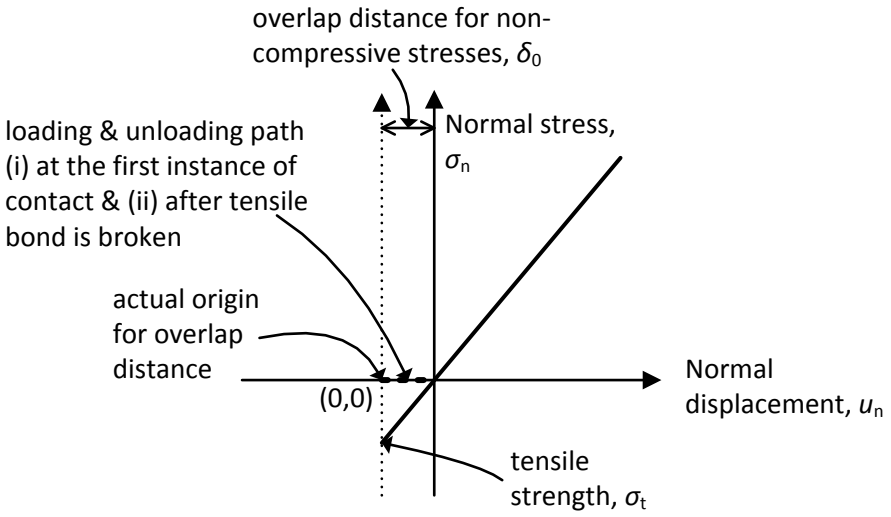

Fig. 6.8. Normal contact law at a rock joint with tensile resistance

$$\mu = \mu_0 - 0.0593 \times (1 - e^{-u_s / 0.35}) \tag{6.7}$$

where μ_0 is the nominal friction coefficient (specified through the strength reduction procedure in Section 6.3.2) and u_s is the cumulative shear displacement along the slide surface. Fig. 6.9 shows the shear softening model plotted against the experimental values. The stress-update algorithm that was used for this shear softening model is detailed in Appendix F.

6.3.5 Buoyancy

In this numerical study, because the water level was assumed to be horizontal, the effect of buoyancy can be introduced by applying a vertical upward force, F^{u}, which is proportional to the submerged volume of the blocks based on Archimedes principle.

$$F^{\mathrm{u}} = \rho_{\mathrm{w}} V_{\mathrm{submerged}} g \tag{6.8}$$

where ρ_{w} is the density of water, g is the gravity acceleration and $V_{\mathrm{submerged}}$ is the submerged volume of the solid.

6.3.6 Viscous damping

In this study, viscous damping was applied only in the normal direction:

$$F^{n} = k_{\mathrm{n}} A_{\mathrm{c}} (u_{\mathrm{n}} - \delta_0) - 2\xi \sqrt{m k_{\mathrm{n}} A_{\mathrm{c}}} V_n \tag{6.9}$$

where m is the effective mass of the two bodies in contact, V_n is the relative normal velocity of the two bodies, while ξ is the damping ratio for the critical viscous damping coefficient

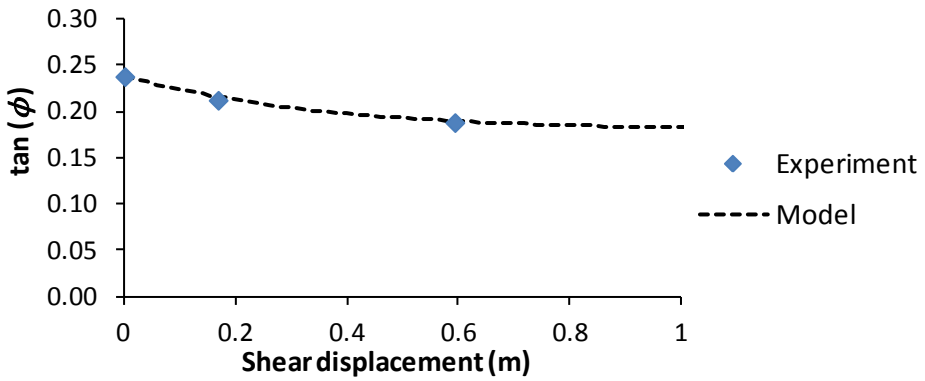

Fig. 6.9. Shear softening model (Eq. (6.7)) for clay layer at the slide surface, compared against experimental values of Tika & Hutchinson (1999) (interpreted by Vardoulakis, 2002)

$2\sqrt{mk_n A_c}$. A viscous damping ratio of 0.1 was adopted in this study to mimic the effects of plastic straining at the contacts in the normal direction, which was not explicitly accounted in the contact model; cyclic loading of a rock joint can cause breaking of asperities and dissipation of energy. Note that it is desirable to ensure that a DEM model is not overly damped system insomuch as it becomes dominated by viscous effects. The influence of viscous damping ratio is investigated and presented in Section 6.4.3.

6.4 RESULTS AND COMMENTS ON 2-D ANALYSES

Simulations were carried out to demonstrate that the proposed numerical tools in Chapter 3 can be used to study a practical rock engineering problem. The results of the strength reduction analyses are presented here. Unless otherwise mentioned, the normal stiffness of the slide surface was 2 GPa/m and the shear stiffness was 0.1 GPa/m. The joint spacing was 40 m and the corresponding normal and shear stiffnesses can be found in Table 6.4 (p. 162). The water table was assumed to be 90 m above the slide surface (*el.* 710 m a.s.l.). The shear softening contact law (Eq. (6.7)) was used to model the slide surface in this central analysis. The slope was generated with local damping until the kinetic energy, unbalanced forces and slope displacements were sufficiently low, before the strength reduction process was carried out. At this stage, local damping was removed and viscous damping at the contacts was activated.

6.4.1 Time step

For computational efficiency, it is desirable to adopt the largest time step for a numerical study whilst maintaining accuracy. However, a large time step can result in numerical instability. Fig. 6.10 shows the influence of time step on the slope response. The strength reduction rate was kept constant at 0.1°/sec for all these tests. The results show that 0.002 sec/step led to significant discrepancies compared to other smaller time steps. From this study, it was decided that the time step of 0.001 sec/step was to be adopted for the rest of the numerical calculations.

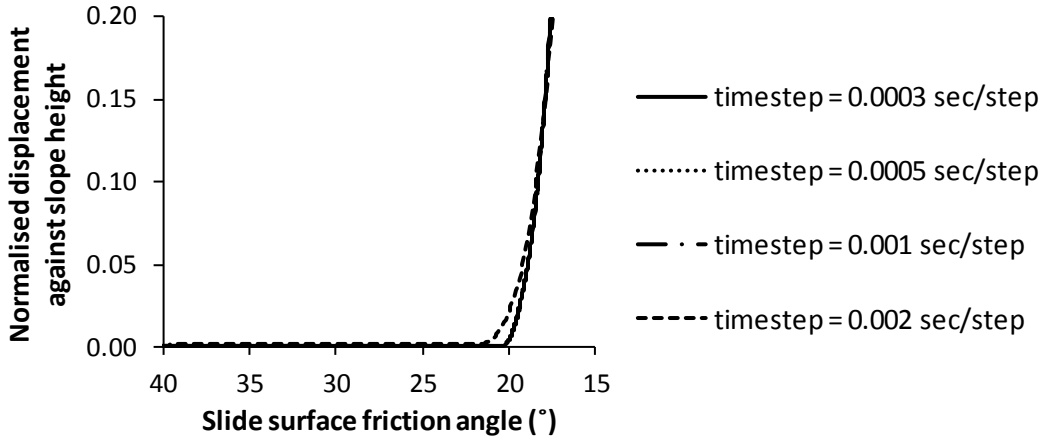

Fig. 6.10. Influence of time step on the slope response

6.4.2 Strength reduction rate

Again, for computational efficiency, it is desirable to use the highest strength reduction rate for a numerical study; a strength reduction rate which is twice slower, will double the simulation time. Fig. 6.11 shows the influence of the rate of strength reduction on the slope response. The lower the strength reduction rate, the more abrupt is the slope displacement at failure. The results showed that a strength reduction rate of 0.025 °/sec was reasonable, because the results were very close to the critical friction angle given by a lower strength reduction rate, 0.0125 °/sec.

6.4.3 Viscous damping ratio

The choice of damping ratio (Eq. (6.9)), $\xi = 0.1$, which was made in Section 6.3.6, was

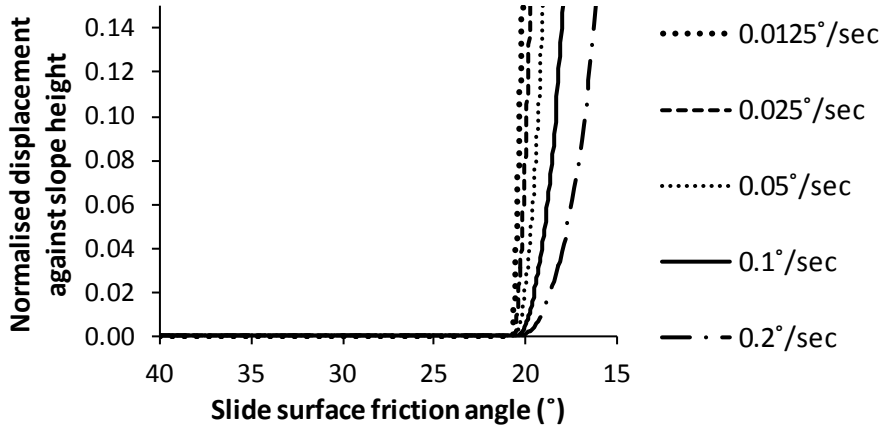

Fig. 6.11. Influence of strength reduction rate on the slope response

verified by running simulations with different damping ratios. The results of this study are consistent with the expectation that the lower the viscous damping ratio, the higher is the friction angle required for stability. Fig. 6.12 shows that the undamped model experienced substantial displacements from the beginning of strength reduction. The simulation with a minimal damping ratio of 0.01 also failed much earlier than the other simulations which were run with larger damping ratios. Note that some researchers have also found that it was necessary to use at least a very small damping ratio to model an undamped system, i.e. to prevent rounding errors from affecting the simulations (Kveldsvik et al., 2009b; O'Donnovan et al., 2012). For larger viscous damping ratios (ξ =0.05 - 0.5, believed to be a range of practical engineering interest), the difference in the critical friction angles from ξ = 0.1 was little, i.e. approximately ±0.15°, which is smaller than the effects of uncertainties concerning other parameters of the model.

The reason that the slope displacement at low damping ratios (ξ = 0.0 and ξ = 0.01) exhibited distinct behaviour (see Fig. 6.12) was investigated in detail. A three-block model, shown in Fig. 6.13, was used in the investigation. These three blocks were part of the DEM model with 40 m joint spacing. In this test, the contact shear behaviour was assumed to be elastic perfectly plastic. High viscous normal contact forces (ξ = 0.8) were initially applied until the block movements were sufficiently small (after 4.3 seconds). Viscous damping was then removed, and the DEM calculation was carried out without damping. Note that at this stage, although the blocks appeared to be stationary, minor oscillations of contact forces

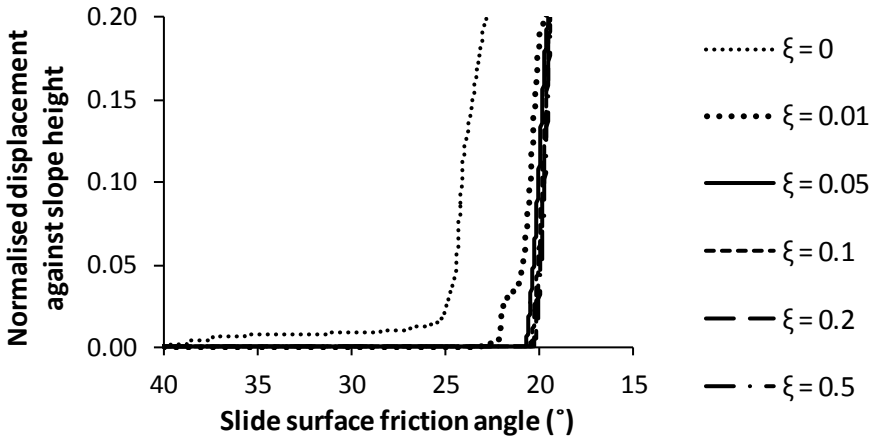

Fig. 6.12. Influence of viscous damping ratio on slope response

persisted.

The results are shown in Fig. 6.14. From 4.3 seconds to 30 seconds, the shear forces between the blocks were sometimes above their frictional limits, the frequency of which grew with each 'slipping' event; every time 'slipping' occurs, a fraction of elastic energy

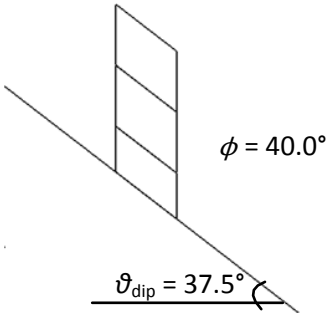

Fig. 6.13. Three-block column sitting on an inclined plane (the blocks are part of the Vaiont slope model)

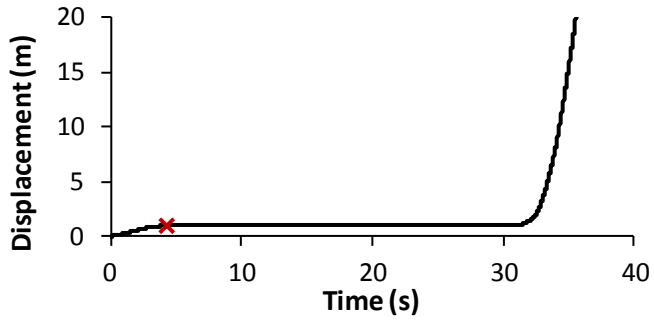

(a)

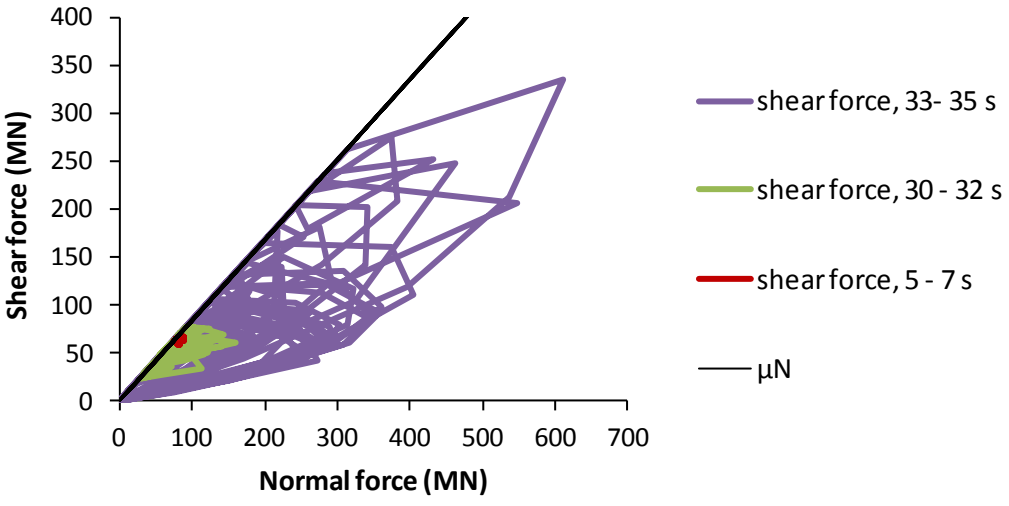

(b)

Fig. 6.14. Behaviour of the three-block column sitting on the inclined plane: (a) Displacement of the bottom block with time (the red cross marks the removal of damping) (b) contact forces of the block touching the base

was converted into kinetic energy. Despite these minor 'slipping' events, the blocks were largely stationary. After 30 seconds, the frequency of 'slipping' events had reached a critical level insomuch as sliding movements became obvious. This encouraged more pronounced oscillations of contact forces, and the blocks became unstable.

This observation is analogous to a closed-system consisting of a block initially sitting at rest on an inclined plane, but with a vibrating engine attached to it (see Fig. 6.15). The engine can be imagined as a point mass orbiting about the centre axis of the block. The centrifugal forces due to the orbiting point mass can cause the contact force at the base to fall occasionally outside the friction cone. This will send the block crawling down the slope.

Note that the oscillatory motion observed in this three-block example can be eliminated by using larger damping values, or by allowing the simulation to cycle longer with damping. However, in the modelling of the Vaiont slope, perturbations which were introduced by strength reduction could induce oscillatory motion throughout the simulation. Note that the way that the blocks are generated does not guarantee that the shear forces are uniformly mobilised along the slide surface (consisting of both the inclined and horizontal planes), because the block assembly is statically indeterminate (see Fig. 6.16). Consequently, during the process of strength reduction on the slide surface, some blocks on the slide surface may slip first, and cause local disturbance in the model. It is therefore likely that the results with low damping values in Fig. 6.12 have been dominated by

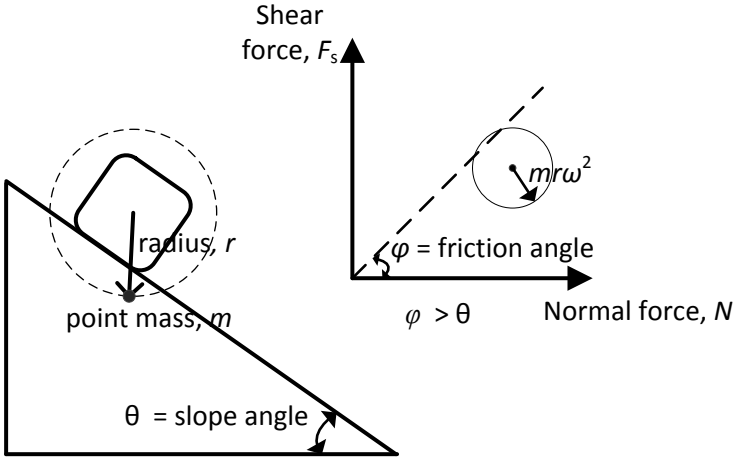

Fig. 6.15. A closed-system with a vibrating engine attached to a block sitting on an inclined plane

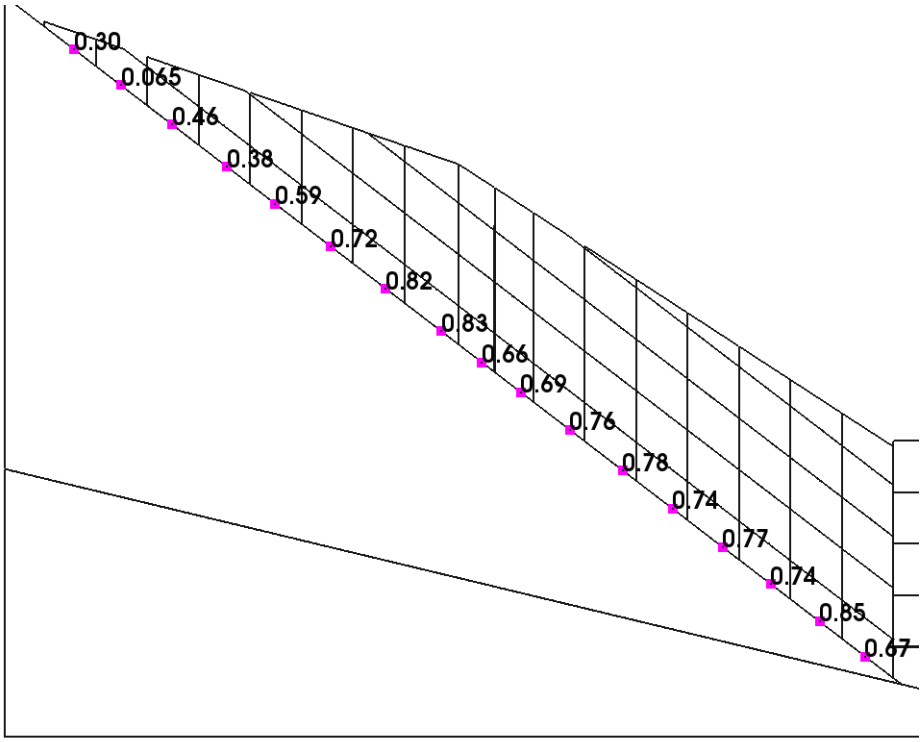

Fig. 6.16. Ratios of shear force to shear strength at the end of the generation stage. Pink dots denote contact points. The friction angles at the slide surface and at the rock joints are both 40°.

vibration effects. Therefore, some damping is necessary to prevent the model from being dominated by these vibration effects.

6.4.4 Verification of the numerical model against Sitar et al. (2005)

Here the DEM simulations are compared with the DDA analysis run by Sitar et al. (2005). The friction angle of the vertical discontinuities was assigned as 40° with zero cohesion and tensile strength (these values were not explicitly mentioned in Sitar et al. (2005), but were adopted from Hendron & Patton (1985) since their result with interslice friction angles of 40° rather than 30° was explicitly used as a benchmark study in Sitar et al. (2005)). The contact law was elastic-perfectly plastic, the reservoir level was below the slide surface (dry condition), and the number of blocks in the model was 233. The contact stiffness (both rock joints and slide surface) in the normal and shear directions were 0.75 GPa/m and 0.3676 GPa/m respectively. These were derived from an elastic modulus of 30 GPa and Poisson's ratio 0.02 used in their numerical model, for the joint spacing used for this comparison exercise (40 m). The reason for using a low Poisson's ratio was not mentioned

by the investigators. Note that the DDA method does not model the deformability of the rock joints because the method imposes a non-penetration rule between contacts. In Sitar et al. (2005), the critical friction angle is 15° for 23 blocks and 16° for 105 blocks. Here the critical sliding friction angle was found to be 16.6°, at which the slope experienced an abrupt and large displacement (see Fig. 6.17). The difference is marginal and can be attributed to the difference in the numerical methods. Rigid blocks with compliant contacts were used here whereas deformable blocks with non-compliant contacts were used in the DDA models by Sitar et al. (2005).

6.4.5 Influence of number of blocks

The number of blocks generated from mean spacing of 20 m, 30 m, 40 m, 60 m, 80 m and 120 m are shown in Table 6.6. Fig. 6.18 (a) shows the influence of joint spacing and Fig. 6.18 (b) shows the results in terms of block number (log-scale). Note that the stiffness of rock joints has been approximately compensated to maintain the rock mass deformability. Thus the difference in results can be mainly attributed to the geometrical effects arising from

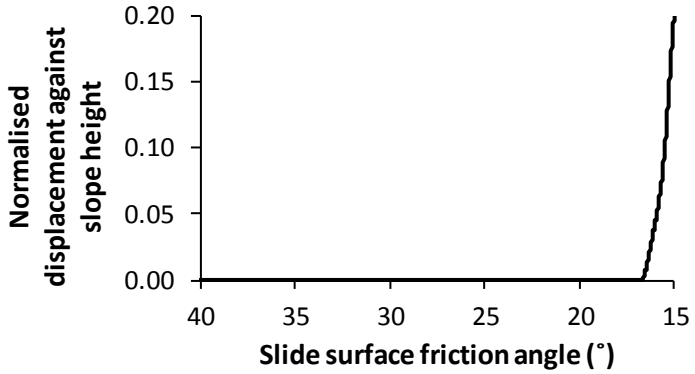

Fig. 6.17. Displacement with slide surface friction angle to compare with Sitar et al. (2005). Mean joint spacing: 40 m.

Table 6.6: Number of blocks in the numerical model generated from several mean spacings

mean joint spacing (m)	number of blocks	failure friction angle (°)
300	4	18.7
150	15	20.9
120	58	21.0
80	83	21.2
60	132	20.9
40	225	20.6
30	411	20.6
20	741	20.6

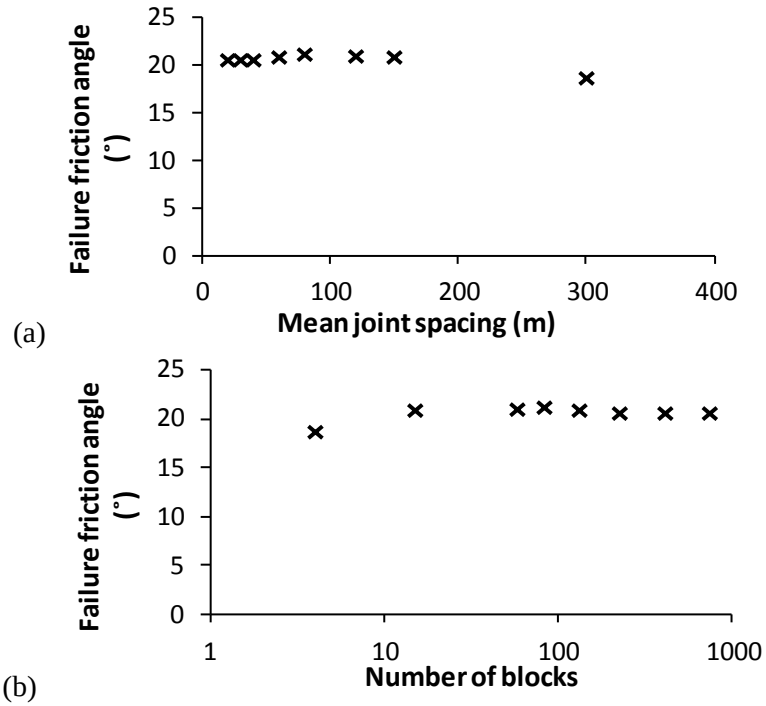

Fig. 6.18. Influence of (a) mean joint spacing and (b) the number of blocks on the friction angle required for stability (slide surface)

the discretisation of blocks. For a small number of blocks (less than 100 in Fig. 6.18 (b)), the slope becomes more prone to failure as the number of blocks increases, i.e. the friction angle required for stability increases. This trend is consistent with the results obtained by Sitar et al. (2005). For more than 100 blocks, the friction angle required for stability is no longer sensitive to the number of blocks.

6.4.6 Influence of the water level

The influence of the water table was investigated. The results are shown in Fig. 6.19. The friction angle required for stability increased with the height of the water table, and is consistent with the findings of other investigators. The friction angle required for stability with 90 m water level (*el*. 710 m a.s.l.) above the slide surface (20.6°) is 1.8° higher than under dry conditions (18.8°). The influence of water level was reported to be minimal by Kenney (1967), i.e. raising the water level to 700 m a.s.l. required an increase of 1.5 - 2.5° for stability. Paronuzzi et al. (2013) found from their finite element analyses that increasing the water level to *el*. 700 m a.s.l. required an increase of 1.9 - 2.3° for stability. Note that the approximated critical friction angle by Paronuzzi et al. (2013) for one of the western sections of the slope is 20.5°, and is very close to the results here. Alonso & Pinyol (2010) showed

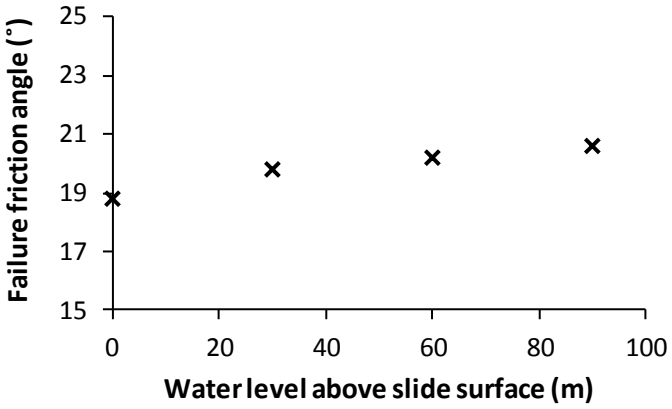

Fig. 6.19. Influence of water level on the friction angle required for stability (slide surface)

that an increase of water level of 120 m above the slide surface required an increase of friction angle of 1 – 2.7° for stability (inferred from the factor of safety for the slide surface and rock mass friction angle). The difference in critical friction angles between dry and wet conditions calculated by Sitar et al. (2005) was larger, i.e. 4 – 5°, because the pore pressure was assumed to be 0.3 times the overburden pressure. In MacLaughlin (1999), the influence of water level (horizontal water table) on the failure friction angle was 1 – 2°, and is consistent with the findings here. It can be seen from Fig. 6.19 that the rise in failure friction angle, $\Delta\varphi$, is greatest when the water level increases from 0 – 30 m ($\Delta\varphi$ = 1.0°) than 30 – 60 m ($\Delta\varphi$ = 0.4°) or 60 – 90 m ($\Delta\varphi$ = 0.4°). This observation is consistent with the analytical calculations presented by Alonso & Pinyol (2010), in which the factor of safety for the slope was shown to decrease with the rise of water level in a non-linear manner.

6.4.7 Influence of slide surface properties

The influence of the slide surface properties in terms of shear stiffness on the slope stability was investigated. The stiffness values of the rock joints and slide surface in this numerical model were independent. The results of this study are shown and discussed in the following.

Fig. 6.20 shows the influence of slide surface shear stiffness, k_s, on the friction angle required for stability. The simulation was run with shear stiffness values of 0.01 GPa/m to 1.8 GPa/m. The failure friction angle is almost independent of the shear stiffness of the slide surface. For k_s = 0.01 – 1.8 GPa/m, the failure friction angle fluctuated between 20.2 - 20.6°, showing that the failure friction angle is insensitive to the shear stiffness of the slide surface.

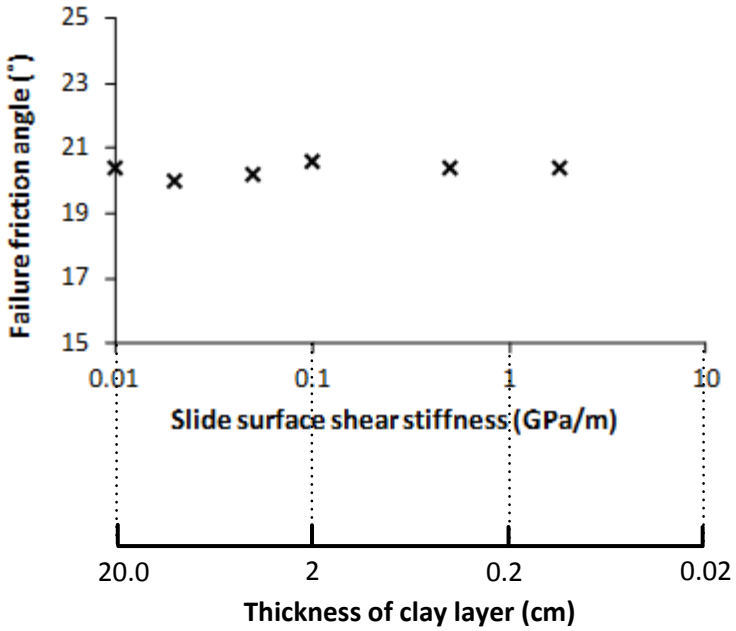

Fig. 6.20. Influence of slide surface shear stiffness on the friction angle required for stability (slide surface). The equivalent thickness of the clay layer for different shear stiffness values had been extrapolated from experimental shear tests reported by Ferri et al. (2011).

This is not surprising since, for failures which involve displacements of material along a slip surface, the stiffness of the slip surface is not normally considered in routine design calculations in geotechnical practice.

6.4.8 Influence of rock joint properties

The influence of the rock mass properties on the slope stability was indirectly investigated through the contact properties between the rock blocks in the DEM calculations. The influence of several parameters were investigated, namely the rock mass deformability, friction angle and 'rock joint' orientation.

6.4.8.1 Influence of rock mass deformability (through rock joint stiffness)

The influence of rock mass deformability is investigated by varying the stiffness values of the contacts between rock blocks. Fig. 6.21 shows that the critical sliding friction angle is sensitive to the rock mass deformability. The equivalent rock mass deformability was derived from Eqs. (6.1) and (6.2) (p. 162). The stiffer the rock mass, the larger the slope's resistance against sliding. The gradient is approximately constant (gradient = -1.4°/log cycle) in a log-scale (see Fig. 6.22). This relationship is in contrast with the slide surface

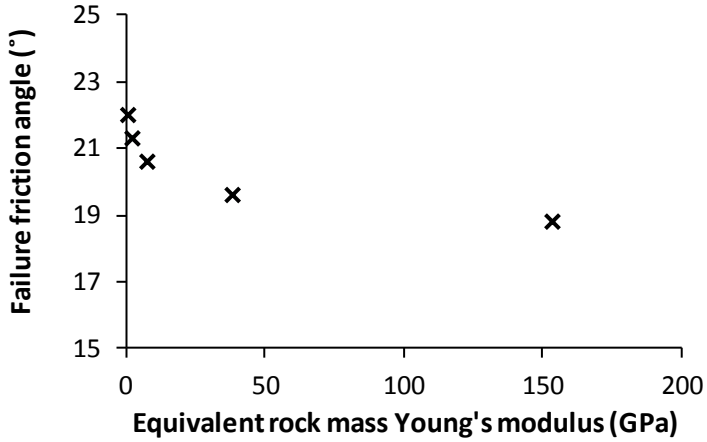

Fig. 6.21. Influence of equivalent rock mass deformability on the friction angle required for stability (slide surface). Refer to Eqs. (6.1) and (6.2) for the method of approximating the rock mass deformability

shear stiffness, in which its influence on the slope stability is minor (the slope stability is almost independent of the shear stiffness of the slide surface). It is noteworthy that both observations are consistent with the analysis of the Carsington embankment failure using finite element analysis of Potts et al. (1990), who found that:

> *"First, increasing the pre-peak foundation stiffness by a factor of 2 decreases failure elevation and safety factor by small amounts, as a more rigid base to the yellow clay layer concentrates strain in it."*
>
> *"Seventhly, the stiffness of the mudstone fill has a significant effect, an increase by 2.5 times reducing progressive failure and increasing the safety factor by about 4%."*

In comparison with the case of Carsington Embankment, the increase in stiffness of the rock mass by 2.5 times for the Vaiont rock slope was found to decrease the failure friction angle by approximately 2.7% (0.56 °), and is of the same order of magnitude as observed by Potts et al. (1990). It is possible that the greater kinematic constraint afforded by a stiffer rock mass could increase the slope's resistance to sliding. While the stability of the slope is almost independent of the slide surface shear stiffness (due to the scatter of the data points), the gradient of the best-fit line (plot of failure friction angle against shear stiffness) in Fig. 6.22 is positive. This suggests that the Vaiont slope becomes slightly more critical as the slide surface becomes stiffer. The stiffness of the shear surface is proportional to the brittleness of the clay layer and inversely proportional to its thickness.

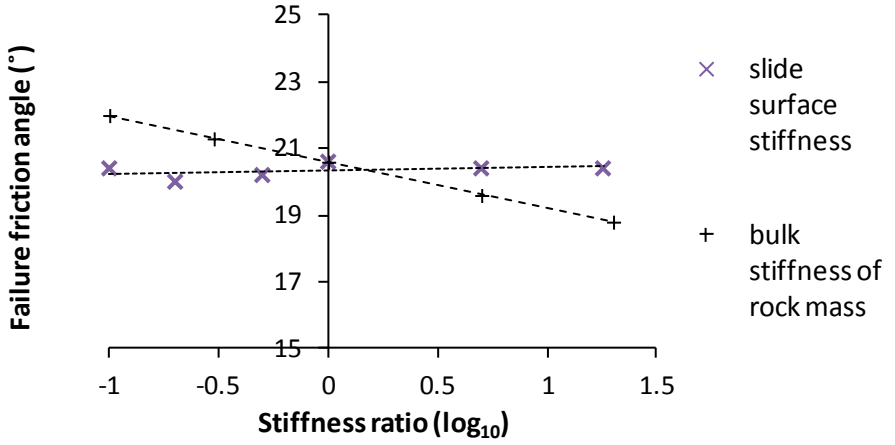

Fig. 6.22. Influence of rock mass and slide surface stiffness on the friction angle required for stability (slide surface).

6.4.8.2 Influence of rock joint friction angle

The upper and lower bounds of the rock mass friction angle as estimated by Hendron & Patton (1987) are 40° and 30° respectively. Note that these values were suggested for analytical calculations using the method of slices. Some of the lower friction angles suggested in the literature could have been influenced by their back analyses. The sensitivity of the rock joint friction angle values on the slope stability was investigated, and the results are shown in Fig. 6.23. The results show that the decreasing the rock joint friction angle from 40° to 30° increases the failure slide surface friction angle by approximately 0.6° (3 %). This result is consistent with the DDA results of MacLaughlin (1997), in which the slide surface friction angles at failure were the same (with precision of ±1° in her analysis) for rock joint friction angles of 40° and 30°, when the reservoir was filled (Table 6.2 in MacLaughlin, 1997). In Hendron & Patton (1985), decreasing the rock joint friction angles from 40° to 30° reduced the slope's factor of safety by 10%. The factor of safety used in Hendron & Patton (1985) is the ratio of the strength of the slide surface to the strength required for translational force equilibrium (only). It is well-known in slope stability analysis that force equilibrium calculated using the method of slices is sensitive to the assumption of inter-slice forces. On the other hand, moment equilibrium is less sensitive to the assumption of inter-slice forces. Overall equilibrium is satisfied when both force and moment equilibriums are satisfied. It is therefore reassuring that, compared to the analytical

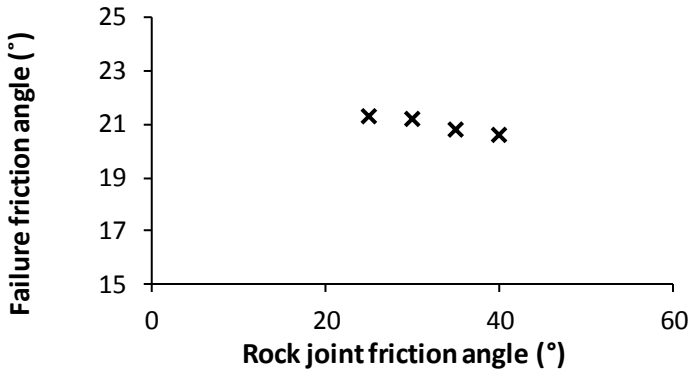

Fig. 6.23. Influence of rock joint friction angle on the friction angle required for stability (slide surface)

calculations carried out by Hendron & Patton (1985), the results of the discontinuum numerical calculations which satisfy both force and moment equilibriums are less sensitive to the inter-slice friction angles.

6.4.8.3 Influence of rock joint dip angles

In the previous simulations, as with Sitar et al. (2005) and MacLaughlin (1997), the joints across the bedded structure were vertical. In Broili (1968), although it was maintained that the major faults and joints were vertical, there was a mention that shear faults dipping 40° - 50° South were observed at the bend between the back and seat of the "chair". In Alonso & Pinyol (2010), these shear planes (used in their stability analysis) were assumed to form at the bisector plane between the seat and the back of the chair. Here, the influence of cross-joint orientations (dip angle = 50°) was investigated. It is also of interest to investigate the influence of the dip angle of sub-horizontal beddings on the DEM model. These dip angles may vary depending on the angle that was subtended between the slide direction and the dip-direction of the bedding plane (see Fig. 6.24 for illustration). A similar analysis was presented by Gens & Alonso (2006) to explain the Aznalcóllar dam failure in Spain. They found that three-dimensional effects arising from the direction of movement of the embankment and the dip-direction of the bedding planes beneath the embankment are important factors governing the stability of the embankment and the location of failure. In the numerical study here, a dip angle of 1.8° was adopted; it corresponds to an apparent dip angle which may arise from a true dip angle of 10° in a near-perpendicular direction ($\pm 10°$ from perpendicular, i.e. $\alpha = 80°$ in Fig. 6.24). The seat of the "chair" was also inclined to be

parallel with the bedding planes. The results are plotted in Fig. 6.25. The results suggest that an inclined cross-joint (dip angle 50°) is less critical than a vertical discontinuity by approximately 1.7°. This finding is consistent with the conventional geotechnical engineering practice of using vertical slices when performing limit equilibrium calculations for the stability of slopes and embankments. Compared to the central analysis with horizontal bedding planes, an increase in the sub-horizontal bedding plane inclination by 1.8° resulted in an increase in friction angle required for stability by approximately 0.5°. This study suggests that the critical friction angle for a jointed rock slope with a non-planar slip-surface is sensitive to its joint patterns.

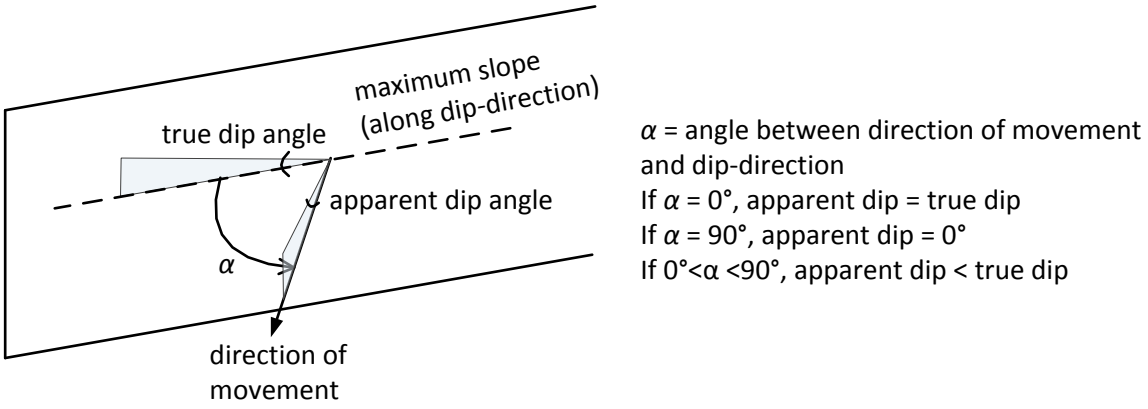

Fig. 6.24. Illustration of the influence of direction of movement and dip-direction on apparent dip angle

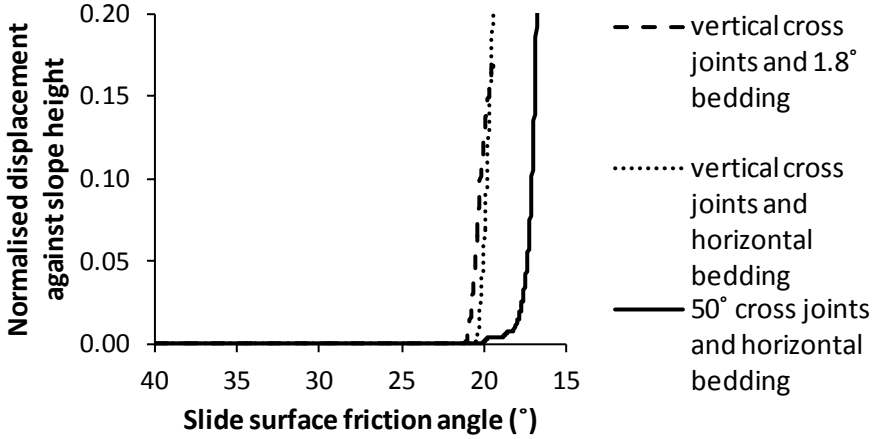

Fig. 6.25. Influence of rock joint orientation on the critical sliding friction angle

6.4.9 Observations on failure mechanism

It is of interest to study the failure mechanism of this slope, because it can give indications as to why its stability is sensitive to the rock mass deformability. From the simulations here, the failure mechanism was observed to change with displacement. First, shearing across rock joints was predominant (see Fig. 6.26 (b)). As displacement accumulated, there were separations between rock strata, and a large tensile opening was created across the rock strata (see Fig. 6.26 (c)). This was also observed in DDA simulations of Sitar et al. (2005). The failure modes of the inclined joints investigated in the previous section are shown in Fig. 6.27.

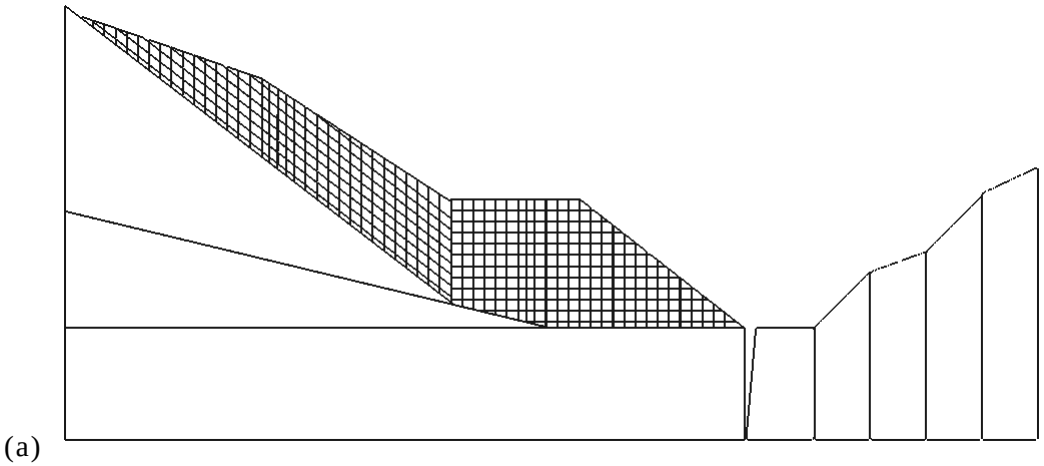

(a)

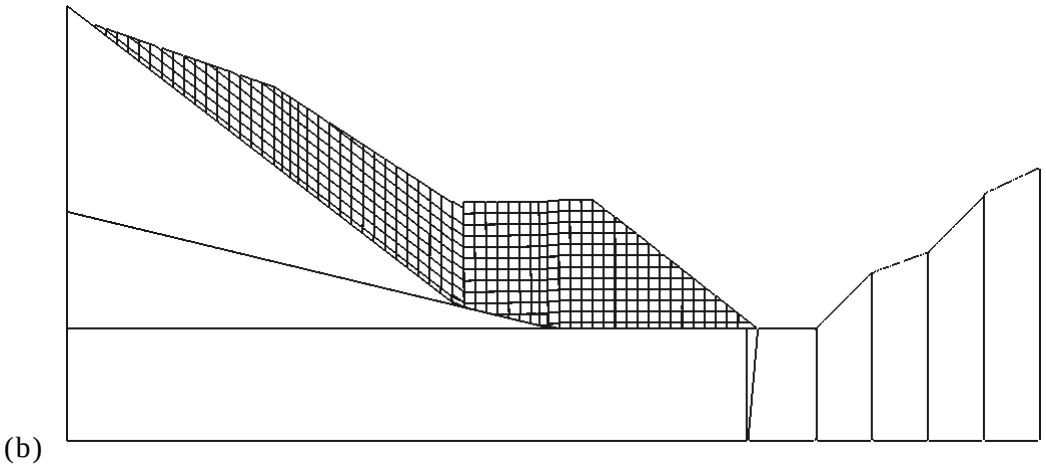

(b)

Fig. 6.26. Failure mechanism (a) initial condition (b) at 30 m displacement: shearing across joints, (c) at 118 m displacement: tensile opening across joints. Mean spacing 20 m.

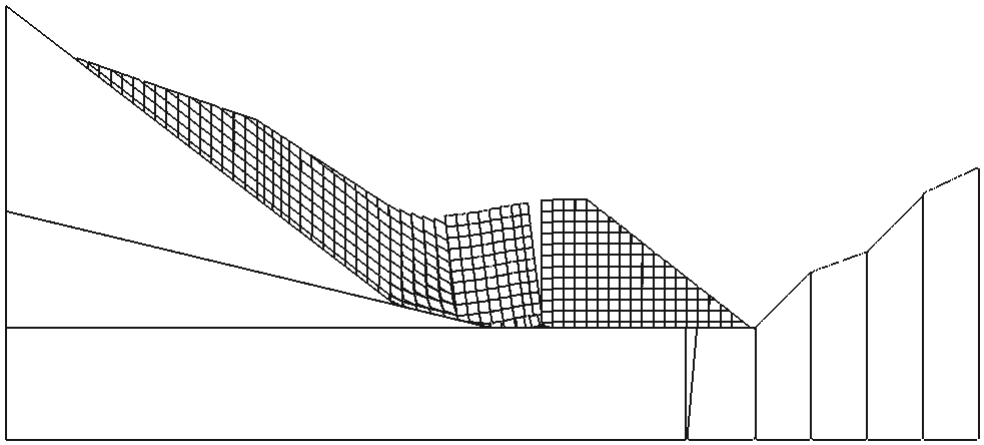

(c)

Fig. 6.26. (cont.)

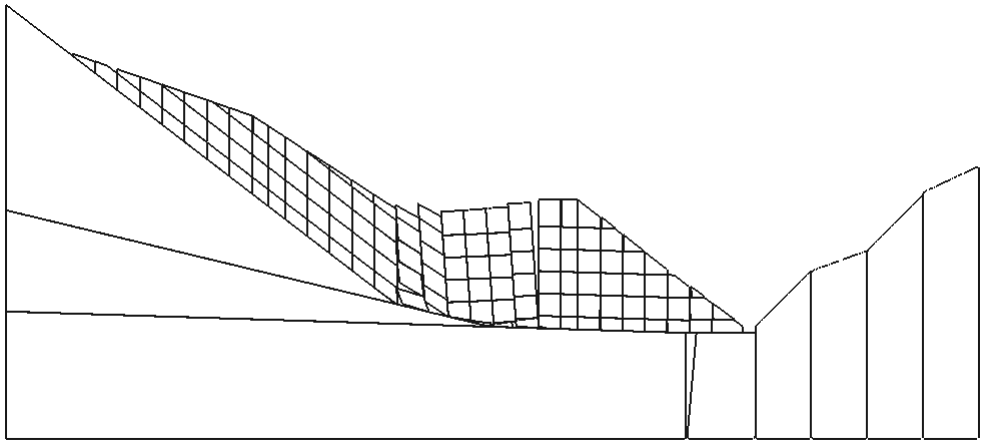

(a)

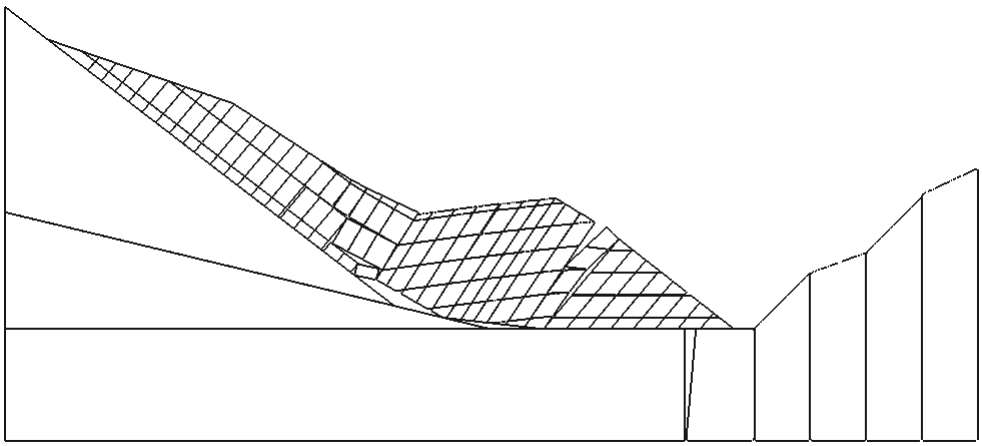

(b)

Fig. 6.27. Failure mechanism for (a) inclined sub-horizontal joints and seat of slide surface (dip angle 1.8°) (b) inclined cross-joints (dip angle = 50° South).

For a chair-shape slope, it appears that tensile failure can be a possible failure mechanism when the shear resistance across discontinuities is high. This is not surprising for jointed rock masses because their tensile strength is almost non-existent. From gathered field observations, Kiersch (1964) maintained that:

> *"The result has been subsurface development of extensive tubes, openings, cavities and widening of joints and bedding planes. Sinkholes formed in the floor of the outer valley, particularly along the Malm formation on the upper slopes."*

When several possible failure mechanisms might manifest, the assumption of a particular failure mechanism in analytical slope stability calculations should be verified to ensure that it is the most critical one.

For rock joint friction angles 30° and below, shearing across the rock joints was the predominant failure mechanism, even for large displacements (see Fig. 6.28). Field observations indicate that tensile openings were present at the slope surface but they were not as pronounced as Fig. 6.26 (c). Rather, the slope was found to move more uniformly as in Fig. 6.28 (rock joint friction angle 30°). This suggests that the residual rock mass friction angle at failure (after large straining) in the field is likely to be closer to 30°. Note that strength degradation of the rock mass was indirectly implied by Hendron & Patton (1985) and Anderson (1985) who adopted lower friction angle values for velocity analyses. Strength degradation in terms of rock mass shear strength was also suggested by Alonso &

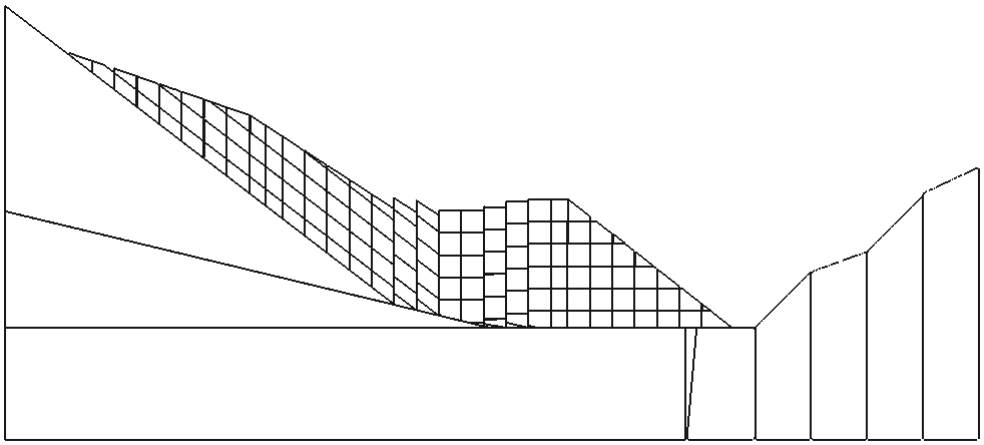

Fig. 6.28. Failure mode for 30° rock joint friction angle (at 84 m displacement)

Pinyol (2010).

It was observed from the simulations undertaken in this chapter that, for high slide surface friction angle, the contact forces were distributed uniformly across the slope (see Fig. 6.29 (a)). When shear resistance from the slide surface was low, much of the resistance against sliding was contributed by arching across the rock mass between the back and the seat of the chair-shaped slope (see Fig. 6.29 (b)). As the rock mass slid past the "bend" between the back and the seat of the slope, arching was present at the "bend" resisting the movement (see Fig. 6.29 (c)).

Many investigators speculated that the sudden collapse observed in the field is related to the resistance afforded by the rock mass (Mencl, 1966a; Mencl, 1966b; Hutchinson, 1987; Alonso& Pinyol, 2010). For instance, Hutchinson (1987) and Alonso & Pinyol (2010) suggested that, although the slip surface had reached its slide limit, the slope movement was held by the internal shear resistance of the rock mass. Abrupt failure took place when the internal shear resistance was overcome by the slope. Although the failure mechanism in Fig. 6.29 is consistent with their speculations, the large forces observed in Fig. 6.29 (c) could be

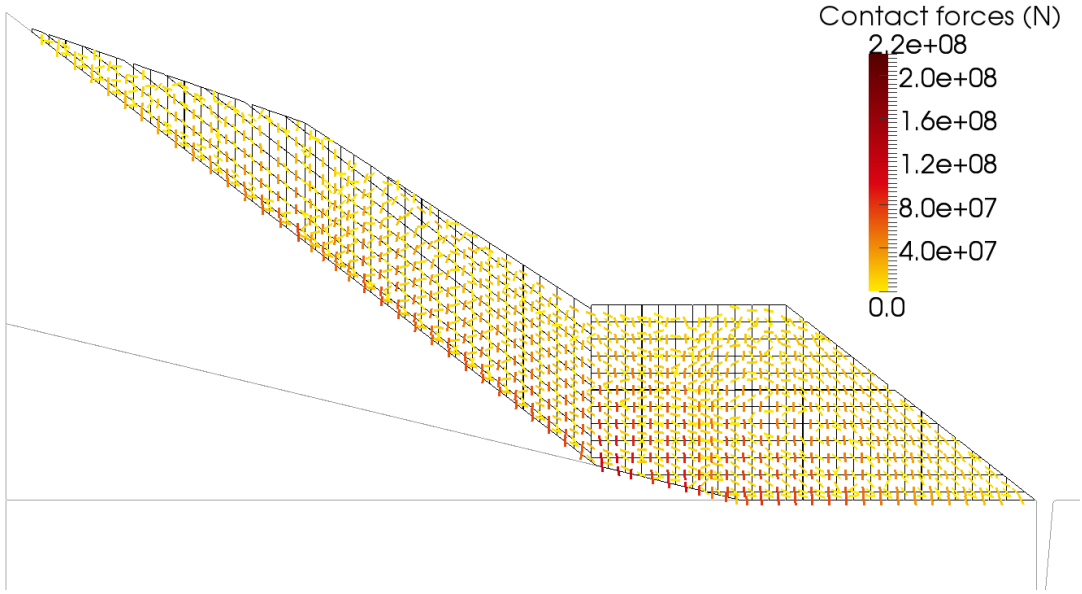

(a)

Fig. 6.29. Contact forces when (a) slide surface friction angle = 35.65°, (b) slide surface friction angle = 20.65° (before failure) (c) slide surface friction angle = 20.23° (after failure), displacement 20 m

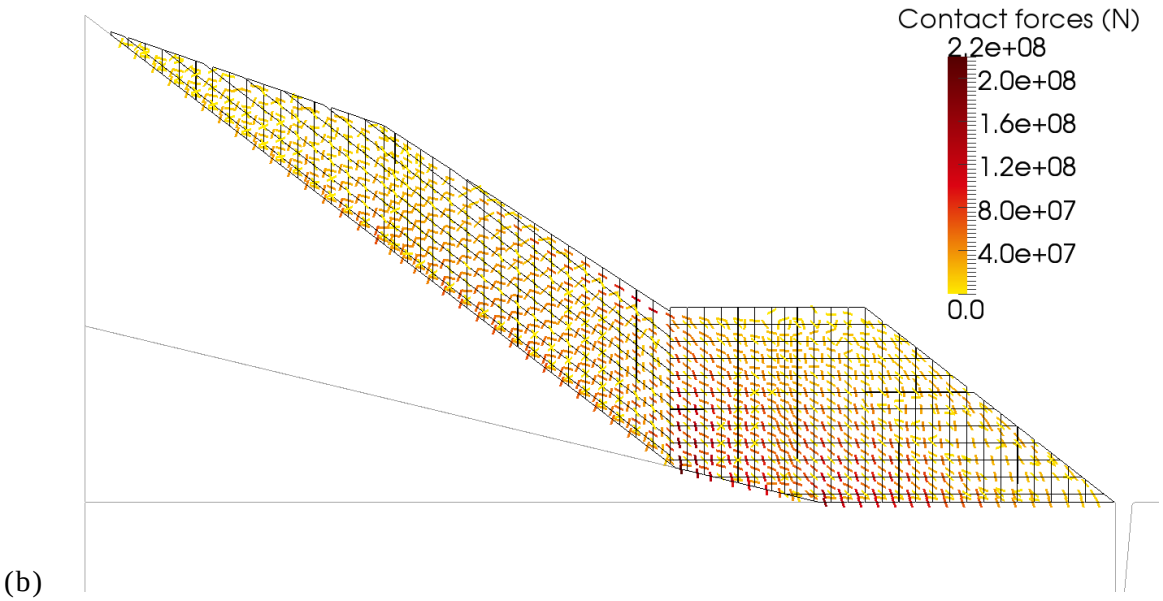

(b)

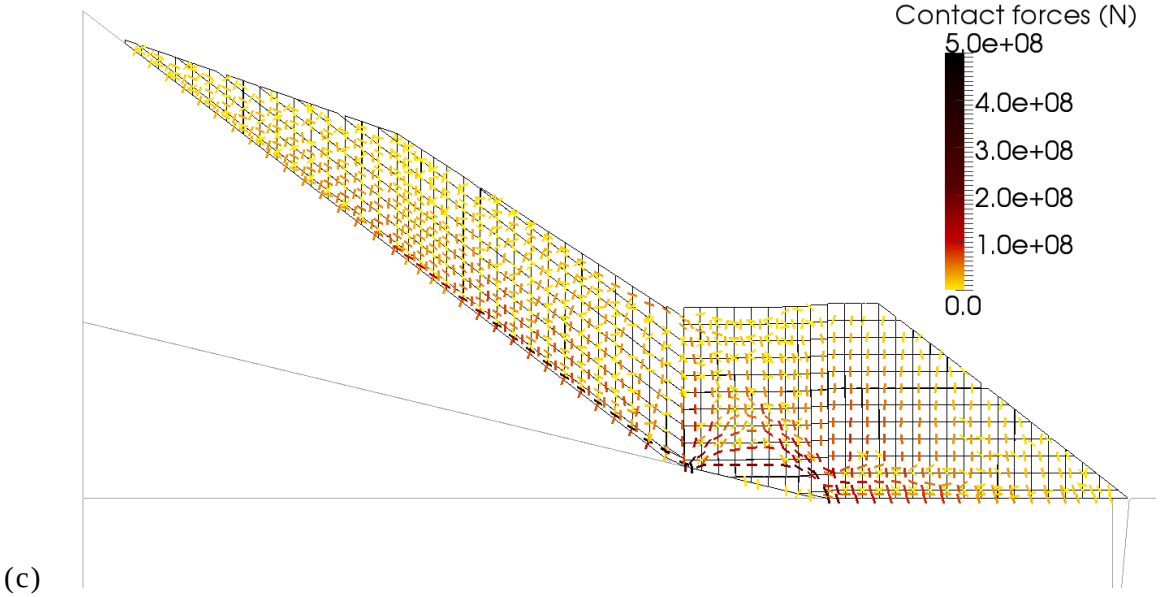

(c)

Fig. 6.29. (cont.)

caused by the limitations of the numerical tools in capturing physical behaviours, such as yielding and fracturing. These large forces in reality could be followed by the crushing or yielding of the rock material.

6.4.10 Summary of 2-D simulations

Using credible upper-bound shear strengths for the rock mass, it was found from the DEM simulations that the nominal sliding friction angles were approximately 20.6° when the water table is 90 m above the slide surface. This result is close to the back calculated friction

angles by other investigators (see Table 6.3, p.158). For a horizontal water table, the consequence of filling the reservoir and rainfall (90 m equivalent water level above slide surface) increased the friction angle required for stability by 1.8°. With regard to the rock mass properties, an increase in the bulk stiffness by 5 times reduced the friction angle required for stability by 1°, increasing the slope resistance against sliding. A decline in rock joint friction angles from 40° to 30° increased the friction angle required for stability by 0.6°. Increasing the inclination of the seat of the chair-shaped slope by 1.8° increased the friction angle required for stability by 0.5°. The shear stiffness of the slide surface was found to affect the slope stability marginally. Therefore, of all the parameters which have been investigated, the influence of water table on the stability of the Vaiont slope was found to be most important.

Overall, the friction angles required for stability obtained from the DEM calculations were higher than the 12° suggested by Hendron & Patton (1987) from site investigations (they suggested that an additional 2° should be added to the measured 10° to account for the influence of rock asperities since the clay thickness varies at the slide surface). The 2-D DEM models led to similar conclusions as 2-D limit equilibrium analyses presented by other researchers (see Table 6.3, p.158).

6.5 THREE-DIMENSIONAL ANALYSIS

A three-dimensional analysis was undertaken to capture the influence of the eastern boundary, which was maintained to be important by Hendron & Patton (1987). This analysis also shows the capability of the numerical algorithms to perform 3-D calculations and capture 3-D geological details.

6.5.1 Numerical model

The 3-D numerical model and setup are discussed in this section.

6.5.1.1 Sliding surface

The slope slid on top of the strong Oolitic limestone formation (see Fig. 6.2, p. 152, and Fig. 6.3, p. 155). The attitude of the strong layer below the Oolitic limestone can help reconstruct the strata of the overlying formation (cf. Broili, 1967).

According to Broili (1967, p. 63), the Oolitic limestone at the "back" of the western edge has an average dip direction of 6 - 13° and dip of 38°. At the middle-eastern area, the "back" has a dip direction of 353° and dip of 43°. From the western to the eastern end of the slope, the slide surface has an apparent dip of 36 - 40° in the N-S direction (Broili, 1967, p. 69).

Recall that the East-West section of the "seat" of the sliding surface forms a bowl-shaped structure (see Fig. 6.3, p. 155). The Oolitic limestone dips from 8°-17° eastward with dip direction being 70 - 90° (Broili, 1967, p. 63). The average dip of the sliding surface rising eastward and westward was 13° and the lowest depression of the section was at 545m (Broili, 1967, p. 71). According to Hendron & Patton (1985, p. 25), the bedding planes are steeper (17 - 22°) on the west end and flatter (10 - 11°) in the centre. It steepens again to 30 - 40° closer to the east. The east boundary was found to be stair-stepped by Broili (1967) and Hendron & Patton (1985). But this stair-shaped structure was not predefined in the model here, and was allowed to develop on its own in the course of simulation. That is to say, the bedding at the "seat" was allowed to continue to dip eastward, rather than making it curve upward close to the eastern end. In this chapter, the following sliding surfaces were adopted (the notation of dip-direction/dip is used):

Back-West: 9.5°/38° (Broili, 1967)

Back-Centre and East: 353°/43° (Broili, 1967)

Seat-West: 80°/19.5° (Hendron & Patton, 1985)

Seat-Centre: 80°/10.0° (dip direction adopted from Broili (1967) and dip adopted from Hendron & Patton (1985))

The shear softening model (Eq. (6.7)) only acts on the slide surface west of the eastern boundary. The shear resistance afforded by the slide surface extending eastward beyond the eastern boundary is assumed to be that of the rock mass rather than the clay layer.

6.5.1.2 Discontinuities and bedding planes

According to Müller (1968, p.14), two major sets of discontinuities were present. The first dips subvertically and strikes N-S. The second strikes normal to the first, i.e., about E-W, and also dips vertically. Müller (1968, p. 9) found that the layers dip generally 35 - 45° to the North. Broili (1967) suggested that the beddings dip 45 - 50° northward and changed at

the gorge to 12-18° eastward. Based on this information and the direction of the slide surface, the directions of the bedding planes adopted were (the notation of dip-direction/dip is used):

Bedding planes of the "back": 0°/45°

Bedding planes of the "seat": 80°/10°

The former was chosen because it conforms to both suggestions by Müller (1968) and Broili (1967); the latter was chosen so that the bedding planes are parallel to the seat of the slide surface.

6.5.1.3 Numerical parameters

In this 3-D model (see Figs. 6.30 and 6.31), the joint spacing is set to 80 m, and the joint normal and shear stiffness are 0.096 GPa/m and 0.0384 GPa/m respectively. The slide surface normal and shear stiffness are 2 GPa/m and 0.1 GPa/m respectively. Two vertical eastern faults were introduced into the model, with dip directions 0° and 110° respectively (see Fig. 6.1, p. 152). The rock joint friction angles are 40° while the friction angles of the

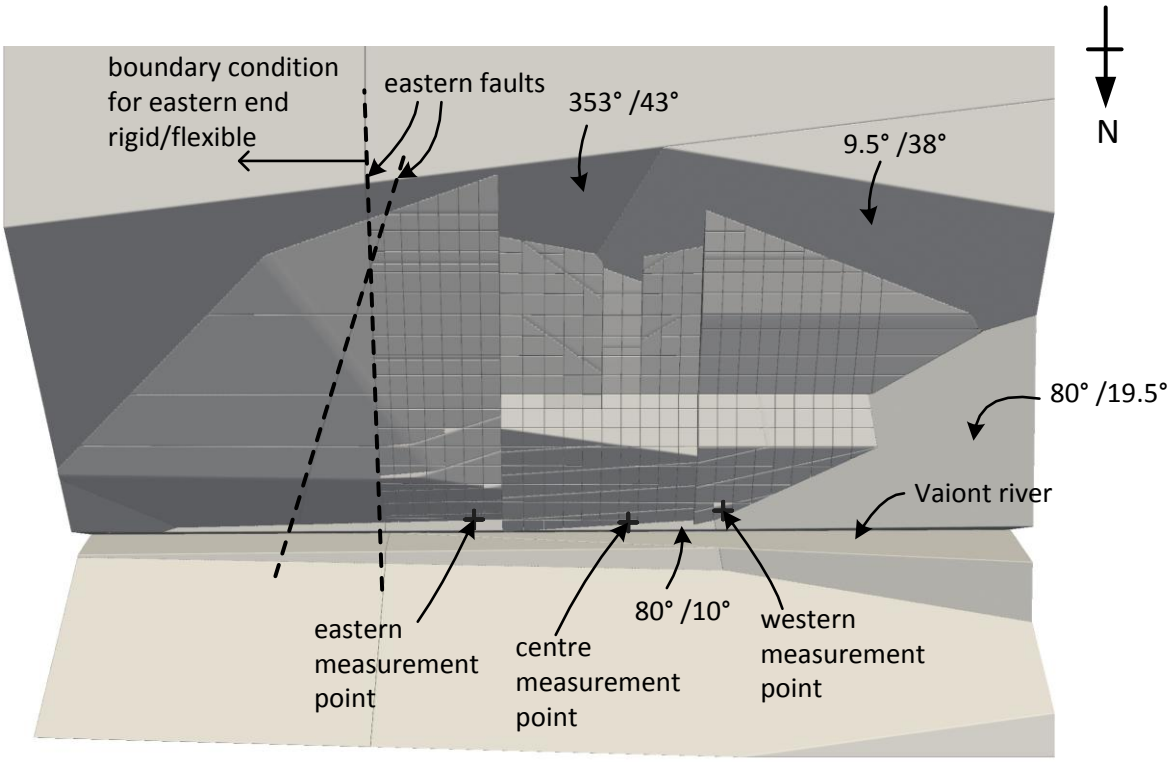

Fig. 6.30. Plan view of initial slope model. The displacement of three blocks are measured.

eastern faults were set to 36° (Hendron & Patton, 1985, p. 61), both of which adopt the elastic-perfectly plastic contact model in the shear direction.

(a)

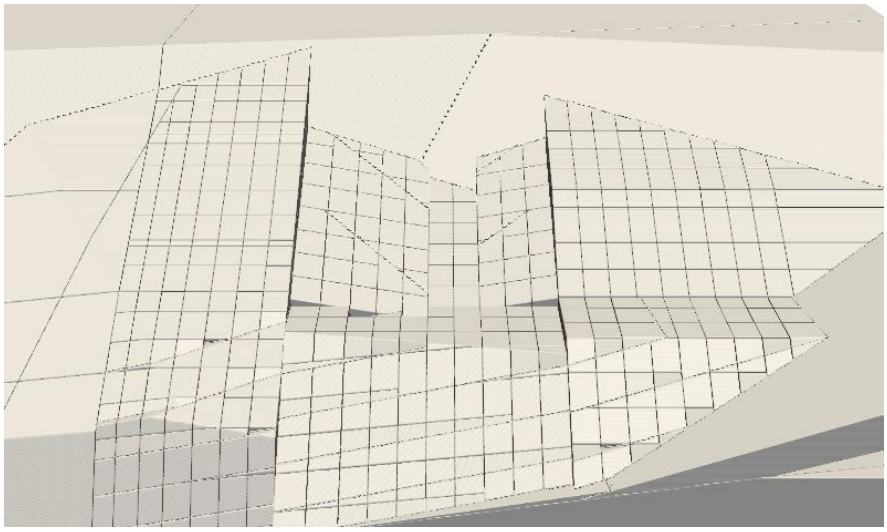

(b)

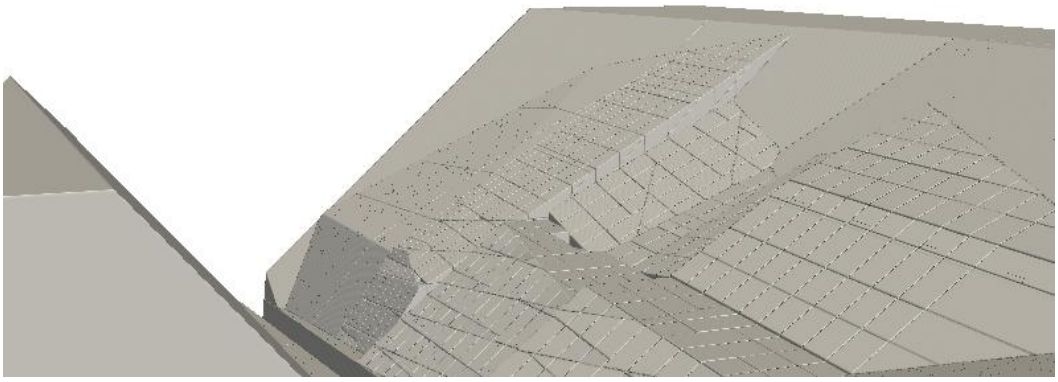

(c)

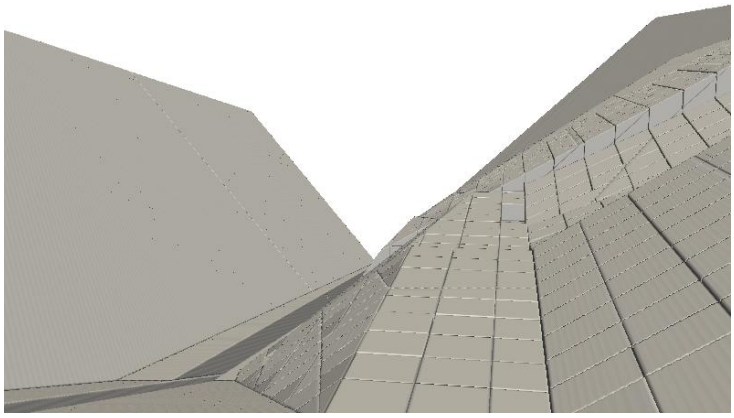

Fig. 6.31. Views of slope model (a) view from front , (b) view from western end, (c) view from western end facing east along slope profile in 3-D model. Jagged appearances are numerical artifacts of the display tool.

6.5.2 Results and comments

Two types of analyses were run. The first employed strength reduction on the slide surface to bracket the failure friction angle, as in the 2-D case. The rate of strength reduction is the same as that used in 2-D for the central analysis, i.e. 0.025°/s, unless otherwise mentioned. The second involves generating the slope at a specified friction angle, with a reservoir water level before filling, i.e. 460 m a.s.l. Thereafter, the water level was raised gradually. The water table was assumed to be horizontal.

6.5.2.1 Influence of eastern boundary and water level

The time-step used in 2-D (0.001 sec/step) was first verified as to whether it was still valid in this 3-D model. The slope response from using three different time-steps, 0.0005 sec/step, 0.001 sec/step and 0.002 sec/step is shown in Fig. 6.32. The results obtained from using 0.001 sec/step and 0.0005 sec/step are very close to each other, while the results obtained from using 0.002 sec/step showed significant deviation. Therefore, as with the 2-D models, the time-step for the 3-D models was chosen as 0.001 sec/step.

Fig. 6.33 shows that the results of strength reduction for the slope with rigid and flexible eastern boundaries, i.e. whether or not kinematic freedom is restricted (see Fig. 6.30, p. 191). This result confirms that the additional shear resistance of the eastern boundary hypothesised by Hendron & Patton (1985) is important. From Fig. 6.33, it is worth highlighting that, compared to the 2-D case, the slide behaviour is more ductile. This result

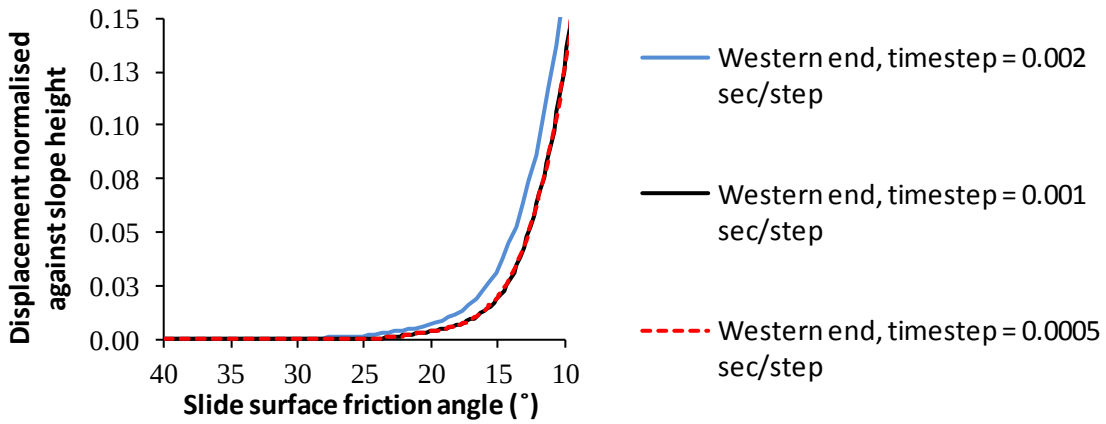

Fig. 6.32 Slope displacements versus slide surface friction angle (strength reduction) for different time-steps in 3-D. Strength reduction rate = 0.5°/sec. The displacements are normalised by 575 m, which is the same as the 2-D models.

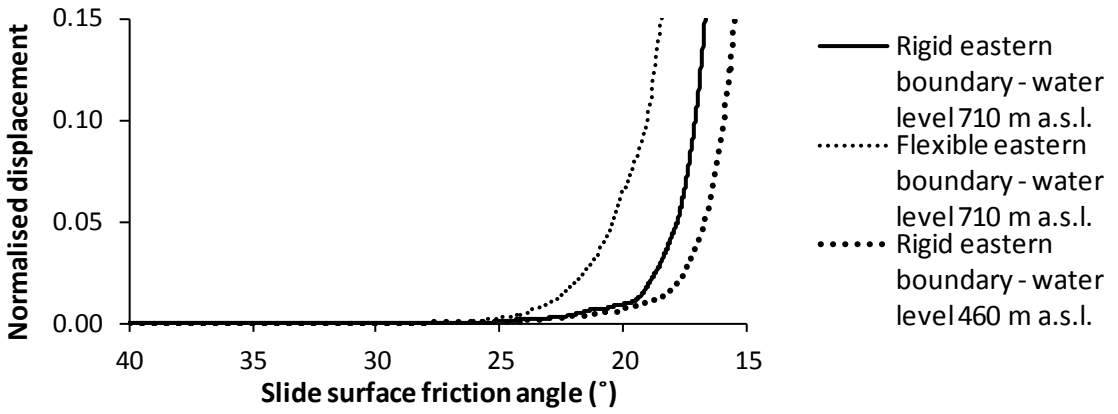

Fig. 6.33 Influence of eastern boundary and water level on the critical friction angle

is reasonable because, in 3-D, there exists larger kinematic freedom about which the rock mass can move. Conversely, in 2-D, movement is constrained to a plane, and failure will be more abrupt. Because of the ductile failure mechanism in Fig. 6.33, it is difficult to define the failure friction angle precisely. Determining failure for engineering structures which exhibit non-linear load-displacement behaviour is less straightforward, unlike rigid-perfectly plastic material. The differences between collapse and safe loads for a footing foundation have been discussed in Atkinson (2007). It will be helpful therefore to analyse the results here for the Vaiont slope using the same concepts. With rigid eastern boundaries and reservoir water level 710 m a.s.l. (solid line in Fig. 6.33), onset of failure was observed at approximately 26°. The ultimate failure friction angle, associated with complete loss of resistance, is approximately 18°. Note these values compare well with the failure friction angles found by Paronuzzi et al. (2013) through 2-D finite element analyses conducted on different slope sections, i.e. 17.5 - 27°. From Fig. 6.33, friction angles above 20° appear to be safe. The displacement-strength curve for a flexible eastern boundary is approximately 3° more critical than the case with rigid eastern boundaries. On the other hand, for water level 460 m a.s.l., i.e. before filling of reservoir, the curve is approximately 1.5° less critical than the case with reservoir water level 710 m a.s.l. This influence of water level compares well with the 2-D case (approximately 1.8°).

Although the geologically complex Vaiont rock slope is simplified in the 3-D model (Fig. 6.30, p. 191), the model captures the essential geometrical features of the slope. There

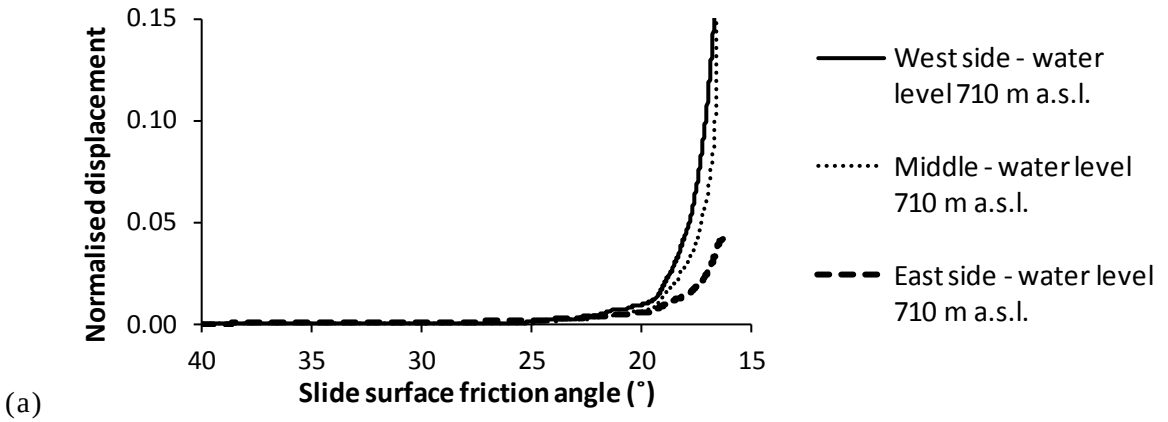

(a)

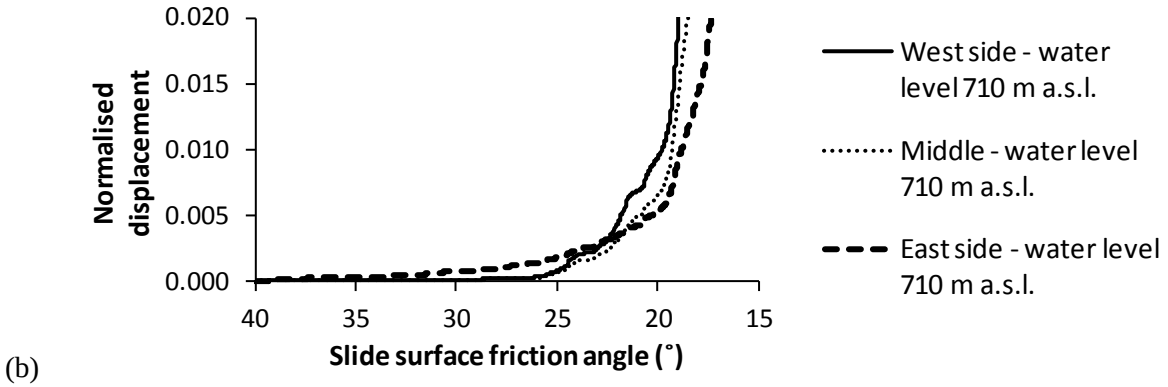

(b)

Fig. 6.34 Displacement of different parts of the slope (rigid eastern boundaries) with strength reduction: (a) and (b) are drawn using different scales in the vertical axes

is interesting insight that the slope at different sections did not move uniformly (see Fig. 6.34). At high friction angles, the eastern end of the slope experienced larger movements compared to the centre and western ends of the slope (see Fig. 6.34 (b)). For friction angles smaller than approximately 23° (closer to ultimate failure), the cumulative displacements at the western end of the slope were larger than the eastern end. It is interesting to note that from field measurements (Müller, 1964), the western end of the slope experienced larger displacements than the eastern end. However, from the 2-D back analyses by Hendron & Patton (1985) and Paronuzzi et al. (2013), the eastern end of the slope was found to be more critical than the western end. The 3-D results in Fig. 6.34 can explain these contradictory results in terms of kinematics. The loss of stability in the eastern end does not lead to an abrupt failure.

The failure friction angle (between 18 - 26°) in this 3-D study is nowhere near 12° as suggested by Hendron & Patton (1985). It is still a topic of debate as to whether the actual shear strength of the clayey slide surface reached residual values (Vardoulakis, 2002) after

the first slide, and whether there was strength recovery. Recent site investigations by Paronuzzi & Bolla (2012) suggested that the slide surface involved a thick shear zone (40 - 50 m), in which the friction angle is closer to crushed angular rock material.

6.5.2.2 Simulations with rising water level

According to field measurements, the slope experienced creep up to approximately 3 m before the actual slide (Müller, 1964). The actual slide was believed to be triggered by the velocity softening effect at the clay layer discussed previously in Section 6.1.4 (cf. Ferri et al. (2011)); the slope experienced some movement with reservoir water filling, and the slope movement hit a critical velocity beyond which it could not be arrested even though the reservoir water level was lowered. Therefore, there is a wide range of slide surface friction angles (before ultimate collapse) at which this phenomenon could have taken place. The exact slide surface friction angle values are not investigated here because it is impractical to simulate the slope movement using the same time scale as the actual field conditions.

3-D simulations were carried out to model more realistically the situation before the actual Vaiont slide. The simulations were carried out using two peak slide surface friction angle values, i.e. 26° and 21°. These friction angles were above the ultimate failure friction angles for the case of reservoir water level 460 m and 710 m a.s.l. (see Fig. 6.33). The initial water level was assigned as 460 m a.s.l. for each simulation, and the water level was increased with time (red line in Fig. 6.35). The rate of reservoir filling was 0.25 m/s. Like all the previous simulations, the slope was generated with local damping until the kinetic energy, unbalanced forces and slope displacements were sufficiently low, before the raising of water level was carried out. At this stage, local damping was removed and viscous damping at the contacts was activated. Shear softening of the stiff clay layer (Eq. (6.7)) was allowed to take place, but the effect of shear softening with velocity was not studied here (cf. Ferri et al., 2011). The results for the peak slide surface friction angles 26° and 21° are shown in Fig. 6.35 (a) and (b) respectively. The results show that for peak slide surface friction angle of 26°, the eastern end of the slope initially experienced larger displacements compared to the western end. For peak slide surface friction angle of 21°, the western end of the slope experienced larger displacements, which is more consistent with field

measurements. The results for the relative displacements between eastern and western sections are consistent with the previous trends obtained from running strength reduction on the slide surface (see Fig. 6.34, p. 195).

It is important to mention that the rate of strength reduction (friction angle) or the rate of raising the water level was not investigated here due to time constraints. The simulations for the latter are not of the same time-scale as the filling of the actual reservoir. A brief discussion is nonetheless mentioned. Movement was found to take place very slowly in the numerical model and can be seen to continue for a long duration (see Fig. 6.35 (a) and (b)). Note that, as with the case in 2-D, after local damping is switched off at the end of the generation stage, the damping mechanism in the numerical model is minimal, i.e. viscous

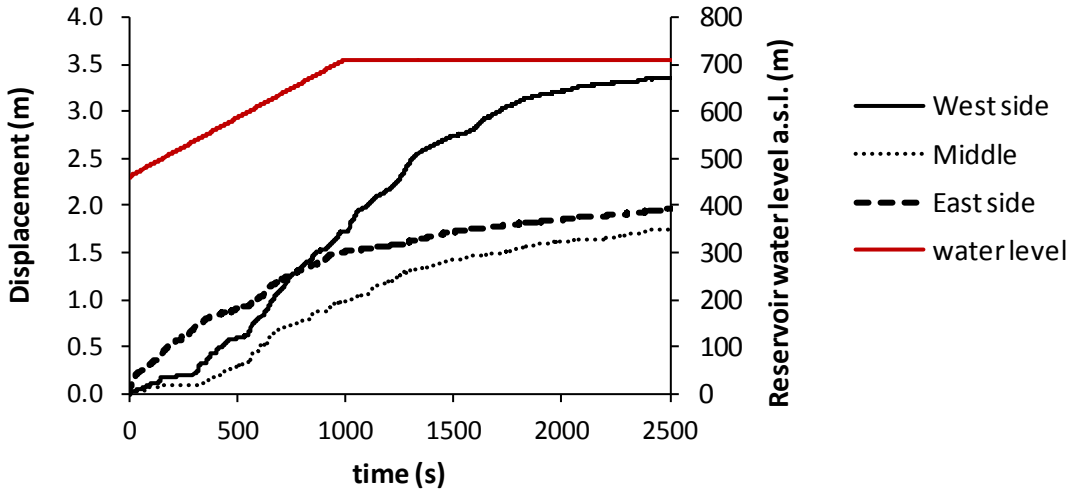

(a)

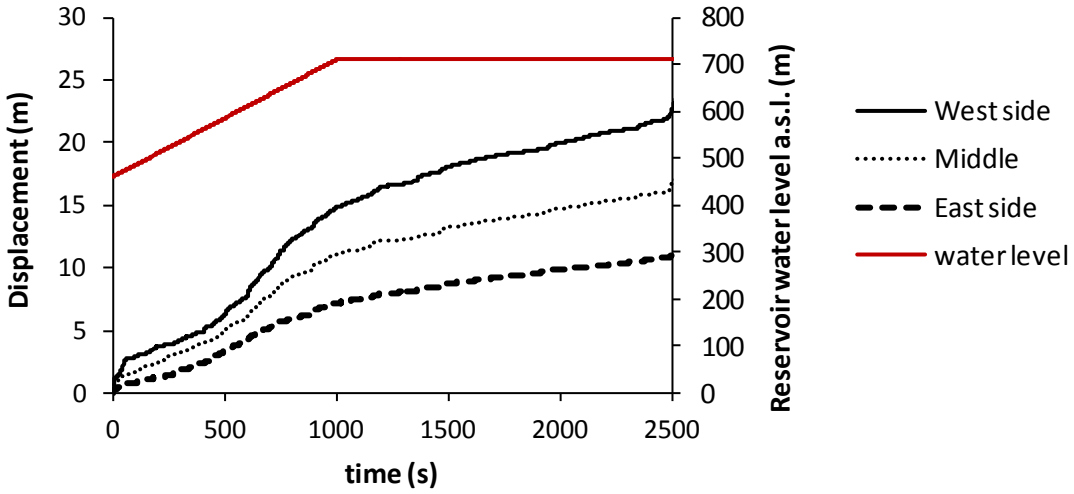

(b)

Fig. 6.35 Slope movement with reservoir filling at slide surface friction angles (a) 26° and (b) 21°

contact damping coefficient ξ = 0.1. This behaviour of slow movement is reasonable if some parts of the slope had failed, and the blocks were allowed to continue to readjust themselves dynamically. To check that this behaviour is not a numerical artifact, the simulation was repeated for slide surface friction angle 35°, and the slope was able to stabilise without difficulty (see Fig. 6.36).

6.5.2.3 Discussion of failure shape

Recall that the discordance between bedding planes at the eastern "seat" of the slope and the bowl-shape of the slide surface perpendicular to the slide direction was highlighted by Broili (1967) and Hendron & Patton (1985). In the DEM simulations, angular distortion was also observed at the eastern periphery/boundary of the slope (H-H section of failed slope in Fig. 6.37 is shown in Fig. 6.38), and is consistent with field observations. In Figs. 6.37 and 6.38, separations and relative rotations between rock blocks can be observed towards the eastern end; and the rock blocks towards the centre and western areas are arranged more uniformly. Because of the geometrical discordance between the slide surfaces (see Fig. 6.38), the rock slope did not shear entirely along the weaker eastern fault ($\phi_{\text{eastern\_fault}}$ = 36° compared to ϕ_{joint} = 40°).

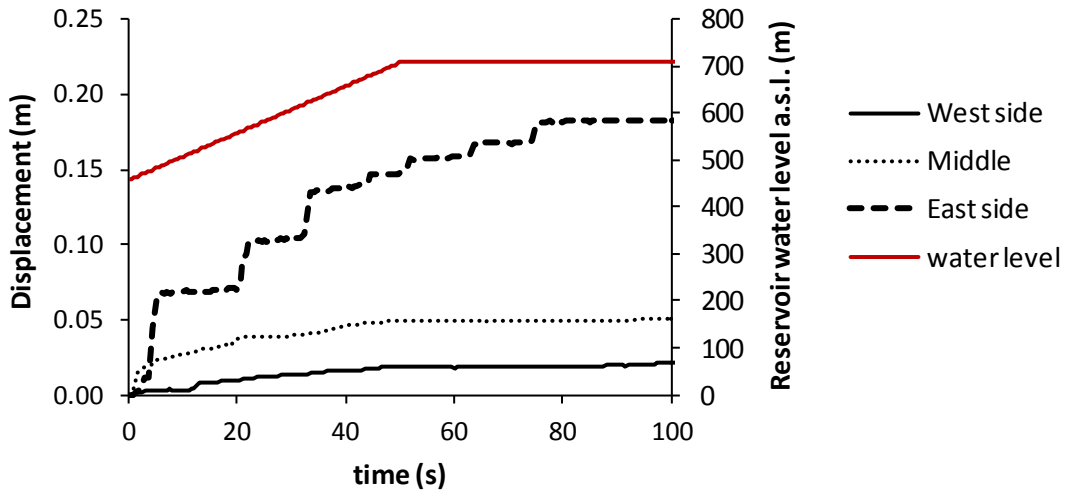

Fig. 6.36 Slope movement with reservoir filling at slide surface friction angle 35°. Reservoir water filling rate = 5 m/s, and no shear softening at the slide surface.

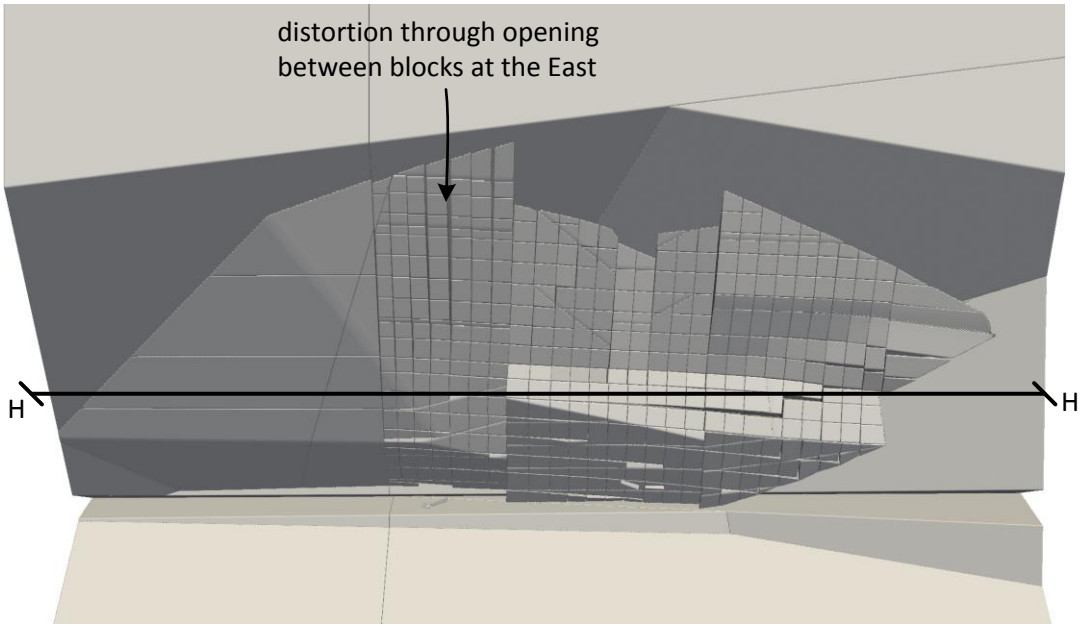

Fig. 6.37 Plan view of failed slope model. H-H' section of slope after failure is shown in Fig. 6.38.

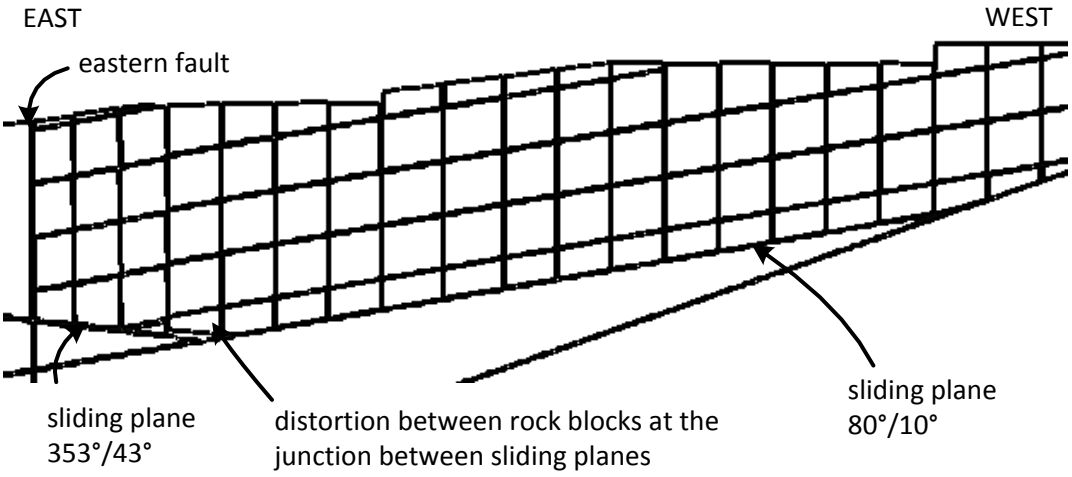

Fig. 6.38 H-H section of slope model in Fig. 6.37 (Note that the eastern end of the slope is on the left). Jagged lines are numerical artifacts of the display tool.

6.6 CONCLUDING REMARKS

The numerical algorithms proposed in this thesis (Chapter 3) were used to model a case study, namely the 1963 Vaiont rock slide in Italy. A prominent feature of this case study is a chair-shaped slope, and its abrupt failure. The stability of this slope was investigated through parametric analysis in 2-D, showing that the numerical tools are versatile and can be used to examine various physical and geometrical parameters. It was found that, because of

the peculiar shape of the slope and slide surface, the deformability parameters which have been hitherto neglected by other investigators are important. The back-calculated failure friction angle in 2-D from this numerical study is approximately 20.6°, and is within the range of friction angles deduced by other investigators (see Table 6.3, p. 158).

A 3-D analysis was undertaken to capture the influence of the eastern boundary, the importance of which was highlighted by Hendron & Patton (1985). The resistance afforded by the eastern boundary was found to be important, making the slope less critical to collapse by approximately 3°. The results show that behaviour in 3-D is complex. For a rigid eastern boundary, the slope was found to exhibit signs of failure beginning from 26°, before complete loss of resistance at 18°. Note that the eastern section, which was found to be more critical by Hendron & Patton (1985) from back calculations, experienced less movement than the western section in the field (Müller, 1964). The 3-D simulations showed that, for high slide surface friction angles, the eastern end of the slope experienced larger movement than the western end. But for low friction angles (approximately smaller than 23°), the western end of the slope experienced larger displacements than the eastern end. This is more consistent to field observations, and suggest that some parts of the Vaiont slope may have already failed at the beginning before reservoir filling, but movement was successfully arrested by stronger parts of the slope which had not failed. To sum up, this chapter shows that the numerical tools were able to capture specific geological detail in both 2-D and 3-D, and give useful insights to an actual case study, about which there is still incomplete understanding amongst the geotechnical community.

CHAPTER 7
CONCLUSIONS

7.1 SUMMARY OF THESIS CONTRIBUTIONS AND CONCLUSIONS

In this thesis, novel numerical tools for modelling a jointed rock mass using the distinct element method (DEM) have been proposed. In particular, two novel algorithms were presented in Chapter 3, namely rock slicing for block generation and contact detection between polygonal (2-D) and polyhedral (3-D) particles.

7.1.1 Rock slicing algorithm (Chapter 3)

In existing block generation algorithms, the updating and maintenance of a multi-level hierarchical polyhedron data structure require tedious bookkeeping procedures in computer code. The literature review in Chapter 2 suggests that bookkeeping becomes more manageable when a two-level data structure (Heliot, 1988) is used instead of a three-level data structure (Warburton, 1985).

A novel block generation algorithm based on the sequential subdivision approach, which employs a single-level data structure, has been proposed in Chapter 3. This is believed to be the simplest possible data structure that could be used to define a polyhedron in a computer code for block generation. The identification of blocks has been reduced to a set of linear programming optimisation problems which can be solved efficiently using standard software for linear programming, such as CPLEX (2003). Unlike existing methods, information with regard to vertices and edges are not involved in the rock slicing procedure, and the algorithm only needs to keep track of the faces of each polyhedron. In this respect, this algorithm is less sensitive to numerical rounding errors. During block identification, problems related to incompatible hierarchical data structures, i.e. vertices, edges or faces not joining correctly, are not present. Because only a single level data structure is used, the increase of complexity from 2-D to 3-D is minimal. Therefore, in terms of implementation, it is also more tractable to engineers who do not have block generation software at their disposal. The feature of joint shape or persistency is modelled by introducing additional constraints to the linear program. To increase the efficiency of the algorithm, the use of

bounding spheres is proposed so that the majority of non-intersecting cases can be ruled out quickly.

7.1.2 Contact detection algorithm (Chapter 3)

The literature review in Chapter 2 suggests that existing contact detection algorithms to-date between polyhedral particles suffer from one of the following limitations: (i) tedious housekeeping procedures are required, e.g., to identify the different types of interaction – face-face, face-edge, face-vertex, edge-edge, edge-vertex, or vertex-vertex, (ii) relying on a heuristic approach to find a good-enough contact point which is non-unique, or (iii) the calculation procedures for the overlap distance and contact normal are ambiguous at sharp corners.

To address the challenges in the previous paragraph, a novel contact detection algorithm between polygonal and polyhedral particles has been mathematically formulated such that it can be calculated using convex optimisation techniques, for which there exist efficient solution procedures. As with the rock slicing algorithm, a single-level data structure is used to define the polyhedron and polygon in both 2-D and 3-D respectively, i.e. lines in 2-D and faces in 3-D. The contact point is calculated from an appropriately defined centre which falls inside the overlap volume, i.e. the analytic centre of inequalities defining the pair of interacting polyhedra. The contact normal can be calculated from the gradient vector of an inner "potential particle" whose corners are rounded (cf. Houlsby, 2009). Like the proposed rock slicing algorithm, the increase in complexity of this contact detection algorithm is minimal when 3-D problems are considered rather than 2-D ones. This is in contrast to existing algorithms in the literature in which the upgrade from 2-D to 3-D requires additional thorough code development. Another minor advantage of the algorithm is that, since information on edges, vertices and their adjacency relations are not required by the algorithm, this can lead to memory savings.

7.1.3 Examples and validation (Chapter 4)

In Chapter 4, the proposed rock slicing algorithm has been shown to be capable of generating slope profiles, concave blocks, non-persistent joints and block assemblies which are representative of the assigned joint patterns. Because the jointed rock mass has to be

represented as polygons or polyhedra in the DEM, simplification of the assigned joint patterns is inevitable. By comparison to the block assembly presented in Kim et al. (2007) which was generated using the commercial DEM software, UDEC (Itasca, 2004), the block assembly generated using the proposed algorithm (Chapter 3) is believed to be more consistent with the engineering practice of introducing a safety factor and not underestimating the forces of nature (Terzaghi, 1936); dangling joints are not erased but must terminate at existing joints during the sequential subdivision calculation. However, the same block assembly in UDEC could be generated using the proposed rock slicing algorithm, if more advanced clustering algorithms (Yu et al., 2009) are implemented. The rock slicing algorithm has also been shown to scale linearly with the number of generated blocks, when used together with bounding spheres. This finding is important because the typical problem size in engineering tends to grow with time, and the algorithm will not become obsolete in the future.

The contact detection algorithm was found to be robust in collision tests involving various contact scenarios, and was found to be computationally efficient. The robustness of both the block generation and contact detection algorithms has been examined using a range of simulations, some of which involve comparisons against analytical and numerical solutions for typical problems in rock engineering, i.e., 3-D wedge sliding, 3-D roof fall, 2-D roof buckling and 2-D slope slumping. The favourable comparison indicates that the tools are robust at modelling both stability and stiffness type problems. Close agreement was obtained in a comparison exercise against the numerical simulations carried out by Tsesarsky & Talesnick (2007) using FLAC (Itasca, 2000) for a jointed beam problem; the DEM models consisted of 6 rigid blocks with compliant contacts, while the FLAC model consisted of 3750 elements (25 × 25 finite difference zones for each block). Additional effort was invested in deriving more accurate contact models from the published experimental data to explain the discrepancy observed between the numerical simulations and experimental measurements reported in Talesnick et al. (2007). Better agreement with the experimental measurements was obtained using the more accurate contact models, suggesting that the proposed numerical tools in Chapter 3 are reliable, in that the global behaviour of a jointed

rock structure, for which there is no prior programmed outcome, can be captured through local rules implemented at the contact between particles. Another lesson of this exercise is that, in practice, the errors due to the geometrical simplification of contacts using the proposed contact detection algorithm is likely to be secondary compared to the errors due to using inaccurate contact constitutive models. This observation is important because uncertainties as to whether discrepancies are caused by either numerical artifacts or inaccurate physical constitutive models would cause the interpretation of results significantly more difficult for engineers.

7.1.4 Modelling of underground openings (Chapter 5)

A substantial fraction of the thesis is then devoted to verifying and demonstrating the capabilities of the numerical tools at solving problems for which the DEM has found practical application. Chapter 5 illustrates how the engineer can use these numerical tools to design the support structures for underground openings from the beginning of the design process. The failure patterns for rock masses with more than two joint sets were explored first in the chapter, and the failure patterns were found to be numerous. It is difficult to associate the observed failure patterns with a particular joint pattern, indicating that the conventional geotechnical practice of supporting a large circumference of an opening is essential for moderately to heavily jointed rock masses. This finding is in contrast to 2-D models consisting of two joint sets only; previous investigators found that their failure patterns follow common trends (Yeung & Leong, 1997; Solak & Schubert, 2004; Solak, 2009).

To apply the numerical tools in Chapter 3 in a more realistic setting, i.e. for support design, it was necessary to couple the tools with rock support algorithms in the literature. The algorithms which have been proposed in the literature to model rock bolts were reviewed, from which one was implemented into the DEM code. In a similar manner, one of the lining support algorithms proposed in the literature was implemented into the DEM code. The numerical tools have been found to be capable of examining the influence of various support parameters, such as rock bolt length and spacing, and lining axial and bending stiffness, as well as the contact stiffness at the rock-lining interface. Several block

assemblies generated from the same joint statistical distribution were analysed, and the results indicate that the prediction of support loads can be analysed more appropriately using a statistical approach when making engineering judgement.

The DEM simulations, for openings with lining support only and rock bolt support only, were verified against elastic solutions which have been proposed in the literature. Comparisons against elastic solutions were possible because the opening in the DEM simulations was wished-in-place and the support structures were installed immediately. The results of the comparison were encouraging, suggesting that these numerical tools can be used to model more complex engineering problems robustly. Verification against elastic solutions is considered more robust by comparison to validation against field measurements, because uncertainties in terms of physical parameters may cause models with different combinations of input to arrive at the same solution (cf. Einstein et al., 2010). When less support is provided, the predicted support forces by the numerical models are larger than the elastic solutions. This is not surprising since plastic displacements were likely to have had occurred.

Two ways of designing support structures, consisting of both rock bolts and lining, were then illustrated. In the first method, the optimal bolt spacing is first sought, followed in turn by the lining thickness. The second method employs a rock bolt and lining interaction diagram. The diagram can help the engineer evaluate the relative benefit of introducing more rock bolts or increasing the lining thickness. The analyses in this chapter indicate that the relative stiffness of the rock bolt, lining and rock mass are important parameters in governing the effectiveness of the overall support system. This finding also demonstrates that the design philosophy of relative stiffness developed from continuum principles could also be captured using the proposed numerical tools in Chapter 3. Specific numerical findings in this chapter are unlikely to be universal because there exists a large number of variables which could affect the performance of an actual tunnel opening. Nonetheless, it has been shown that the tools proposed in Chapter 3, can be used together with rock support algorithms, to examine the various parameters which govern the performance of a supported underground opening. This exercise is important because it corresponds more closely to the

actual problems for which the tools would be applied by practising engineers. Suggestions have also been made with regard to the practical application of these tools for support design.

7.1.5 Case study of 1963 Vaiont rock slide (Chapter 6)

The thesis concludes by modelling a case history using the proposed numerical tools – the 1963 Vaiont rock slide. The purpose is to demonstrate that the proposed numerical tools are capable of capturing specific physical and geometrical detail in 2-D and 3-D. A well-known feature of this rock slide is its chair-shaped slope, and its abrupt failure. The stability of this slope was investigated through parametric analysis in 2-D, showing that these numerical tools are versatile and are capable of examining various physical and geometrical parameters. A 3-D analysis was undertaken to investigate the influence of the eastern boundary, the importance of which was highlighted by Hendron & Patton (1985).

The results of the 2-D numerical study show that the most important parameter affecting the slope stability is the reservoir water level. The study also shows, because of the peculiar shape of the slope and slide surface, the rock mass deformability which has been hitherto neglected by other investigators is important. The 3-D results show that the shear resistance afforded by the eastern boundary is significant; the friction angle required for stability was found to be approximately 3° lower compared to the case when the eastern boundary was flexible. However, the back calculated failure friction angles (for the reservoir water level 710 m a.s.l.) for both 3-D and 2-D are above 12°, i.e. the value suggested by Hendron & Patton (1987) for the slip surface with clay layers. In 2-D, the failure friction angle was found to be approximately 20.6° for the western section (A-A in Broili, 1967). The determining of failure is more difficult in 3-D, because the slope behaviour was found to be ductile and non-uniform across the slope. The strength of the slope was found to be completely lost at 18°, but was found to exhibit signs of failure, i.e. large displacements, from 26° onwards. This is more representative of the field condition in which the slope was moving (or failing) progressively with the raising of water level, rather than sliding abruptly. The actual slide is believed to be triggered by the shear softening effect with velocity (Ferri et al., 2011) which is not investigated here. Because simulations

of the same time-scale as the filling of reservoir were not carried out in this numerical study, only a crude range of plausible friction angles at the slip surface could be bracketed from the 3-D simulations, i.e. between 18 - 26°. Overall, this case study shows that these numerical tools are able to capture specific geological detail in both 2-D and 3-D, and give useful insights to an actual case study, which is of interest to the geotechnical community.

7.2 RECOMMENDATIONS FOR FUTURE WORK

These numerical studies were concerned mainly with showing the usefulness and capabilities of the numerical tools proposed in Chapter 3. In the subsequent chapters, several peripheral conclusions were drawn, some of which suggest additional research that is worth pursuing.

The 2-D models in Chapter 5 assumed that the opening was wished-in-place and that the support structures were installed immediately. The procedures proposed here, i.e. interaction diagrams, may lead to more interesting observations if well-known tunnel design concepts developed for ground response curves are considered (cf. Hudson & Harrison, 1997). The interaction diagrams could also be applied on 3-D models.

In the case study on the Vaiont rock slide (Chapter 6), a more realistic constitutive model, with shear softening and a non-linear shear strength envelope could be used to model the rock mass. It is also worthwhile for the modeller to devise a robust methodology to model the slide surface so that there is shear softening with velocity. Because the rock slope was found to be overly sensitive to perturbations when shear resistance was modelled as a function of velocity, this work was not pursued further.

7.3 OVERALL THESIS SUMMARY

Efficient numerical tools in the DEM have been proposed in this thesis to model the jointed rock mass. Their robustness had been tested rigorously through numerous verification exercises, by comparing the DEM calculations with analytical, numerical and experimental work of other researchers. The thesis also demonstrates how the numerical tools can be used to help make support design decisions for underground openings. The numerical tools have also been shown to be capable of capturing specific geological detail of a case study and give useful insights through sensitivity analyses.

REFERENCES

Alonso, E. E., & Pinyol, N. M. (2010). Criteria for rapid sliding I. A review of Vaiont case. Engineering Geology, 114(3-4), 198-210.

Alonso-Marroquín, F. (2008). Spheropolygons: A new method to simulate conservative and dissipative interactions between 2D complex-shaped rigid bodies. EPL (Europhysics Letters), 83(1), 14001.

Anderson, D. L. (1985). Static slope analysis method used for the Vaiont slide analyses. In A. J. Hendron Jr & F. D. Patton (Eds.), The Vaiont slide, a geotechnical analysis based on new geologic observations of the failure surface. Washington: US Army Corps of Engineers.

Andrade, J. E., Lim, K. W., Avila, C. F., & Vlahinić, I. (2012). Granular element method for computational particle mechanics. Computer Methods in Applied Mechanics and Engineering, 262-274.

Asadollahi, P., Invernizzi, M. A., Addotto, S., & Tonon, F. (2010). Experimental Validation of Modified Barton's Model for Rock Fractures. Rock Mechanics and Rock Engineering, 43(5), 597-613.

Baecher, G. B. (1983). Statistical analysis of rock mass fracturing. Journal of the International Association for Mathematical Geology, 15(2), 329-348.

Baena, D., & Castro, J. (2011). Using the analytic center in the feasibility pump. Operations Research Letters, 39(5), 310-317.

Bandis, S. C., Lumsden, A. C., & Barton, N. R. (1983). Fundamentals of rock joint deformation. International Journal of Rock Mechanics and Mining Sciences & Geomechanics Abstracts, 20(6), 249-268.

Barton, N. (1973). Review of a new shear-strength criterion for rock joints. Engineering Geology, 7(4), 287-332.

Barton, N. (2002). Some new Q-value correlations to assist in site characterisation and tunnel design. International Journal of Rock Mechanics and Mining Sciences, 39(2), 185-216.

Barton, N., By, T. L., Chryssanthakis, P., Tunbridge, L., Kristiansen, J., Loset, F., Bhasin, R. K., Westerdahl, H., Vik, G. (1994). Predicted and measured performance of the 62-m span Norwegian-Olympic-Ice-Hockey-Cavern at Gjovik. International Journal of Rock Mechanics and Mining Sciences & Geomechanics Abstracts, 31(6), 617-641.

Barton, N., Lien, R., & Lunde, J. (1974). Engineering classification of rock masses for the design of tunnel support. Rock Mechanics Felsmechanik Mécanique des Roches, 6(4), 189-236.

Bawden, W. F. (1993). The use of rock mechanics principles in Canadian underground hard rock mine design. Comprehensive rock engineering. Vol. 5, 247-290.

Belloni, L. G., & Stefani, R. (1987). The vajont slide: instrumentation- Past experience and the modern approach. Engineering Geology, 24(1-4), 445-474.

Bergen, G. V. d. (1999). A fast and robust GJK implementation for collision detection of convex objects. J. Graph. Tools, 4(2), 7-25.

Beyabanaki, S. A. R., Mikola, R. G., & Hatami, K. (2008). Three-dimensional discontinuous deformation analysis (3-D DDA) using a new contact resolution algorithm. Computers and Geotechnics, 35(3), 346-356.

Bhasin, R., & Kaynia, A. M. (2004). Static and dynamic simulation of a 700-m high rock slope in western Norway. Engineering Geology, 71(3-4), 213-226.

Bhasin, R. K., Barton, N., Grimstad, E., Chryssanthakis, P., & Shende, F. P. (1996). Comparison of predicted and measured performance of a large cavern in the Himalayas. International Journal of Rock Mechanics and Mining Sciences & Geomechanics Abstracts, 33(6), 607-626.

Bieniawski, Z. T. (1983). Geomechanics classification (RMR system) in design applications to underground excavations. Paper presented at the Proceedings - International Symposium on Engineering Geology and Underground Construction, Lisbon.

Bobet, A. (2009). Elastic solution for deep tunnels. Application to excavation damage zone and rockbolt support. Rock Mechanics and Rock Engineering, 42(2), 147-174.

Bobet, A., & Einstein, H. H. (2011). Tunnel reinforcement with rockbolts. Tunnelling and Underground Space Technology, 26(1), 100-123.

Boon, C. W., Houlsby, G. T., & Utili, S. (2011). A new contact detection algorithm for non-spherical particles in the Discrete Element Method. In S. Pietruszczak & G. N. Pande (Eds.), 2nd International Symposium on Computational Geomechanics, COMGEO II, Cavtat-Dubrovnik; Croatia, 27-29 April 2011.

Boon, C. W., Houlsby, G. T., & Utili, S. (2012). A new algorithm for contact detection between convex polygonal and polyhedral particles in the discrete element method. Computers and Geotechnics, Vol. 44, 73-82.

Boon, C. W., Houlsby, G. T., & Utili, S. (2013). A new contact detection algorithm for three-dimensional non-spherical particles. Powder Technology, Vol. 248, 94-102.

Boyd, S. P. (2004). Website for source code examples in Convex Optimization. Retrieved from http://www.stanford.edu/~boyd/cvxbook/cvxbook_examples/

Boyd, S. P., & Vandenberghe, L. (2004). Convex Optimization: Cambridge University Press.

Boyd, S. P., & Wegbreit, B. (2007). Fast computation of optimal contact forces. IEEE Transactions on Robotics, 23(6), 1117-1132.

Broili, L. (1967). New knowledge on the geomorphology of the Vaiont slide slip surfaces. Rock Mechanics and Engineering Geology, 5(1), 38-88.

Bym, T., Marketos, G., Burland, J. B., & O'Sullivan, C. (2013). Use of a two-dimensional discrete-element line-sink model to gain insight into tunnelling-induced deformations. Geotechnique, 63(9), 791-795.

Byrd, R. H., Nocedal, J., & Waltz, R. A. (2006). KNITRO: An integrated package for nonlinear optimization. Large-Scale Nonlinear Optimization, 35-59.

Caron, R. J., McDonald, J. F., & Ponic, C. M. (1989). A degenerate extreme point strategy for the classification of linear constraints as redundant or necessary. Journal of Optimization Theory and Applications, 62(2), 225-237.

Carranza-Torres, C. (2009). Analytical and numerical study of the mechanics of rockbolt reinforcement around tunnels in rock masses. Rock Mechanics and Rock Engineering, 42(2), 175-228.

Case, J., & Chilver, A. H. (1971). Strength of Materials and Structures: an Introduction to the Mechanics of Solids and Structures. Edward Arnold. 2nd Edition.

Chang, S.-W., & Chen, C.-S. (2008). A non-iterative derivation of the common plane for contact detection of polyhedral blocks. International Journal for Numerical Methods in Engineering, 74(5), 734-753.

Cho, N., Martin, C. D., & Sego, D. C. (2007). A clumped particle model for rock. International Journal of Rock Mechanics and Mining Sciences, 44(7), 997-1010.

Chowdhury, R. (1978). Analysis of the vajont slide - new approach. Rock Mechanics Felsmechanik Mecanique des Roches, 11(1), 29-38.

Chryssanthakis, P., Barton, N., Lorig, L., & Christianson, M. (1997). Numerical simulation of fiber reinforced shotcrete in a tunnel using the discrete element method. International Journal of Rock Mechanics and Mining Sciences & Geomechanics Abstracts, 34(3-4), 590.

Cleary, P. W. (2010). DEM prediction of industrial and geophysical particle flows. Particuology, 8(2), 106-118.

Cleary, P. W., & Sawley, M. L. (2002). DEM modelling of industrial granular flows: 3D case studies and the effect of particle shape on hopper discharge. Applied Mathematical Modelling, 26(2), 89-111.

Cleary, P. W., Stokes, N., & Hurley, J. (1997). Efficient collision detection for three-dimensional super-ellipsoidal particles. Paper presented at the Proceedings of the 8th International Computational Techniques and Applications Conference, CTA97, Adelaide.

Cohen, J. D., Lin, M. C., Manocha, D., & Ponamgi, M. (1995). I-COLLIDE: An interactive and exact collision detection system for large-scale environments. Paper presented at the Proceedings of the 1995 Symposium on Interactive 3D Graphics, Monterey, CA, USA.

CPLEX. (2003). IBM ILOG CPLEX 9.0 User's manual.

Crammond, E. (2007). Squaring the circle: arbitrarily shaped particle modelling in distinct element analysis, M. Eng. project report: Department of Engineering Science, Oxford University.

Crandall, S. H., Dahl, N. C., & Lardner, T. J. (1978). An introduction to the mechanics of solids (2 ed.). New York: McGraw Hill.

Cundall, P. A. (1971). A computer model for simulating progressive, large scale movement in blocky rock system. Paper presented at the Sympo. ISRM. , Nancy, France.

Cundall, P. A. (1988). Formulation of a three-dimensional distinct element model--Part I. A scheme to detect and represent contacts in a system composed of many polyhedral blocks. International Journal of Rock Mechanics and Mining Sciences & Geomechanics Abstracts, 25(3), 107-116.

Cundall, P.A. (1987). Distinct element models of rock and soil structure, in Analytical and Computational Methods in Engineering Rock Mechanics, E.T. Brown, ed. London: Allen & Unwin, Ch. 4, pp. 129 – 163.

Cundall, P. A., & Strack, O. D. L. (1979). Discrete numerical model for granular assemblies Geotechnique, 29(1), 47-65.

Davis, R. O., & Selvadurai, A. P. S. (1996). Elasticity and Geomechanics: Cambridge University Press.

Dawson, E. M., Roth, W. H., & Drescher, A. (1999). Slope stability analysis by strength reduction. Geotechnique, 49(6), 835-840.

Dershowitz, W., & Carvalho, J. (1996). Key-block tunnel stability analysis using realistic fracture patterns Paper presented at the 2nd North American Rock Mechanics Symposium

Dershowitz, W., & Herda, H. H. (1992). Interpretation of fracture spacing and intensity. Paper presented at the U.S. Symposium on Rock Mechanics.

Dershowitz, W. S., & Einstein, H. H. (1988). Characterizing rock joint geometry with joint system models. Rock Mechanics and Rock Engineering, 21(1), 21-51.

Diederichs, M. S., & Kaiser, P. K. (1999). Stability of large excavations in laminated hard rock masses: the voussoir analogue revisited. International Journal of Rock Mechanics and Mining Sciences, 36(1), 97-117.

Diederichs, M. S., Lato, M., Hammah, R., & Quinn, P. (2007). Shear Strength Reduction (SSR) approach for slope stability analyses. In E. Eberhardt, D. Stead & T. Morrison

(Eds.), Proceedings of the 1st Canada-US Rock Mechanics Symposium, Vancouver, Canada, 27-31 May 2007. Taylor & Francis, pp. 319-327.

Dobrohotoff, P., Azeezullah, S., Maggi, F., & Alonso-Marroquin, F. (2012). Optimal description of two-dimensional complex-shaped objects using spheropolygons. Granular Matter, 14(5), 651-658.

Dubois, F. (2011). Numerical modeling of granular metdia composed of polyhedral particles. In F. Radjai & F. Dubois (Eds.), Discrete Numerical Modeling of Granular Materials, pp. 233-261, Wiley.

Dubois, F., Jean, M., Renouf, M., Mozul, R., & Martin, A. (2011). Polyhedral particles in LMGC90, from http://www.lmgc.univ-montp2.fr/LMGC90/LMGC90/Methods/Entrees/2011/11/9_Polyhedral_and_non-convex_particles.html

Duncan, J. M., & Goodman, R. E. (1968). Finite element analyses of slopes in jointed rock. Contract Report S-68-3, U.S. Army Engineers Waterways Experiment Station.

Eberhardt, E., Stead, D., & Coggan, J. S. (2004). Numerical analysis of initiation and progressive failure in natural rock slopes-the 1991 Randa rockslide. International Journal of Rock Mechanics and Mining Sciences, 41(1), 69-87.

Eberly, D. (2001). Intersection of convex objects: the method of separating axes, from http://www.geometrictools.com

Einstein, H. H., & Locsin, J. L. Z. (2012). Modeling rock fracture intersections and application to the Boston area. Journal of Geotechnical and Geoenvironmental Engineering, 138(11), 1415-1421.

Einstein, H. H., & Schwartz, C. W. (1979). Simplified analysis for tunnel support. ASCE J Geotech Eng Div, 105(4), 499-518.

Einstein, H. H., Sousa, R. L., Karam, K., Manzella, I., & Kveldsvik, V. (2010). Rock slopes from mechanics to decision making. Chapter 1 in Rock Mechanics in Civil and Environmental Engineering. In J. Zhao , V. Labiouse , J.-P. Dudt and J.-F. Mathier (Eds.). London: CRC Press, 2010. pp. 3-13.

Einstein, H. H., Veneziano, D., Baecher, G. B., & O'Reilly, K. J. (1983). The effect of discontinuity persistence on rock slope stability. International Journal of Rock Mechanics and Mining Sciences and, 20(5), 227-236.

Elmouttie, M., Poropat, G., & Krähenbühl, G. (2010). Polyhedral modelling of rock mass structure. International Journal of Rock Mechanics and Mining Sciences, 47(4), 544-552.

Favier, J. F., Abbaspour-Fard, M. H., Kremmer, M., & Raji, A. O. (1999). Shape representation of axi-symmetrical, non-spherical particles in discrete element simulation using multi-element model particles. Engineering Computations (Swansea, Wales), 16(4), 467-480.

Fayol, M. (1885). Sur les movements de train provoques par l'exploitation des mines. Bull. Soc. Indust. Min, 14, 818.

Feng, Y. T., Han, K., & Owen, D. R. J. (2012). Energy-conserving contact interaction models for arbitrarily shaped discrete elements. Computer Methods in Applied Mechanics and Engineering, Vol. 205–208, pp. 169-177.

Feng, Y. T., & Owen, D. R. J. (2004). A 2D polygon/polygon contact model: algorithmic aspects. Engineering Computations, 21(2-4), 265-277.

Ferri, F., Di Toro, G., Hirose, T., Han, R., Noda, H., Shimamoto, T., De Rossi, N. (2011). Erratum: Low-to high-velocity frictional properties of the clay-rich gouges from the slipping zone of the 1963 Vaiont slide, northern Italy. Journal of Geophysical Research B: Solid Earth, 116(11).

Ferri, F., Di Toro, G., Hirose, T., Han, R., Noda, H., Shimamoto, T., De Rossi, N. (2011). Low- to high-velocity frictional properties of the clay-rich gouges from the slipping zone of the 1963 Vaiont slide, northern Italy. Journal of Geophysical Research B: Solid Earth, 116(9).

Fraige, F. Y., Langston, P. A., Matchett, A. J., & Dodds, J. (2008). Vibration induced flow in hoppers: DEM 2D polygon model. Particuology, 6(6), 455-466.

Fu, G., He, L., & Ma, G. (2010). 3D rock mass geometrical modeling with arbitrary discontinuities. International Journal of Applied Mechanics, 2(4), 871-887.

Fu, P., Walton, O. R., & Harvey, J. T. (2012). Polyarc discrete element for efficiently simulating arbitrarily shaped 2D particles. International Journal for Numerical Methods in Engineering, 89(5), 599-617.

Funatsu, T., Hoshino, T., Sawae, H., & Shimizu, N. (2008). Numerical analysis to better understand the mechanism of the effects of ground supports and reinforcements on the stability of tunnels using the distinct element method. Tunnelling and Underground Space Technology, 23(5), 561-573.

Galindo-Torres, S. A. (2010). Spheropolygons and spheropolytopes for the simulation of soils. Ph.D., Universidad Nacional de Colombia, Colombia.

Galindo-Torres, S. A., Alonso-Marroquín, F., Wang, Y. C., Pedroso, D., & Muñoz Castaño, J. D. (2009). Molecular dynamics simulation of complex particles in three dimensions and the study of friction due to nonconvexity. Physical Review E, 79(6), 060301.

Garboczi, E. J., & Bullard, J. W. (2013). Contact function, uniform-thickness shell volume, and convexity measure for 3D star-shaped random particles. Powder Technology, Vol. 237, 191-201.

Garga, V. K., & Wang, B. (1993). A numerical method for modelling large displacements of jointed rocks. II. Modelling of rock bolts and groundwater and applications. Canadian Geotechnical Journal, 30(1), 109-123.

Gens, A., & Alonso, E. E. (2006). Aznalcóllar dam failure. Part 2: Stability conditions and failure mechanism. Geotechnique, 56(3), 185-201.

Ghaboussi, J., & Barbosa, R. (1990). Three-dimensional discrete element method for granular materials. International Journal for Numerical and Analytical Methods in Geomechanics, 14(7), 451-472.

Ghee, E. H., Zhu, B. T., & Wines, D. R. (2011, 14-16 February 2011). Numerical analysis of twin road tunnels using two- and three-dimensional modeling techniques. Paper presented at the 2nd International FLAC/DEM Symposium: Continuum and Distinct Element Modeling in Geo-Engineering, Melbourne, Australia.

Gilbert, E. G., Johnson, D. W., & Keerthi, S. S. (1988). A fast procedure for computing the distance between complex objects in three-dimensional space. Robotics and Automation, IEEE Journal of, 4(2), 193-203.

Gill, P. E., Murray, W., & Wright, M. H. (1981). Practical Optimization: Emerald Group Publishing Limited.

Goodman, R. E. (1989). Introduction to Rock Mechanics (2 ed.): John Wiley & Sons.

Goodman, R. E. (1995). Block theory and its application. Geotechnique, 45(3), 383-423.

Goodman, R. E., Shi, G., & Boyle, W. (1982). Calculations of support for hard, jointed rock using the keyblock principal. 883-898.

Goodman, R. E., & Shi, G. H. (1985). Block theory and its application to rock engineering. Prentice-Hall International Series in Civil Engineering and Engineering Mechanics, p. 338.

Grasselli, G., & Egger, P. (2003). Constitutive law for the shear strength of rock joints based on three-dimensional surface parameters. International Journal of Rock Mechanics and Mining Sciences, 40(1), 25-40.

Hammah, R. E., Yacoub, T., Corkum, B., & Curran, J. H. (2008). The practical modelling of discontinuous rock masses with finite element analysis. Paper presented at the 42nd U.S. Rock Mechanics Symposium (USRMS), June 29 – July 2, San Francisco, Canada.

Hammah, R. E., Yacoub, T., Corkum, B., Wibowo, F., & Curran, J. H. (2007). Analysis of blocky rock slopes with finite element Shear Strength Reduction analysis. Rocscience Inc., Toronto, Canada.

Han, K., Feng, Y. T., & Owen, D. R. J. (2006). Polygon-based contact resolution for superquadrics. International Journal for Numerical Methods in Engineering, 66(3), 485-501.

Harkness, J. (2009). Potential particles for the modelling of interlocking media in three dimensions. International Journal for Numerical Methods in Engineering, 80(12), 1573-1594.

Hart, R., Cundall, P. A., & Lemos, J. (1988). Formulation of a three-dimensional distinct element model—Part II. Mechanical calculations for motion and interaction of a system composed of many polyhedral blocks. International Journal of Rock Mechanics and Mining Sciences & Geomechanics Abstracts, 25(3), 117-125.

Heliot, D. (1988). Generating a blocky rock mass. International Journal of Rock Mechanics and Mining Sciences & Geomechanics Abstracts, 25(3), 127-138.

Hendron Jr, A. J., & Patton, F. D. (1985). Vaiont slide, a geotechnical analysis based on new geologic observations of the failure surface Technical Report - US Army Engineer Waterways Experiment Station (pp. 324).

Hendron Jr, A. J., & Patton, F. D. (1987). The vaiont slide - A geotechnical analysis based on new geologic observations of the failure surface. Engineering Geology, 24(1-4), 475-491.

Hoek, E., & Bray, J. W. (1981). Rock Slope Engineering: The Institution of Mining and Metallurgy.

Hoek, E., Kaiser, P. K., & Bawden, W. F. (1995). Support of Underground Excavations in Hard Rock: Taylor & Francis Group.

Hoek, E., Carranza-Torres, C. T., Corkum, B. (2002). Hoek-Brown failure criterion – 2002 edition. Paper presented at the Proceedings of the fifth North American rock mechanics symposium, Toronto, Canada, Vol. 1, 267-273.

Hogue, C. (1998). Shape representation and contact detection for discrete element simulations of arbitrary geometries. Engineering computations, 15(3), 374-390.

Hogue, C., & Newland, D. (1994). Efficient computer simulation of moving granular particles. Powder Technology, 78(1), 51-66.

Höhner, D., Wirtz, S., & Scherer, V. (2012). A numerical study on the influence of particle shape on hopper discharge within the polyhedral and multi-sphere discrete element method. Powder Technology, 226(0), 16-28.

Höhner, D., Wirtz, S., & Scherer, V. (2013). Experimental and numerical investigation on the influence of particle shape and shape approximation on hopper discharge using the discrete element method. Powder Technology, Vol. 235, 614-627.

Hopkins, M. A. (2004). Discrete element modeling with dilated particles. Engineering Computations (Swansea, Wales), 21(2-4), 422-430.

Houlsby, G. T. (2009). Potential particles: a method for modelling non-circular particles in DEM. Computers and Geotechnics, 36(6), 953-959.

Hudson, J. A. (2012). Design methodology for the safety of underground rock engineering. Journal of rock mechanics and geotechnical engineering, 4(3), 205-214.

Hudson, J. A. (2013). Private communication.

Hudson, J. A. & Harrison, J.P. (1997). Engineering Rock Mechanics: An Introduction to the Principles. Pergamon, Elsevier.

Hutchinson, J. N. (1987). Mechanisms producing large displacements in landslides on pre-existing shears. Paper presented at the Memoir of the Geological Society of China.

Ikegawa, Y., & Hudson, J. A. (1992). Novel automatic identification system for three-dimensional multi-block systems. Engineering computations, 9(2), 169-179.

Itasca. (2000). FLAC - Fast Lagrangian Analysis of Continua, ver. 4: Itasca Consulting Group Inc.

Itasca. (2004). UDEC - Universal Distinct Element Code, ver. 4: Itasca Consulting Group Inc.

Itasca. (2007). 3DEC - 3 Dimensional Distinct Element Code, ver. 4.1, User's guide: Itasca Consulting Group Inc.

Itasca. (2013). 3DEC - 3 Dimensional Distinct Element Code, ver. 5.0, User's guide: Itasca Consulting Group Inc.

Ivanova, V. M. (1995). Three-dimensional stochastic modeling of rock fracture systems. Master of Science, Massachusetts Institute of Technology, United States.

Ivars, D. M., Pierce, M. E., Darcel, C., Reyes-Montes, J., Potyondy, D. O., Paul Young, R., & Cundall, P. A. (2011). The synthetic rock mass approach for jointed rock mass modelling. International Journal of Rock Mechanics and Mining Sciences, 48(2), 219-244.

Ivars, D. M., Potyondy, D. O., Pierce, M., & Cundall, P. A. (2008). The smooth-joint contact model. Paper presented at the 8th. World Congress on Computational Mechanics (WCCM8), 5th. European Congress on Computational Methods in Applied Sciences and Engineering (ECCOMAS 2008), Venice, Italy.

Jaeger, C. (1979). Rock mechanics and engineering: Cambridge university press.

Jensen, R. P., Bosscher, P. J., Plesha, M. E., & Edil, T. B. (1999). DEM simulation of granular media—structure interface: effects of surface roughness and particle shape. International Journal for Numerical and Analytical Methods in Geomechanics, 23(6), 531-547.

Jiang, M., & Yin, Z. Y. (2012). Analysis of stress redistribution in soil and earth pressure on tunnel lining using the discrete element method. Tunnelling and Underground Space Technology, 32, 251-259.

Jiang, Y., Tanabashi, Y., Li, B., & Xiao, J. (2006). Influence of geometrical distribution of rock joints on deformational behavior of underground opening. Tunnelling and Underground Space Technology, 21(5), 485-491.

Jin, F., Xin, H., Zhang, C., & Sun, Q. (2011). Probability-based contact algorithm for non-spherical particles in DEM. Powder Technology, 212(1), 134-144.

Jing, L. (2000). Block system construction for three-dimensional discrete element models of fractured rocks. International Journal of Rock Mechanics and Mining Sciences, 37(4), 645-659.

Jing, L., & Stephansson, O. (2007). Fundamentals of Discrete Element Methods for Rock Engineering: Theory and Applications: Theory and Applications: Elsevier Science.

Johnson, S. M., & Williams, J. R. (2009). Sub-discretized surface model with application to contact mechanics in multi-body simulation. Powder Technology, 193(3), 319-331.

Kazerani, T., & Zhao, J. (2010). Micromechanical parameters in bonded particle method for modelling of brittle material failure. International Journal for Numerical and Analytical Methods in Geomechanics, 34(18), 1877-1895.

Keneti, A. R., Jafari, A., & Wu, J.-H. (2008). A new algorithm to identify contact patterns between convex blocks for three-dimensional discontinuous deformation analysis. Computers and Geotechnics, 35(5), 746-759.

Kenney, T. C. (1967). Stability of the Vajont slope. Rock Mechanics and Engineering Geology, 5(1), 10-16.

Kiersch, G. A. (1964). Vajont reservoir disaster. Civil Engineering, Vol. 34, 32-39.

Kilburn, C. R. J., & Petley, D. N. (2003). Forecasting giant, catastrophic slope collapse: Lessons from Vajont, Northern Italy. Geomorphology, 54(1-2), 21-32.

Kim, B. H., Cai, M., Kaiser, P. K., & Yang, H. S. (2007). Estimation of Block Sizes for Rock Masses with Non-persistent Joints. Rock Mechanics and Rock Engineering, 40(2), 169-192.

Kim, Y. I., Amadei, B., & Pan, E. (1999). Modeling the effect of water, excavation sequence and rock reinforcement with discontinuous deformation analysis. International Journal of Rock Mechanics and Mining Sciences, 36(7), 949-970.

Kleder, M. (2005). Centroid of a convex n-dimensional polyhedron, from http://www.mathworks.co.uk/matlabcentral/fileexchange/8514-centroid-of-a-convex-n-dimensional-polyhedron

Kodam, M., Bharadwaj, R., Curtis, J., Hancock, B., & Wassgren, C. (2009). Force model considerations for glued-sphere discrete element method simulations. Chemical Engineering Science, 64(15), 3466-3475.

Koziara, T. (2008). Aspects of computational contact dynamics. Ph.D., University of Glasgow, United Kingdom.

Kozicki, J., & Donzé, F. V. (2008). A new open-source software developed for numerical simulations using discrete modeling methods. Computer Methods in Applied Mechanics and Engineering, 197(49-50), 4429-4443.

Kuipers, J. B. (1999). Quaternions and Rotation Sequences: A Primer With Applications to Orbits, Aerospace, and Virtual Reality: Princeton Univers. Press.

Kulatilake, P. H. S. W., Malama, B., & Wang, J. (2001). Physical and particle flow modeling of jointed rock block behavior under uniaxial loading. International Journal of Rock Mechanics and Mining Sciences, 38(5), 641-657.

Kulatilake, P. H. S. W., Ucpirti, H., Wang, S., Radberg, G., & Stephansson, O. (1992). Use of the distinct element method to perform stress analysis in rock with non-persistent joints and to study the effect of joint geometry parameters on the strength and deformability of rock masses. Rock Mechanics and Rock Engineering, 25(4), 253-274.

Kulatilake, P. H. S. W., Wathugala, D. N., & Stephansson, O. V. E. (1993). Stochastic three dimensional joint size, intensity and system modelling and a validation to an area in stripa mine, Sweden. Soils and Foundations, 33(1), 55-70.

Kulhawy, F. H. (1978). Geomechanical model for rock foundation settlement. ASCE J Geotech Eng Div, 104(2), 211-227.

Kveldsvik, V., Einstein, H., Nilsen, B., & Blikra, L. (2009a). Numerical Analysis of the 650,000 m2 Åknes Rock Slope based on Measured Displacements and Geotechnical Data. Rock Mechanics and Rock Engineering, 42(5), 689-728.

Kveldsvik, V., Kaynia, A. M., Nadim, F., Bhasin, R., Nilsen, B., & Einstein, H. H. (2009b). Dynamic distinct-element analysis of the 800 m high Åknes rock slope. International Journal of Rock Mechanics and Mining Sciences, 46(4), 686-698.

Lawrence, K. P. (2009). Load prediction for a moored conical drillship in level unbroken ice: a discrete element and experimental investigation. Ph.D., University of Waterloo, Canada.

Li, C., & Stillborg, B. (1999). Analytical models for rock bolts. International Journal of Rock Mechanics and Mining Sciences, 36(8), 1013-1029.

Li, J., Xue, J., Xiao, J., & Wang, Y. (2012). Block theory on the complex combinations of free planes. Computers and Geotechnics, 40(0), 127-134.

Lin, D., Fairhurst, C., & Starfield, A. M. (1987). Geometrical identification of three-dimensional rock block systems using topological techniques. International Journal of Rock Mechanics and Mining Science & Geomechanics Abstracts, 24(6), 331-338.

Lin, M. C., & Canny, J. F. (1991). A Fast Algorithm for Incremental Distance Calculation. Paper presented at the IEEE International Conference on Robotics and Automation, 9-11 April, 1991.

Liu, H. Y., Small, J. C., Carter, J. P., & Williams, D. J. (2009). Effects of tunnelling on existing support systems of perpendicularly crossing tunnels. Computers and Geotechnics, 36(5), 880-894.

Liu, X. L., & Lemos, J. V. (2001). Procedure for contact detection in discrete element analysis. Advances in Engineering Software, 32(5), 409-415.

Lo, K. Y., Lee, C. F., & Gelinas, P. (1972). Alternative interpretation of the Vaiont Slide. . Paper presented at the Stability of Rock Slopes: 13th Symposium on Rock Mechanics, University of Illinois Urbana-Campaign.

Lorig, L. J. (1985). A simple numerical representation of fully bonded passive rock reinforcement for hard rocks. Computers and Geotechnics, 1(2), 79-97.

Lu, G., Third, J. R., & Müller, C. R. (2012). Critical assessment of two approaches for evaluating contacts between super-quadric shaped particles in DEM simulations. Chemical Engineering Science, Vol. 78, 226-235.

Lu, J. (2002). Systematic identification of polyhedral rock blocks with arbitrary joints and faults. Computers and Geotechnics, 29(1), 49-72.

Lu, M., & McDowell, G. R. (2007). The importance of modelling ballast particle shape in the discrete element method. Granular Matter, 9(1-2), 69-80.

Mack, S., Langston, P., Webb, C., & York, T. (2011). Experimental validation of polyhedral discrete element model. Powder Technology, 214(3), 431-442.

MathWorks. (2010). MATLAB ver. 7.10. Natick, Massachusetts: The MathWorks Inc.

Mencl, V. (1966a). The influence of stiffness of a sliding mass on the stability of slopes. Rock Mechanics and Engineering Geology, 4(2), 127-131.

Mencl, V. (1966b). Mechanics of landslides with non-circular slip surface with special reference to the Vaoint slide. Geotechnique, 16(4), 329-337.

Mirghasemi, A. A., Rothenburg, L. L., & Matyas, E. L. (1997). Numerical simulations of assemblies of two-dimensional polygon-shaped particles and effects of confining pressure on shear strength. Soils and Foundations 37(3), 43–52.

Mirtich, B. (1998). V-Clip: fast and robust polyhedral collision detection. ACM Transactions on Graphics (TOG), 17(3), 177-208.

Mollon, G., & Zhao, J. (2013). Generating realistic 3D sand particles using Fourier descriptors. Granular Matter, 15(1), 95-108.

Montgomery, D. C., & Runger, G. C. (2010). Applied Statistics and Probability for Engineers: John Wiley & Sons.

Moosavi, M., & Grayeli, R. (2006). A model for cable bolt-rock mass interaction: Integration with discontinuous deformation analysis (DDA) algorithm. International Journal of Rock Mechanics and Mining Sciences, 43(4), 661-670.

Muir Wood, A. M. (1975). Circular tunnel in elastic ground. Geotechnique, 25(1), 115-127.

Müller-Salzburg, L. (1964). The rock slide in the Vajont valley. Rock Mechanics and Engineering Geology, 2, 148-212.

Müller-Salzburg, L. (1968). New considerations on the Vaiont slide. Rock Mechanics and Engineering Geology, 6, 1-91.

Müller-Salzburg, L. (1987). The vajont catastrophe- A personal review. Engineering Geology, 24(1-4), 423-444.

Munjiza, A., Owen, D. R. J., & Bicanic, N. (1995). Combined finite-discrete element method in transient dynamics of fracturing solids. Engineering computations, 12(2), 145-174.

Nezami, E. G., Hashash, Y. M. A., Zhao, D., & Ghaboussi, J. (2004). A fast contact detection algorithm for 3-D discrete element method. Computers and Geotechnics, 31(7), 575-587.

Nezami, E. G., Hashash, Y. M. A., Zhao, D., & Ghaboussi, J. (2006). Shortest link method for contact detection in discrete element method. International Journal for Numerical and Analytical Methods in Geomechanics, 30(8), 783-801.

Nonveiller, E. (1967). Shear strength of bedded and jointed rock as determined from the Zalesina and Vaiont slides. Paper presented at the Proceedings of the Geotechnical Conference, Oslo.

Nonveiller, E. (1987). The vajont reservoir slope failure. Engineering Geology, 24(1-4), 493-512.

O'Donovan, J., O'Sullivan, C., & Marketos, G. (2012). Two-dimensional discrete element modelling of bender element tests on an idealised granular material. Granular Matter, 14(6), 733-747.

Oda, M., Yamabe, T., Ishizuka, Y., Kumasaka, H., Tada, H., & Kimura, K. (1993). Elastic stress and strain in jointed rock masses by means of crack tensor analysis. Rock Mechanics and Rock Engineering, 26(2), 89-112.

Odling, N. (1992). Network properties of a two-dimensional natural fracture pattern. pure and applied geophysics, 138(1), 95-114.

O'Rourke, J. (1998). Computational Geometry in C: Cambridge University Press.

O'Sullivan, C. (2011). Particulate discrete element modelling: Spon Press/Taylor & Francis.

Paronuzzi, P., & Bolla, A. (2012). The prehistoric Vajont rockslide: An updated geological model. Geomorphology, Vol. 169-170, pp. 165-191.

Paronuzzi, P., Rigo, E., & Bolla, A. (2013). Influence of filling-drawdown cycles of the Vajont reservoir on Mt. Toc slope stability. Geomorphology, Vol. 191, 75-93.

Peters, J. F., Hopkins, M. A., Kala, R., & Wahl, R. E. (2009). A poly-ellipsoid particle for non-spherical discrete element method. Engineering Computations (Swansea, Wales), 26(6), 645-657.

Petit, D., Pradel, F., Ferrer, G., & Meimon, Y. (2001). Shape effect of grain in a granular flow. Paper presented at the Powders and Grains: Proceedings of the Fourth International Conference on Micromechanics of Granular Media, Sendai, Japan.

Pine, R. J., Coggan, J. S., Flynn, Z. N., & Elmo, D. (2006). The Development of a new Numerical Modelling Approach for Naturally Fractured Rock Masses. Rock Mechanics and Rock Engineering, 39(5), 395-419.

Pinyol, N. M., & Alonso, E. E. (2010). Criteria for rapid sliding II. Thermo-hydro-mechanical and scale effects in Vaiont case. Engineering Geology, 114(3-4), 211-227.

Pollard, D. D., & Aydin, A. (1988). Progress in understanding jointing over the past century. Geological Society of America Bulletin, 100(8), 1181-1204.

Potvin, Y. (1988). Empirical open stope design in Canada. Ph.D., University of British Columbia.

Potyondy, D. O., & Cundall, P. A. (2004). A bonded-particle model for rock. International Journal of Rock Mechanics and Mining Sciences, 41(8), 1329-1364.

Pournin, L. (2005). On the behaviour of spherical and non-spherical grain assemblies, its modeling and numerical simulations. Ph.D., Ecole Polytechnique Federale de Lausanne, Switzerland.

Pournin, L., & Liebling, T. M. (2005). A generalization of distinct element method to tridimensional particles with complex shapes. Paper presented at the Powders and Grains 2005, Stuttgart.

Priest, S. D. (1993). Discontinuity analysis for rock engineering: Routledge, Chapman & Hall, Incorporated.

Priest, S. D., & Hudson, J. A. (1976). Discontinuity spacings in rock. International Journal of Rock Mechanics and Mining Sciences & Geomechanics Abstracts, 13(5), 135-148.

Ramamurthy, T. (2007). Engineering in rocks for slopes, foundations and tunnels. New Delhi: Prentice-Hall of India Private Limited.

Rockfield. (2003). ELFEN, ver. 3.7: Rockfield Software Limited.

Rocscience (2007). RocLab, ver. 1.03 Rocscience Inc., Toronto, Ontario.

Saussine, G. (2004). Contribution a la modelisation de granulats tridimensionnels: application du ballast. Ph.D., Universite Montpellier II, France.

Saussine, G., Cholet, C., Gautier, P. E., Dubois, F., Bohatier, C., & Moreau, J. J. (2006). Modelling ballast behaviour under dynamic loading. Part 1: A 2D polygonal discrete element method approach. Computer Methods in Applied Mechanics and Engineering, 195(19-22), 2841-2859.

Seidel, R. (1991). Small-dimensional linear programming and convex hulls made easy. Discrete & Computational Geometry, 6(1), 423-434.

Semenza, E., & Ghirotti, M. (2000). History of the 1963 Vaiont slide: The importance of geological factors. Bulletin of Engineering Geology and the Environment, 59(2), 87-97.

Shen, B., & Barton, N. (1997). The disturbed zone around tunnels in jointed rock masses. International Journal of Rock Mechanics and Mining Sciences, 34(1), 117-125.

Shi, G. H. (1988). Discontinuous deformation analysis: A new numerical model for the statics and dynamics of block systems. Ph.D., University of California, Berkeley.

Shi, G. H. (2006). Cutting joint blocks and finding removable blocks for general free surfaces using 3-D DDA.

Shi, G. H., & Goodman, R. E. (1985). Two dimensional discontinuous deformation analysis. International Journal for Numerical and Analytical Methods in Geomechanics, 9(6), 541-556.

Sitar, N., MacLaughlin, M. M., & Doolin, D. M. (2005). Influence of kinematics on landslide mobility and failure mode. Journal of Geotechnical and Geoenvironmental Engineering, 131(6), 716-728.

Šmilauer, V. (2010). Ph.D. thesis, Cohesive particle model using the discrete element method on the Yade platform: Czech Technical University, Universite Grenoble I.

Šmilauer, V., Catalano, E., Chareyre, B., Dorofeenko, S., Duriez, J., Gladky, A., Kozicki, J., Modenese, C., Scholtès, L., Sibille, L., Stránský, J. & Thoeni, K. (2010). Yade Documentation (V. Šmilauer, ed.), The Yade Project, 1st ed., 2010. http://yade-dem.org/doc/.

Smith, K. C., Fisher, T. S., & Alam, M. (2009). Quasi-static Compaction of Polyhedra by the Discrete Element Method. Powders and Grains 2009, Proceedings of the 6th International Conference on Micromechanics of Granular Media, 90-93.

Solak, T. (2009). Ground behavior evaluation for tunnels in blocky rock masses. Tunnelling and Underground Space Technology, 24(3), 323-330.

Solak, T., & Schubert, W. (2004). Influence of block size and shape on the deformation behavior and stress development around tunnels. Paper presented at the EUROCK 2004 & 53rd Geomechanics Colloquium, Salzburg, Austria.

Son, M., & Cording, E. J. (2007). Ground–liner interaction in rock tunneling. Tunnelling and Underground Space Technology, 22(1), 1-9.

Sornette, D., Helmstetter, A., Andersen, J. V., Gluzman, S., Grasso, J. R., & Pisarenko, V. (2004). Towards landslide predictions: Two case studies. Physica A: Statistical Mechanics and its Applications, 338(3-4), 605-632.

Starfield, A. M., & Cundall, P. A. (1988). Towards a methodology for rock mechanics modelling. International Journal of Rock Mechanics and Mining Sciences and, 25(3), 99-106.

Staub, I., Fredriksson, A., & Outters, N. (2002). Strategy for a Rock Mechanics Site Descriptive Model: Development and testing of the theoretical approach. SKB Report, R02-02. Stockholm, Sweden: Swedish Nuclear Fuel and Waste Management.

Stead, D., Eberhardt, E., & Coggan, J. S. (2006). Developments in the characterization of complex rock slope deformation and failure using numerical modelling techniques. Engineering Geology, 83(1-3), 217-235.

Steiner, W., & Markus, M. (1996). Design of tunnel liners, how important are bending moments? Paper presented at the Geotechnical aspects of underground construction in soft ground, 15 – 17 April, 1996, London.

Stillborg, B. (1994). Professional users handbook for rock bolting (2 ed.): Trans Tech Publications, Limited.

Talesnick, M. L. (2006). Use of voissoir beam centrifuge data for the validation of numerical frameworks and constitute models, from http://www.technion.ac.il/~talesnik/Voussoir%20validation%20Notes.htm

Talesnick, M. L. (2007). Determination of shear interface parameters between rock blocks for centrifuge modeling. Rock Mechanics and Rock Engineering, 40(4), 405-418.

Talesnick, M. L., Ya'Acov, N. B., & Cruitoro, A. (2007). Modeling of a multiply jointed voussoir beam in the centrifuge. Rock Mechanics and Rock Engineering, 40(4), 383-404.

Terzaghi, K. (1936). Presidential Address. Paper presented at the Proceedings of the First International Conference on Soil Mechanics and Foundation Engineering, Cambridge, Mass.

Thornton, C. (2000). Numerical simulations of deviatoric shear deformation of granular media. Geotechnique, 50(1), 43-53.

Tika, T. E., & Hutchinson, J. N. (1999). Ring shear tests on soil from the Vaiont landslide slip surface. Geotechnique, 49(1), 59-74.

Tillemans, H.-J., & Herrmann, H. J. (1995). Simulating deformations of granular solids under shear. Physica A: Statistical and Theoretical Physics, 217(3-4), 261-288.

Timoshenko, S., & Young, D. H. (1965). Theory of Structures: McGraw-Hill.

Trafalis, T. B., & Malyscheff, A. M. (2002). An analytic center machine. Machine Learning, 46(1-3), 203-223.

Tsesarsky, M., & Hatzor, Y. H. (2006). Tunnel roof deflection in blocky rock masses as a function of joint spacing and friction - A parametric study using discontinuous

deformation analysis (DDA). Tunnelling and Underground Space Technology, 21(1), 29-45.

Tsesarsky, M., & Talesnick, M. L. (2007). Mechanical response of a jointed rock beam - Numerical study of centrifuge models. International Journal for Numerical and Analytical Methods in Geomechanics, 31(8), 977-1006.

Ülker, E., & Turanboy, A. (2009). Maximum volume cuboids for arbitrarily shaped in-situ rock blocks as determined by discontinuity analysis-A genetic algorithm approach. Computers and Geosciences, 35(7), 1470-1480.

Vardakos, S. S., Gutierrez, M. S., & Barton, N. R. (2007). Back-analysis of Shimizu Tunnel No. 3 by distinct element modeling. Tunnelling and Underground Space Technology, 22(4), 401-413.

Vardoulakis, I. (2002). Dynamic thermo-poro-mechanical analysis of catastrophic landslides. Geotechnique, 52(3), 157-171.

Veveakis, E., Vardoulakis, I., & Di Toro, G. (2007). Thermoporomechanics of creeping landslides: The 1963 Vaiont slide, northern Italy. Journal of Geophysical Research F: Earth Surface, 112(3).

Voight, B., & Faust, C. (1982). Frictional heat and strength loss in some rapid landslides. Geotechnique, 32(1), 43-54.

Wachs, A., Girolami, L., Vinay, G., & Ferrer, G. (2012). Grains3D, a flexible DEM approach for particles of arbitrary convex shape — Part I: Numerical model and validations. Powder Technology, 224(0), 374-389.

Wächter, A., & Biegler, L. T. (2006). On the implementation of an interior-point filter line-search algorithm for large-scale nonlinear programming. Mathematical Programming, 106(1), 25-57.

Wang, J., Yu, H., Langston, P., & Fraige, F. (2011). Particle shape effects in discrete element modelling of cohesive angular particles. Granular Matter, 13(1), 1-12.

Wang, S. (1992). Fundamental studies of the deformability and strength of jointed rock masses at three dimensional level. Ph.D., The University of Arizona.

Warburton, P. M. (1980). A stereological interpretation of joint trace data. International Journal of Rock Mechanics and Mining Sciences & Geomechanics Abstracts, 17(4), 181-190.

Warburton, P. M. (1981). Vector stability analysis of an arbitrary polyhedral rock block with any number of free faces. International Journal of Rock Mechanics and Mining Sciences & Geomechanics Abstracts, 18(5), 415-427.

Warburton, P. M. (1985). A computer program for reconstructing blocky rock geometry and analyzing single block stability. Computers & Geosciences, 11(6), 707-712.

Wellmann, C., Lillie, C., & Wriggers, P. (2008). A contact detection algorithm for superellipsoids based on the common-normal concept. Engineering Computations (Swansea, Wales), 25(5), 432-442.

Williams, J. R., & O'Connor, R. (1995). Linear complexity intersection algorithm for discrete element simulation of arbitrary geometries. Engineering computations, 12(2), 185-201.

Williams, J. R., & O'Connor, R. (1999). Discrete Element Simulation and the Contact Problem. Archives of Computational Methods in Engineering, 6(4), 279-304.

Williams, J. R., & Pentland, A. P. (1992). Superquadrics and modal dynamics for discrete elements in interactive design. Engineering computations, 9(2), 115-127.

Wu, C.-Y., & Cocks, A. C. F. (2006). Numerical and experimental investigations of the flow of powder into a confined space. Mechanics of Materials, 38(4), 304-324.

Wu, J.-H. (2008). New edge-to-edge contact calculating algorithm in three-dimensional discrete numerical analysis. Adv. Eng. Softw., 39(1), 15-24.

Wu, J.-H., Juang, C. H., & Lin, H.-M. (2005). Vertex-to-face contact searching algorithm for three-dimensional frictionless contact problems. International Journal for Numerical Methods in Engineering, 63(6), 876-897.

Xu, N., Tian, H., Kulatilake, P. H. S. W., & Duan, Q. (2011). Building a three dimensional sealed geological model to use in numerical stress analysis software: A case study for a dam site. Computers and Geotechnics, 38(8), 1022-1030.

Yeung, M. R., Jiang, Q. H., & Sun, N. (2007). A model of edge-to-edge contact for three-dimensional discontinuous deformation analysis. Computers and Geotechnics, 34(3), 175-186.

Yeung, M. R., & Leong, L. L. (1997). Effects of joint attributes on tunnel stability. International Journal of Rock Mechanics and Mining Sciences, 34(3-4), 348.e341-348.e318.

Young, W., Budynas, R., & Sadegh, A. (2011). Roark's Formulas for Stress and Strain, 8th Edition: McGraw-Hill Education.

Yu, Q., Ohnishi, Y., Xue, G., & Chen, D. (2009). A generalized procedure to identify three-dimensional rock blocks around complex excavations. International Journal for Numerical and Analytical Methods in Geomechanics, 33(3), 355-375.

Zadhesh, J., Jalali, S. M. E., & Ramezanzadeh, A. (2013). Estimation of joint trace length probability distribution function in igneous, sedimentary, and metamorphic rocks. Arabian Journal of Geosciences, March, 2013, pp. 1-9.

Zhang, L. (2010). Method for estimating the deformability of heavily jointed rock masses. Journal of Geotechnical and Geoenvironmental Engineering, 136(9), 1242-1250.

Zhang, L., & Einstein, H. (2010). The Planar Shape of Rock Joints. Rock Mechanics and Rock Engineering, 43(1), 55-68.

Zhang, L., & Einstein, H. H. (2000). Estimating the intensity of rock discontinuities. International Journal of Rock Mechanics and Mining Sciences, 37(5), 819-837.

Zhang, L., Einstein, H. H., & Dershowitz, W. S. (2002). Stereological relationship between trace length and size distribution of elliptical discontinuities. Geotechnique, 52(6), 419-433.

Zhang, Y., Xiao, M., & Chen, J. (2010). A new methodology for block identification and its application in a large scale underground cavern complex. Tunnelling and Underground Space Technology, 25(2), 168-180.

Zhang, Y., Xiao, M., Ding, X., & Wu, A. (2012). Improvement of methodology for block identification using mesh gridding technique. Tunnelling and Underground Space Technology, Vol. 30, 217-229.

Zhang, Z. X., & Lei, Q. H. (2013). Object-oriented modeling for three-dimensional multi-block systems. Computers and Geotechnics, Vol. 48, 208-227.

Zhao, D., Nezami, E. G., Hashash, Y. M. A., & Ghaboussi, J. (2006). Three-dimensional discrete element simulation for granular materials. Engineering Computations (Swansea, Wales), 23(7), 749-770.

APPENDIX A – CONTACT DETECTION BETWEEN POTENTIAL PARTICLES

The more comprehensive version of this material has been reported in Boon et al. (2013). Houlsby (2009) previously proposed the concept of potential particles where an arbitrarily shaped convex particle can be defined using a 2nd degree polynomial function. A particle can be defined as:

$$f = (1-k)\left(\sum_{i=1}^{N} \left\langle a_i\alpha + b_i\beta + c_i\gamma - d_i \right\rangle^2 - r^2 \right) + k(\alpha^2 + \beta^2 + \gamma^2 - R^2) \tag{A.1}$$

where (a_i, b_i, c_i) is the normal vector of the i^{th} plane defined with respect to the particle local (α, β, γ) coordinate system, and d_i is the distance of the plane to the local origin. $\langle\ \rangle$ are Macaulay brackets, i.e., $\langle\alpha\rangle = \alpha$ for $\alpha > 0$; $\langle\alpha\rangle = 0$ for $\alpha \leq 0$. The planes are assembled such that their normal vectors point outwards. They are summed quadratically and expanded by a distance r, which is also related to the radius of the curvature at the corners. Further, a "shadow" spherical particle is added; R is the radius of the sphere, with $0 < k \leq 1$ denoting the fraction of sphericity of the particle (see Fig. A.1 (a) and (b)). Houlsby (2009) calls this function a "potential particle", which has the following properties:

- $f = 0$ defines the particle surface,
- $f < 0$"inside" the particle,
- $f > 0$ "outside" the particle,
- the particle is strictly convex, and any surface *f=constant* is strictly convex.

For computational reasons, Eq. (A.1) is normalised:

$$f = (1-k)\left(\sum_{i=1}^{N} \frac{\left\langle a_i\alpha + b_i\beta + c_i\gamma - d_i \right\rangle^2}{r^2} - 1 \right) + k\left(\frac{\alpha^2}{R^2} + \frac{\beta^2}{R^2} + \frac{\gamma^2}{R^2} - 1 \right) \tag{A.2}$$

To perform contact detection between a pair of potential particles f_A and f_B, Houlsby (2009) proposes that one can solve one of the constrained minimisation problems below:

- minimise f_A subject to the constraint $f_B = 0$
- minimise $f_A + f_B$ subject to the constraint $f_A - f_B = 0$

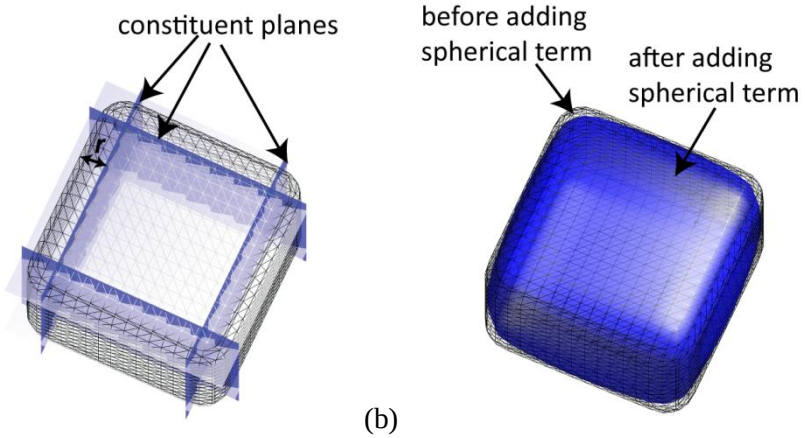

Fig. A.1. Construction of potential particles (images reprinted from Boon et al. (2013) with permission from Elsevier) (a) constituent planes are squared and expanded by a constant r. Then, a fraction of sphere is then added. (b) k = 0.4

The equations in 2-D has been presented and solved using the Newton-Raphson method in Houlsby (2009). The modelling of highly angular (almost polyhedral) particles was first explored at the beginning of this dissertation by extending the equations to 3-D. For angular particles in 3-D, the Newton-Raphson method was found to encounter issues related to numerical convergence. The equations were then formulated into a second-order cone program (SOCP), which has been widely established to be theoretically and practically tractable.

Consider the optimisation problem:

$$\left.\begin{array}{c} \text{minimise } f_{\mathrm{A}} + f_{\mathrm{B}} \\ \text{subject to} \\ f_{\mathrm{A}} = f_{\mathrm{B}} \end{array}\right\} \quad \text{(A.3)}$$

where f_{A} and f_{B} are the potential functions of Particle A and B which according to the definition in Eq. (A.2) can be expressed as:

$$\left.\begin{array}{l} f_{\mathrm{A}} = \dfrac{(1-k_{\mathrm{A}})}{r_{\mathrm{A}}^2}\left(\sum_{i=1}^{N_{\mathrm{A}}}\left\langle a_{i\mathrm{A}}\alpha_{\mathrm{A}} + b_{i\mathrm{A}}\beta_{\mathrm{A}} + c_{i\mathrm{A}}\gamma_{\mathrm{A}} - d_{i\mathrm{A}}\right\rangle^2 - r_{\mathrm{A}}^2\right) + \dfrac{k_{\mathrm{A}}}{R_{\mathrm{A}}^2}(\alpha_{\mathrm{A}}^2 + \beta_{\mathrm{A}}^2 + \gamma_{\mathrm{A}}^2 - R_{\mathrm{A}}^2) \\ f_{\mathrm{B}} = \dfrac{(1-k_{\mathrm{B}})}{r_{\mathrm{B}}^2}\left(\sum_{i=1}^{N_{\mathrm{B}}}\left\langle a_{i\mathrm{B}}\alpha_{\mathrm{B}} + b_{i\mathrm{B}}\beta_{\mathrm{B}} + c_{i\mathrm{B}}\gamma_{\mathrm{B}} - d_{i\mathrm{B}}\right\rangle^2 - r_{\mathrm{B}}^2\right) + \dfrac{k_{\mathrm{B}}}{R_{\mathrm{B}}^2}(\alpha_{\mathrm{B}}^2 + \beta_{\mathrm{B}}^2 + \gamma_{\mathrm{B}}^2 - R_{\mathrm{B}}^2) \end{array}\right\} \quad \text{(A.4)}$$

where $(\alpha_A, \beta_A, \gamma_A)$ and $(\alpha_B, \beta_B, \gamma_B)$ are the local coordinates with respect to Particle A and B respectively. It is convenient to optimise over the global Cartesian coordinate system (*x*, *y*, *z*), so that:

$$\mathbf{Q}_A \boldsymbol{\alpha}_A + \mathbf{x}_{0A} = \mathbf{Q}_B \boldsymbol{\alpha}_B + \mathbf{x}_{0B} \tag{A.5}$$

where $\boldsymbol{\alpha}_A = (\alpha_A, \beta_A, \gamma_A)$ and $\boldsymbol{\alpha}_B = (\alpha_B, \beta_B, \gamma_B)$, while $\mathbf{x}_{0A}$ and $\mathbf{x}_{0B}$ denote the positions of Particle A and B. $\mathbf{Q}_A$ and $\mathbf{Q}_B$ are rotation matrices which can be used to transform vectors in the local reference systems to the global coordinate system (Chapter 3).

For the purpose of minimisation, the Macaulay brackets in Eq. (A.2) can be replaced with auxiliary slack variables p_i and adding additional constraints so that:

$$\left.\begin{aligned} f_A &= \frac{(1-k_A)}{r_A^2}\left(\sum_{i=1}^{N_A} p_{iA}^2 - r_A^2\right) + \frac{k_A}{R_A^2}(\alpha_A^2 + \beta_A^2 + \gamma_A^2 - R_A^2) \\ a_{iA}\alpha_A + b_{iA}\beta_A + c_{iA}\gamma_A - d_{iA} &\le p_{iA}, \quad i = 1,..., N_A, \\ p_{iA} &\ge 0, \quad i = 1,..., N_A, \end{aligned}\right\} \tag{A.6}$$

By further introducing:

$$\left.\begin{aligned} p_{iAk} &= \frac{\sqrt{1-k_A}}{r_A} p_{iA}, \quad i = 1,..., N_A, \\ \alpha_{Ak} &= \frac{\sqrt{k_A}}{R_A}\alpha_A \\ \beta_{Ak} &= \frac{\sqrt{k_A}}{R_A}\beta_A \\ \gamma_{Ak} &= \frac{\sqrt{k_A}}{R_A}\gamma_A \end{aligned}\right\} \tag{A.7}$$

the potential function can be expressed in terms of these new variables:

$$f_A = \sum_{i=1}^{N} p_{iAk}^2 + \alpha_{Ak}^2 + \beta_{Ak}^2 + \gamma_{Ak}^2 - 1 \tag{A.8}$$

Introducing slack variables s_A and s_B with $s_A \ge 0$ and $s_B \ge 0$, and the constants w_{Ap}, w_{As}, w_{Bp} and w_{Bs}:

$$\left.\begin{aligned} w_{\mathrm{Ap}} &= \frac{r_{\mathrm{A}}}{\sqrt{1-k_{\mathrm{A}}}} \quad \text{(planar component of particle A)} \\ w_{\mathrm{As}} &= \frac{R_{\mathrm{A}}}{\sqrt{k_{\mathrm{A}}}} \quad \text{(spherical component of particle A)} \\ w_{\mathrm{Bp}} &= \frac{r_{\mathrm{B}}}{\sqrt{1-k_{\mathrm{B}}}} \quad \text{(planar component of particle B)} \\ w_{\mathrm{Bs}} &= \frac{R_{\mathrm{B}}}{\sqrt{k_{\mathrm{B}}}} \quad \text{(spherical component of particle B)} \end{aligned}\right\} \quad \text{(A.9)}$$

we can express the optimisation problem as a second order cone program:

$$\left.\begin{aligned} &\text{minimise } s_{\mathrm{A}}+s_{\mathrm{B}} \\ &\text{subject to} \\ &\sqrt{\sum_{i=1}^{N_{\mathrm{A}}} p_{i\mathrm{Ak}}^2 + \alpha_{\mathrm{Ak}}^2 + \beta_{\mathrm{Ak}}^2 + \gamma_{\mathrm{Ak}}^2} \le s_{\mathrm{A}} \\ &\sqrt{\sum_{i=1}^{N_{\mathrm{B}}} p_{i\mathrm{Bk}}^2 + \alpha_{\mathrm{Bk}}^2 + \beta_{\mathrm{Bk}}^2 + \gamma_{\mathrm{Bk}}^2} \le s_{\mathrm{B}} \\ &s_{\mathrm{A}} = s_{\mathrm{B}} \\ &w_{\mathrm{As}}\alpha_{\mathrm{Ak}}Q_{\mathrm{A11}} + w_{\mathrm{As}}\beta_{\mathrm{Ak}}Q_{\mathrm{A12}} + w_{\mathrm{As}}\gamma_{\mathrm{Ak}}Q_{\mathrm{A13}} - (w_{\mathrm{Bs}}\alpha_{\mathrm{Bk}}Q_{\mathrm{B11}} + w_{\mathrm{Bs}}\beta_{\mathrm{Bk}}Q_{\mathrm{B12}} + w_{\mathrm{Bs}}\gamma_{\mathrm{Bk}}Q_{\mathrm{B13}}) \\ &= x_{0\mathrm{B}} - x_{0\mathrm{A}} \\ &w_{\mathrm{As}}\alpha_{\mathrm{Ak}}Q_{\mathrm{A21}} + w_{\mathrm{As}}\beta_{\mathrm{Ak}}Q_{\mathrm{A22}} + w_{\mathrm{As}}\gamma_{\mathrm{Ak}}Q_{\mathrm{A23}} - (w_{\mathrm{Bs}}\alpha_{\mathrm{Bk}}Q_{\mathrm{B21}} + w_{\mathrm{Bs}}\beta_{\mathrm{Bk}}Q_{\mathrm{B22}} + w_{\mathrm{Bs}}\gamma_{\mathrm{Bk}}Q_{\mathrm{B23}}) \\ &= y_{0\mathrm{B}} - y_{0\mathrm{A}} \\ &w_{\mathrm{As}}\alpha_{\mathrm{Ak}}Q_{\mathrm{A31}} + w_{\mathrm{As}}\beta_{\mathrm{Ak}}Q_{\mathrm{A32}} + w_{\mathrm{As}}\gamma_{\mathrm{Ak}}Q_{\mathrm{A33}} - (w_{\mathrm{Bs}}\alpha_{\mathrm{Bk}}Q_{\mathrm{B31}} + w_{\mathrm{Bs}}\beta_{\mathrm{Bk}}Q_{\mathrm{B32}} + w_{\mathrm{Bs}}\gamma_{\mathrm{Bk}}Q_{\mathrm{B33}}) \\ &= z_{0\mathrm{B}} - z_{0\mathrm{A}} \\ &w_{\mathrm{As}}a_{i\mathrm{A}}\alpha_{\mathrm{Ak}} + w_{\mathrm{As}}b_{i\mathrm{A}}\beta_{\mathrm{Ak}} + w_{\mathrm{Ak}}c_{i\mathrm{A}}\gamma_{\mathrm{Ak}} - w_{\mathrm{Ap}}p_{i\mathrm{Ak}} \le d_{i\mathrm{A}}, \quad i = 1,\ldots,N_{\mathrm{A}}, \\ &w_{\mathrm{Bs}}a_{i\mathrm{B}}\alpha_{\mathrm{Bk}} + w_{\mathrm{Bs}}b_{i\mathrm{B}}\beta_{\mathrm{Bk}} + w_{\mathrm{Bk}}c_{i\mathrm{B}}\gamma_{\mathrm{Bk}} - w_{\mathrm{Bp}}p_{i\mathrm{Bk}} \le d_{i\mathrm{B}}, \quad i = 1,\ldots,N_{\mathrm{B}}, \\ &p_{i\mathrm{Ak}} \ge 0, \quad i = 1,\ldots,N_{\mathrm{A}}, \\ &p_{i\mathrm{Bk}} \ge 0, \quad i = 1,\ldots,N_{\mathrm{B}}, \\ &s_{\mathrm{A}} \ge 0 \\ &s_{\mathrm{B}} \ge 0 \end{aligned}\right\} \quad \text{(A.10)}$$

where the bound constraints $p_{i\mathrm{Ak}} \geq 0$ and $p_{i\mathrm{Bk}} \geq 0$ in Eq. (A.10) can be omitted from the formulation because they are minimised over their squared value, and the linear inequality constraints can be satisfied if they assume non-negative values. Note that Eq. (A.10) can be solved using conic optimisation software such as MOSEK (2010). Further, because MOSEK does not allow variables to be repeated in separate cones (s_{A} and s_{B} in our case), the linear constraint $s_{\mathrm{A}} = s_{\mathrm{B}}$ has to be specified. In other optimisation codes, one can remove this linear constraint and replace s_{A} and s_{B} by the same variable.

References

Houlsby, G. T. (2009). Potential particles: a method for modelling non-circular particles in DEM. Computers and Geotechnics, 36(6), 953-959.

MOSEK (2010). The Optimisation Tools Manual: MOSEK ApS.

APPENDIX B – CALCULATION OF VERTICES

There are many ways by which the vertices of a polyhedron can be deduced from its faces. A brute-force method is used here. The calculation procedure here assumes that a vertex is an intersection between three planes. The same assumption was made by Heliot (1988) in his block generation algorithm; the probability that more than three joint planes intersecting at the same point precisely in 3-D space is low. For a polyhedron defined by N linear inequalities $a_i^{\mathrm{T}} x - d_i \leq 0$ where i is the plane number, the vertices can be calculated as:

Loop over the face i = 1... N:
    Loop over the face j = (i+1)...N:
        Loop over the face k = (i+2)...N:
            Check that all the planes are non-parallel to each other. Then, calculate the intersection between the three planes, and check whether it is on the polyhedron using Eq. (B.1). If yes, it is a vertex of the polyhedron.
        end
    end
end

Note that redundant vertices could emerge if it is an intersection between more than three planes. They can nevertheless be identified by checking if the distances of the new intersections (vertices) to the existing vertices are close to zero. To check whether a point is on the polyhedron, the following function can be used (Boyd & Vandenberghe, 2004):

$$g = \max(\mathbf{a}_1^{\mathrm{T}}\mathbf{x} - d_1, \mathbf{a}_2^{\mathrm{T}}\mathbf{x} - d_2, \ldots, \mathbf{a}_N^{\mathrm{T}}\mathbf{x} - d_N) \tag{B.1}$$

If $g > 0$, the point is outside the polyhedron; and if $g < 0$, the point is inside the polyhedron. The point is on the polyhedron if $g = 0$.

References

Heliot, D. (1988). Generating a blocky rock mass. International Journal of Rock Mechanics and Mining Sciences & Geomechanics Abstracts, 25(3), 127-138.

APPENDIX C – CALCULATION OF AXES ALIGNED BOUNDING BOXES

Axes aligned bounding boxes (Cohen et al., 1995) are required in some DEM codes to establish neighbouring particles before running the more expensive contact detection test. Once the vertices of a polyhedron are calculated, the minima and maxima coordinates along the global *x*, *y* and *z* axes are required to define the axes aligned bounding boxes (see Fig. C.1). For a vertex with position vector $\boldsymbol{\alpha}$ defined with respect to the local coordinate system, its global coordinates $\mathbf{v}$ can be calculated as:

$$\mathbf{v} = \mathbf{x}_0 + \mathbf{Q}\boldsymbol{\alpha} \tag{C.1}$$

where $\mathbf{x}_0$ is the position of the polyhedron (normally the centroid) and $\mathbf{Q}$ is the rotation matrix which defines the orientation of the polyhedron (Chapter 3). As the polyhedron moves, it is necessary to update its minima and maxima coordinates based on the positions of its vertices along the global *x*, *y* and *z* axes, based on its new position and new orientation (see Fig. C.1).

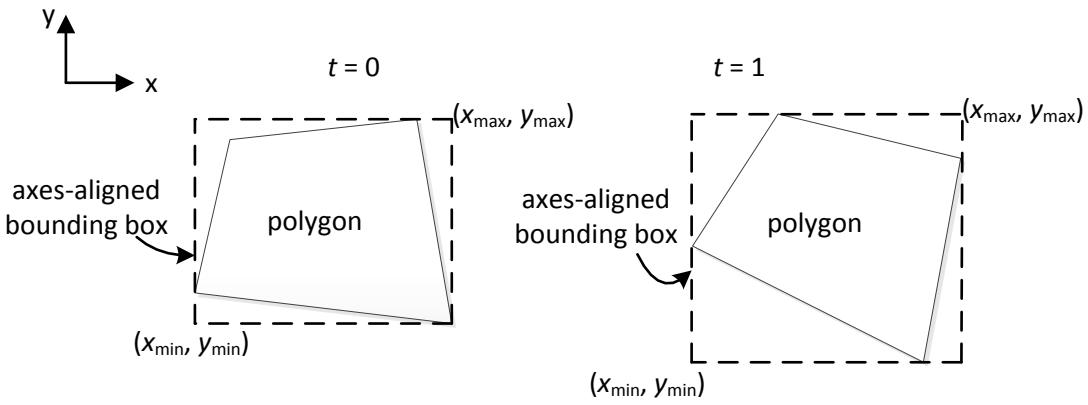

Fig. C.1. Illustration of axes aligned bounding boxes for a polygon in 2-D

References

Cohen, J. D., Lin, M. C., Manocha, D., & Ponamgi, M. (1995). I-COLLIDE: An interactive and exact collision detection system for large-scale environments. Paper presented at the Proceedings of the 1995 Symposium on Interactive 3D Graphics, Monterey, CA, USA.

APPENDIX D – CALCULATION OF CONTACT LENGTH AND AREA

The contact length between a pair of polygons is calculated as the overlapping length passing through the contact point in the direction perpendicular to the contact normal. Consider two overlapping particles, Particle A and Particle B, whose contact point is $\mathbf{p}_c$ and contact normal is $\mathbf{n} = (n_x, n_y)$. Define the vector perpendicular to the contact normal as $\mathbf{v} = (-n_y, n_x)$. The contact length can be calculated by first finding the points on Particle A and Particle B which intersect the line $\mathbf{p}(t) = \mathbf{p}_c + t\mathbf{v}$, where t is a positive scalar. These intersections can be calculated in the same manner as the calculation of overlap distance (Chapter 3). As illustrated in Fig. D.1, after the intersections are obtained, i.e. point $\mathbf{p}_{A1}$ on Particle A and point $\mathbf{p}_{B1}$ on Particle B, the distances of the two points $\mathbf{p}_{A1}$ and $\mathbf{p}_{B1}$ to the contact point are calculated. The point which is closer to the contact point is one of the endpoints defining the contact length. The other endpoint of the contact length can be found in the same way by calculating the intersections of the particles with the line pointing in the opposite direction, i.e. $\mathbf{p}(t) = \mathbf{p}_c - t\mathbf{v}$.

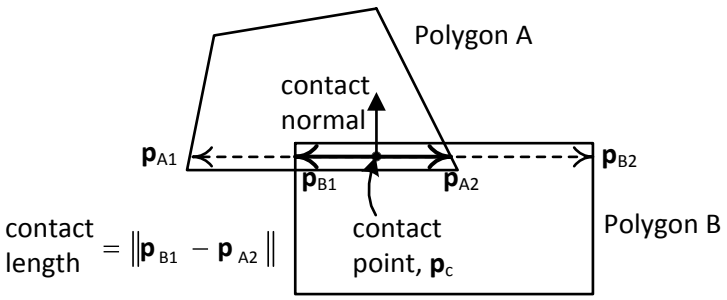

Fig. D.1. Illustration of the calculation of contact length between two polygons in 2-D

In 3-D, the contact area between a pair of polyhedra is obtained as the area intersecting the contact plane in the overlap region (see Fig. D.2). Define the contact plane as a plane passing through the contact point and whose normal vector is taken as the contact normal, i.e. the contact plane is perpendicular to the contact normal. The contact area can be calculated by tracing along the blocks faces which intersect the contact plane. With the contact normal, $\mathbf{n} = (n_x, n_y, n_z)$, an arbitrary vector $\mathbf{v}_{start}$ (of non-zero magnitude) which lies on the contact plane is determined, i.e. from one of the following possibilities: $(-n_y, n_x, 0)$,

(n_z, 0, -n_x) or (0, n_z, -n_y). Then find the point $\mathbf{p}_0$ lying on the boundary of the overlapping region using the same method that is used in the calculation of overlap distance (Chapter 3), i.e. taking the intersection with the polyhedra which is closer to the starting point of the search. Define the normal vector of the block face (with respect to the global coordinates) at the point $\mathbf{p}_0$ as $\mathbf{n}_{face}$. The trace vector, which is directed along the intersection between the block face and the contact plane, can be calculated as $\mathbf{v}_{trace} = \mathbf{n} \times \mathbf{n}_{face}$. Searching along $\mathbf{v}_{trace}$ from $\mathbf{p}_0$, a new point $\mathbf{p}_1$ lying on a different block face is calculated. Note that, in the aforementioned intersection calculation, the block face which had been used to derive $\mathbf{v}_{trace}$ is omitted from the search calculation because the next point should terminate at a new face. The same procedure is repeated to find the point $\mathbf{p}_2$.

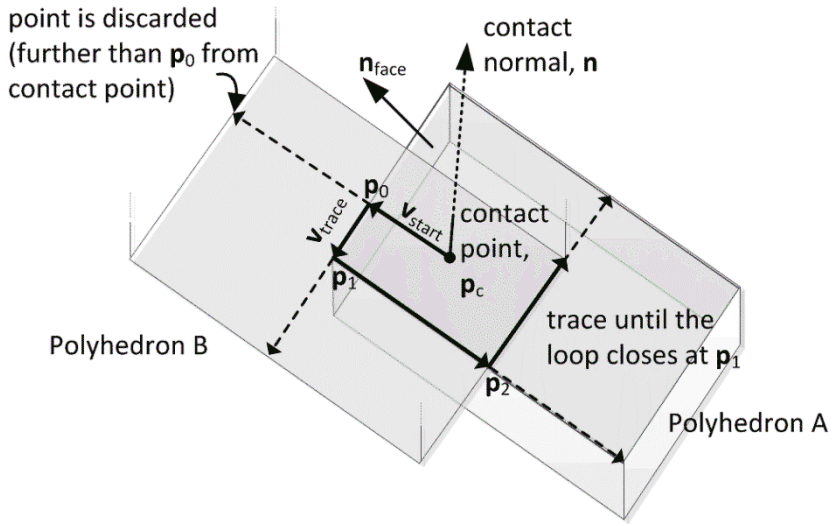

Fig. D.2. Illustration of the calculation of contact area between two polyhedron in 3-D

To search consistently in the same direction, the cross product between the previous and current search direction, i.e. $\mathbf{w} = \mathbf{v}_{prev} \times \mathbf{v}_{current}$, is compared against the dot product with the contact normal, i.e. $\mathbf{n} \cdot \mathbf{w}$. The sign of $\mathbf{n} \cdot \mathbf{w}$ should always be consistent throughout the tracing procedure; if it is different, the opposite direction, $-\mathbf{v}_{current}$, is adopted. The area enclosed by the points $\mathbf{p}_1$, $\mathbf{p}_2$ and the contact point $\mathbf{p}_c$ can be calculated as the area of a triangle enclosed by the two vectors $\mathbf{v}_1 = (\mathbf{p}_1 - \mathbf{p}_c)$ and $\mathbf{v}_2 = (\mathbf{p}_2 - \mathbf{p}_c)$:

$$A = 0.5|v_1 \times v_2| \tag{D.1}$$

To calculate the full contact area, the tracing continues until a closed loop is formed until the point $\mathbf{x}_1$ is rediscovered. Note that the point $\mathbf{p}_0$ is not used to calculate the contact area.

It is possible that the points on Particle A and Particle B found from bracketing during the tracing procedure are very close to each other (see $\mathbf{p}_1$ in Fig. (D.3)). When this case happens, the tracing point at $\mathbf{p}_1$ should take the block face (from Particle A or Particle B) which forms the tighter loop. In this calculation, the normal vector of the two faces ($\mathbf{n}_{faceA}$ from Particle A and $\mathbf{n}_{faceB}$ from Particle B) should be projected onto the contact plane (with normal vector **n)**:

$$\mathbf{n}_{fcpA} = \mathbf{n}_{faceA} - (\mathbf{n}_{faceA} \cdot \mathbf{n})\mathbf{n} \tag{D.2}$$

after which it is normalised. The same operation is repeated for the face on Particle B (with normal vector $\mathbf{n}_{faceB}$) to obtain $\mathbf{n}_{fcpB}$ and the previous face (with normal vector $\mathbf{n}_{facePrev}$) to obtain $\mathbf{n}_{fcpPrev}$. A comparison is made between the dot products $\mathbf{n}_{fcpA} \cdot \mathbf{n}_{fcpPrev}$ and $\mathbf{n}_{fcpB} \cdot \mathbf{n}_{fcpPrev}$. The more negative of the two is chosen because they subtend a larger angle, i.e. create a tighter loop.

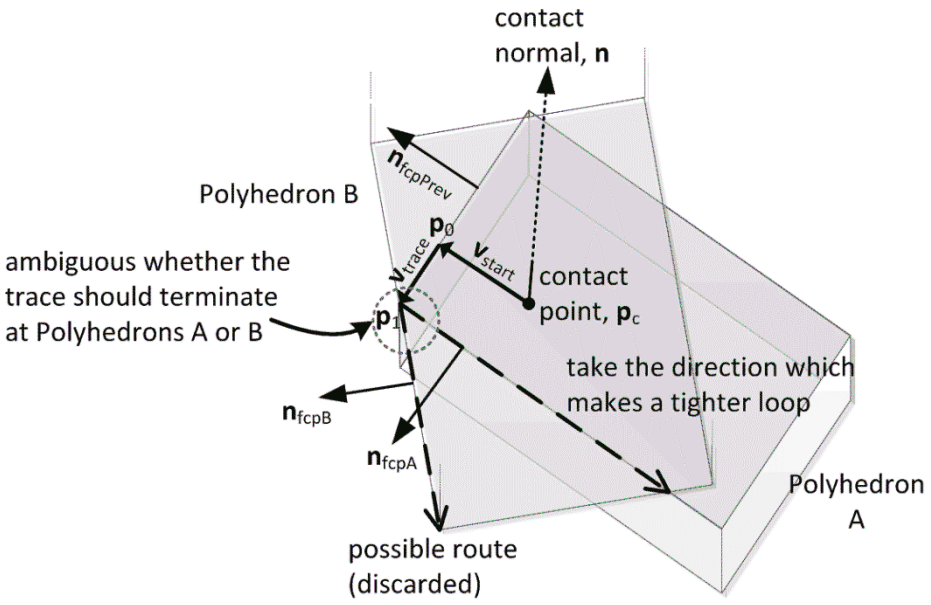

Fig. D.3. Illustration that the direction which makes a tighter loop is chosen for tracing for the calculation of contact area

APPENDIX E – CLOSED FORM SOLUTION FOR THREE-HINGED BEAM

The three-hinged beam model in Chapter 4 can be simplified as illustrated in Fig. E.1. Rather than using an axis of symmetry, a rigid block was employed providing twice the stiffness (compare with Fig. 4.14, p. 81). The abutment blocks in Fig. E.1 are assumed to be non-compliant so that the deformation at the interfaces are solely caused by the deformation at the faces of the rotating block. A block of dimension ($L_1 \times L_2$) is flanked by two abutment blocks, one of which is frictionless (left block in Fig. E.1). Therefore, shear forces are absent at this interface as in the roof midspan in Fig. 4.14 (p. 81). The overturning moment due to the block weight is resisted by the pair of horizontal thrusts acting at the centroid of the overlap area at both abutments (**B** and **C** in Fig. E.1) which form a restoring couple. As the block rotates, the coordinates of the vertices **A** and **M** in Fig. E.1 can be tracked using a rotation matrix. Assuming that there is no overlap at $\theta = 0°$, and with $s = \delta/|\sin(\theta)|$ and $t = \delta/|\cos(\theta)|$, the centroids of the overlap areas (**B** and **C** in Fig. E.1) can be calculated from simple geometrical relationships. The lever arm for the restoring moment l can be calculated as the y-distance between **B** and **C**. The overlap distance, d, is calculated as:

$$d = \frac{\mathbf{I}_y - \mathbf{B}_y}{\mathbf{I}_y - \mathbf{A}_y}\delta \tag{E.1}$$

where the subscript y denotes the y-coordinate of the points. Based on the schematic in Fig. E.1., the load-rotation relationship can be written as:

$$W = \frac{2lK_N d}{L_1} \tag{E.2}$$

This solution assumes the lever arm for the overturning moment does not change and is equal to half the block length, L_1. The load-rotation response curve, e.g. Fig. 4.15, can be calculated easily using a spreadsheet.

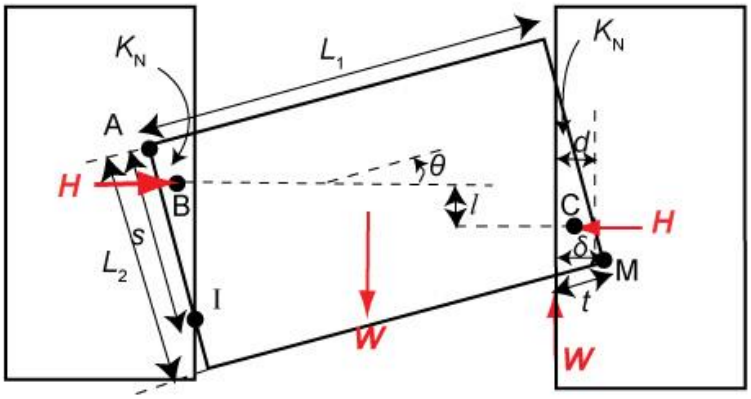

Fig. E.1. Schematic for the derivation of the three hinged-beam response (see Fig. 4.6) using symmetry (after Boon et al. (2012) with permission from Elsevier). Overlap is exaggerated to make annotations clear.

APPENDIX F – STRESS-UPDATE ALGORITHM (SHEAR DIRECTION)

The total shear displacement increment, **du**, consists of elastic and plastic components, i.e. $\mathbf{du}_e$ and $\mathbf{du}_p$, such that:

$$\mathbf{du} = \mathbf{du}_e + \mathbf{du}_p \tag{F.1}$$

from which the increment of plastic displacement can be expressed as:

$$\mathbf{du}_p = \mathbf{du} - \frac{\mathbf{F}_i - \mathbf{F}_0}{K_s} \tag{F.2}$$

where $\mathbf{F}_i$ and $\mathbf{F}_0$ are the shear forces at the current and previous time step and K_s is the shear stiffness (units: N/m).

For the case when the coefficient of friction μ is modelled as strain hardening or strain softening, it is useful to denote $\mu = g(\beta)$, so that, μ, is a function g of an internal state variable β. Then, define the increment of the internal state variable $d\beta$ as a scalar product of $\mathbf{du}_p$ to the power of half:

$$d\beta = (\mathbf{du}_p \mathbf{du}_p)^{1/2} \tag{F.3}$$

so that

$$\beta_i = \beta_0 + d\beta \tag{F.4}$$

where β_i and β_0 are the values of the internal state variable at the current and previous time step respectively. By assuming that the plastic strain increment is in the direction of current shear stress,

$$\mathbf{du}_p = \Lambda \mathbf{F}_i \tag{F.5}$$

the state variable β_i can be expressed as:

$$\beta_i = \beta_0 + \Lambda(\mathbf{F}_i \mathbf{F}_i)^{1/2} \tag{F.6}$$

and the shear force as:

$$\mathbf{F}_i = \frac{K_s \mathbf{du} + \mathbf{F}_0}{K_s \Lambda + 1} \tag{F.7}$$

Define the yield surface as:

$$f = (\mathbf{F}_i \mathbf{F}_i)^{1/2} - \mu_i F_n \tag{F.8}$$

where F_n is the magnitude of normal force at the contact and μ_i is the corresponding friction coefficient at the current time step.

In the stress update algorithm, the plastic multiplier Λ is sought so that the shear force $\mathbf{F}_i$ is on the yield surface, i.e. $f = (\mathbf{F}_i \mathbf{F}_i)^{1/2} - \mu_i F_n = 0$. To bracket Λ on the yield surface, a pair of values of Λ are needed, i.e. values that result in negative and positive values of *f*. One of the bracketing ends of Λ can be taken as 0, i.e. for the case of full elastic update outside the yield surface. The other bracketing value for Λ should result in the shear stress being inside the yield surface. As a first approximation, it can be taken as $\Lambda = \dfrac{\mathbf{du}}{\mathbf{F}_0}$. If this shear stress is outside the yield surface, Λ is iteratively increased until it lies inside the yield surface. With a pair of bracketing range for Λ, the remaining unknowns in the yield surface (Eq. (F.8)) are the shear force $\mathbf{F}_i$ and the current friction coefficient μ_i. The first can be calculated from Eq. (F.7), and the second from $\mu_i = g(\beta_i)$ where β_i can in turn be calculated from Eq. (F.6). Bracketing algorithms can be used for this purpose.

APPENDIX G – SOLUTION FOR BOLT FORCES FROM CARRANZA-TORRES (2009)

The full equations have been provided by Carranza-Torres (2009), and are not reproduced here. His solution for bolt forces requires two dimensionless variables as input, namely α and β, defined as:

$$\alpha = \frac{n_b A_b}{2\pi a s_l} \tag{G.1}$$

$$\beta = \frac{\alpha E_b}{2G} \tag{G.2}$$

where n_b is the number of rock bolts assuming that the bolt pattern covers the entire circumference, a is the opening radius s_l is the bolt spacing in the longitudinal (out-of-plane) direction along the opening axis, A_b is the cross-sectional area of the bolt, E_b is the Young's modulus of the bolt, and G is the shear modulus of the rock mass.

Substituting α into β, we obtain:

$$\begin{aligned}\beta &= \left(\frac{n_b A_b}{2\pi a s_l}\right)\frac{E_b}{2G} \\ &= \left(\frac{n_b}{2\pi a s_l}\right)\frac{\left(E_b A_b \big/ L_b\right)L_b}{2G} \\ &= \left(\frac{n_b}{2\pi a s_l}\right)\frac{K_a L_b}{2G} \\ &= \left(\frac{1}{s_\theta s_l}\right)\frac{K_a s_{mean}}{2G}\end{aligned} \tag{G.3}$$

where s_θ is the bolt spacing in the tangential direction (units: m), s_l is the bolt spacing in the longitudinal direction along the tunnel axis, L_b is the characteristic length of the bolt put into tension across the rock discontinuities (or the mean distance between reinforced rock joints along the bolt direction), s_{mean} is the mean rock discontinuity spacing, and K_a is the bolt stiffness acting across a rock joint (units: N/m) which can be derived experimentally based on the procedures recommended by Stillborg (1994). Note that the assumption of $E_b A_b = K_a s_{mean}$ is consistent conceptually with the equations that are used in Goodman (1989) to

derive the rock mass deformability from the rock joint stiffness (Eqs. (5.6) and (5.7), p. 127 in main text). To calculate the bolt forces from Eq. (15) in Carranza-Torres (2009), the variables $\beta A_b / \alpha$ can be calculated as $\frac{K_a s_{mean}}{2G}$.

References

Carranza-Torres, C. (2009). Analytical and numerical study of the mechanics of rockbolt reinforcement around tunnels in rock masses. Rock Mechanics and Rock Engineering, 42(2), 175-228.

Goodman, R. E. (1989). Introduction to Rock Mechanics (2 ed.): John Wiley & Sons.

Stillborg, B. (1994). Professional users handbook for rock bolting (2 ed.): Trans Tech Publications, Limited.

APPENDIX H – SOLUTION FOR HOOP FORCES OF LINING UNDER ISOTROPIC PRESSURE

The expressions to calculate the axial lining forces are derived here for plane-strain. For an elastic medium with shear modulus, G, subjected to isotropic pressure, p_0, the radial displacements for an opening of radius, a, can be calculated through the expression:

$$\frac{\Delta u_{\text{ground}}}{a} = \frac{p_0 - \Delta p}{2G} \tag{H.1}$$

where Δu_{ground} is the radial displacement and Δp is the internal support pressure. The tangential strains of a thin-walled cylinder subjected to an external pressure is:

$$\varepsilon_{\theta\theta} = \frac{a\Delta p}{E_{\text{L}} t}(1 - v_{\text{L}}^2) \tag{H.2}$$

where t is the thickness, E_{L} is the Young's modulus and v_{L} is the Poisson's ratio of the cyliner. The radial displacement of the lining, Δu_{lining}, can then be calculated as:

$$\frac{\Delta u_{\text{lining}}}{a} = \frac{a\Delta p}{E_{\text{L}} t}(1 - v_{\text{L}}^2) \tag{H.3}$$

In the algorithm to model lining support, the pressure exchanged between the lining and the ground is calculated from the penetration distance, Δu_{node}, of the lining nodes into the ground. The penetration distance can be expressed as:

$$\frac{\Delta u_{\text{node}}}{a} = \frac{\Delta p}{K_{\text{L}} a} \tag{H.4}$$

where K_{L} is the contact stiffness between the ground and lining. The displacements have to satisfy the following compatibility equation:

$$\frac{\Delta u_{\text{ground}}}{a} = \frac{\Delta u_{\text{lining}}}{a} + \frac{\Delta u_{\text{node}}}{a} \tag{H.5}$$

Combining the equations and ignoring v_{L}^2 to be consistent with the DEM models, we obtain:

$$\Delta p = \frac{p_0 E_{\text{L}} t K_{\text{L}}}{2K_{\text{L}} G a + \dfrac{2E_{\text{L}} t G}{a} + E_{\text{L}} t K_L} \tag{H.6}$$

from which we can deduce the hoop force, N, as $N = a\Delta p$.

APPENDIX I – SMOOTHING OUT OF THE BENDING MOMENT (CORRECTION FOR THE NUMERICAL ARTIFACTS CAUSED BY THE POLYGONAL APPROXIMATION OF A CIRCULAR OPENING)

The bending moment for each linear segment forming the polygonal lining can be fitted with a parabola $wx^2 + by + c$, so that the pressure Δp acting along each linear segment can be approximated as $\Delta p = 2w$. Then, these pressures are assumed to act radially on a circular ring structure (see Fig. I.1). There will be out-of-balanced radial forces because the frictional resistance at the lining-rock interface has not been accounted yet (Muir Wood, 1975). Here, the shear resistance afforded by the lining-rock interface is approximated as (see Fig. I.2):

$$\tau = A\cos\theta + B\sin\theta + C \tag{I.1}$$

The first term, after integration around the ring, should be equal and opposite to the out-of-balanced vertical forces $F_{\text{verticalOUB}}$; the second term on integration should be equal and opposite to the out-of-balanced horizontal forces $F_{\text{horizontalOUB}}$; and the third term on integration should be equal and opposite to the out-of-balanced moment M_{OUB} (after accounting for the first two terms), so that:

$$A = -\frac{F_{\text{verticalOUB}}}{\pi a} \tag{I.2}$$

$$B = -\frac{F_{\text{horizontalOUB}}}{\pi a} \tag{I.3}$$

$$C = -\frac{M_{\text{OUB}}}{2\pi a^2} \tag{I.4}$$

where a is the radius of the ring. The bending moment on a ring subject to an arbitrary pressure distribution can be calculated following standard procedures for an indeterminate ring structure (Timoshenko & Young, 1965, Chapter 8).

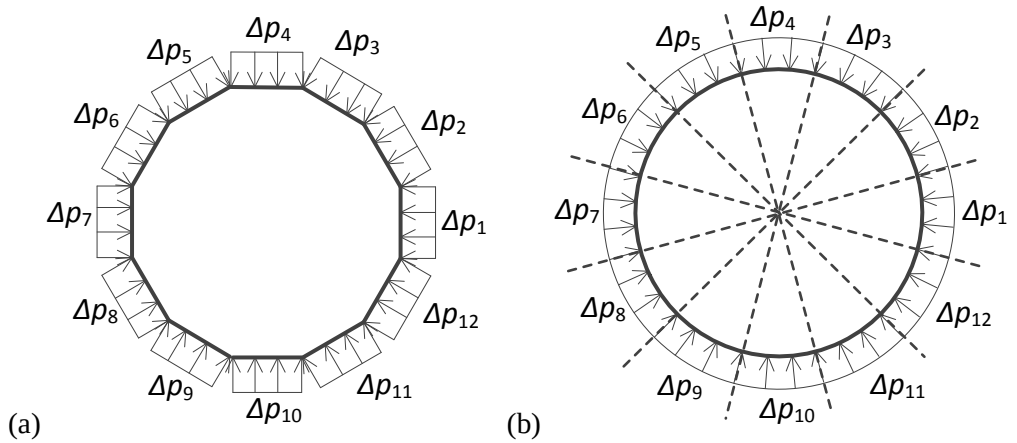

Fig. I.1. Pressure distribution on (a) a polygonal frame is assumed to act radially on (b) a ring

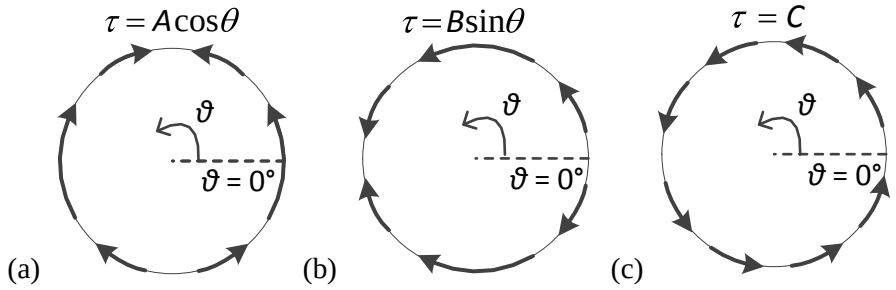

Fig. I.2. Shear patterns for different terms in Fig. (I.1) to account for (a) the vertical out-of-balanced forces, (b) the horizontal out-of-balanced forces and (c) out-of-balanced moment

References

Muir Wood, A. M. (1975). Circular tunnel in elastic ground. Geotechnique, 25(1), 115-127.

Timoshenko, S., & Young, D. H. (1965). Theory of Structures: McGraw-Hill.